

The Pennsylvania State University  
The Graduate School  
The Eberly College of Science

**MANGANITE AND  $\text{YBa}_2\text{Cu}_3\text{O}_7$  SPINTRONIC DEVICES**

A Thesis in

Physics

by

Eric T. Wertz

©2004 Eric T. Wertz

Submitted in Partial Fulfillment  
of the Requirements  
for the Degree of

Doctor of Philosophy

December 2004

The thesis of Eric Wertz has been reviewed and approved\* by the following:

Qi Li

Professor of Physics

Thesis Advisor

Chair of Committee

Jainendra K. Jain

Erwin W. Mueller Professor of Physics

Roy F. Willis

Professor of Physics

Thomas N. Jackson

Professor of Electrical Engineering

Jayanth R. Banavar

Professor of Physics

Head of the Department of Physics

\*Signatures are on file in the Graduate School.

## Abstract

Manganite and  $\text{YBa}_2\text{Cu}_3\text{O}_7$  (YBCO) spintronic devices were created and tested. High tunneling magnetoresistance, a high resistance demagnetized state, and applied field angular dependences were found in manganite magnetic tunnel junctions. A switching signal and applied field angular dependence was seen YBCO/manganite spin diffusion measurement devices. Various unique YBCO/-manganite critical current suppression devices were measured and showed rather small gains.

$\text{La}_{0.67}\text{Sr}_{0.33}\text{MnO}_3/\text{SrTiO}_3/\text{La}_{0.67}\text{Sr}_{0.33}\text{MnO}_3$  (LSMO/STO/LSMO) magnetoresistive tunnel junctions were produced and tested. The junction resistance was measured as a function of temperature and magnetic field applied at various out-of-plane angles. A tunneling magnetoresistance (TMR) of 360% was found at 5K for the LSMO/STO/LSMO junctions. The TMR signal was present up to a temperature of 275K. Angular measurements showed increased switching fields with similar TMR values. An unusual high resistance state was found when the samples were demagnetized at low temperatures. Demagnetized samples showed higher TMR values and sharp switching in low magnetic field sweeps than when measured in standard high magnetic field sweeps. A TMR of 457% was found at 5K for the same LSMO/STO/LSMO junction quoted above. Differences in resistance between the demagnetized state and the lowest measured resistance state show that the TMR could be as large as 800% at 5K. Current-voltage (IV) measurements were taken and fit with a Simmons model to obtain the insulating barrier height and thickness.  $\text{La}_{0.67}\text{Ca}_{0.33}\text{MnO}_3$  (LCMO) / STO / LSMO junctions were also created and displayed anomalous temperature and angular

dependence with varying TMR values.

LSMO/YBCO/LSMO spin diffusion measurement devices were created. Voltage was measured between a LSMO pad and a gold pad in contact with a thin YBCO layer subject to an injection current from a bottom LSMO layer. A voltage in such a configuration has been proposed to be generated by the diffusion of spin in the YBCO layer. Spin-like switching effects were seen. The voltage showed sharp switching between two states. An inversion in the switching between the two states was found based on the orientation of the sample in relation to the magnetic field. Effects were seen to differ from hall signals of a single LSMO layer. A spin diffusion length in YBCO at 100K was estimated be,  $\delta_s \approx 0.1\mu m$ . A variety of YBCO/STO/LSMO and YBCO/STO/LaNiO<sub>3</sub> (LNO) critical current suppression devices were created. The critical current of the YBCO was measured as a function of current injected from the LSMO/LNO layer. LSMO is a colossal magnetoresistive material (CMR) and is believed to have a highly spin polarized current (>80%). LNO is a unpolarized normal metal. The non-equilibrium state imposed by an injected polarized spin overpopulation in superconducting YBCO has been proposed to have a larger critical current suppression than the unpolarized case. However, differences between the two injection cases are not found to be appreciable. Gains ( $-dI(C)/dI(Inj)$ ) are found to be  $\approx 1 - 3$  at temperatures from 80K - 20K for both injection scenarios. The largest gain for any device was  $\approx 5$ , far below the critical temperature of YBCO.

# Contents

---

<b>List of Figures</b>	<b>ix</b>
<b>List of Tables</b>	<b>xv</b>
<b>Acknowledgements</b>	<b>xvi</b>
<b>1 Introduction</b>	<b>1</b>
1.1 Introduction . . . . .	1
<b>2 Experimental Techniques and Materials</b>	<b>5</b>
2.1 Pulsed Laser Deposition . . . . .	5
2.2 YBa <sub>2</sub> Cu <sub>3</sub> O <sub>7</sub> Deposition . . . . .	12
2.2.1 YBCO Crystal and Electronic Structure . . . . .	12
2.2.2 Typical Ablation Characteristics . . . . .	15
2.2.3 YBCO deposition parameters . . . . .	18
2.3 La <sub>0.33</sub> Sr <sub>0.67</sub> MnO <sub>3</sub> and LaNiO <sub>3</sub> deposition . . . . .	20
2.3.1 LSMO and LNO Crystal and Electronic Structure . . . . .	20
2.4 SrTiO <sub>3</sub> deposition . . . . .	26
2.5 Substrates . . . . .	27

2.6	Evaporation of Gold Contacts . . . . .	28
2.7	SiO <sub>2</sub> , Au, and Cr sputtering . . . . .	30
2.8	Photolithographic Processing . . . . .	32
2.8.1	Ion milling . . . . .	35
2.8.2	Au/YBCO contact recovery after Ion Milling . . . . .	38
2.9	Low Temperature Measurement Apparatus . . . . .	43
2.10	Transport Measurement Setup . . . . .	46
<b>3</b>	<b>Colossal Magnetoresistive Tunnel Junctions</b>	<b>50</b>
3.1	Introduction . . . . .	50
3.2	LSMO/STO/LSMO Magnetic Tunnel Junctions . . . . .	59
3.2.1	Device Fabrication, Characterization, and Measurement Technique . . . . .	59
3.2.2	Standard Tunneling magnetoresistance and Angular Effects. . . . .	66
3.2.3	TMR Measurements in Demagnetized State . . . . .	80
3.2.4	I-V Measurements . . . . .	87
3.3	Anomalous angular TMR effects in LCMO/STO/LSMO tunnel junctions . . . . .	95
<b>4</b>	<b>Spin Diffusion Devices</b>	<b>100</b>
4.1	Introduction . . . . .	100
4.2	Device and Measurement . . . . .	113
4.2.1	Device Geometry and Fabrication . . . . .	113
4.2.2	Data and Discussion . . . . .	116

<b>5</b>	<b>Critical Current Suppression Injection Devices</b>	<b>140</b>
5.1	Introduction . . . . .	140
5.1.1	Controllable Weak Links and Quasi-particle injection devices . . . . .	140
5.1.2	Spin Injection Critical Current Suppression Devices . . . . .	146
5.2	Devices and Measurements . . . . .	156
5.2.1	YBCO/LBMO Cross Strip $I_C$ Suppression Device . . . . .	156
5.2.2	YBCO/LBMO $I_C$ suppression device with unpatterned LBMO . . . . .	157
5.2.3	YBCO/I/LSMO Four Terminal $I_C$ Suppression Device . . . . .	159
5.2.4	YBCO/I/LSMO Five Terminal $I_C$ Suppression Device . . . . .	163
5.2.5	YBCO/I/LSMO Multi-Terminal $I_C$ Suppression Device . . . . .	166
<b>6</b>	<b>Conclusions and Future Work</b>	<b>175</b>
<b>A</b>	<b>Determination of Maximum Beam Current and Beam Stabilization for the ion mill.</b>	<b>179</b>
<b>B</b>	<b>Magnetic Field vs. Current for GMW model 5403 Electromagnet</b>	<b>182</b>
<b>C</b>	<b>YBa<sub>2</sub>Cu<sub>3</sub>O<sub>7</sub> (YBCO) PLD parameters</b>	<b>184</b>
<b>D</b>	<b>La<sub>0.67</sub>Sr<sub>0.33</sub>MnO<sub>3</sub> (LSMO) PLD Parameters</b>	<b>186</b>
<b>E</b>	<b>LaNiO<sub>3</sub> (LNO) PLD Parameters</b>	<b>188</b>
<b>F</b>	<b>SrTiO<sub>3</sub> (STO) PLD Parameters</b>	<b>190</b>

<b>G Notes on the Excimer Laser</b>	<b>192</b>
G.0.6 General Notes . . . . .	192
G.0.7 New Gas Fill Procedure . . . . .	195
<b>H PLD Multi-Target Rotation System</b>	<b>198</b>
<b>I Substrate Heater</b>	<b>207</b>
<b>J Photolithographic Processing</b>	<b>210</b>
<b>K Labview Programs</b>	<b>212</b>
K.0.8 Resistance vs. Temperature Program . . . . .	212
K.0.9 Resistance vs. Magnetic Field Program . . . . .	214
K.0.10 Temperature Control Programs . . . . .	216
K.0.11 The IV programs . . . . .	218
K.0.12 The dI/dV program . . . . .	222
<b>L Sputtering conditions for Au and SiO<sub>2</sub></b>	<b>224</b>
<b>M Ion Milling Conditions</b>	<b>226</b>
<b>N Sherlock Holmes</b>	<b>228</b>
<b>Bibliography</b>	<b>230</b>

## List of Figures

---

2.1	Basic PLD configuration. [Argonne National Laboratory Website] . . . . .	6
2.2	Structural phase diagram of $\text{YBa}_2\text{Cu}_3\text{O}_X$ . [Mourachkine 2002] . . . . .	13
2.3	The $\text{YBa}_2\text{Cu}_3\text{O}_7$ orthorhombic unit cell. [Mourachkine 2002] . . . . .	15
2.4	Formation of cone like structures on the ablated surface of a YBCO target. [Foltyn 1991b] . . . . .	16
2.5	Splitting of the five-fold degenerate 3d levels in LSMO. [Tokura 1999] . . .	22
2.6	$e_g$ and $t_{2g}$ d-orbitals of the Manganese (Mn) atom. [Cox 1992] . . . . .	22
2.7	Electronic phase diagram of $\text{La}_{1-x}\text{Sr}_x\text{MnO}_3$ . [Tokura 1999, Urushibara 1995, Fujishiro 1998] . . . . .	24
2.8	The cubic STO unit cell and the psuedo-cubic LSMO unit cell. [Lyonnet 2000]	24
2.9	Thickness vs spin speed for Shipley Microposit S1800 series photoresist - [Shipley Company]. . . . .	33
2.10	Contact resistance vs. temperature for Au contacts on various pre-ion milled YBCO samples. . . . .	41
2.11	Contact resistance vs. temperature for Au contacts on various pre-ion milled YBCO samples, before and after annealing. . . . .	42
2.12	Timing schematic for electrical current-voltage measurements. . . . .	49
3.1	Tunneling in a F/I/S(BCS) junction [Tedrow 1970-73] . . . . .	52

3.2	Tunneling magnetoresistance as a function of applied voltage in a Co/STO-/LSMO junction. [Teresa 1999] . . . . .	56
3.3	Tunneling in a CoFe/Al <sub>2</sub> O <sub>3</sub> /Co (F/I/F) junction [Moodera 1995] . . . . .	57
3.4	Schematic of junction fabrication process. . . . .	61
3.5	Resistance vs. field for a LSMO bridge. . . . .	63
3.6	Resistance vs. temperature for the top and bottom LSMO layers of a LSMO/STO/LSMO heterostructure. . . . .	64
3.7	Resistance vs. magnetic field for a LSMO/STO/LSMO junction at various temperatures. . . . .	70
3.8	Resistance vs. magnetic field for a LSMO/STO/LSMO junction at various temperatures. . . . .	71
3.9	Tunneling magnetoresistance % vs. temperature for two LSMO/STO/LSMO junctions. . . . .	72
3.10	Resistance vs. magnetic field for a LSMO/STO/LSMO junction with fields applied at various out-of-plane angles. . . . .	73
3.11	Resistance vs. applied magnetic field for a LSMO/STO/LSMO at 5K with fields applied at 0° and 90° relative to the plane of the sample. . . . .	74
3.12	Zero field rotation of a premagnetized LSMO/STO/LSMO junction. . . . .	75
3.13	Low field hysteresis scan for a LSMO/STO/LSMO junction. . . . .	76
3.14	Resistance vs. temperature for a LSMO/STO/LSMO junction. (1) . . . . .	79
3.15	Resistance vs. applied magnetic field for a LSMO/STO/LSMO junction after demagnetization at 5K. . . . .	83
3.16	Hysteresis for a LSMO/STO/LSMO junction after demagnetization at 5K. . . . .	84
3.17	Resistance vs. Angle for rotation of a LSMO/STO/LSMO junction in a constant magnetic field after demagnetization at 5K. . . . .	85

3.18	Resistance vs. temperature for a LSMO/STO/LSMO junction. (2) . . . . .	86
3.19	Current vs. voltage for two LSMO/STO/LSMO junctions at various temperatures and resistive states. . . . .	89
3.20	Current vs. voltage for a LSMO/STO/LSMO junctions at various temperatures and resistive states, including the demagnetized state. . . . .	90
3.21	Conductance (dI/dV) vs. voltage for a LSMO/STO/LSMO junctions at various temperatures and resistive states, including the demagnetized state. . . . .	91
3.22	Tunneling magnetoresistance % vs. applied current for two LSMO/STO/LSMO junctions. . . . .	92
3.23	Tunneling magnetoresistance % vs. applied current for a LSMO/STO/LSMO junction in two resistive states. . . . .	93
3.24	Resistance vs. applied magnetic field for a LCMO/STO/LSMO junction at 100K with fields applied at various out-of-plane angles. . . . .	97
3.25	Resistance vs. applied magnetic field for a LCMO/STO/LSMO at 150K and 50K with fields applied at various out-of-plane angles. . . . .	98
3.26	Resistance vs. temperature for a LCMO/STO/LSMO junction. . . . .	99
4.1	Schematic of a bipolar spin switch device. [Hershfield 1997] . . . . .	101
4.2	Sketch of chemical potentials and density of states in spin injection scenario for Johnsons spin diffusion device. [van Son 1987, George 2003] . . . . .	102
4.3	Giant planar hall effect in (Ga,Mn)As. [Tang 2003] . . . . .	107
4.4	Giant planar hall effect in $\text{La}_{0.84}\text{Sr}_{0.16}\text{MnO}_3$ . [Bason 2004] . . . . .	108
4.5	Diagram of field rotation plane relative to the film plane. [Ogrin 2000] . . . . .	109
4.6	Voltage vs. angle and magnetic field for planar hall effects in a Co thin film. [Ogrin 2000] . . . . .	110
4.7	Resistance vs. magnetic field for a (Ga,Mn)As/ $\text{Al}_2\text{O}_3$ /Au (F/I/N) junction. [Gould 2004] . . . . .	112

4.8	Schematic of diffusion measurement device fabrication process. . . . .	115
4.9	Schematic of spin diffusion measurement device. . . . .	116
4.10	Resistance vs. magnetic field for a LSMO/YBCO/LSMO spin diffusion device. Data is shown for fields applied at various in-plane angles. . . . .	118
4.11	Resistance vs. magnetic field for a LSMO/YBCO/LSMO spin diffusion device. The displayed data is for fields applied at various out-of-plane angles. (1) . . . . .	120
4.12	Resistance vs. magnetic field for a LSMO/YBCO/LSMO spin diffusion device. The displayed data is for fields applied at various out-of-plane angles. (2) . . . . .	121
4.13	Resistance vs. magnetic field for a LSMO/YBCO/LSMO spin diffusion device. Data is shown for fields applied at various out-of-plane angles. (3) . . . . .	122
4.14	Cross resistance vs. angle for a LSMO/YBCO/LSMO spin diffusion device in a constant applied magnetic field. . . . .	124
4.15	Resistance vs. magnetic field for a LSMO/YBCO/LSMO spin diffusion device. Data is shown for parallel current and field at various temperatures. . . . .	126
4.16	Gold to gold resistance vs. magnetic field for a LSMO/YBCO/LSMO spin diffusion device. . . . .	128
4.17	Resistance vs. magnetic field for a LSMO/YBCO/LSMO spin diffusion device. Data is shown for fields applied at various out-of-plane angles. (1000Å YBCO) . . . . .	130
4.18	Cross resistance vs. magnetic field for a patterned single layer LSMO thin film. Data is shown for fields applied at various in-plane angles. . . . .	132
4.19	Cross resistance vs. applied magnetic field for a patterned single layer LSMO thin film. Data is shown for fields applied at various out-of-plane angles. . . . .	134
4.20	Resistance vs. magnetic field for a patterned single layer LSMO thin film. Data is shown for fields applied at various out-of-plane angles. . . . .	136

4.21	Resistance vs. magnetic field for a patterned single layer LSMO thin film. Data is shown for fields applied at various in-plane angles. . . . .	137
5.1	Schematic of 3 terminal controllable weak link (CLINK). [Wong 1997] . . .	141
5.2	Schematic of a quasiparticle injection device. [Boguslavskij 1994] . . . . .	144
5.3	Schematic of current summation effect in 3 terminal device. . . . .	145
5.4	Schematic of spin injection $I_C$ suppression device with unpatterned injection layer. [Vas'ko 1997] . . . . .	149
5.5	Schematic of 4 terminal spin injection $I_C$ suppression device. [Dong 1997] .	151
5.6	Picture of YBCO/LBMO $I_C$ suppression cross strip device. . . . .	157
5.7	Critical current vs. injected current for a YBCO/LBMO injection device with unpatterned LBMO. . . . .	158
5.8	Schematic and picture of a YBCO/STO/LSMO side injection 4 terminal device.	159
5.9	Critical current vs. injection current and V-I curves for side injection 4 terminal suppression device. . . . .	162
5.10	Schematic of YBCO/STO/LSMO five terminal injection device. . . . .	164
5.11	Critical vs. injection current for a several five terminal YBCO/STO/LSMO devices. . . . .	165
5.12	Multi-terminal device for YBCO/STO/(LSMO or LNO) device. . . . .	167
5.13	Schematic of transmission line model. [Gim 2001, Berger 1972] . . . . .	167
5.14	Normalized and raw critical vs. injection current for various multi-terminal injection devices . . . . .	171
A.1	Determination of maximum ion mill beam current. . . . .	180
A.2	Beam current shown as a function of time after initial startup. . . . .	181
B.1	Magnetic field vs. current for GMW model 5403 electromagnet. . . . .	183

H.1	PLD rotation system base plate flange . . . . .	199
H.2	PLD rotation system middle platform plates and shield . . . . .	200
H.3	PLD rotation system platform supports, carousel supports, and carousel rotation shaft . . . . .	201
H.4	PLD rotation system target holders . . . . .	202
H.5	PLD rotation system carousel plates . . . . .	203
H.6	Side view of PLD target rotation system . . . . .	204
H.7	Top view of PLD target rotation system . . . . .	205
I.1	PDL heater parts . . . . .	208
I.2	PDL heater schematic (side view) . . . . .	209

## List of Tables

---

2.1	Lattice mismatch of materials and substrates. . . . .	28
3.1	Tunneling magnetoresistance results from other studies. . . . .	58
3.2	Calculated tunneling barrier height and thickness by Simmons equation fit for two LSMO/STO/LSMO tunnel junctions. . . . .	94
C.1	Optimal parameters for pulsed laser deposition of YBCO . . . . .	185
D.1	Optimal parameters for pulsed laser deposition of LSMO . . . . .	187
E.1	Optimal parameters for pulsed laser deposition of LNO . . . . .	189
F.1	Optimal parameters for pulsed laser deposition of STO . . . . .	191
H.1	Table of parts purchased for target rotator system. . . . .	206
L.1	Sputtering conditions for Au and SiO <sub>2</sub> in the EMPRL facility . . . . .	224
L.2	Sputtering conditions for Au in our lab . . . . .	225
M.1	Ion milling parameters and rates. . . . .	227

## Acknowledgements

---

I'd like to give special thanks to:

Qi Li, Ben Sheng-Yong Xu, Yufeng Hu, Huisheng Wang, Anna Clark, Ricky O'Haire, Xiaoxing Xi, David Sarge, Fawn Houtz, Ed Basgall, Weidong Si, Chris Nordquist, Karl Nelson, Arsen Sukiasyan, Jun Chen, Pasquale Orgiani, Rob Morasco, Chris Beetle, Roger Herman, Milton Cole, John Passaneau, and Barry Dutrow. And, especially Randi Neshteruk and Chris Woods, without whom I'd still be in graduate school.

My Parents, Herman & Susan Wertz. Hans, Nicky, and Josie. Uncle Ed, June, Laura, and Caroline. Uncle Bob and Nicky. Uncle Art. My Grandparents, Charlie & Agnes Dotts. My Grandparents, Clarence & Dorothy Sampey.

Tony and Sylvie Ragucci, Nat and Margo Janke-Gilman. James "Conel" Kurtz. Amy and Greg Mitchell-Cook. Erik and Jen Stieler. Susan Riddiford. Charlie Cino. Jana, Mary, Mandy, and the rest of the depraved history group.

State College Community Theater. No Refund Theater. The Next Stage. The Cartoon Network's [Adult Swim].

A specially thanks is given to my cat, Jasmine, for many useful discussions. And, to my wonderful wife, Mari-Anne. I love you.

*December 2004*

*Eric T. Wertz*

## Chapter 1

# Introduction

---

### 1.1 Introduction

Four recent major physics discoveries form much of the basis of this thesis. In chronological order the first was Johnson and Silsbee's proposal and construction of a spin injection and detection device in 1985, followed by their invention of the bipolar spin switch in 1988 [Johnson 1985, Johnson 1988a, 1988b, 1988c]. These devices made possible the measurement of the diffusion length of spin within a paramagnetic metal. The bipolar spin switch device consisted of a bottom ferromagnetic layer, a middle metallic layer, and two top electrodes, one metal, one ferromagnetic. In Johnson and Silsbee's model, a relative voltage between the top two electrode's develops from and is proportional to an imposed overpopulation of coherently aligned spins in the metallic layer. This condition can be created by injecting spins, via a transport current, from the bottom ferromagnet into the middle metallic layer. By manipulating the magnetization of the top and bottom ferromagnetic layers, a change in voltage can be measured and used to determine the spin scattering rate in the metallic material. Jedema *et al.* have recently found very good results in Co/Al microstructures [Jedema 2001-03]. Presently spintronics is a broadly applied and accepted concept.

Second was the discovery of high- $T_c$  superconductivity. In 1986, Bednorz and Muller, discovered high temperature superconductivity in the copper oxide  $\text{La}_2\text{SrCuO}_4$  (LSCO)

[Bednorz 1986]. LSCO was found to have a transition temperature ( $T_c(0)$ ) of 30K. (Later it was improved to have a maximum  $T_c(0)$  of 38K.) Soon after, Wu *et al.* discovered superconductivity above 77K in another copper oxide,  $\text{YBa}_2\text{CuO}_{7-\delta}$  (YBCO) [Wu 1987]. YBCO was found to have a transition temperature of 93K. For the first time superconductivity could be studied above liquid nitrogen temperatures making it more financially attainable for experimental work and technological applications. Since then, an explosion of experimental work has been put forth. Even with the large amount of accumulated experimental data, the underlying microscopic electronic mechanism of these new high temperature superconducting materials remains a mystery.

The third discovery came in 1993 when the colossal magnetoresistance effect was discovered in manganite thin films independently by Helholt *et al.* and Chahara *et al.* [Helholt 1993, Chahara 1993]. The manganites were originally studied in a bulk form in 1950 by Wollan and Koehler [Wollan 1953-55]. Under certain doping conditions manganites are ferromagnetic. As thin films, these ferromagnets displayed unusually high changes in resistivity with the application of a high magnetic field (on the order of 1 Tesla), thus giving them their name colossal magnetoresistive (CMR) materials. These materials were found to have a high spin polarization in their transport current [Soulén 1998, Park 1998, Wei 1997]. Also, the perovskite oxide structure was a good match for the YBCO perovskite structure and accompanying substrates.

The fourth key discovery was giant magnetoresistive (GMR) tunnel junctions. GMR tunneling was developed by Moodera *et al.* and the pair of Miyazaki and Tezuka at roughly the same time in 1995 [Moodera 1995, Miyazaki 1995]. Devices consist of two ferromagnets separated by an insulating layer. Moodera's junctions, made of  $\text{Co}/\text{Al}_2\text{O}_3/\text{CoFe}$ , revealed a tunneling magnetoresistance (TMR) ratio of up to 10% at room temperature. These experiments were almost immediately applicable in technological applications and revolutionized magnetic read head technology.

One immediately apparent combination of the above discoveries is the application of CMR materials in GMR junctions. The high degree of polarization in CMR materials seems to make their application to TMR junctions very promising. But, CMR TMR junctions have never been found to work successfully above room temperature and have not usually displayed results indicative of their highly polarized current.

$\text{La}_{0.67}\text{Sr}_{0.33}\text{MnO}_3 / \text{SrTiO}_3 / \text{La}_{0.67}\text{Sr}_{0.33}\text{MnO}_3$  (LSMO / STO / LSMO) magnetoresistive tunnel junctions were created and tested in this study. Devices showed a large TMR ( $\approx 350\%$ ) at low temperatures and maintained these switching effects to 275K. The dependence on out-of-plane applied magnetic fields was investigated. The TMR magnitude was largely unchanged while the switching fields were found to increase. Low field switching was found when the samples were reoriented angularly. The temperature dependence for the resistance showed evidence of a deteriorated region between the LSMO/STO interface that may provide an explanation for the disappearance of the TMR signal below the Curie temperature of the LSMO.

A unusual high resistance state was found for perpendicularly demagnetization at low temperatures. Demagnetized samples showed higher TMR values and sharper switching in low magnetic field sweeps than when measured with the standard high magnetic field sweep technique. A TMR  $\approx 450\%$  was found at low temperatures, for the same LSMO/STO/LSMO junctions mentioned above. I-V characteristics were also measured and fit to a Simmons model.  $\text{La}_{0.67}\text{Ca}_{0.33}\text{MnO}_3(\text{LCMO})/\text{STO}/\text{LSMO}$  junctions were also created. The TMR displayed anomalous angular and temperature dependence.

A spin diffusion measurement device, similar to Johnson and Silsbee's bipolar spin device, was constructed and tested in this study. YBCO was the metallic material, with a bottom LSMO injection layer. Two leads, one gold, one LSMO were arranged on either side of the YBCO layer. The LSMO pad detects change due to spin population and the Au acts as a ground. A detection voltage was measured. A switching signal, which resemble

those of the before mentioned TMR junctions, arose for thin YBCO samples. Various lead configurations were investigated. The detection voltage showed sharp switching between two states. An inversion in the switching between the two states was found based on the orientation of the sample in relation to the magnetic field. The signal maybe due to a combination of spin diffusion signal, anomalous Hall effects, and magnetoresistive background effects. However, device results were seen to differ from hall-like measurements of a single LSMO layer. A spin diffusion length in YBCO at 100K was estimated be,  $\delta_s \approx 0.1\mu m$ .

Since 1997, several groups have studied the suppression of critical current in YBCO due to spin injection. Devices used to measure this effect consist of a ferromagnetic layer in contact with a superconducting layer. Current is applied through the interface and a test current measures the critical current of the superconductor. The imposed spin current creates a polarization in what would otherwise be a overall spin neutral system. It has been proposed this may cause a larger critical current suppression than normal non-polarized quasiparticle injection. However, results in this field of study are widely scattered and disputed, and recently many early results have been called into question.

Several different critical current suppression devices were constructed and tested in this thesis. Unique devices were designed in such a way as to reduce problems associated with earlier devices. Comparison between devices made with ferromagnetic layers and those with normal metallic layers yielded little to no difference. In general device gains,  $(-dI_C/dI_{inj})$ , were small ( $<5$ ).

A great deal of effort was devoted to the creation and measurement of the devices, data acquisition programs, and photolithographic processes presented in this thesis. The experimental techniques presented in chapter 2.1 are intended to provide a clear and concise record for future projects.

# Experimental Techniques and Materials

---

### 2.1 Pulsed Laser Deposition

Pulsed laser deposition (PLD), also known as laser ablated deposition (LAD), is a powerful tool for the experimental physicist. It provides a simple yet effective process for the growth of a wide class of exotic materials into thin film heterostructures. Materials grown for this thesis were mostly perovskite crystal oxides. But, PLD growth is far from limited to these materials and is a branch of experimental research unto itself. Good reviews are available in [Jackson 1994, Saenger 1994, Chrisey 1994].

PLD has many advantages over other deposition techniques including evaporation, sputtering, molecular beam epitaxy (MBE), and chemical vapor deposition (CVD) [Fukushima 1995, Willmott 2000, Foote 1992, Wellstood 1993]. Compared to the above, PLD has high deposition rates ( $> 60$  nm/min well within possible limits). The energy source (laser) is outside the vacuum. Almost any materials can be deposited including those with high melting temperatures. The deposition species created during PLD have high energies ( $\sim 50$ eV) that promote surface mobility. Thin films of new materials are quickly attainable with PLD, since deposited films roughly reproduce the composition of the target. And, PLD is tolerant of high background oxygen pressures ( $> 100$  mT). But, most importantly, PLD is capable of creating *in situ* heterostructures of several materials with complex stoichiometries.

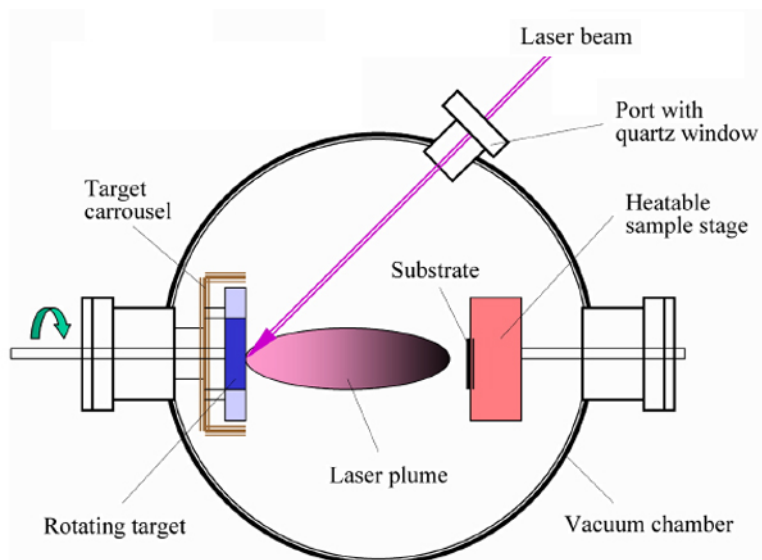


**Figure 2.1:** Basic PLD configuration. [Argonne National Laboratory Website]

A problem that plagues PLD is the deposition of large particulates during film growth. While in some cases these particulates are not critical in determining the electrical properties of a film, they are a problem in thin film heterostructure devices. (For YBCO, rougher films can actually have a higher critical current by providing more vortex pinning centers [Siegal 1992].) Defects can cause leakage current and electrical shorts between layers which can dominate the devices electrical properties. With the correct choice of deposition parameters and a careful investigation of the growth structure corresponding to those conditions, particle production can be minimized. Very smooth and mostly particle free films, ( $< 10^4$  particles/cm<sup>2</sup>), have been reported [Foote 1992, Schilling 1993].

The Basic PLD apparatus consists of a stainless steel vacuum chamber with a transparent optical window. The system is pumped to a high vacuum state ( $< 10^{-5}$  Torr). Laser light pulses arrive via the window and impinge on a target material. Material is then ablated onto a heated substrate located opposite the target at low vacuum or in a desired background gas.

In our apparatus, Laser light pulses were provided by an KrF Lambda Physics 305i excimer laser. The laser was filled with a premixed .097% F: 2.76% Kr: Ne Balance gas purchased from Spectra Gases. The light produced was of frequency 248 nm delivered in a 17 ns wide pulse. Light pulses of any energy in the range of 600mJ - 1300mJ could be produced by the laser. After a new fill of gas, the laser could typically maintain an energy of  $> 1000$  mJ for a one month period, after which a new fill of gas was required (see Appendix G for the gas fill procedure). The cross-sectional area of the beam was  $1 \times 2$  cm as it exited the laser. The laser and the optical table which contained all the lenses and collimators were mounted on two tables rigidly secured together.

Before the laser beam entered the chamber it was collimated by a smaller area hole in an aluminum plate in order to select the central uniform region of the beam area [Schilling 1993, Timm 1996]. Different area collimation plates were used to regulate total energy delivered to the target in order to obtain acceptable deposition rates. The collimated beam was then focused through the chambers quartz window onto the target via an external lens with a focal length of 30 cm. The lens to chamber distance was small  $\approx 11$ cm. Positioning the lens close to the window (rather than near the laser) is done to ensure the energy density of the light arriving at the quartz window stays low ( $< 0.1$  J/cm<sup>2</sup>). High energy densities can damage the quartz. The normal of the target surface was at a  $45^\circ$  angle to the incident beam. The focused spot area are was  $\sim .11$  cm<sup>2</sup>.

The light was focused on the target by placing a small wire grid on the collimator and observing the pattern produced at the target using laser alignment paper (Kentek) [Foote 1992]. The lens was adjusted in such a way as to provide a perfect image of the aperture and screen. Focusing the beam is important in order to prevent a diffuse border which would cause a non-uniform ablation region [Dam 1994, Timm 1996]. The pattern shown on the fax paper was also used to measure the focused beam area at the target, by viewing the region under a microscope and measuring it with calipers.

The spherical vacuum chamber (made by Kurt J Lesker) was 12 inches in diameter, contained multiple 3  $\frac{3}{4}$ , 6, and 10 inch ports, and was made of 304 stainless steel. Laser light was directed into the chamber through a fused quartz window (from Quartz Scientific) which transferred  $\approx 90\%$  of the impinging light intensity. While most material is preferentially deposited opposite the target, diffuse deposition material is constantly be deposited onto the chamber window. Light intensity inside the chamber was checked between every 10  $\sim$  20 runs to ensure the correct energy was present. When the energy loss became too great, the window was cleaned in dilute HCl acid ( $\approx 10\%$ ), rinsed with distilled water, and then rinsed clean with acetone and isopropanol. If the energy was still too low after cleaning the window was rotated so the beam could pass through a cleaner area, although this was seldom required. Usually more than 50 films could be made before any adjustment or cleaning was required (most films were 1000  $\text{\AA}$  or less).

Two vacuum gauges were used to monitor pressure inside the chamber. A Balzers PKR 251 compact full range vacuum gauge was used to monitor pressures  $<1$  Torr. The dual compact gauge was primarily used to monitor initial pump down pressures (usually  $5 \times 10^{-7}$  Torr) and the oxygen pressure maintained during deposition ( $\sim 100$  mTorr). The second gauge was a Granville-Philips 275 mini-convectron gauge used primarily for monitoring pressure during sample cool down ( $\sim 600$  Torr) and pressure when venting the system to prevent over pressurizing the chamber. Both gauges were located on a T-joint attached to the chamber. The T-joint prevented deposited materials from having a direct path to the gauge openings. Still, over time (1  $\sim$  2 years) gauges would become covered with material and had to be cleaned according to procedures in the manuals in order to assure proper readings.

A MKS mass flow controller maintained a steady 100 SCCM (standard cubic centimeter per minute) flow of 99.9995% pure oxygen into the chamber during deposition. The oxygen inlet was a stainless steel tube extending into the chamber which opened slightly above and

to the side of the surface of the heater, with the tube axis directed at the heater. Oxygen inlet tubes directed at the substrate during deposition are found to yield YBCO films with higher superconducting transition temperatures [Singh 1989]. In some PLD systems the oxygen inlet tubes is placed very close to the the target in order to create a higher level of atomic and/or ionic oxygen [Inam 1988]. But, inlets placed too close to the target may interfere unfavorably by thermalizing the ablated species [Singh 1989]. Also, inlet tubes placed too close to the substrate may cause non-uniform cooling effects due to the close proximity [Schilling 1993].

Substrates, onto which material was to be deposited, were glued to a heater using silver paste (from Aremco, part 597A) which was diluted with distilled water. Glue that was too strong made substrate removal after deposition difficult, and glue that was too dilute yielded poor thermal uniformity. The heater was cleaned first with sand paper (180 grit). The sand paper was held with a large flat sanding block (larger than the entire heater surface) to ensure a flat surface and prevent poor surface contact between the heater and the substrate. Then the heater was blown clean with pressurized nitrogen gas under a fume hood to remove loose grit. (Some dust can be detrimental to ones health. Sanding should always be done with a breath filter in place and blowing should always be done under the fume hood.) Then the heater was wiped clean with a lint free cleanroom towel (tex wipes), acetone, and isopropanol.

The glued substrate was slowly warmed to  $80^{\circ}\text{C}$  and baked in air for a few minutes prior to placement in the chamber. For baking the power was provided to the heater by a variable autotransformer set to  $\sim 5$  volts. This was done to dry the glue quickly and provide better adherence than would be achieved with room temperature drying. Usually maximum substrate size was  $1 \times 1$  cm subject to PLD uniform deposition area.

The heater stage consisted of a coiled heating wire clamped between two  $50 \text{ mm} \times 50 \text{ mm} \times 1 \text{ mm}$  Inconel plates (from Goodfellow). The formula for Inconel is Ni72/Cr16/Fe8.

Inconel was chosen for its excellent thermal conduction. The heater plates were isolated from the rest of the stage by ceramic  $\text{Al}_2\text{O}_3$  posts (from Ceramaseal). The posts were mounted on a mechanism that allowed *ex situ* x-y-z adjustment of the stage (See Appendix H for schematics of the heating stage). The heater plates and posts were enclosed in a thin Inconel sheet box to lower radiative heating of the chamber and the heater base.

The heating wire was composed of a nickel/chromium center wire with a magnesium oxide insulating sheath enclosed by a stainless steel sheath (available from Thermocoax). The total resistance of the heater at room temperature was  $\approx 7 \Omega$ . To prevent damage to the chambers electrical vacuum feedthrough, the resistive heating wire coil was isolated by attaching both ends to low resistance 'cold wires' near the heater plates. The cold wire was similar to the heating wire above except it had a zirconium copper center conductor (Also available from Thermocoax).

A non-shielded thermocouple, with .015 diameter wire leads, (Type K made by Omega Engineering Inc.) was spot welded to the back heating plate in order to protect it from deposited materials and make sanding and cleaning of the front heater plate easier. This yielded a temperature reading that was slightly above the actual substrate temperature ( $\approx 50^\circ\text{C}$  higher). Although the temperature reading was higher, it was consistent. In general, for PLD, actual temperature values always vary from system to system. All temperature values referred to in this thesis are those of the thermal couple reading. The leads of the thermocouple were Nickel and Chrome. The electrical vacuum feedthrough had a nickel and a chrome lead, and the wire that connects the feedthrough to the temperature controller was also nickel and chrome (from Omega). This was done to prevent thermal EMF's from causing variations in the temperature readings during deposition. Although all attempts were made to isolate the leads, some slight heating still occurs.

A internal shutter was available to shield the heater from the target during target pre-ablation.

During deposition, power was supplied to the heater by a temperature controller (Eurotherm). Current to the heater was adjusted to maintain a constant temperature via a PID feed back loop. PID values for the heater were  $P = 50$ ,  $I = 40$ ,  $D = 7$ . These values were attained by following the procedure set forth in the temperature controller manual in order to obtain a critically damped response. These settings were found to yield excellent temperature control from 200 - 900°C in a variety of oxygen pressures. The heater was capable of reaching temperatures up to 900°C (6.5 Amps). Temperature of the heater could also be monitored by an external infrared pyrometer by viewing the heater through a window. The emissivity of Inconel is  $\sim \epsilon = 0.9$  at temperatures around 800°C.

Care should always be taken when handling and cleaning the heater. The ceramic posts are brittle and can chip and break with rough handling. Also the spot welded thermocouple is weak and may detach. This can have devastating effects if it goes unnoticed and the stage is turned on. The allowed high current of the power supply can be controlled and should be set only slightly above levels needed for the highest temperature necessary. On one occasion, a unlimited heater in our lab melted when the thermocouple became unattached.

In PLD, Several materials can be ablated *in situ* to form complex heterostructures. In our system this was accomplished by having the targets mounted on a rotation carousel. Circular targets with a typical diameter of  $\sim 2.5$  cm and thickness of  $3 \sim 10$  mm, were clamped in 306 stainless steel holders which could be rotated inside the chamber via an external motor ( $\sim 7$  rotations per minute). These holders themselves were attached to a rotational carousel, making it possible to select any of up to 4 targets for *in situ* heterostructural deposition. (See Appendix H for carousel and target holder design.) The laser focus was usually placed half way between the center and the outer edge of the target. Targets have a tendency to be of a more uniform consistency near their centers due to the sintered pressing process.

Target to substrate distance for all targets was  $\sim 8$  cm. The length of the plume is a

function of laser energy and oxygen pressure [Goerke 1995, Inam 1988]. These parameters were adjusted to place the surface of the heater just inside the edge of the visible ablation plume. In YBCO studies, while smaller distances promote smoother films, distances of 8-10 cm yield films which are more homogeneous, have better stoichiometry, and have acceptable defect levels  $< 10^5$  particles/cm<sup>2</sup> [Goerke 1995, Schilling 1993, Heinsohn 1997]. This target-substrate distance also fell within in a commonly used model prediction for distance vs. pressure for YBCO [Kim 1992].

The vacuum system was pumped with a water cooled Turbo molecular pump with a pumping speed of 180 l/sec (Balzers model TPU 180H) backed by an oil-less rotational pump with a pumping speed of 7 m<sup>3</sup>/h and a possible base pressure of 2 mbar (Vacuubrand MD8 by Elnik). The maximum rotational speed of the turbo pump blades was 830Hz. The rotational speed was lowered to 200 ~ 400 Hz in conjunction with the introduction of oxygen via the mass flow controller to maintain the desired deposition pressure ~ 100 mTorr. The flow rate was always held at 100 SCCM.

## 2.2 YBa<sub>2</sub>Cu<sub>3</sub>O<sub>7</sub> Deposition

### 2.2.1 YBCO Crystal and Electronic Structure

The first successful YBa<sub>2</sub>Cu<sub>3</sub>O<sub>7</sub> PLD thin films were made by Dijkkamp *et al.* [Dijkkamp 1987]. The rather simple production of these complex stoichiometric films, combined with the euphoria of the discovery of their  $> 77$ K superconducting transition temperature, vaulted the previously obscure pulsed laser deposition technique to the forefront in thin film production.

YBa<sub>2</sub>Cu<sub>3</sub>O<sub>7- $\delta$</sub>  (YBCO), Yttrium Barium Copper Oxide, has a perovskite structure. When the oxygen doping, 7- $\delta$ , is greater than 6.4, it is a type-II superconductor (see figure 2.2). YBCO is optimally doped, that is attains it's highest  $T_c$  at 7- $\delta = 6.95$ . For the

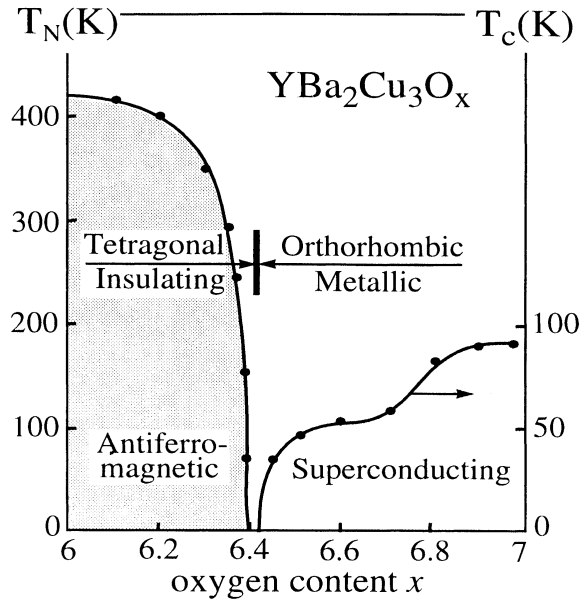


**Figure 2.2:** Structural phase diagram of  $\text{YBa}_2\text{Cu}_3\text{O}_7$ . [Mourachkine 2002]

superconducting doped regime YBCO has an orthorhombic structure (a,b,and c axis are perpendicular and have different lengths). The lattice parameters for optimally doped YBCO ( $\text{O}_{6.95}$ ) are approximately  $a=3.82\text{\AA}$   $b=3.89\text{\AA}$  and  $c=11.8\text{\AA}$  [Cava 1990].

Growth of YBCO thin films is often classified as c-axis or a-axis. C-axis refers to films grown with the c-axis vector parallel to the normal vector of the substrate. A-axis films have the a-axis perpendicular to the surface normal. Both a-axis and b-axis films are referred to as a-axis since the a and b lattice constants are so close it is difficult to distinguish between the two [Inam 1988].

The YBCO structure consists of two  $\text{CuO}_2$  planes separated by a Y atom. The Yttrium atom's primary role is simply to hold the  $\text{CuO}_2$  planes apart and does little electrically. Y has a valence of +3. Outside the  $\text{CuO}_2$ -Y- $\text{CuO}_2$  sandwich lies a BaO plane and Cu-O chains. The Ba has a valence of +2.

A good way to think of the YBCO structure (see figure 2.3) is as two primitive unit cells of  $\text{BaCuO}_{3-x}$  with a unit cell of  $\text{YCuO}_{3-y}$  in between [Olsson 1994]. However, the outer ends of the structure the  $\text{BaCuO}_{3-x}$  cubes are missing the oxygen atoms in the a-axis direction. The remaining O-Cu-O's in the b direction direction are often referred to as the copper oxide chains.

The parent compound of YBCO is oxygen under-doped  $\text{YBa}_2\text{Cu}_3\text{O}_6$ .  $\text{YBa}_2\text{Cu}_3\text{O}_6$  is an antiferromagnetic Mott insulator. Mott insulators are materials in which the conductivity vanishes with decreasing temperature even though band theory would predict it to be metallic. In a Mott insulator the conduction is blocked by electron-electron repulsion.

When  $\text{YBa}_2\text{Cu}_3\text{O}_6$  is hole doped, by adding oxygen, it becomes a metallic superconductor (see figure 2.2). Oxygen that is added or removed from  $\text{YBCO}_{6<x<7}$  is the oxygen in the Cu-O chains (see figure 2.3). It is usually accepted that the superconductivity takes place in the copper oxide planes and the Cu-O chains act as a charge reservoir. Theoretically an oxygen atom takes two electrons from another atom. But when oxygen is doped into YBCO, the number of holes created is not exactly two [Ghigna 1998]. In the underdoped regime, a doped oxygen atom adds a little more than two holes. In the optimally doped regime, a doped oxygen adds precisely two holes. And, in the overdoped regime, a doped oxygen adds only one hole. The electronic mechanics of YBCO are indeed complex.

In  $\text{YBa}_2\text{Cu}_3\text{O}_7$ , the  $\text{CuO}_2$  planes above and below the Y are also slightly puckered such that their oxygens lean towards the center Y. It has been found that the  $T_c$  of a cuprate superconductor is related to the buckling angle of  $\text{CO}_2$  planes such that the flatter plane has the higher  $T_c$  [Chmaissem 1999].

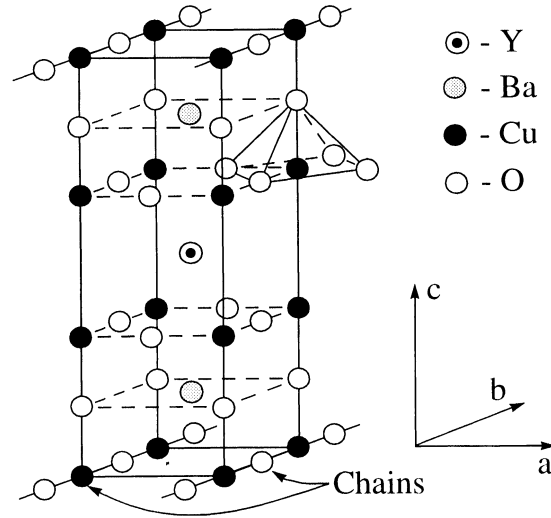


**Figure 2.3:** The  $\text{YBa}_2\text{Cu}_3\text{O}_7$  orthorhombic unit cell. [Mourachkine 2002]

### 2.2.2 Typical Ablation Characteristics

The YBCO target used to make the thin films presented in this thesis was a fine grain pressed target with near 100% density purchased from a private company. For details on making YBCO targets see [Wu 1987, Schilling 1993, Jorgensen 1987, Börner 1989, Yan 1987]. The target was cleaned before each deposition by sanding it with fine grain sand paper and then blowing it clean with a nitrogen gun. The sanded surface was black with a shiny sandy texture. Polishing the target reduces the production of particulates on the deposited films surface [Jackson 1994, Chang 1990, Wellstood 1993, Inam 1988, Timm 1996, Kingston 1990]. Before deposition the surface was pre-ablated for 1 minute ( $\sim 6$  rotations of the target) to remove any remaining grit or contamination. This provided at least 5 pulses delivered to every ablated region. This is an important step as many large particles are ejected in the first several ablations of a newly sanded target. Particle production falls abruptly after the 3-4 pulses are applied [Kumuduni 1995].

A fluorescent plume is emitted from a target during pulsed deposition. Excited atomic

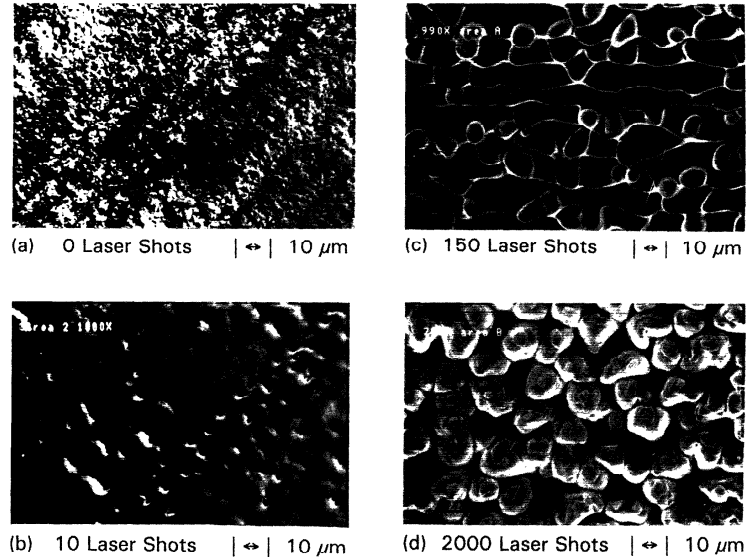


**Figure 2.4:** Formation of cone like structures on the ablated surface of a YBCO target. The target surface is shown after (a) 0, (b) 10, (c) 150, and (d) 2000 laser shots to the surface. The view is along the incident laser beam which was at a  $45^\circ$  angle to the target surface. [Foltyn 1991b]

species are created in the rapid evaporation of material. These excited molecules decay and emit light. This is especially apparent at the border of the plume where  $YO^+$  and  $BaO^+$  form more stable oxides. The light emitted is red, giving the YBCO plume border its color [Jackson 1994, Dyer 1990].

Laser light arrives at a  $45^\circ$  degree angle to the normal of the target surface. The plume however, when ablation first begins, is initially directed along the normal of the surface of the target. As deposition continues the plume tilts from normal to the target surface back towards the line of the impending laser light. This was particularly apparent with the YBCO target.

This tilt is caused by the changing surface of the target as material is ablated away. For YBCO, The initially smooth surface begins to develop cone like structures which grow in the direction of the impending light [Kumuduni 1995, Foltyn 1991b]. See figure 2.4.

The cones reach an equilibrium height after several ablations. At this point, the cones have a tendency to flake off, causing particulate to be deposited on the film surface [Willmott 2000, Timm 1996, Kingston 1990]. The target was sanded before every deposition to keep the plume centered and prevent the target surface from forming cones that are too large and could break off [Wellstood 1993].

The center position of the deposited material was found by using a large piece of silicon substrate. The substrate was clipped to the heater with spot welded Inconel strips. A deposition was then made with all deposition parameters unchanged except for the substrate temperature which was held at  $500^{\circ}\text{C}$ . Higher temperatures cause the silicon to react with the oxygen and YBCO, destroying the surface [Fenner 1991]. After a relatively thick deposition ( $> 2500\text{\AA}$ ) a clear deposited center is visible by eye on the silicon. This silicon sample can also be used to determine a fairly accurate deposition rate by wet etching away some material and using a profilometer to measure the step height. Dilute nitric acid was used to etch the YBCO [Shih 1988]. A better deposition rate is investigated in the same way except from a deposited film made at the determined deposition parameters. This kind of accuracy is important for films that are to be grown for devices with ultra-thin layers ( $< 100\text{\AA}$ ).

When growing heterostructures it was critical to ensure all target surfaces had the same distance from the heater. A small discrepancy in height between targets caused their deposition centers to be off relatively, making uniform multilayered structures of the correct desired thickness impossible to create, especially in the case of layers with thickness less than  $200\text{\AA}$ . The height of the target surface from the steel holder backing plate was 18 mm in our system, and the target to heater distance was 8 cm.

### 2.2.3 YBCO deposition parameters

Deposition parameters for the successful growth of YBCO were found through an exhaustive search. The focus was to make films as smooth as possible while maintaining high superconducting transition temperatures. The determination of the best parameters is a difficult process. Substrate temperature, oxygen pressure, target-substrate distance, laser energy, target density, frequency of applied laser pulses, and initial target surface conditions all play a role in film production and are dependent on each other when adjusted to create the best film. Therefore, determining the best setting for one parameter, fixing it, and then moving on to the next does not guarantee the attainment of the most ideal conditions [Heinsohn 1997]. Only by noting the deposition of similar materials from others work, carefully considering relative sensitivity of the parameters, and making several films does one arrive at a good set of conditions. The following parameters were deemed best for the desired growth within our particular system. It should be noted that conditions vary widely from system to system although most are comparable to those used in our system [Muzeyyan 1994, Wong 1997, Bendre 1989, Zheng 1992, Mukaida 1990, Olšan 1993, Schweitzer 1995].

Oxygen pressure was held at 100mTorr for deposition. This is obtained with a 100 SCCM oxygen flow and the Turbo pump rotational frequency  $\sim 350$  Hz. Higher pressures cause mixed phase growth (c and a axis mix) causing broader superconducting transitions [Goerke 1995, Mukaida 1992]. Lower pressures did not provide enough oxygen during growth yielding low transition temperatures to no transition.

Temperature was fixed at  $805^{\circ}\text{C}$  as measured by the thermocouple on the back of the heater. It should be noted that since this sensor was shielded and isolated from the the rest of the chamber it's reading, while consistent, was slightly higher than the actual substrate temperature. Infrared measurements made by a infrared pyrometer on the front heater

plate yielded temperatures  $\approx 780^\circ\text{C}$ . The emissivity of Inconel is  $\approx \epsilon = 0.9$  at  $800^\circ\text{C}$ . All deposition temperatures quoted in this thesis are those of the thermocouple mounted on the heater unless otherwise noted. Higher temperatures,  $> 815^\circ\text{C}$ , yielded damaged samples with no transition temperature and a cloudy grainy appearance. Lower temperatures,  $< 790^\circ\text{C}$ , provided mixed phase a and c axis growth [Chang 1990, Schilling 1993, Wu 1994, Goerke 1995, Mukaida 1990]. Indeed, temperature is a critical parameter in the growth of YBCO, with deviations as little as  $10^\circ\text{C}$  causing discernable effects both visually and electrically [Inam 1988].

The laser energy was set to yield a  $1.3 \text{ J/cm}^2$  energy density in a  $0.11 \text{ cm}^2$  area focused on the target. This corresponds to an energy level of  $700 \text{ mJ}$  from the laser combined with the  $15 \text{ mm} \times 8 \text{ mm}$  aperture. Energy densities below  $1.0 \text{ J/cm}^2$  were found to cause slow deposition rates and poor stoichiometry [Dam 1994]. Higher energies were found to yield 'splashing' of large particles on to the substrate surface. By keeping the energy close to the lower limit of ablation, particle production is minimized [Willmott 2000].

The frequency of applied pulses was  $4 \text{ Hz}$ . Pulse frequency variation between  $1 - 10 \text{ Hz}$  has not been found to be a significant factor in YBCO thin film growth [Heinsohn 1997]. This frequency was chosen to be within the range of  $1 - 10 \text{ Hz}$  and incommensurate with the frequency of the target rotation ( $\approx 7 \text{ rotations/minute}$ ).

Deposition coats the inside of the chamber windows and over time can cause significant reduction of transmitted light. Energy transmitted into the chamber should be checked often by use of the Molelectron energy meter.

These conditions yield a deposition rate  $\approx 0.89 \text{ \AA}$  per pulse. This rate is similar to the YBCO PLD growth rates given by other groups [Wellstood 1993, Goerke 1996, Ece 1994, Zheng 1992, Mukaida 1990, Mukaida 1992, Olšan 1993, Schweitzer 1995]. See appendix C for a complete table of YBCO deposition parameters.

For a  $1200 \text{ \AA}$  YBCO film grown on a STO substrate, the transition temperature,  $T_c(0)$ ,

where the resistivity reaches zero was  $\sim 89\text{K}$ . The transition width,  $\delta T_c$  the temperature width in which the superconducting transition takes place was  $\sim 1\text{K}$ . Typical resistivity,  $\rho$ , at 300K was  $5 \times 10^{-4} \Omega\text{-cm}$ . Typical resistivity at 100K was  $2 \times 10^{-4} \Omega\text{-cm}$ . Yielding a resistivity ratio of  $\rho(300\text{K})/\rho(100\text{K}) \approx 3$  which matches a standard often used in the determination of YBCO film quality [Kim 1992, Jackson 1994, Mukaida 1990, Mukaida 1989]. X-ray diffraction data displayed clear peaks consistent with c-axis YBCO growth. The critical current density at 77K was found to be on the  $10^{-6} \text{Amps/cm}^2$ .

For most devices in this study it was necessary to grow YBCO on top of a bottom ferromagnetic (LSMO), metal (LNO), or insulating (STO) layer. Deposition parameters were kept the same as the optimal conditions when growing YBCO on top of these previously grown layers of material. These bottom layers did have some effect on the top grown YBCO. The transition temperature generally dropped by about 5-10K, and the transition width increased to 3-6K. A resistivity ratio was hard to determine for YBCO heterostructure since any resistivity measurement also measured the bottom layers resistance in parallel. Critical currents of such structures are the subject of chapter 5.

## 2.3 $\text{La}_{0.33}\text{Sr}_{0.67}\text{MnO}_3$ and $\text{LaNiO}_3$ deposition

### 2.3.1 LSMO and LNO Crystal and Electronic Structure

$\text{La}_{0.33}\text{Sr}_{0.67}\text{MnO}_3$  (LSMO), lanthanum strontium manganese oxide, is a colossal magnetoresistive (CMR) ferromagnetic material with a perovskite crystal structure. It has a pseudocubic structure with a lattice parameter of  $a = 3.87\text{\AA}$ . This lattice structure and parameter is a close match to STO and YBCO, making LSMO a good candidate for heterostructural growth of superconductor/insulator/ferromagnetic devices.

LSMO is referred to as a colossal magnetoresistive material due to its large change in resistance with applied magnetic field. However fields required to generate appreciable

effects are  $\geq 1$  Tesla. LSMO is predicted to have highly spin polarized current which has been verified by various experiments [Wei 1997, Okimoto 1995, Park 1998].

The parent compound of LSMO is LaMnO<sub>3</sub> (LMO). LMO is a antiferromagnet insulator and the Mn atoms have a valence of +3 [Pauthenet 1970]. In LMO, the spin ordering of the magnetic Mn<sup>+3</sup> ions is parallel in the planes and antiparallel between them [Wollan 1953-55].

An isolated Mn ion has five degenerate outer 3d orbitals available to the 3d electrons. The spins of electrons that occupy these outer shells point in the same direction due to Hund's rule coupling and occupy the subsequent four lowest levels. In LMO, the crystal field and mixing with the oxygen orbitals splits the five degenerate 3d orbitals. Two levels split off to form an upper energy state that is occupied by one electron. This state is referred to as  $e_g$ . The two levels have a  $d_{x^2+y^2}$  and  $d_{3z^2+r^2}$  configuration. The three remaining levels contain three electrons and lower their energy to form what are called the  $t_{2g}$  levels. The  $t_{2g}$  levels have  $d_{xy}$ ,  $d_{yz}$ , and  $d_{zx}$  configurations. See figures 2.5 and 2.6.

These  $e_g$  and  $t_{2g}$  states can be further split into two hyperfine levels due to Jahn-Teller distortion effect. The Jahn-Teller theorem states that a magnetic ion in a crystal site in which the symmetry prevents the orbital degeneracy from reaching an energy minimized configuration, will lower its energy by distorting the crystal in such a way as to lower the symmetry enough to remove the degeneracy. For LMO the Jahn-Teller is an axial elongation of the oxygen isohedron. This splits the two  $e_g$  levels into an upper and lower state, and splits the lower  $t_{2g}$  levels into one higher and two lower states. See figure 2.5. Note, this distortion will lower the energy of a Mn<sup>+3</sup> ion, but the energy would be unchanged for a Mn<sup>+4</sup> ion. Therefore, Mn<sup>+3</sup> ions have a larger tendency to distort their local environment than Mn<sup>+4</sup> ions do.

In LaMnO<sub>3</sub> the  $e_g$  electrons are unable to move due to the strong coulomb repulsion and the Hund's rule coupling. There is an anti-ferromagnet (AF) superexchange interaction between the well localized  $t_{2g}$  electrons, which causes this material to be AF. When LaMnO<sub>3</sub>

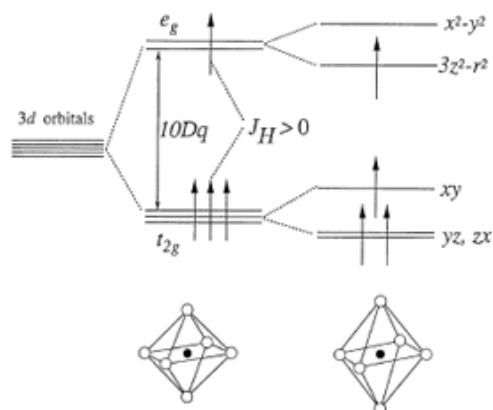


**Figure 2.5:** Field splitting of the five-fold degenerate atomic 3d levels into lower  $t_{2g}$  and higher  $e_g$  levels. The Jahn-Teller crystal distortion, sketched on the right, lifts the degeneracy to the final states shown. [Tokura 1999]

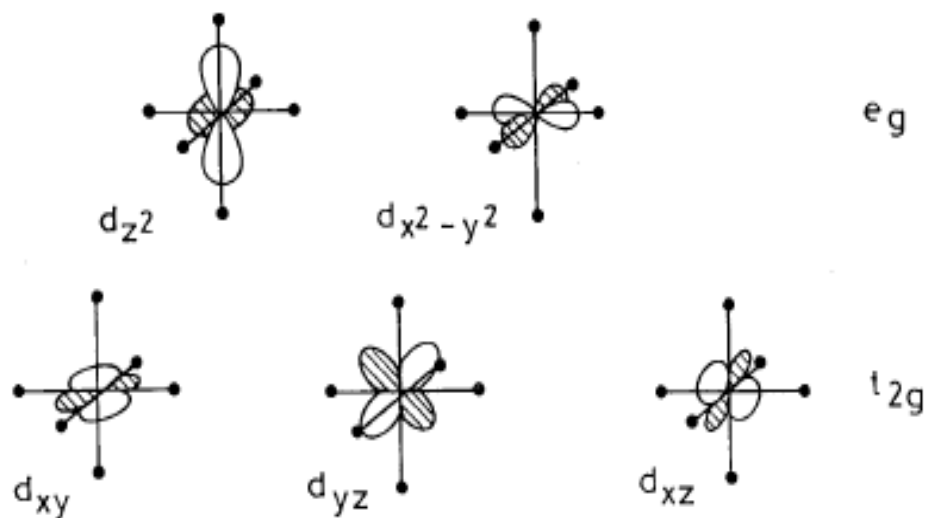


**Figure 2.6:**  $e_g$  and  $t_{2g}$  d-orbitals of the Manganese (Mn) atom. [Cox 1992]

is hole doped with Ca, Sr, Ba, or Pb, some of the Mn atoms take on a valence of +4. Neighboring  $\text{Mn}^{+3}$  and  $\text{Mn}^{+4}$  ions, in the configuration  $\text{Mn}^{+3}\text{-O-Mn}^{+4}$ , can exchange their valence by the simultaneous jump of an  $\text{Mn}^{+3}$   $e_g$  electron to the O p-orbital and an O p-orbital electron to the empty  $\text{Mn}^{+4}$   $e_g$  orbital. As shown by Anderson and Hasegawa the probability of this transfer is proportional to  $\cos(\theta/2)$ , where  $\theta$  is the angle between the Hund coupled  $t_{2g}$  spins of the neighboring  $\text{Mn}^{+4}$  and  $\text{Mn}^{+3}$  ions [Anderson 1955]. The degeneracy of the  $\text{Mn}^{+4}\text{-O-Mn}^{+3}$  and  $\text{Mn}^{+3}\text{-O-Mn}^{+4}$  is then lifted. There is therefore an energy gain for parallel alignment of the neighboring  $t_{2g}$  spins ( $\theta = 0$ ). Although the parallel alignment of the  $t_{2g}$  spins in neighboring Mn atoms is unfavorable to the anti-ferromagnetic exchange interaction, this interaction is overcome in order to gain the kinetic energy as the number of vacant  $e_g$  increases. As a result the AF phase changes to a ferromagnetic phase with doping.

This mechanism of the arising ferromagnetism and a metallic state is termed the "double exchange" mechanism and was first devised by Zener as an early explanation the conduction mechanism of doped  $\text{LaMnO}_3$  [Zener 1951]. This model provides a good explanation for conduction in the system, however, it has not been found to provide a adequate explanation of the CMR effects. As of today there is not an agreed on explanation of the magneto-resistance and conduction of CMR materials. A good review of CMR materials and theory is provided by Dagotto [Dagotto 2001].

$\text{LaNiO}_3$  (LNO), Lanthanum nickel oxide, is a normal metal with a perovskite lattice structure similar to LSMO. It's lattice parameter is  $a = 3.83\text{\AA}$ , also making it a good candidate for heterostructural growth of superconductor/insulator/normal metal devices. LNO has a good metallic behavior, a low resistivity, and generally maintains a smooth surface when deposited by PLD [Guo 1999].

The LSMO target used for PLD deposition was a fine grain pressed target made in our lab by Yufeng Hu [Hu 2004]. The target was cleaned and pre-ablated similarly to YBCO

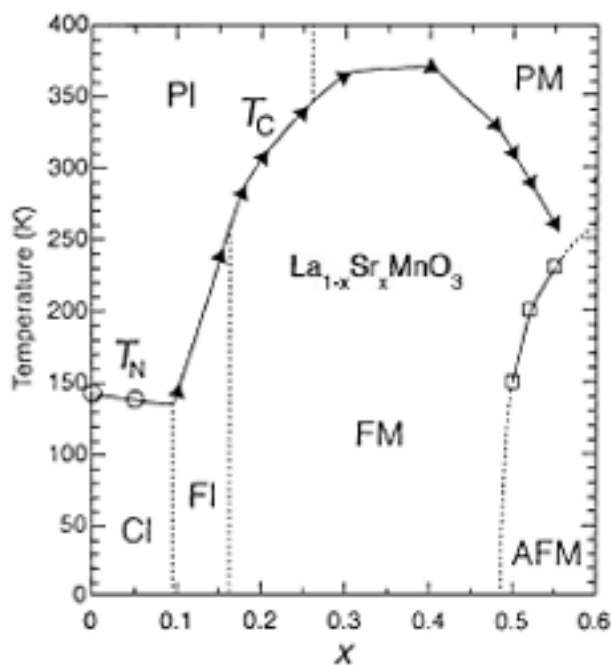


**Figure 2.7:** Electronic phase diagram of  $\text{La}_{1-x}\text{Sr}_x\text{MnO}_3$ . PM, PI, FM, FI, AFM, and CI denote paramagnetic metal, paramagnetic insulator, ferromagnetic metal, ferromagnetic insulator, anti-ferromagnetic metal, and spin-canted insulator states respectively.  $T_C$  is the Curie temperature, and  $T_N$  the Néel temperature.  $X = 2/3$  was the LSMO used in this study. [Tokura 1999, Urushibara 1995, Fujishiro 1998]

### The (cubic) perovskite unit cell

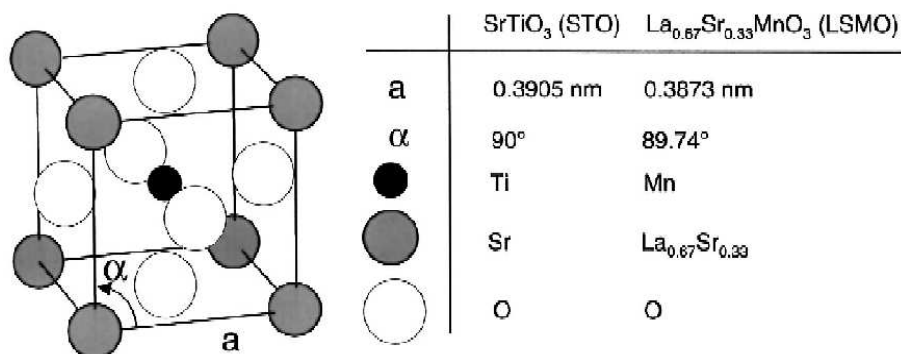


**Figure 2.8:** The cubic STO unit cell and the pseudo-cubic LSMO unit cell.  $\text{LaNiO}_3$  also has this structure. [Lyonnet 2000]

(see above). Plume tilt during deposition was not as dramatic as YBCO, but particle 'splashing' began to take place if the target went unsanded for too long. During ablation, the LSMO plume has a light blue color.

The LNO target was fine grain pressed target made in our lab by undergraduate student Rick O'Haire using the method of Wold [Wold 1957]. Target cleaning as prior to deposition was done similar to YBCO. During ablation the LNO target also has a light blue color.

Deposition parameters for the successful growth of LSMO and LNO were found through an exhaustive search. The focus, again, was to make films as smooth as possible while still maintaining the materials essential features.

Deposition parameters for LSMO and LNO were not as sensitive to change as YBCO. Good films could be made over a broad range of conditions so long as they were fairly thick ( $>300\text{\AA}$ ). Both were deposited in 200 mTorr of oxygen. It was possible to grow both films at lower pressures, but thin layers ( $400 - 600\text{\AA}$ ) grown in heterostructure layers were found to require at least 200 mTorr to assure the films receive enough oxygen. For the LSMO, the ferromagnetic transition or Curie temperature,  $T_p$  (the temperature at which LSMO changes from a paramagnetic to a ferromagnetic state), was above 300K for deposition at 200mT. Films made at low oxygen pressure also had a higher resistivity and, for LSMO, lower ferromagnetic transition temperatures ( $<300\text{K}$ ).

Temperature was held at  $805^\circ\text{C}$  (the same as YBCO) for both LNO and LSMO. Both materials have a broad range of allowance for temperature deviation for thicker films ( $>300\text{\AA}$ ), but films made at lower temperatures had low transition temperatures and higher resistivities. Films made at higher temps were often insulating.

The laser energy was set to yield a  $1.5\text{ J/cm}^2$  energy density in a  $.11\text{ cm}^2$  area focused on the target. This corresponds to a laser output energy level of 900mJ with the 18mm x 8.5mm aperture for LSMO and the 15mm x 8mm for LNO. The larger area for LSMO was provided simply to yield a higher deposition rate that was more comparable to the

other materials. Higher energy densities were found to yield 'splashing' of large particles on to the substrate surface. The frequency of applied pulses was 4 Hz. Some growth dependence on frequency was seen by atomic force microscopy (AFM). Slower frequencies did not necessarily yield smoother films. 4 Hz was determined to provide the smoothest films for frequencies less than 10Hz.

These conditions lead to deposition rate  $\sim 0.5\text{\AA}$  per pulse for both LSMO and LNO, which lies within the range of normal growth rates for PLD given by other groups [Yu 1996]. See Appendix D and E for a complete table of LSMO and LNO deposition parameters.

For a  $1200\text{\AA}$  film grown on a STO substrate, LSMO gave a ferromagnet transition temperature  $> 300\text{K}$ . Typical resistivity was  $2000\ \mu\Omega\text{-cm}$  at  $300\text{K}$ , and  $400\ \mu\Omega\text{-cm}$  at  $100\text{K}$ . X-ray diffraction data displayed clear peaks consistent with c-axis growth. For LNO, a  $500\text{\AA}$  film grown on STO substrate yielded a clear metallic behavior. Typical resistivity was  $1400\ \mu\Omega$  at  $300\text{K}$ , and  $840\ \mu\Omega$  at  $100\text{K}$ . Films were found via AFM to be very smooth and largely defect free.

## 2.4 SrTiO<sub>3</sub> deposition

SrTiO<sub>3</sub> (STO), strontium titanate, is a insulator with a cubic perovskite crystal structure similar to that of LSMO and LNO (see figure 2.8). It's lattice parameter is  $a = 3.905\ \text{\AA}$ . Table 2.1 shows the lattice mismatch of YBCO, LSMO, and LNO in relation to STO.

Initially, STO deposition parameters were obtained from Anna Clark and then adjusted for our system [Clark 2001]. A purchased fine grain pressed STO target purchased was initially used for deposition. A better single crystal target was later. Films produced by the single crystal target were far superior in both smoothness and film characteristics to the fine grain pressed target. The ablation plume of STO had a white color. Oxygen pressure was kept at  $150\text{mT}$  and the temperature at  $700^\circ\text{C}$ . The laser energy was set to yield a  $1.4\ \text{J/cm}^2$  energy density in a  $.11\ \text{cm}^2$  area focused on the target. This corresponded to a laser

output energy of 700mJ with the 15mm x 8mm aperture. The deposition rate at these conditions was  $\sim 1\text{\AA}$  per pulse. Films were found via AFM to be very smooth and largely defect free. For a complete table of STO PLD parameters see Appendix F.

These conditions were found primarily during the development of magnetoresistive tunnel junctions presented in chapter 3. Junction measurements yielded an estimated value of the resistivity of the STO layer of  $2 \times 10^4 \Omega\text{-cm}$ . See the magnetoresistive tunnel junction section 3.2.1 for more discussion of STO film properties.

## 2.5 Substrates

For this study STO (001) was the insulating substrate of choice due to its' smooth surface and the readily available literature of PLD of the above mentioned materials.  $\text{NbGaO}_3$  ( $\text{NGO}_3$ ), Niobium Gallium oxide ( $\text{NGO}_3$ ), and  $\text{LaAlO}_3$  ( $\text{LAO}_3$ ), Lanthanum Aluminum oxide, were also used on occasion. Both also have a perovskite crystalline structure. Although LAO has a step like surface which can cause twinning in films and also does not make it ideal for photolithographic processing later on. Table 2.1 shows the YBCO, LNO, LSMO lattice mismatch with three mentioned substrates. The lattice mismatch  $\delta$  is defined by

$$\delta = (a_{P\text{substrate}} - a_{P\text{bulk}}) / a_{P\text{substrate}} \quad (2.1)$$

where  $a_{P\text{substrate}}$  and  $a_{P\text{bulk}}$  are the lattice constants of the substrate and bulk crystal respectively. Positive values correspond to tensile strain and negative values provide compressive strain All lattice constants, except YBCO and LNO, were obtained from Yufeng Hu [Hu 2004].

STO was thermally treated before film deposition. To remove contamination and uniformly terminate the surface, the STO substrate was annealed in 100mT of oxygen for 10 min. at  $900^\circ\text{C}$ . This annealing step has been shown to yield well ordered STO surfaces [Zegenhagen 1998, Hirata 1994]. Annealing in a similar fashion also yields a smooth well

	YBCO(a) (3.82Å )	YBCO(b) (3.89Å)	LSMO (3.87Å)	LNO (3.834Å)
STO (3.905Å)	2.2%	0.4%	0.9%	1.8%
NGO <sub>3</sub> (3.862Å)	1.1%	-0.7%	-0.2%	0.7%
LAO <sub>3</sub> (3.794Å)	-0.7%	-2.5%	-2.0%	-1.1%

**Table 2.1:** Lattice mismatch of materials and substrates. The lattice mismatch  $\delta$  is given by  $\delta = (a_{Psubstrate} - a_{Pbulk})/a_{Psubstrate}$  where  $a_{Psubstrate}$  and  $a_{Pbulk}$  are the lattice constants of the substrate and bulk crystal respectively. (YBCO [Mourachkine 2002], LNO [Garcia-Munoz 1992])

terminated surface for NGO<sub>3</sub> [Ohnishi 1999]. There is also a standard chemical treatment for STO followed by a similar annealing step that is often used to yield an atomically flat surface [Kawasaki 1994]. The process involves etching the substrate in a buffered hydrofluoric acid etch. This process was done for several substrates, but no apparent effects were perceived in device properties. Therefore, the process was abandoned. The termination of the (001) STO created by this annealing is found to have a TiO<sub>2</sub> termination layer [Zegenhagen 1998] (the other possible termination for (001) would be the SrO layer).

## 2.6 Evaporation of Gold Contacts

Gold (Au) was used to make contact to samples in order to make electrical measurements. Gold was evaporated onto samples immediately after their removal from the PLD deposition chamber. YBCO is especially susceptible to surface damage caused by water [Yan 1987, Sheats 1993, Huh 1998, Barns 1987]. LSMO and LNO surfaces were found to also degrade over time, but not as quickly and severely as YBCO. Au was found to yield negligible surface resistance (value  $< 10^{-6} \Omega \text{cm}^2$ ) when immediately deposited on YBCO, LSMO, and LNO.

To evaporate gold, samples were placed in a stainless steel vacuum chamber similar to that of the before mentioned PLD system (section 2.1). Upon evaporation both the sample

and the stage could become warm due to the hot evaporation source. Therefore, a metal clamp was used to hold the samples inside the chamber rather than adhesive which can cause significant outgassing and contamination upon heating. The vacuum system was pumped to  $< 10^{-6}$  Torr before deposition, via a turbomolecular pump (TMP) with a 210L/sec pumping speed (Balzers model TMU 261 P) backed by a oil-less rotational pump with pumping speed of 7.5m<sup>3</sup>/h and a base pressure of 2mbar (Vaccubrand by Elnik Systems model MD 8). The TMP was held at full speed (1000 Hz) during evaporation. Typically pressure rose from  $< 10^{-6}$  to  $\sim 2 \times 10^{-6}$  Torr during deposition due to outgassing of the chamber upon heating from the source.

Distance from the source to the sample turned out to be of critical importance. When YBCO samples were too close ( $\sim 6$  inches away), the surface of the YBCO would become damaged due to source heating. This in turn caused a huge contact resistance between the gold and the YBCO ( $\sim 1\Omega\text{cm}^2$ ). Contact recovery attempts were made by post-oxygen annealing, but were unsuccessful. Also, the annealing caused the Au films to de-wet on the surface of YBCO [Jia 1990, Roshko 1991]. Therefore, samples were kept at the maximum distance from the source as allowed by the chamber (12 inches), and the deposition rate was kept low, 0.9Å/sec. These conditions yielded a negligible contact resistance of Au/YBCO when deposited on new and unprocessed YBCO films.

Tungsten evaporation boats were purchased from Kurt J. Lesker (part number EVSME5005W). The boats were held between two brass clamps connected to a power supply external to the chamber. Three to four 1 mm diameter gold pellets were placed in the tungsten boats (Purchased from ESPI). Care was taken not to over load the boat. Melted gold in an overloaded boat would flow down the leads causing changes to the boats resistance and therefore causing changes to the deposition rates as pertaining to applied voltage and also causing uneven deposition.

Gold held in the boat began to melt at an applied 20 volts, entirely melted at 30 volts,

and produced a deposition rate of 0.9 Å per second at 34 volts. 0.9 Å per second was used for deposition. The rate and thickness was measured by a thickness monitor (Inficon XTC/2) located just to the side of the centered samples, and at the same radius, 12 inches, from the boat as the samples. (The tooling factor for the XTC/2 in this configuration was 104.4.)

Before deposition, the samples and thickness monitor were shielded and the source was allowed to deposit material for 1 minute in order to burn off and outgas any contaminants from the evaporation leads [Liu 1989]. 350 Å of gold was typically evaporated on the samples. A full evaporation boat was capable of evaporating  $\sim 900\text{\AA}$  of gold in one run. (An alternate stage was available to hold samples closer than 12 inches to the source. A thickness of 2000  $\sim$  3000 Å could be attained.) 350 Å was found to be more than enough to provide full coverage, yet thin enough to be easily wet etched with TFA gold etch and keep its hold to the YBCO when sonicated in an ultrasound (see next section Photolithographic processing). Gold that is thicker than 1000Å should not be sonicated. It will most likely peel off.

## 2.7 SiO<sub>2</sub>, Au, and Cr sputtering

In the device fabrication process it was often necessary to deposit a layer of silicon dioxide, SiO<sub>2</sub>, in order to allow gold leads to contact central regions of a device without shorting to lower layers. Often a very thin Chromium (Cr) layer was deposited on top of the SiO<sub>2</sub> to promote adhesion of the Au. Without the thin chrome layer, the adhesion of the Au to SiO<sub>2</sub> was extremely poor.

Sputtering was done both in the Electronic Materials and Processing Research Laboratory (EMPRL) cleanroom at the Pennsylvania State University and in our own lab.

In the EMPRL both DC and RF sputtering were available. SiO<sub>2</sub>, Cr and Au were all deposited by sputtering in an argon atmosphere. The sputtering guns (Kurt J. Lesker) held

2 inch diameter, 1/4 - 1/8" thick targets and were at a distance of 4-5 inches from the samples. The samples were placed on a stage that could be rotated *in situ* to move the sample under either gun. The sample stage was uncooled. While this allowed some warming to occur during the depositions, the samples never reached a temperature  $> 100^{\circ}\text{C}$ . The vacuum system was pumped to a base pressure  $< 5 \times 10^{-7}$  Torr before deposition. A shutter was available to protect the samples while targets were pre-sputtered for 3 mins. This was done to remove any surface contaminants on the target.

$\text{SiO}_2$  was RF sputtered with an applied power of 125 watts (with  $\sim 5$  watts of reflected power) in a 3mTorr background pressure of argon. These conditions yielded a deposition rate of  $50\text{\AA}/\text{min}$ . Sputtering rates are very dependent on background pressure, and are found to increase with decreasing pressure. Deposited films were typically  $2000 \sim 4000 \text{\AA}$  thick, or at least thick enough to ensure any necessary step height was overtaken by at least  $1000\text{\AA}$ . The  $\text{SiO}_2$  target was 1/8" thick and 99.995% pure (from Kurt J Lesker).

Gold and Chromium were DC sputtered at an applied power of 50 watts in 5mTorr background pressure of argon. These conditions yielded a deposition rate of  $240\text{\AA}/\text{min}$  for gold. Deposited gold films were typically  $3000 \sim 4000 \text{\AA}$  or at least thick enough to ensure any necessary step height was overtaken by at least  $1500\text{\AA}$ . Gold layers deposited over a step that are too thin yield no contact, or contacts that are weak and break upon sample cooling. Chromium films were typically only  $20 \sim 40\text{\AA}$  thick. This thickness is more than sufficient to enhance the bond strength of Au to the  $\text{SiO}_2$ . For a complete table of sputtering conditions see appendix L.

DC sputtering was also available in our own lab. The sputtering gun shared a vacuum chamber with a ion mill (see Au/YBCO recovery in section 2.8.2). The chamber and pumps were similar to those used in the evaporation and PLD systems (see PLD and gold evaporation sections 2.1 and 2.6) The sputtering gun, made by AJA Corp., held a 2 inch diameter, 1/4" thick gold target from Kurt J. Lesker. Samples were placed on a fixed

water cooled sample stage 6 inches from the gun. Sputtering at 30 watts in a 3 mTorr ( $4 \times 10^{-3}$  mbar) background pressure of Argon yielded a deposition rate of  $163 \text{ \AA}/\text{min}$  when the face of the sample was parallel to the surface of the gun, and  $109 \text{ \AA}/\text{min}$  when the face of the sample was at a  $45^\circ$  angle to the gun surface. Note the relation between the deposition rate for the parallel stage and the stage at  $45^\circ$  is  $\cos(45) * 163 \approx 109$ . Therefore, deposition rates at other angles can be approximated.

## 2.8 Photolithographic Processing

All heterostructural devices were patterned using photolithographic techniques. Shipley Microposit S1811 photoresist (1811) was spun on samples and patterned to allow selective etching of the thin film heterostructure. See Appendix J for exact photolithographic processing parameters.

First a  $1.1 \mu\text{m}$  layer of Shipley 1811 photoresist was spun onto the sample. Notice the "11" in 1811 corresponds to the thickness of the resist ( $1.1 \mu\text{m}$ ) when the resist is spun at the standard speed and time of 4000rpm for 40 seconds. See figure 2.9 for the thickness and spin speeds of the Shipley 1800 series photoresists.

Shipley 1827, and 1805 were also available. 1827 was a little thick to provide sharp enough features and 1805 is a little too thin when it comes to ion milling. The ion milling rate for 1811 at 300V was  $\approx 30 \text{ \AA}/\text{mA-min}$ , or  $105 \text{ \AA}/\text{min}$  for a 3.5mA beam current. The Shipley 1811 in the EMPRL facility is actually 1827 which is diluted on site. A mixture of 100mL of 1827 with 40mL of Type-P Microposit thinner yields 1811 resist. The spin times given above were typical for most 1811 concoctions. Thickness should always be checked when a new bottle of resist is used.

The samples were spun at 4000 rpm for 40 seconds. Samples were then soft baked at  $100^\circ\text{C}$  for 1 minute and then cooled on a room temperature metal block for 1 minute.

Samples were aligned to a chrome on glass mask. Three masks were designed during

### MICROPOSIT S1800 PHOTO RESIST UNDYED SERIES

Figure 1. Spin Speed Curves

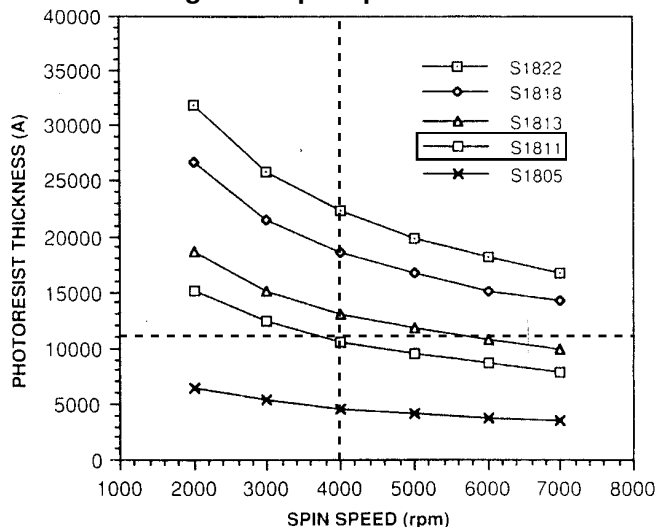


**Figure 2.9:** Thickness vs spin speed for Shipley Microposit S1800 series photoresist [Shipley Company].

this study. One was processed by the MRI at Penn State. The other two were processed by a professional company called HTA Photomask. Mask designs were initially drawn with Autocad software. In industry, masks are usually drawn with a program called L-Edit which creates a file type that works well with most mask writing equipment. Autocad files had to be converted into such files. HTA Photomask charged a fee for this conversion. In hind sight, it is much better to write masks with L-edit. New editions of this software are much better than what available at the onset of this study. The MRI had trouble converting Autocad files into files that would work with their equipment, also their mask writing equipment had a long waiting period. HTA Photomask could convert and write a mask in a week for about the same cost. Also, it was possible to keep a mask on file with Photomask to make extra copies later if need be. Blank masks were purchased from a company called Nanofilm in order to make additional copies or custom patterns.

Once a sample was aligned with the mask it was exposed to UV light (See Appendix J for

precise times). Alignment procedures and equipment controls are available in a publication offered by the EMPRL, and are fairly accurate as long as the photoresist thickness is correct [EMPRL]. The then exposed sample was developed in a mixture of MF351 (buffered sodium hydroxide) and distilled water in a 1:5 ratio. Samples were developed for 45 seconds, placed in a water bath for 1 minute, and blown dry with a nitrogen gun. Water sensitive samples ( $\text{MgB}_2$ ), with feature sizes  $> 20 \mu\text{m}$ , could be developed in 10 seconds with agitation.

$\text{SiO}_2$  was patterned with a liftoff procedure. That is, first the photoresist was patterned,  $\text{SiO}_2$  was deposited on top, and then the photoresist was removed with acetone lifting off any unwanted  $\text{SiO}_2$  and leaving behind the desired pattern. It was often difficult to remove small isolated areas of resist in this process. Ultrasounding samples helped as well as warming the acetone if liftoff was a problem. The boiling point of acetone is about  $80^\circ\text{C}$ . Warming was done just below this temperature. Care should be taken not to allow the acetone to completely dry out. If this occurs a layer of contamination is created on the surface of the samples that is for the most part impossible to remove. For very difficult liftoffs, soaking the sample overnight in acetone usually worked. In most cases the remaining patterned  $\text{SiO}_2$  adhered well to any perovskite material used in this study.

YBCO could be wet etched with dilute nitric, phosphoric, or sulfuric acid. A mixture of 1:400 nitric acid to water etched YBCO at approximately  $2000 \text{ \AA}/\text{min}$ . A mixture of 1:20 phosphoric acid to water etched YBCO at approximately  $1000 \text{ \AA}/\text{min}$ . The phosphoric etch was found to leave behind a residue in etched areas. While LSMO was undamaged by the YBCO etches, LNO was readily etched by both. There is always a certain amount of under etching when wet etching is used. For the YBCO, an under-etch of at least  $1\text{-}2 \mu\text{m}$  always occurred if the YBCO film was to be entirely etched away. This should be considered in any photomask design.

LSMO and LNO could be etched with a 1:10:100 mixture of sulfuric acid, hydrogen peroxide, and distilled water. The etching rate was  $2000 \text{ \AA}/\text{min}$ . This mixture could also be

used to etch other CMR materials such as LCMO and PSMO. This etch, however, would usually destroy any YBCO present in the sample. LNO could also be etched with dilute phosphoric acid and nitric acid.

Thin gold layers were etched with TFA gold etched (purchased from Transene Company, Inc.), diluted in a 1:1 mixture with distilled water yielding an etching rate of  $2000\text{\AA}/\text{min}$ . For thicker layers ( $\geq 5000\text{\AA}$ ) the TFA to water ratio was increased to 2:1 respectively allowing a etching rate of  $5000\text{\AA}/\text{min}$ . The TFA, which primarily consists of an aqueous solution of Iodine and Potassium Iodine, was fairly benign, and left YBCO [Eidelloth 1991], LSMO, and LNO layers completely undamaged.

Chromium, Cr, could be wet etched with a solution (purchased from Transene Company, Inc.) which contained nitric acid. Therefore Cr was often patterned with a lift off process to prevent damaging lower layers.

While wet etching was very successful for etching away the top gold contacts, and also very useful for single layer films, several problems were encountered when etching YBCO, LSMO, STO and LNO heterostructures. First and foremost the etch used for LSMO and LNO would completely destroy any above or below layers. Also, under-etching was always a problem. It was often very difficult to obtain devices that had features  $< 20\mu\text{m}$ . heterostructures which included thin STO barriers often left behind some residue afterwards. STO is only readily etched by hydrofluoric acid which was far to strong (as well as extremely dangerous) to use in conjunction with LSMO, YBCO, or LNO. A better and more precise method of etching the films was realized in ion milling.

### 2.8.1 Ion milling

A broad beam argon ion mill (Veeco/Commonwealth Scientific) was used to etch the heterostructure devices and was found to be very successful. The mill used standard collimated grids to create a 3cm diameter uniform milling area. To obtain a high accuracy milling

rates, samples were usually kept inside a 2cm diameter region. The beam arriving at the sample had a neutral charge. The ion mill had a filament located in the path of the exiting ions. When heated via an applied current, this filament supplied electrons to the ion beam to provide the neutralized beam. The filament current was automatically controlled by the power supply in such a way as to provide total beam neutralization (TBN mode).

For most etching a 300 volt beam voltage ( $V_b$ ) provided ions with sufficient energy to eat through Au, YBCO, LSMO, LNO, and STO layers at an acceptable rate while still allowing accurate timed control of the total etched distance. A 100V beam was used in some special applications (See Au/YBCO contact recovery section 2.8.2). A 500V volt beam was used to etch MgB<sub>2</sub> films and some other applications.

For broadbeam ion milling, the beam current ( $I_B$ ) is limited by the total of the beam voltage ( $V_B$ ) and the accelerator voltage ( $V_A$ ),  $V_{Tot} = V_B + V_A$  [Kaufman 1989]. The maximum allowed  $I_B$  can be found by plotting the accelerator current as a function of beam current. When the dependence deviates from a linear relationship the maximum beam current has been surpassed. The maximum beam current was determined in this way for our system (See Appendix A).

A 5 SCCM flow of 99.9995% pure argon was provided to the source via a flow controller for all settings of the mill. With the turbo pump running at full speed (830 Hz), this gas flow provided a  $6 \times 10^{-4}$  Torr pressure in the chamber during milling. (The pressure gauge in use was calibrated to nitrogen and gave a displayed reading of  $1.2 \times 10^{-4}$  Torr. This reading must be converted to obtain the actual argon pressure  $6 \times 10^{-4}$  Torr.)

It is important to allow an open flow area from the turbo pump to the ion source free of any formidable obstacles. The turbo pump was just strong enough to allow a plasma to develop in the ion the source. Any large obstructions between the source and the pump created a higher ambient pressure  $> 10^{-3}$  Torr which wouldn't allow a stable plasma to be created. The broad beam source also requires a large open area from the end of the ion

source to the sample stage. At one time our ion gun was mounted in an chamber extension with a small diameter (4.5 inches). In this configuration, the ion gun would often sputter material from the walls of the extension on to the sample surface creating a conducting layer even when films had been milled through to an insulating substrate. In a private communication with Veeco/Commonwealth it was found that up to 1/3 of the emitted beam could be striking the wall of the chamber in this configuration.

Samples in the ion mill were mounted on a stainless steel stage with an internal copper tubing cooling grid. The samples were glued into place using 'GE varnish' (from Lakeshore, part VGE-7031). The varnish has excellent thermal conductivity and low outgassing in the vacuum environment. Liquid nitrogen was continuously flowed at a slow rate to the stage during deposition. Cooling was done to protect samples from any source induced heating and to reduce pitting in the 1811 photoresist used in patterning. The stage was set at an angle of  $45^\circ$  relative to the beam. This was done to prevent a large flux of milled material from being deposited back into the gun. This protects the gun and allows longer filament life. While a slight shadow effect may take place due to the angle of the beam to the sample, a  $1000\text{\AA}$  film would only be under etched by  $0.05\ \mu\text{m}$ . This is negligible in most of our devices where the smallest feature  $\sim 10\ \mu\text{m}$ . The distance from the sample to the ion gun source was 15 cm.

Etching rates were determined by timed ion milling of test samples which were measured afterward with a profiler (Dektak III). Rates were found to differ as a function of total milled time. Faster rates were found for smooth unmilled samples. As milling time increased the rate was found to decrease. This may be due to the increased roughness of the surface with milling. In a simplistic model, momentum transfer of the ions would be less direct on an uneven surface, yielding the slower rate. For precise milling rates it is always best to use several test samples to get a good idea of the time and beam current required to yield the desired etching distance rather than rely on a linear approximation from other data.

Materials and etching rates are given in a table in appendix M. Rates are expressed as distance in angstroms per milliamp-minutes,  $\text{\AA}/\text{mA}\cdot\text{min}$ , and distance per minute at a constant 3.5mA beam current,  $(\text{\AA}/\text{min})_{I=3.5\text{mA}}$ . The reason for the "distance in angstroms per milliamp-minutes" is the ion mill is controlled automatically by the power supply and sometimes the beam current can be slightly higher or lower ( $\pm 0.5\text{mA}$ ) than the set value for extended periods of time. Depending on the milling application this can cause significant over or under etching. Note that the unit "milliamp-minutes" is simply proportional to the number of ions delivered by the mill.

The total milled distance was controlled by time in conjunction with the milling rates. This allowed a bottom layer to be maintained where a top layer of material was milled away. While the surface of the bottom layer would incur some damage, its electrical properties were usually relatively unchanged if the material was thick enough (usually  $> 400 \text{\AA}$ ).

### 2.8.2 Au/YBCO contact recovery after Ion Milling

For some devices it was necessary to ion mill through the top layer of a heterostructure (LSMO) and make a gold contact to a YBCO layer underneath. This posed many problems. The surface of the underlying YBCO layer sustained a large amount of damage when milled with the usual 300V beam. A large contact resistance arose ( $> 1 \Omega\cdot\text{cm}^2$ ) for gold deposited on the damaged YBCO surface. Many steps were taken in order to minimize the contact resistance.

First, a system was constructed in which ion milling and gold sputtering could be performed *in situ*. YBCO exposed to water in the air can become damaged and contaminated, causing larger contact resistances than ion milling alone. Also, sputtered gold is a more energetic species than evaporation, yielding better gold implantation.

The ion mill and sputter gun were mounted perpendicularly to each other in a spherical chamber. For details on sputtering and milling see sections 2.7 and 2.8.1. A shield inside the

chamber protected the sputtering gun from contamination when the ion mill was running and vice versa. The sample was held at a  $45^\circ$  angle to the axis of both the ion mill and sputterer.

After the construction of the ion mill/sputtering system, the dependence of the contact resistance on different ion beam voltages was investigated. A series of experiments were performed on 2 layer samples consisting of a  $500\text{\AA}$  top LSMO layer and a  $800\text{\AA}$  bottom YBCO layer. The top LSMO layer including  $100\text{\AA}$  of YBCO was milled away with a 300V beam and then the bottom YBCO layer was cleaned with various ion mill settings. A  $300\text{\AA}$  Gold layer was then deposited on the remaining YBCO and contact resistance measurements were made using a 4 point junction measurement. The measured gold pads were  $20 \times 20\ \mu\text{m}$  in area. A contact resistance on the order of  $1000\ \mu\Omega\text{-cm}^2$  at 77K could be recovered when the sample was cleaned with a 100V beam. However, to reach this contact resistance it was necessary to mill away at least  $100\text{\AA}$  with the 100V beam.

In an attempt to further decrease the contact resistance the 2 layer LSMO/YBCO samples were milled in a variety of ways using 300V to remove the LSMO and 100V to clean the YBCO. Figure 2.10 shows the results of the contact resistance obtained from various milling conditions. Contact resistance was largely independent of the initial milling conditions as long as the last  $100\text{\AA}$  milled in the YBCO was done with a 100V ion beam setting.

Finally, by annealing the samples at  $450^\circ\text{C}$  in 600 Torr of oxygen for 1 hour the contact resistance was lowered by another two orders of magnitude to  $10\ \mu\Omega\text{-cm}^2$ . It is very important however that the top gold layer be thicker than  $1500\text{\AA}$ . Thinner gold was found to agglomerate or de-wet on the surface when annealed. This dewetting actually created a higher contact resistance than unannealed samples and may be due to the exposure of the surface during annealing. The gold pads were, in general, always deformed during annealing and became a great deal rougher. Although deformed during annealing the gold was still

readily patterned and etched away with the usual wet etch procedure.

$10 \mu\Omega\text{-cm}^2$  was the best contact resistance that could be recovered and was acceptable for device applications in this study. Longer annealing times yielded little change in resistance. This contact resistance value is similar to values obtained for recovery of damage incurred to a single YBCO film when exposed to photolithographic processing [Du 2001].

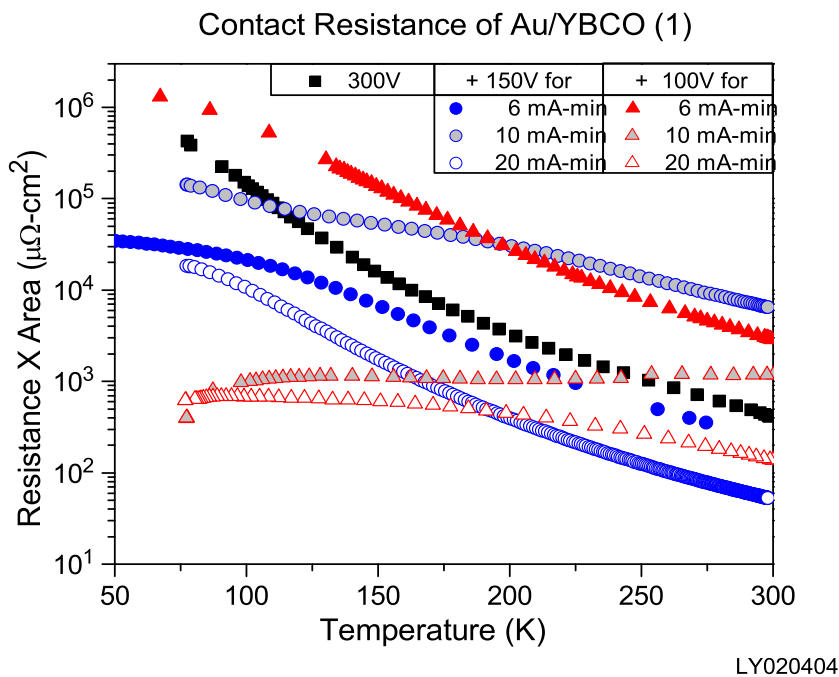


**Figure 2.10:** Contact resistance vs. temperature for Au contacts on various pretreated YBCO samples. All samples initially consisted of a  $500\text{\AA}$  LSMO /  $800\text{\AA}$  YBCO heterostructure. The entire top LSMO layer including  $100\text{\AA}$  of YBCO was milled away using a 300V ion beam voltage. The remaining YBCO was then "cleaned" by milling with 150V and 100V ion beam voltages. A  $300\text{\AA}$  Au layer was then deposited *in situ* by DC sputtering. The 300V data is for a ion milled sample with no low voltage cleaning. Low voltage 150V and 100V beams were then applied for various times, expressed as mA-min. (6 mA-min  $\equiv$  2 minutes with a 3 mA beam current.) The lowest contact resistance,  $\approx 1000 \mu\Omega\text{-cm}^2$ , was achieved with the 100V conditions. 30 mA-min at 100V milled away  $100\text{\AA}$  of YBCO. The gold pads were  $20 \times 20\mu\text{m}$  in Area.

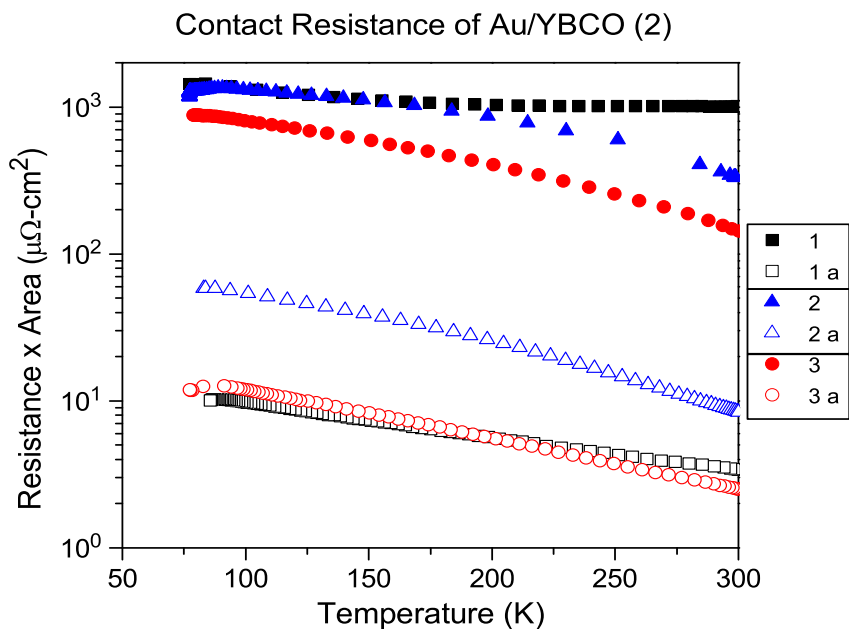


**Figure 2.11:** Contact resistance vs. temperature for Au contacts on various pre-ion milled YBCO samples, before and after annealing. Three samples treated with various ion milling conditions are shown before and after annealing in 600 Torr of oxygen at 450° for 1 hour. All samples initially consisted of a 500Å LSMO / 800Å YBCO heterostructure. In sample #1, the top 500(Å) of LSMO was milled away with a 300V beam, and then 200Å of YBCO was removed with a 100V beam. Data sets (1) and (1a) are the contact resistance before and after annealing respectively. In sample #2, the top 500(Å) of LSMO was milled away with a 300V beam, and then 100Å of YBCO was removed with a 100V beam. Data sets (2) and (2a) are the contact resistance before and after annealing respectively. And in sample #3, the 400(Å) of LSMO was milled away with a 300V beam, and then the remaining 100Å of LSMO plus 100Å of YBCO was removed with a 100V beam. Data sets (3) and (3a) are the contact resistance before and after annealing respectively. The gold pads were 20 x 20μm in Area.

## 2.9 Low Temperature Measurement Apparatus

For preliminary testing, a low temperature dip probe was used to make electrical measurements. The probe consisted of a long thin walled (.025") 1/2" diameter stainless steel tube with a copper sample stage attached to the bottom. Samples were glued to the copper stage with 'GE varnish' (from Lakeshore, part VGE-7031). The varnish is strong, has excellent thermal conductivity at low temperatures and is easily removed with acetone. Low temperature grease (Apiezon grease N) also can be used to attach samples and provides good thermal conductivity and easy sample attachment and removal. However, grease can be extremely difficult to remove from a sample with a rough surface. Trichloroethylene (TCE) must be used in order to remove it.

A Lakeshore silicon diode thermometer (part DT-470-BO-11), with an accuracy of +/- 0.25K was attached to the copper stage near the sample location. Twisted pairs phosphor bronze wire ran from a military style 19 pin connector (Part no. MS3112E14-19P on probe, MS3116F14-19S on connecting cable) at the top, down the length of the tube and attached to open electrically isolated leads on the copper stage. Connections from the sample to the insulated leads were made with thin 0.05mm diameter gold wire. The gold wire was soldered with indium to the stage leads and either pressed on with indium or silver pasted to the sample. (Silver paste from Ted Pella, Inc., Gold and Indium wire from Alfa Aesar) When indium was pressed onto gold pads, often the indium would stick to the pressing point. When the pressing point was pulled away the gold pad would sometimes be accidentally pulled off along with the indium. To prevent this from happening, gold wires were often indium soldered to samples. The application of melted indium to the surface prevented the accidental removal of the gold pads.

A copper sheath enclosed the dip probes sample block to prevent non-uniform air currents from causing unregulated temperature fluctuations. The probe was simply lowered

in to a liquid nitrogen or a liquid helium bath to decrease the temperature. No precise temperature control was made.

A probe enclosed in a vacuum environment was used for precise temperature controlled measurements. The probe was similar to that mentioned above, except the entire length of stainless steel tubing and the sample block were enclosed in a long narrow stainless steel can capable of producing a vacuum tight seal. (An 18 pin LEMO vacuum tight connector was necessary to make the electrical feedthrough, part# HGG.2B.318.CLLP) The copper sample stage also had a length of resistive heating wire coiled around the bottom end (made by California Fine Wire). By evacuating the probe can with a rotary pump and controlling current in the heating wire with a temperature controller (340 Lakeshore) a fixed temperature could be obtained to an accuracy of  $\pm .001\text{K}$  (relative to the thermometer reading, see above paragraph for thermometer accuracy relative to the actual temperature). The heating was controlled via a PID feedback loop configuration. PID parameters for this probe were  $P = 500$ ,  $I = 70$ , and  $D = 0$ . The entire can, probe and all, was lowered into a helium dewar to provide cooling. A small amount of helium 'exchange' gas was added to the vacuum space to provide a better cooling power to the sample block from the liquid helium bath. This was done to increase the cooling power, making the temperature easier to stabilize. With no exchange gas, temperature stabilization could take hours and PID values were very sensitive to small changes. The probe temperature was controlled by a computer via a IEEE GPIB connection in conjunction with a Labview program (see Appendix K).

A cryostat with an external electromagnet was used for all field measurements. The system consisted of a Janus STVP-100 continuous flow cryostat with a external GMW 5403 water cooled electromagnet capable of creating magnetic fields up to 0.5 Tesla. The cryostat was cooled by continuously transferring liquid nitrogen or liquid helium through a transfer tube into the system. By providing a continuous flow of coolant to the sample space a better sample temperature uniformity was created. More cooling power is applied directly

to the sample in this way, minimizing localized heating caused electrical currents in devices.

The cryostat was specially optioned to be used with either liquid nitrogen or helium. Liquid helium, due to its zero viscosity, provided a nice even transfer allowing very accurate temperature control ( $\pm .001\text{K}$ ). Usually a pressure of  $\sim 5$  psi was enough to provide an ample cooling liquid flow. This was provided by evaporation of the liquid helium itself inside the storage dewar. It was rarely necessary to pressurize the tank with an external source. The base temperature of the system was  $4.2\text{K}$ , although temperature control was more accurate  $> 10\text{K}$ .

Temperature control with liquid nitrogen was more difficult due to the viscous non-uniform flow but could be readily stabilized for temperatures  $> 100\text{K}$ . Liquid nitrogen cooling was very useful for simple preliminary measurements to  $77\text{K}$ . Cooling procedures are available in the cryostat manual.

The temperature in the cryostat was controlled with two heaters. One was located on the opening of the cooling liquid inlet tube and was referred to as the neck heater. This heater warmed the arriving coolant to just below ( $\sim 1\text{K}$ ) the desired sample temperature. The other heater was located on the sample stage. (A special cable was made for the sample stage heater to be used with the analog voltage output of the 340 Lakeshore controller, as specified by Lakeshore. The cable has a  $75\ \Omega$  resistor in series in order to make the total heater current path resistance  $> 100\ \Omega$ . For more details see the Lakeshore manual.) Both heaters were controlled via a PID feedback loops with the Lakeshore 340 temperature controller. The neck heater PID's were  $P=500$ ,  $I=50$ , and  $D=0$ . The sample stage heater PID's were  $P=600$ ,  $I=300$ , and  $D=0$ . Temperature was be controlled by a computer via a IEEE GPIB connection in conjunction with a Labview program (see Appendix K).

The external electromagnet was powered by two Kepco 20-20M power supplies wired in series, capable of producing a total current of 40 Amps (20 Amps provided by each). Care should be taken to provide an ample cooling water flow if the magnet is to be used at

high currents ( $> 20$  Amps total). The magnet does have safety temperature interlocks that will shut down the power if the magnet gets too hot. However, this will halt data taking until the magnet is cool and there is always some danger the magnet could be damaged.

While the magnet could only reach about 0.5 Tesla (low compared with a superconducting magnet), field stabilization times were negligible (see Appendix B for actual field range). This allowed fast continuous scan measurements with a field step size  $\approx 1.4$  Gauss. The magnet current was actually the controlled parameter with a minimum step size of  $9.6 \times 10^{-3}$  Amps ( $4.8 \times 10^{-3}$  Amps from each of the two supplies). In a private communication with a technician at Kepco, it was explained that resolution of the GPIB interface in the power supply was 12 bits (4096 bytes), yielding the minimum current step of  $4.8 \times 10^{-3}$  Amps for a single supply. Also the technician pointed out, while the applied current can be read from the power supply by the computer, the values returned by a query are sometimes erroneous. The value that is programmed (sent to the power supply) is more accurate. However, the most accurate determination that can be made would be by attaching an ammeter in series with the magnet and reading out the current.

The field was calibrated using a gaussmeter. See the graph in Appendix B. The magnet was controlled by a computer via a IEEE GPIB connection in conjunction with Labview software (see Appendix K).

## 2.10 Transport Measurement Setup

Two Keithley 2400 programmable sourcemeters were used to supply the measurement current and the injection current to the device under test (DUT). The settle time for stabilization of current from these meters was  $< 30 \mu\text{sec}$ . The typical resistance of measured devices was  $< 100 \text{ k}\Omega$ , placing them well within the meters usable range. A Keithley 2812 programmable voltmeter was used to measure the test voltages. The meter was accurate to a 1nV scale. Typical noise levels of the measured samples  $\approx 20 \text{ nV}$ . The internal resistance

of the 2182 was  $> 1 \text{ G}\Omega$ .

A 340 Lakeshore temperature controller was used to monitor temperature and supply power for heaters in the temperature controlled dip probe and the Janus cryostat system. A silicon diode thermometer was used on the dip probes, and gallium arsenide thermometers were used in the Janus cryostat due to the applied magnetic fields. All temperature curves were entered into the controller from data supplied by the thermometer vendor (Lakeshore). A calibrated thermometer was tested in the temperature controlled dip probe. Temperatures from the uncalibrated Si diode were found to be less than 1K off the calibrated levels for temperatures from 4K - 300K.

The 2400, 2182, and 340 were programmed and triggered via a GPIB computer interface. All data collection and device control was done from Labview programs (see Appendix K)

((For future reference.)Once, a temperature controller in our lab was found to yield different readings when connected to the GPIB card in the computer as opposed to when it was not connected. After exhausting all possible grounding or shorting problems it was finally found that the computer's low cost power supply was at fault. Upon its replacement all deviations disappeared. It should be noted that a computer's power supply, in some cases, could be a significant source of noise.)

The electrical measurements were done in such a way as to minimize the time required to apply any measurement currents. This was done to minimize any offsets that may be caused due to resistive heating. It was possible to program the 2182 and the 2400's to trigger simultaneously from a multiple trigger command given from the GPIB interface. A delay time could be programmed into the 2182, which provided a pause time after the initial trigger, to allow the supplied currents to reach their equilibrium values. A delay time of 3 msec was typically used unless otherwise stated. No electric filtering of the data was made in any measurement by the 2182 and the automatic range function in the 2182 was turned off. These functions create uncontrollable delays in the timing of the instrument making

accurate time control impossible.

The time required for the 2182 to make a measurement could be varied, and the standard time unit referred to in the Keithley manual is number of clock cycles. One clock cycle is 16.6ms (1/60Hz). All measurements in this study were done with the 2182 set to measure at 1 clock cycle. Although smaller times could have been selected, a trade off of a higher noise level has to be made. One clock cycle was short enough to reduce heating and actually sits at the minimum of noise production of the 2182 (See 2182 manual).

In a private communication with a Keithley support engineer it was revealed that the 2182 actually requires 3 clock pulses to complete a successful measurement when the device is set to 1 cycle. In the first clock cycle, the voltage measured at the device is recorded. In the second and third cycle, background measurements are made within the 2182 itself. These background measurements are used to subtract noise from the actual measurement, thereby allowing the voltmeter to reach such high levels of accuracy. It is important to take this in to account when applying currents. All applied currents must stay on for at least  $3 \times 16.6 \text{ msec} \approx 50 \text{ msec}$ . Any switching off of current during the two background measurement cycles of the 2182 throw off its noise correction. Currents turned off before the 50 msec minimum created a large noise signal. See figure 2.12.

The total time of the applied current for measurement was then 60 msec. Usually a 3 second delay was set between consecutive measurements, providing a duty cycle (applied time / down time) of  $< 2 \times 10^{-2}$ .

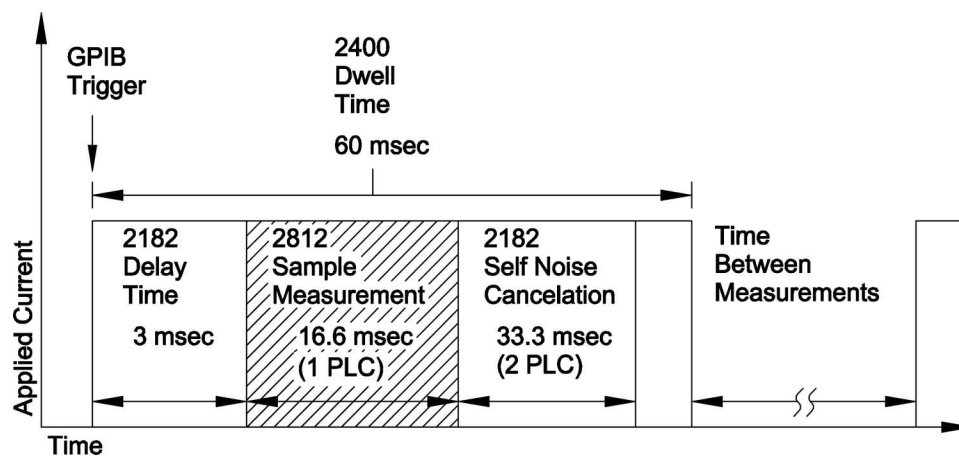


**Figure 2.12:** The timing schematic for the electrical current-voltage measurements. Note, the drawing is not to scale. The Keithley 2182 nanovoltmeter and the 2400 sourcemeter were triggered simultaneously with a GPIB multiple trigger command. Note, all times shown are typical of most measurements made in this study. The sample measurement time and the noise cancellation time are subject to the integration time setting of the 2182. It is assumed the integration time is set to 1 PLC (1 power line cycle =  $1/60\text{Hz}$ ). It is important that the 2400 dwell time always ends outside of the noise cancellation region to avoid the creation of substantial noise.

# Colossal Magnetoresistive Tunnel Junctions

---

### 3.1 Introduction

Magnetoresistive tunnel junctions (MTJ) have received considerable attention lately due to the development of giant magnetoresistance (GMR) in metallic multilayers [Moodera 1995, Miyazaki 1995] and the discovery of colossal magnetoresistance in perovskite ferromagnet thin films [Chahara 1993, Helholt 1993]. The devices consist of an thin insulating barrier between two thin ferromagnetic layers (F-I-F) and have been found to display large changes in resistance when subject to the application of a magnetic field. The insulating barrier interrupts exchange coupling between the bottom and top ferromagnets, allowing the magnetic orientation of one to rotate relative to the other, provided the coercive fields are different. A high resistance state is created when the ferromagnets magnetizations are aligned anti-parallel, and a low resistance state is created when the films are parallel. This effect was coined tunneling magnetoresistance (TMR).

The basis of these tunneling effects stems from the spin of the electron. More precisely, the tunneling is related to the spin of the itinerant electrons in the ferromagnet. In 1936, Mott determined that the current that propagates in a metallic ferromagnet carries with it a spin-polarized current [Mott 1936]. By calculating scattering rates for spin-up and spin-down itinerant electrons in the exchange split d-band of transition metal ferromagnets,

Mott deduced that the electrical current in a ferromagnet metal had a net spin polarization,

$$P = \frac{J_{\uparrow} - J_{\downarrow}}{J_{\uparrow} + J_{\downarrow}}, \quad (3.1)$$

where  $J_{\uparrow}$  and  $J_{\downarrow}$  are the up and down spin current densities.

The polarization (P) of the current in Fe, Co, and Ni was first determined in the pioneering experiments of Tedrow and Meservey (1970-1973) [Tedrow 1970-73]. These experiments were also the first to display spin dependent tunneling. Tedrow and Meservey measured the conductance of thin film superconducting/insulator/ferromagnet junctions in an applied magnetic field. Their junctions consisted of a top ferromagnetic metal (Fe,Co,Ni) strip, an insulating  $\text{Al}_2\text{O}_3$  barrier, and a bottom Al strip. The magnetic field was applied in the plane of the S/I/F heterostructure.

When a type-I BCS superconductor is subject to an applied magnetic field, the up and down spin quasiparticle density of states are Zeeman split by a value of  $2\mu_B B$ , where  $\mu_B$  is the Bohr magneton, and  $B$  is the magnetic field (see figure 3.1). The critical field of a thin film superconductor is much larger when the field is applied parallel to the surface. This allows a measurable split in the quasiparticle density states to be achieved while still maintaining the superconducting state. In a ferromagnetic metal, the bands are exchange split, yielding a different density of states at the Fermi level for up and down spin bands.

In the S-I-F junction, the imbalance of spin states at the ferromagnet Fermi level, combined with the splitting of the superconductor quasiparticle density of states, yields different tunneling probabilities for up and down spins depending on the bias of the junction. This asymmetry was clearly displayed in the tunneling conductance spectra measured by Tedrow and Meservey (figure 3.1).

By measuring relative heights of the peaks in the asymmetric tunneling spectra of their S-I-F junctions, Tedrow and Meservey were able to determine the polarization of several ferromagnets, although their junctions may have been somewhat crude by today's standards.

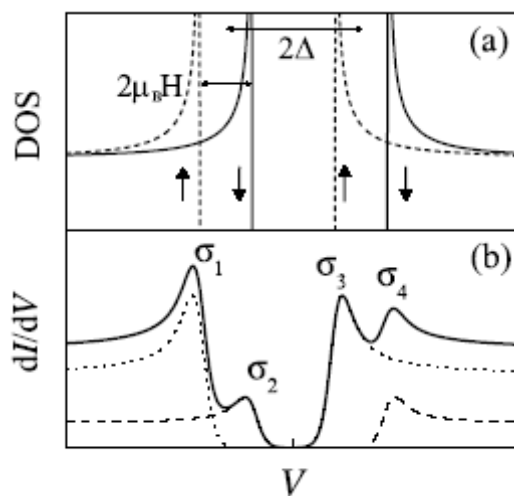


**Figure 3.1:** (a) BCS superconductor density of states split by  $2\mu_B H$  due to applied magnetic field  $H$ .  $2\Delta$  is the superconducting gap. (b) Conductance as a function of voltage for an F-I-S structure in field  $H$  (solid curve). The conductance for each spin orientation is represented by the dotted and dashed curves. The relative heights  $\sigma_i$  were used to determine the polarization of the ferromagnet. [Tedrow 1970-73]

An excellent review is provided in [Tedrow 1994].

TMR was first theoretically investigated and modeled by Julliere in a thin film FIF experiment thirty years ago [Julliere 1975]. Julliere combined the ideas of spin dependant tunneling developed by Tedrow and Meservey [Tedrow 1970-73] with the classic quantum model of tunneling [Simmons 1963-64, Bardeen 1957]. The classical model of tunneling assumes that the two ferromagnetic electrodes are independent systems and the insulating barrier is a perturbation which allows tunneling between the two. Julliere assumed that the tunnel current was proportional to the product of the spin density of states on either side of the junction barrier, and that spin was conserved in the tunneling process.

The conductance when the two ferromagnets of a F-I-F junction are aligned  $G_P(\propto 1/R_P)$  is different than the conductance when they anti-parallel,  $G_{AP}(\propto 1/R_{AP})$ . Tunneling magnetoresistance is usually defined as,

$$TMR = \frac{R_{AP} - R_P}{R_P}, \quad (3.2)$$

as defined by Julliere. In some publications it is defined as  $TMR^* = \frac{R_{AP}-R_P}{R_{AP}}$ , where the  $TMR^*$  only ranges from 0 to 1. All references to TMR in this thesis refer to equation 3.2. The polarization,  $P$ , of a ferromagnet is determined by the difference between the spin dependent density of states at the Fermi level,  $N^\sigma(E_F)$ , and defined as,

$$P = \frac{N^\uparrow(E_F) - N^\downarrow(E_F)}{N^\uparrow(E_F) + N^\downarrow(E_F)} \quad (3.3)$$

The classical quantum theory of tunneling [Tedrow 1994] states that the conductance of the junction is proportional the product of the density of states of the two ferromagnets, such that,

$$G_P \propto N_1^\uparrow(E_F)N_2^\uparrow(E_F) + N_1^\downarrow(E_F)N_2^\downarrow(E_F) \quad (3.4)$$

$$G_{AP} \propto N_1^\uparrow(E_F)N_2^\downarrow(E_F) + N_1^\downarrow(E_F)N_2^\uparrow(E_F) \quad (3.5)$$

where indexes 1 and 2 denote the two ferromagnets.

These 2 equations then yield Juliere's result,

$$TMR = \frac{R_{AP} - R_P}{R_P} = \frac{2P_1P_2}{(1 - P_1P_2)} \quad (3.6)$$

Note this model does not take into account barrier height or thickness.

Julliere's model, although simplistic, provides a good basic insight into the problem of tunneling magnetoresistance. This idea was further extended by Slonczewski in 1989 [Slonczewski 1989] who included the overlap of the ferromagnetic wave functions within the barrier and solved the problem with Schrödinger's equation. Slonczewski used a free-electron model, a rectangular barrier potential, and an internal exchange energy in the magnetic layers of the form  $-h \bullet \sigma$ . It is assumed in such a model that the electron momentum parallel to the junction is conserved in the tunneling process. In Slonczewski's model, the conductance (G) of a F-I-F' tunnel junction is given by

$$G = G_{fbf'}(1 + P_{fb}P_{f'b}\cos\theta) \quad (3.7)$$

where  $P_{fb}$ , is the polarization of the ferromagnetic material given by,

$$P_{fb} = \frac{k^\uparrow - k^\downarrow}{k^\uparrow + k^\downarrow} * \frac{\kappa^2 - k^\uparrow k^\downarrow}{\kappa^2 + k^\uparrow k^\downarrow}. \quad (3.8)$$

$k^\uparrow$  and  $k^\downarrow$  are the up and down electron momentum, and  $i\kappa$  is the imaginary electron momentum inside the barrier. Subscript fb accentuates the two multiplied terms in  $P_{fb}$  as being related to the ferromagnet and the barrier respectively, and f and f' denote two different ferromagnets (for similar ferromagnets f=f'). The angle  $\theta$  is the relative orientation of the magnetization of the two layers to each other, where each layer is assumed to consist of a single domain.  $G_{fbf'}$  is proportional to  $e^{-2\kappa d}$  where d is the thickness of the barrier. The polarization is seen to also depend on the height of the barrier  $V_b$  through  $i\kappa$  where  $\hbar k = [2m(V_b - E_F)]^{1/2}$ .

For parabolic bands,  $k^\uparrow \propto N^\uparrow(E_F)$  and  $k^\downarrow \propto N^\downarrow(E_F)$ . The first term of the polarization is then seen to be equivalent to the definition given by Julliere's model given in equation 3.3. Note for the second term,  $1 > \frac{\kappa^2 - k_\uparrow k_\downarrow}{\kappa^2 + k_\uparrow k_\downarrow} > -1$ . With the appropriate choice of barrier ( $\kappa^2$ ), this suggests the possibility that  $P < 0$ . It is therefore predicted that not only are the polarizations of the ferromagnets in a TMR experiment important, but the choice of insulating barrier as well. Therefore, in a tunneling experiment, the notion that spin polarization is an intrinsic property of the ferromagnet alone is contradicted. For sufficiently high barriers, Slowzewski's result reduces to Julliere's. Therefore, Julliere's model is still often used to quantify some tunnel junction results. When only one spin band is present at the Fermi level, and the barrier is sufficiently tall, Slonczewski definitions are seen to yield a polarization of one, and the conductance is seen to vanish for opposite orientations of the magnetic domains ( $\theta = 180^\circ$ ). This would be applicable to LSMO which is believed to be half metallic.

Experimental investigations, however, have found that much remains unexplained. Recent Co/STO/LSMO junctions made by Teresa *et al* [Teresa 1999] show both positive and negative TMR depending on the application of the voltage bias. See figure 3.2. This indicates a negative polarization for Co where all previous TMR experiments using  $\text{Al}_2\text{O}_3$  as the insulating barrier gave a positive polarization. To date, there still appears to be no completely accurate model of TMR.

After Julliere's work, experimental TMR study lied rather dormant for over 20 years due to difficulty in successful device fabrication and small effects that were not useful for technological applications. The studies were reborn with the advent of giant magnetoresistivity (GMR). GMR tunneling was developed by Moodera *et al.* and the pair of Miyazaki and Tezuka [Moodera 1995, Miyazaki 1995] at roughly the same time in 1995. FIF junctions made of Co/ $\text{Al}_2\text{O}_3$ /CoFe displayed a TMR of up to 10% at room temperature making them useful in technological applications (like GMR read heads in the harddrive of a computer).

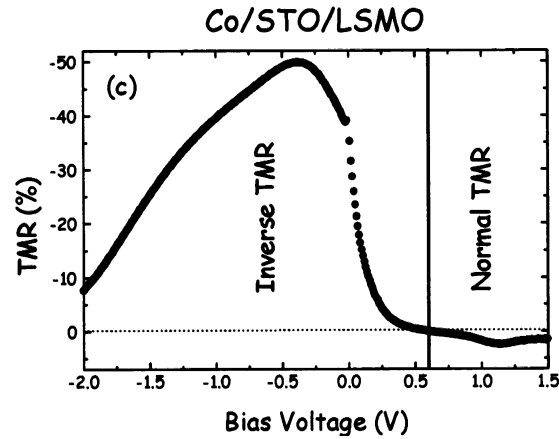


**Figure 3.2:** TMR% as a function of applied voltage for a Co/STO/LSMO junction. Both positive and negative TMR was found depending bias. [Teresa 1999, Fert 2001]

The key to the structures was the experimental development of an excellent thin relatively defect free  $\text{Al}_2\text{O}_3$  barrier.

Recently, interest in TMR has peaked again with the 'rediscovery' of colossal magnetoresistive (CMR) perovskite materials in a thin film form by Helmut [Helmut 1993] and Chahara [Chahara 1993]. See section 2.3.1 for a detailed analysis of the crystal and electronic structure of these materials. CMR materials have increased the interest in the TMR field for several reasons. Early experimental and theoretical calculations indicated that CMR materials,  $\text{La}_{0.67}\text{Sr}_{0.33}\text{MnO}_3$  in particular, were 'half-metallic' [Wei 1997, Okimoto 1995, Park 1998], that is the spin-up and spin-down conduction bands were completely separated at low temperatures providing a 100% polarized spin current. Therefore these materials showed promise in providing a large TMR in comparison with their metallic counterparts. Also, CMR materials were found to exhibit transitions to the ferromagnetic state at temperatures far above room temperature. Therefore it was thought that not only would CMR junctions exhibit large low field effects, but would operate at room temperature, making them ideal for technological applications.

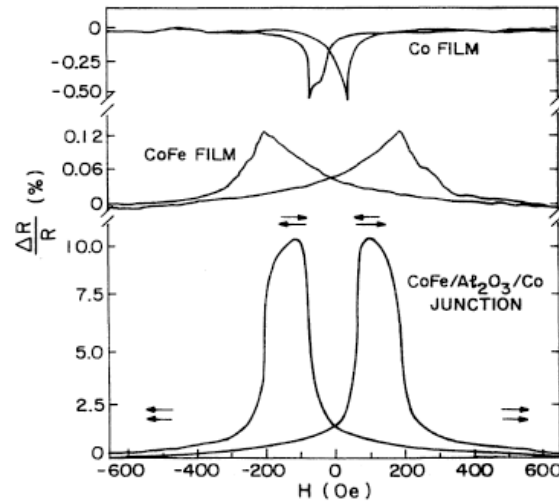


**Figure 3.3:** Percentage of resistance change of a CoFe/Al<sub>2</sub>O<sub>3</sub>/Co tunnel junction as a function of magnetic field (H) in the film plane at 295K. Also, shown is the variation in resistance of a single CoFe and Co film. The arrows indicate the direction of the magnetization states in the two films. [Moodera 1995]

Most CMR junctions have yielded scattered results that are hard to reproduce, and many yield polarizations far below expected values ( $< 50\%$ ). A variety of TMR values have been found in La<sub>0.67</sub>Sr<sub>0.33</sub>MnO<sub>3</sub>/STO/La<sub>0.67</sub>Sr<sub>0.33</sub>MnO<sub>3</sub> structures (see table 3.1). In collaboration with J.Z. Sun, Noh *et al.* [Noh 2001] found a TMR of 100%, Lu *et al.* [Lu 1996] 83%, and Sun [Sun 1997-2001, Sun 1998] 100%. Also, Obata *et al.* [Obata 1999] found a TMR of 150%. All these results provide polarizations of less than 60%. Viret *et al.* [Viret 1997] reported a TMR of 450%\* yielding a polarizations of 83%, and recently, Bowen *et al.* [Bowen 2003] have found a TMR of 1800%\* giving a polarization of 95%, but only in one junction. Bowen's other junctions yielded a TMR of 800%\*. (\* All papers came from the same lab.) Jo *et al.* [Jo 2000] have found a TMR of 630% in La<sub>0.7</sub>Ca<sub>0.3</sub>MnO<sub>3</sub>/NdGaO<sub>3</sub>/La<sub>0.7</sub>Ca<sub>0.3</sub>MnO<sub>3</sub> junctions, yielding a polarization of 83%.

Results from various TMR junction studies.		
TMR (%)	Temp (K)	Ref.
1	300	Ogimoto <i>et al.</i> [Ogimoto 2003]
1	270	Obata <i>et al.</i> [Obata 1999]
12	270	*Bowen <i>et al.</i> [Bowen 2003]
12	4.2	Ogimoto <i>et al.</i> [Ogimoto 2003]
83	4.2	Lu <i>et al.</i> [Lu 1996]
100	4.2	Noh <i>et al.</i> [Noh 2001]
100	4.2	Sun [Sun 1997-2001, Sun 1998]
150	4.2	Obata <i>et al.</i> [Obata 1999]
450	4.2	*Viret <i>et al.</i> [Viret 1997]
630	77	** Jo <i>et al.</i> [Jo 2000]
800	4.2	*Bowen <i>et al.</i> [Bowen 2003]
1800	4.2	*Bowen <i>et al.</i> [Bowen 2003]

**Table 3.1:** Tunneling magnetoresistance results from other studies. All results are for LSMO/STO/LSMO junctions except those of \*\* Jo *et al.*[Jo 2000] which are LCMO/NGO<sub>3</sub>/LCMO. \*Bowen and Viret results are from the same research group.

All large TMR values are displayed at extremely low temperatures  $\approx 4.2\text{K}$ , except Jo *et al.* at  $77\text{K}$ . And, as temperature rises most effects disappear around  $150\text{K}$ , well below the ferromagnetic transition temperatures ( $> 300\text{K}$ ) of CMR materials involved. This has prevented the technological application of CMR junctions. Ogimoto *et al.* [Ogimoto 2003] has reported TMR above room temperature in LSMO structures but the TMR is  $< 1\%$  at room temperature and  $\approx 12\%$  at  $4.2\text{K}$ . Obata *et al.*'s junctions also yield a  $1\%$  TMR at  $270\text{K}$ .

For all the previously mentioned reports the magnetic field is applied in the plane of the film. LSMO grown on STO has an easy magnetization axis in plane of the film ([Hu 2004, Haghiri-Gosnet 2003]). Jo *et al.* have reported the in-plane rotational dependence of LCMO/NGO/LCMO junctions. Jo finds an angular TMR dependence which has to do with the rectangular geometry of the junction and the pinning of the edge domains. To our knowledge, no data has been published to date on the TMR dependence on an out-of-plane applied field for CMR based tunnel junctions.

## 3.2 LSMO/STO/LSMO Magnetic Tunnel Junctions

### 3.2.1 Device Fabrication, Characterization, and Measurement Technique

$\text{La}_{0.67}\text{Sr}_{0.33}\text{MnO}_3/\text{SrTiO}_3/\text{La}_{0.67}\text{Sr}_{0.33}\text{MnO}_3$  tunnel junctions were developed and tested in this study. The heterostructures were grown *in situ* by PLD on STO substrates using the parameters presented in chapter 2. The samples were then quickly removed from the PLD chamber and placed in an evaporator to deposit a  $350\text{\AA}$  thick top gold layer. Time between the *ex situ* move from the PLD vacuum chamber to the evaporation vacuum chamber was kept at a minimum ( $< 5$  minutes). It has been found that small *ex situ* times have a negligible effect on the contact resistance between gold and LSMO [Chen 2001] compared to those made *in situ*.

The junctions were created in a process similar to that presented by Sun *et al* [Sun 1996]. The explanation of the process which follows is depicted in figure 3.4. First, the entire heterostructure was ion milled through using a 300 volt Ar ion beam. Then the top LSMO/STO layers plus about 100 Å into the bottom LSMO layer were milled through to create the tunnel junction area. Finally SiO<sub>2</sub> was sputtered and patterned with a liftoff procedure to allow gold contacts to reach the top of the tunnel junction without shorting to the bottom layer of the device. The final step was sputtering a thick gold layer and patterning it to create the measurement contacts. All PLD, ion milling, and sputtering were done with conditions provided in chapter 2. The perpendicular cross sectional junction areas were 10 x 10 μm (small) and 20 x 20 μm (large) in area.

Junction resistance,  $R_J$ , was measured with a standard four point measurement. A Keithley 2400 sourcemeter provided the current and a Keithley 2182 nanovoltmeter measured the voltage. The timing of the meters was strictly controlled. All control and data acquisition was done with a Labview program. For FIF junction measurements the current was applied for 3 milliseconds prior to a 16ms measurement time required for the 2182 nanovoltmeter, yielding a total applied time  $\approx$  20 msec during measurement. This was done in order to minimize heating effects while maintaining the low noise capability of the meters. See section 2.10 for a more detailed analysis of the measurement timing. Most junctions were measured with an applied constant current of  $1 \times 10^{-7}$  Amps (see figure 3.22).

The samples were primarily measured in a Janus cryostat with an external electromagnet capable of reaching a magnetic field  $\approx$  0.55 Tesla (5500 Gauss) with a step size of 1.36 Gauss. The sample stage could be manually rotated in relation the magnetic field with an accuracy of  $\pm 1^\circ$ . Samples were measured with the magnetic field applied at different out-of-plane angles relative to the plane of the sample (see figures 3.10 and 3.10). A few high field measurements were made in a Quantum Design cryostat with a superconducting magnet capable of attaining 9 Tesla magnetic fields.

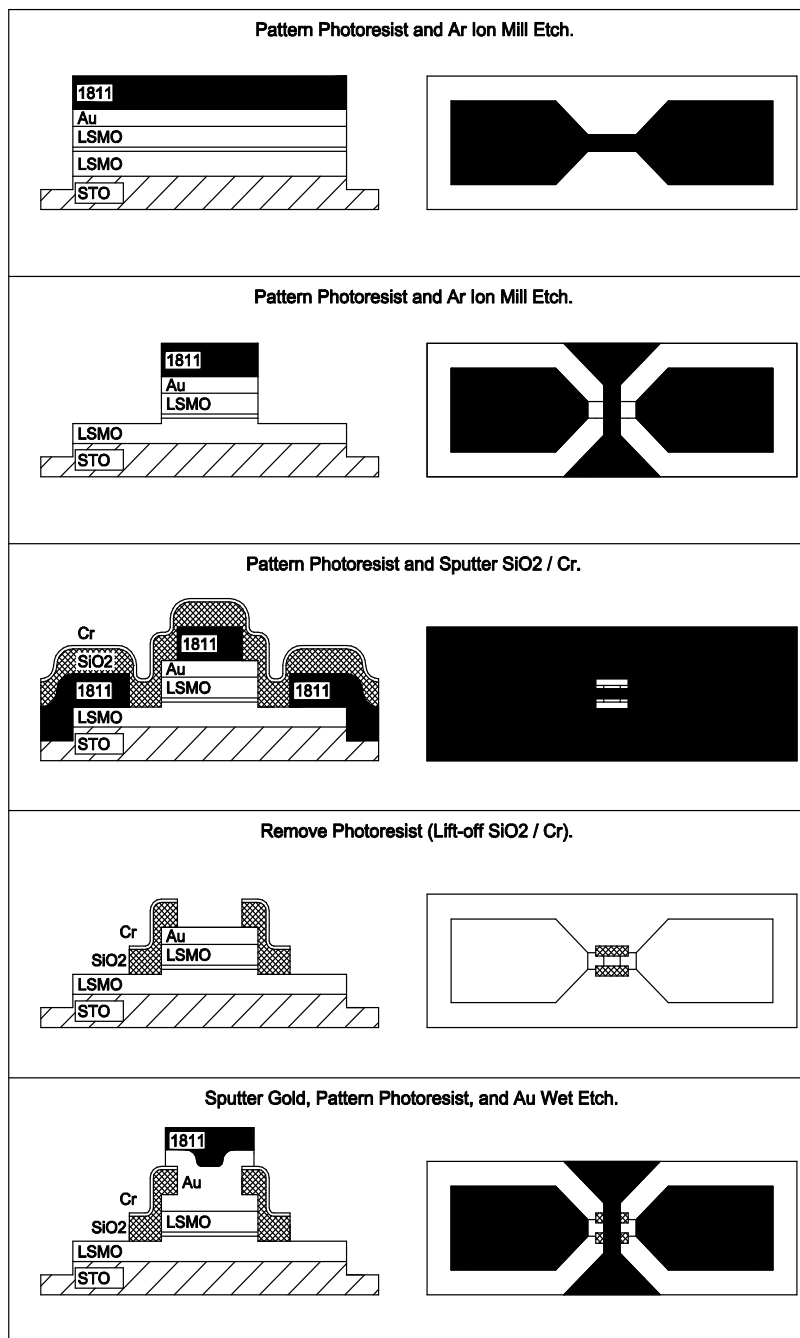


**Figure 3.4:** A schematic of the magnetic tunnel junction fabrication process. All PLD, ion milling, and sputtering were done with conditions provided in chapter 2. Available junction areas were  $10 \times 10 \mu\text{m}$   $20 \times 20 \mu\text{m}$ .

The bottom LSMO layer of most successful junctions was 400Å to 500Å thick. This was thin enough to provide a smooth surface and not so thin as to create problems during device fabrication. Although the deposition of much thinner LSMO films is possible, it can be difficult to prevent the second ion milling step from destroying the thin layer.

An atomic force microscopy (AFM) study was conducted to determine the pulsed laser deposition parameters which yielded the smoothest films while maintaining acceptable physical characteristics. The best single layer 500Å LSMO film showed nice step growth with a surface roughness of less than 10 Å over a 5 x 5 μm area. For thicker films roughness became a factor due to out growths and defects. AFM was critical for the development of good junctions. While certain deposition conditions yielded good electrical properties, this was not an indicator of morphology. Small changes in deposition were found to have large effects on film growth.

The resistance of the bottom LSMO layer after processing (photolithography, ion milling, etc.) was determined by applying a two point measurement to the bottom LSMO leads (see figure 3.6). The Au/LSMO contact pads used to connect the sample LSMO leads to the measurement system had an area  $\approx 400 \times 400 \mu\text{m}$  and an estimated overall resistance less than 10 Ω making their contribution to the two point measurement negligible. In all measured junctions the integrity of the bottom LSMO layer was found to remain intact. Even after milling 100 Å into a 400 Å thick bottom film, the ferromagnetic transition temperature was found to remain above 300K and the resistivity was similar ( $< 1000 \mu\Omega\text{-cm}$ ) to un-milled thicker samples.

The resistance of the top layer was determined by measuring an unpatterned heterostructure. This was believed to be a good indicator of the top LSMO layer properties since the bottom LSMO layer was isolated by the insulating STO. In any case, even if this measurement measures both layers as resistors in parallel, it should still reveal any indication of a transition temperature below 300K. As shown in figure 3.6 no indication of

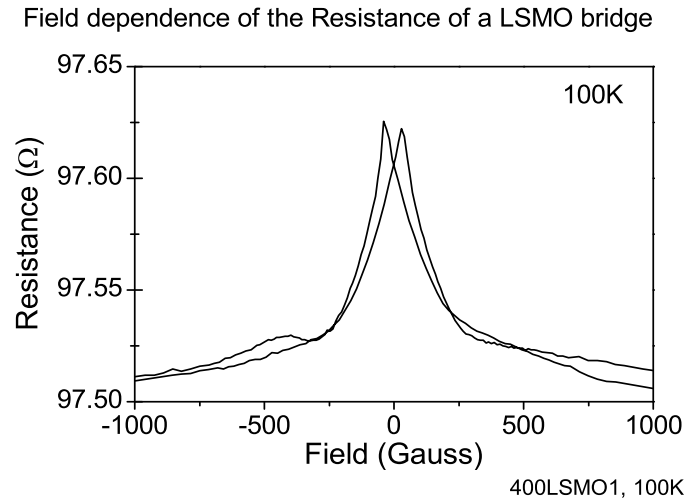


**Figure 3.5:** Resistance vs. Field for a LSMO bridge at 100K. The measured bridge dimensions are  $10\mu\text{m}$  long,  $10\mu\text{m}$  wide, and  $400\text{\AA}$  thick. The field was applied in the plane of the sample, parallel to the current. Note the magnetoresistance is  $< 1\%$  and the overall resistance is several orders less than the LSMO/STO/LSMO junctions. Smaller changes in resistance were seen for out-of-plane applied fields. Due to the anisotropic magnetoresistance effect (AMR) a negative change in resistance of similar magnitude was displayed when the magnetic field is applied in the plane of the film perpendicular to the current.

a transition below 300K is seen. It should be noted that a single LSMO thin film has a small magnetoresistive hysteresis (see figure 3.5), but the magnitude is too small as to play a part in the TMR junction measurements.

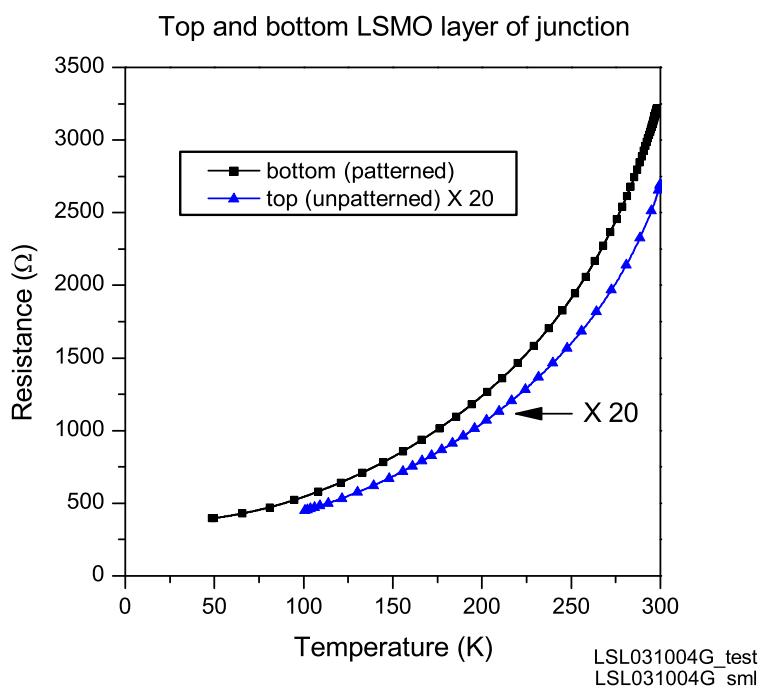


**Figure 3.6:** Resistance vs. temperature for the top and bottom LSMO layers of a LSMO/STO/LSMO heterostructure. The top layer was measured with a four point measurement on an unpatterned sample. It is assumed the curve is largely due to the top layer due to the insulating STO barrier. The top LSMO film was 100Å thick. Top films grown on heterostructures with thick STO layers (>48Å) displayed similar results. The bottom LSMO layer is measured after junction patterning by a 2 point measurement. The data shown here is of patterned bottom leads of device that was 10 μm wide and 300Å thick (after ion milling away top layers). Again, the bottom data is thought to be largely due to the bottom LSMO because of isolating effect of the insulating STO barrier. It should be noted that these two data sets are from two different samples deposited at the same time. However, similar results have been found in other sample sets.

The thickness of the STO insulating layer in successful junctions was 24 to 48 Å. A slight correspondence of junction resistance was found for barrier thickness, however due to surface roughness the insulating layer could be thicker or thinner in certain areas of the junction. Typical overall resistance of the junctions was  $10^3$  to  $10^4$  Ω yielding an estimated value of the resistivity of the STO layer of  $2 \times 10^4$  Ω-cm. The total resistance of the LSMO layers in a  $10 \times 10$  μm junction would be  $< 1$  Ω since the resistivity of LSMO is  $< 1000 \mu$  Ω-cm over the temperature range from 300K to 4.2K. Thus it can be neglected in the estimation of the resistance of the STO barrier.

The high resistance of the STO barrier in relation to the LSMO leads excludes the measurement of these junctions from the problems associated with barriers that have resistances on the order of the leads. When the resistance of the junction leads is on the order of the resistance of the junction itself, a non-uniformity current distribution is created and a four point measurement can cause a false resistance reading [Veerdonk 1997]. The resistance of our junctions is also found to roughly scale linearly with junction area, which also suggests the measurements are a true indication of the real resistance.

The primary deciding factor in obtaining a large TMR effect in our junctions was the PLD growth parameters for the STO layer. In particular the temperature and oxygen pressure maintained during deposition greatly effected device performance. Initially STO was deposited with PLD parameters similar to YBCO, with a pressure of 100mTorr and a temperature of  $805^\circ\text{C}$ . With these conditions junction resistances were found to be rather small ( $\approx 100$  Ω) and TMR values were  $< 1\%$ . The deposition oxygen pressure was slightly increased to 150mTorr and the temperature lowered to 700K. With these conditions a maximum TMR of only 20% was found at 5K for a junction with a 98Å STO barrier. The overall resistance of this junction was still only 100 Ω. AFM images of a STO layer deposited on a bottom LSMO layer were very smooth (roughness  $< 10\text{Å}$ ) and contained few defects. The smoothness and low resistance of these relatively thick STO layers pointed to

oxygen deficient films. Oxygen deficient STO displays a much higher conductivity.

The best junctions were finally created by annealing the samples in oxygen after deposition. The as deposited samples were cooled to 450°C and then annealed for 6 hours in 600 Torr of oxygen, before cooling to room temperature. In previous depositions the samples had always been annealed for 30 minutes at 450°C before cooling. Evidentially this was not long enough to allow the diffusion of oxygen to saturate the STO layer.

### 3.2.2 Standard Tunneling magnetoresistance and Angular Effects.

The best junction produced to date was found in a 10 x 10  $\mu\text{m}$  area junction with a bottom 400Å LSMO layer, a middle 24Å STO layer, and a top 500Å LSMO layer. The TMR ratio was dependant on the initial magnetization state. Most studies ramp a magnetic field to some high value guaranteeing that all magnetic domains are aligned along the field axis. We initially conducted the measurements in this way. However, larger TMR ratios and sharpening switching were found when the junction was demagnetized and the hysteresis scan was kept in a low field region. For now we will discuss the results from the usual high field technique. We will discuss the demagnetization technique and data later.

When the sample was initially subject to a high magnetic field the highest TMR found was  $\approx 360\%$  at a temperature of 5K. See figure 3.7. Using the relation of TMR to polarization given in equation 3.6, the polarization of LSMO given by this result is  $\approx 80\%$ . The TMR signal disappeared at 275K where it displayed a value of  $\approx 1\%$ . In most junctions, STO barriers of 24 - 48Å showed similar results. Normally the devices had a TMR  $\approx 200\%$  at 5K, which disappeared at 225 - 275K. The TMR was not always found to increase with decreasing temperature. Junctions with a top LSMO layer of 100Å were found to have peak TMR signal around 50K after which an abrupt drop was seen to occur (see figure 3.9). The cause of the decrease is unknown. However, a narrowing of the field width of the high resistance peak suggests that the coercive field of the top and bottom layer may be getting

closer together than at higher temperatures.

Most junctions displayed a highly symmetric hysteresis curve, especially in terms of the high and low resistance state values. Figure 3.9 shows the average TMR and the peak TMR (using the highest resistance value of the curve). There is little to no difference between the peak and average value of the TMR signal. Overall junction resistance,  $R_J$ , was typically on the order of  $10\text{k}\Omega$  (see figure 3.14). Changes in resistance with applied field reached up to  $35\text{k}\Omega$ . These changes were often very abrupt and could occur within a change of field of only 1.3 Gauss. The typical field at which these transitions occurred, when the field was applied in the plane of the sample, was 30 - 50 Gauss. This most likely represents the coercive field of a large domain in one of the LSMO layers. Whether the top or bottom layer of the junction had the higher coercive field was difficult to determine. Devices were positioned in the field in such a manner that the long bottom LSMO strip was parallel to the field. This alignment would correspond to the easy in-plane axis of the bottom layer based on geometry.

Junctions were also measured as a function of the out-of-plane angle of the applied magnetic field. While the TMR height was largely unchanged, the coercive fields associated with the junction were found to sharply increase near  $90^\circ$  (Field perpendicular to the plane of the sample). See figure 3.10.

Thin ferromagnetic films have a large perpendicular demagnetization field,  $H_d$ , which must be overcome in order to magnetize a film out-of-plane. (That is unless the perpendicular anisotropic field is large enough, in which case the film has an out-of-plane easy axis. LSMO/STO has a in-plane easy axis.) The potential energy of a ferromagnet due to the magnetization ( $M$ ) is,

$$-\frac{\mu_o}{2} \int_V M \cdot H_d dV = \frac{\mu_o}{2} \int_V M^2 N_d dV, \quad (3.9)$$

where  $N_d$  is the demagnetization factor. In a thin film limit the demagnetization factors are  $N_x \approx 0$ ,  $N_y \approx 0$ , and  $N_z \approx 1$ . For fields smaller than the demagnetization field, the

magnetization will choose a in-plane orientation. A slight misalignment in a perpendicular applied magnetic field yields a small in-plane field component. Depending on in-plane anisotropies, the magnetization orientation will follow this in-plane component if the perpendicular component of the applied field is small in relation to the demagnetization field. For a field scan, the small in-plane field component would obviously change direction as the out of plane component reversed. Therefore, the switching in these measurements may just be the by product of a slight misalignment and a large demagnetization field.

Due to geometry, thickness, stress, and roughness, the upper and lower LSMO films most likely have different coercive and demagnetization fields. Therefore, under the application of an out-of-plane field the magnetization of one film may lean out-of-plane long before the other. After the negative switching event in the TMR scans the junction resistance maintained a low stable state even for large out-of-plane magnetic fields up to 2 Tesla. If one film's magnetization did lean out-of-plane before the other, a slow changes in resistance would be seen at the beginning or end of the TMR curves corresponding to a decrease or increase in the angle between the two magnetizations (change in relative angle from 0 or  $180^\circ \rightarrow 90^\circ$ ). At 5K there is a slight difference in the magnitude of the TMR signal with a slow increase and decrease in the TMR signal. See figure 3.11. Perhaps at low temperatures a large enough difference in coercive and demagnetization fields has been attained between the top and bottom LSMO films so that this effect can be seen. As shown, at low temperatures ( $< 50\text{K}$ ) the coercive field required at  $90^\circ$  could be on the order of 1 Tesla. However, above 50K the TMR curves show abrupt transitions at the ends of there curves which do not support this argument.

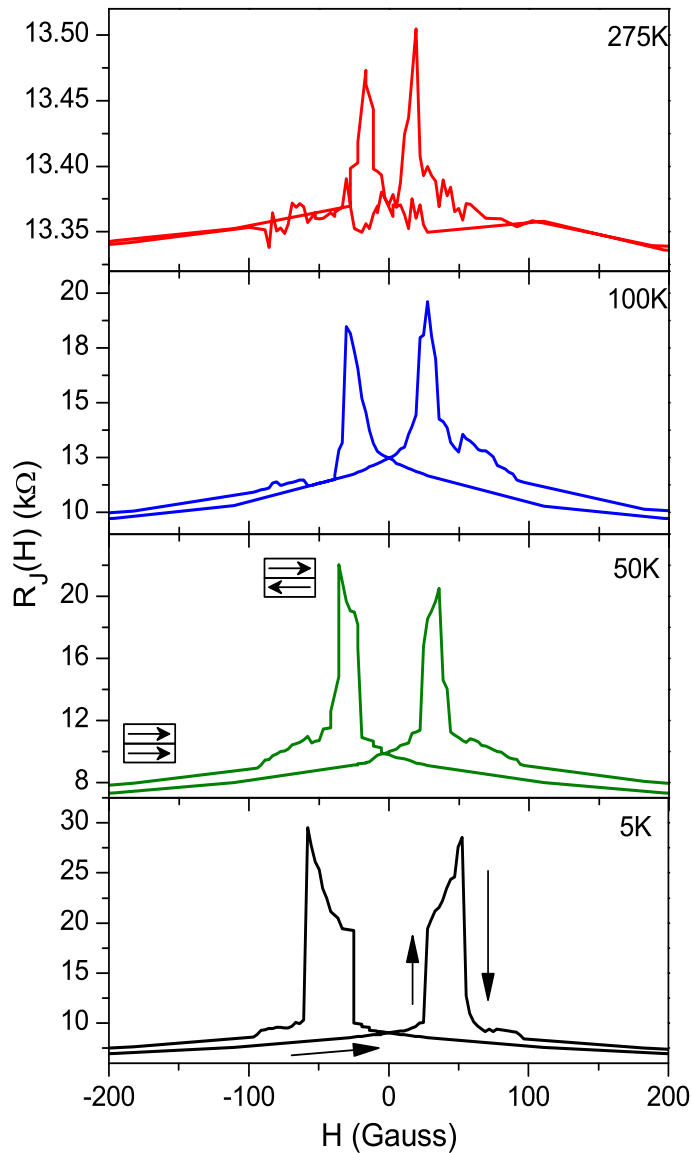
By Slonczewski's model (equation 3.7), one would expect that in-plane TMR results would always be greater than or equal to out-of-plane TMR results. However at 50K, the out-of-plane TMR ( $\theta = 90^\circ$ ) in figure 3.10 was actually slightly larger than the in-plane results. This may be due to the fact that the in-plane switching events occur at much

smaller fields and the step size of the magnet is not small enough to allow the true high resistance state to be displayed. In any case the magnitude of the out-of-plane TMR signal was very close to the in-plane case.

The  $90^\circ$  result in figure 3.10, shows what appears to be clear Barkhausen jumps. This seems to indicate there are many small domains present in the sample. However there is a distinct abrupt jump from the high resistance state to the low resistance state. Possibly the lower layer, which would be smoother and more uniform, has less defects and larger domains. The upper film would be rougher, and may be the cause of the numerous small domains.

A interesting measurement was conducted in which the junctions were magnetized in an initially parallel state. See figure 3.12. This was done by first applying a large magnetic field which was slowly lowered to zero. With zero field being applied the sample was slowly rotated to a different angular orientation, then the magnetic field scan was continued. When the sample was rotated in a zero field, a large change in resistance occurred before any field was applied. For  $180^\circ$  rotations the change in resistance was often as large as the change created in a normal TMR scan. Of course there is a residual magnetic field in our magnet system, but when measured with a gaussmeter it is found to be less than 1 Gauss for any orientation. Also, the change occurred regardless of the premagnetized direction. This seems to indicate that some of the magnetic domains, in one or both of the layers, may have extremely low coercive fields regardless of magnetic field orientation.

The low field hysteresis of the junctions was also tested. See figure 3.13. The sample was first magnetized in a high magnetic field, and the magnetic field was then scanned. When the high resistance state was obtained in a field scan, the scan was reversed. Samples were found to maintain their high resistance state past the magnetic field zero point. While not totally symmetric the transition back to the low resistance state occurred at magnetic fields similar in magnitude to those required to create the high resistance state.



LSL031004G\_sml

**Figure 3.7:** Resistance vs. applied magnetic field for a LSMO/STO/LSMO junction at various temperatures. The junction area was  $10 \times 10 \mu\text{m}$ . The heterostructure had a top/middle/bottom layer thickness of  $500\text{\AA}/24\text{\AA}/400\text{\AA}$  respectively. The magnetic field was applied in the plane of the heterostructure ( $\theta = 0$ ). The temperature dependence of this device's TMR is shown in figure 3.9. Arrows in the 5K plot indicate field scan direction. Pictures in the 50K plot indicate magnetization states of the top and bottom LSMO films.

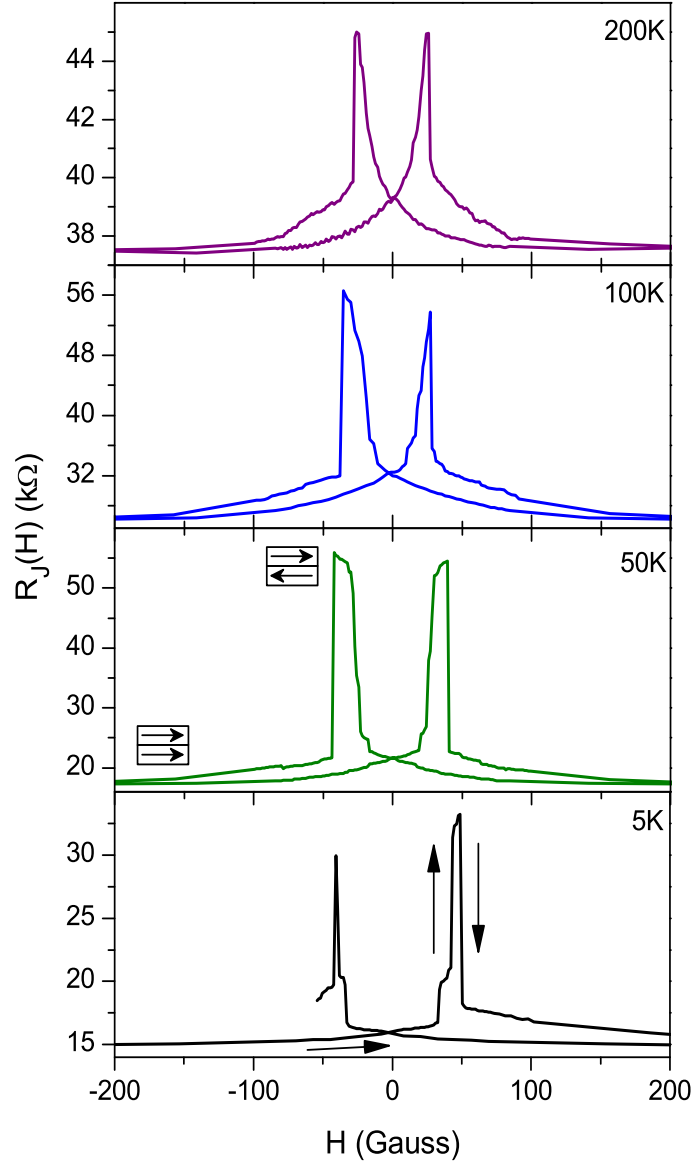
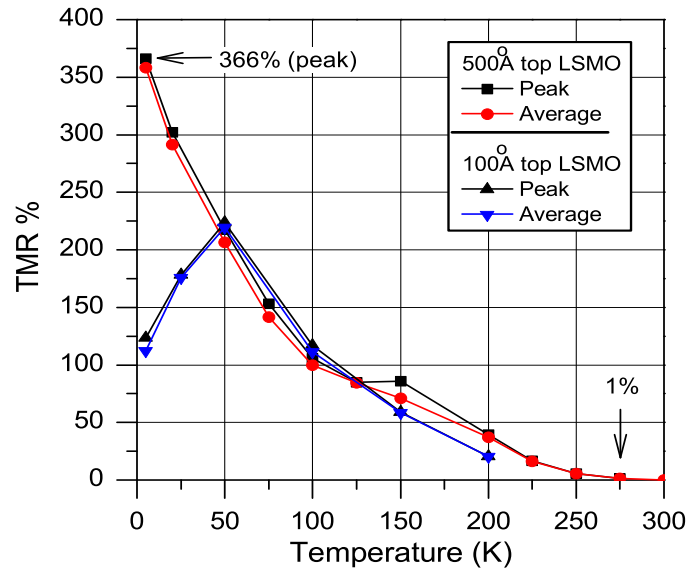


**Figure 3.8:** Resistance vs. applied magnetic field for a LSMO/STO/LSMO junction at various temperatures. The junction area is  $10 \times 10 \mu\text{m}$ . The heterostructure had a top/middle/bottom layer thickness of  $100 \text{ \AA} / 32 \text{ \AA} / 400 \text{ \AA}$  respectively. The magnetic field was applied in the plane of the heterostructure ( $\theta = 0$ ). The temperature dependence of this device's TMR is shown in figure 3.9. Arrows in the 5K plot indicate field scan direction. Pictures in the 50K plot indicate magnetization states of the top and bottom LSMO films.



LSL031004G\_sml  
LSL032904A\_sml

**Figure 3.9:** Tunneling magnetoresistance % vs. temperature for two LSMO/STO/LSMO junctions.  $TMR\% = 100 \times (R_{AP} - R_P)/R_P$ .  $R_P$  was taken as the resistance value at 500 Gauss. The junction with the highest TMR at 5K (500Å top LSMO) is the same as that shown in figure 3.7. The other junction (100Å top LSMO) is the same as that shown in figure 3.8. The peak TMR was calculated using the peak resistance and  $R_P$ . The average TMR was calculated by averaging both peak values in the hysteresis curves and  $R_P$ .

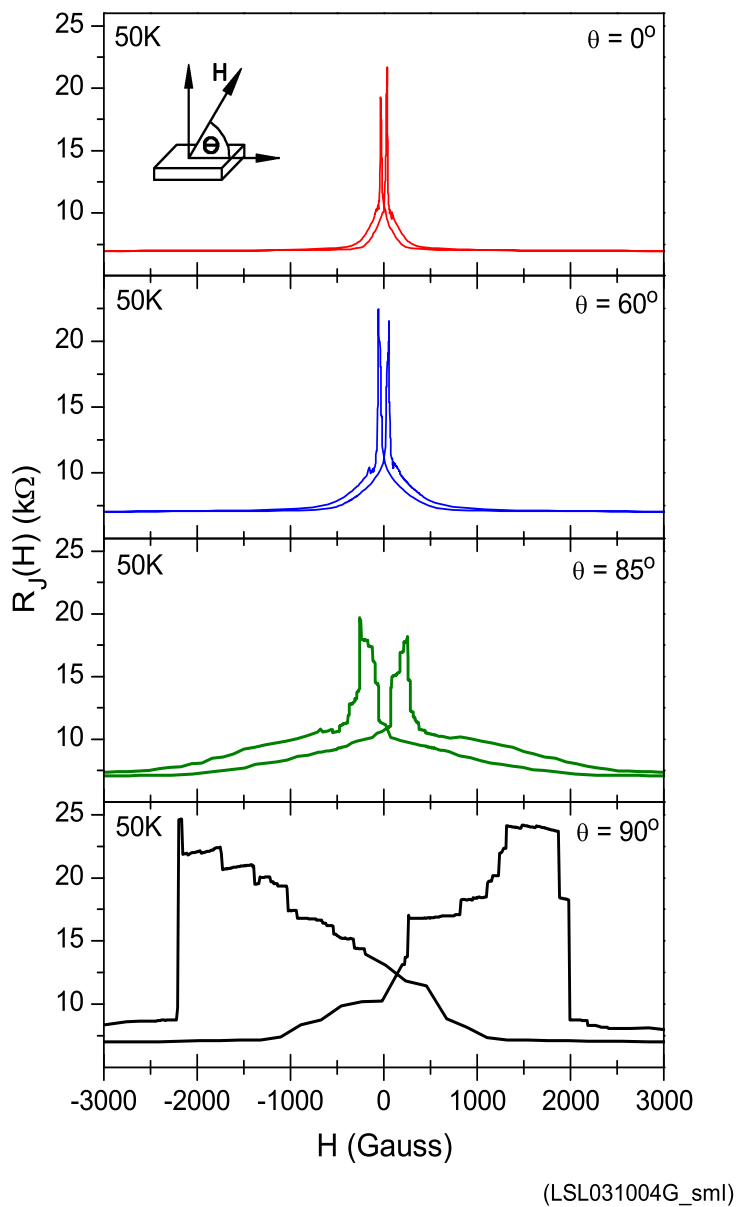


**Figure 3.10:** Resistance vs. applied magnetic field for a LSMO/STO/LSMO junction with fields applied at various out-of-plane angles. The angle,  $\theta$ , is relative to the plane of the heterostructure. This junction is the same as that shown in figure 3.7.

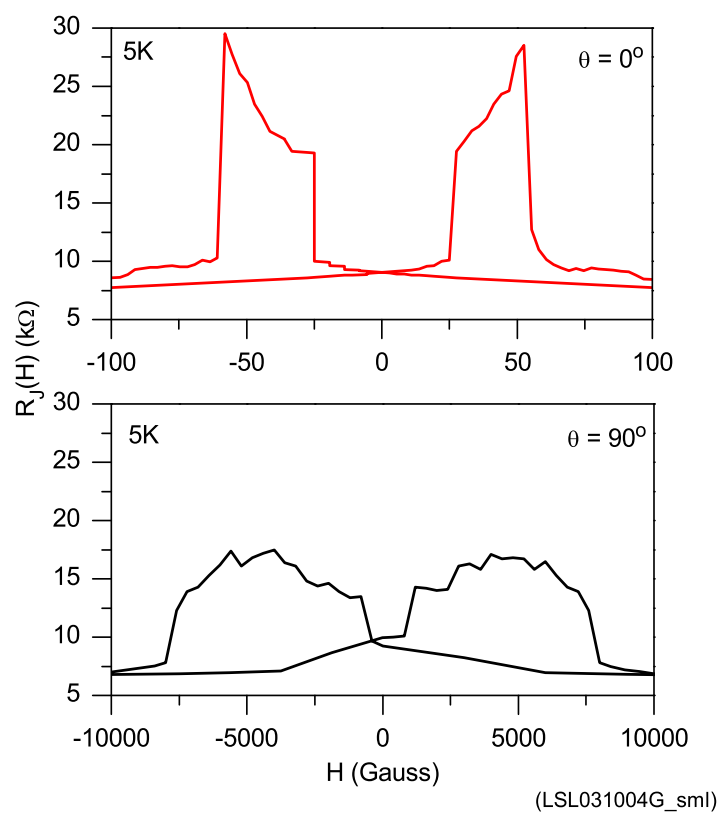


**Figure 3.11:** Resistance vs. applied magnetic field for a LSMO/STO/LSMO at 5K with fields applied at  $0^\circ$  and  $90^\circ$  relative to the plane of the sample. The angle,  $\theta$ , is relative to the plane of the heterostructure. This junction is the same as that shown in figure 3.7. Note the scale of the magnetic field axis.

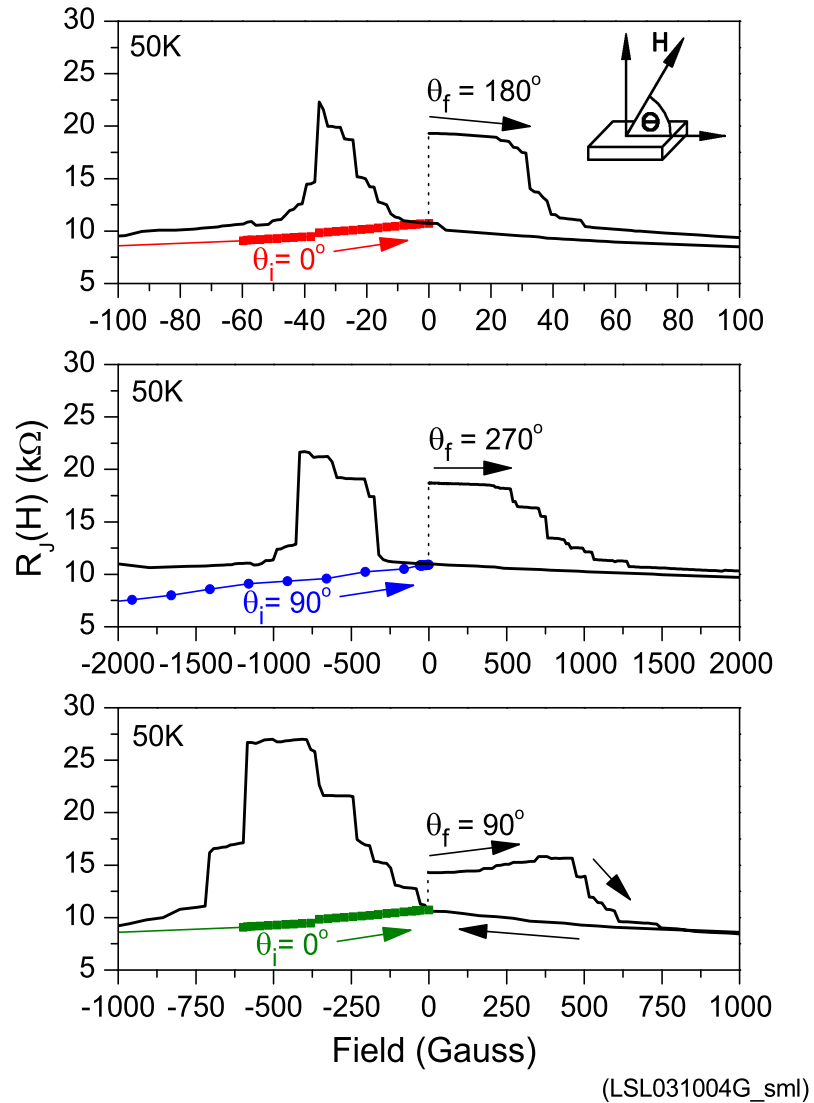


**Figure 3.12:** Zero field rotation of a premagnetized LSMO/STO/LSMO junction. The sample is scanned from a high negative field to zero field at an initial angle,  $\theta_i$ . Then, while holding at zero field, the sample is rotated to a different angle,  $\theta_f$ , and then the field scan is continued. Notice the change in resistance when the sample is rotated. A gaussmeter indicated the field present at an applied zero magnetic field was less than 1 Gauss for any angle. This sample is the same as that presented in figure 3.7.

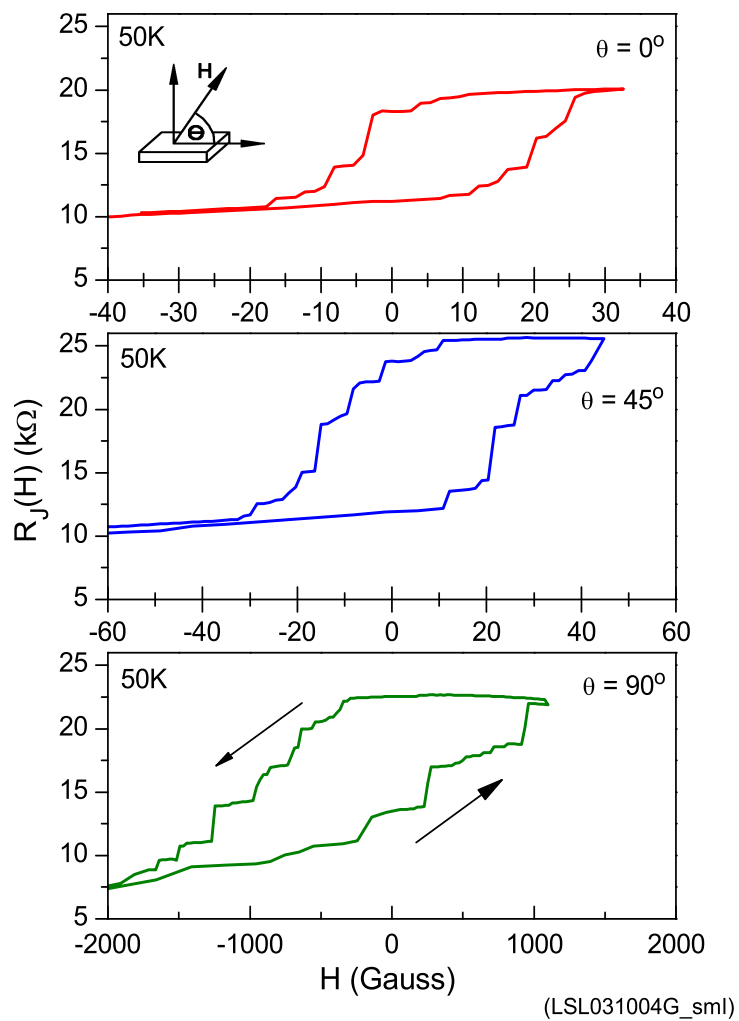


**Figure 3.13:** Low field hysteresis scan for a LSMO/STO/LSMO junction. The samples is scanned from a high negative field until the first high resistance state is reached. Then the field scan direction is then reversed. This is the same junction shown in figure 3.7.

While our junctions still do not display TMR above room temperature, the TMR persists to as high a temperature (275K) as any junction reported to date. The junctions also have the second largest TMR reported for LSMO/STO/LSMO junctions to date, surpassed only by the research group headed by Fert [Bowen 2003, Jo 2000]. However, in relation to Fert's, the cross sectional area of our junctions is 4 to 5 times larger. No previous report contains the long annealing times associated with the junctions presented in this study. In fact Sun [Sun 1997-2001, Sun 1998] and Bowen [Bowen 2003] claim the success of their junctions hinge on their minimal exposure to heat during processing.

In a side experiment, a pre-measured junction which displayed a TMR of 200% at 50K was annealed at 450°C in 600 Torr of oxygen for another 6 hours. Little to no change was found in the TMR or resistance of this junction. It is hard to say if this implies the junctions are oxygen saturated. After device fabrication there is a top gold layer on the devices which would nullify any oxygen diffusion through the surface. Where as, when samples are annealed after deposition the surface is open. In any case, post-deposition heating does not seem to be a factor in our junction performance.

Several interesting features were revealed in the resistance vs. temperature dependence of the junctions. A metal-insulator transition indicative of a ferromagnetic transition appeared near 200K for most junctions. As mentioned before, parallel measurements of the top and bottom LSMO indicated no transition below 300K (See figure 3.6). The overall resistance of the junctions is dominated by the STO layer and the properties of the few LSMO layers adjacent to this layer. This seems to indicate a deteriorated LSMO layer is present at the STO/LSMO interface. Park *et al.* [Park 1998] have shown that the surface of a LSMO film has a reduced magnetization and spin polarization. This is possibly due to a lowered magnetic interaction caused by the surface termination.

The deterioration of the LSMO at the STO interface could be due to strain, deficient oxygen, diffusion of strontium, or irregular termination. Fert *et al.* [Fert 2001] have found

that the drop in transition temperature is not as abrupt for Co/STO/LSMO structures which still provide a TMR, although small ( $\approx 5\%$ ), above 300K. It is suggested that the top STO interface is primarily responsible for the reduced Curie temperature seen in the junctions. In a HRTEM and STEM-EELS study by Pailloux *et al.* [Pailloux 2002] the STO/LSMO(bottom) interface is found to maintain its bulk characteristics to within one layer of the interface and only a weak deterioration of the LSMO Curie temperature is observed.

Another feature of the resistance vs. temperature graphs is the large abrupt jumps in resistance for a zero field cooled sample (see figure 3.14). These jumps are not brought about by the application of any magnetic field. Possibly they are due to spontaneous magnetic domain motion. The figure also shows the resistance curve with a 500 Gauss field applied in the plane of the film. A 500 Gauss field is larger than any in plane coercive fields of the top or bottom films. This is then the minimum of resistance vs. temperature for the sample. Also, a curve is shown in which a high field ( $\approx 5000$  Gauss) was applied in the plane of the sample at 50K and then slowly lowered to zero field before warming.

Resistance vs. Temperature for a LSMO/STO/LSMO Junction  
in Various Magnetic States (1)

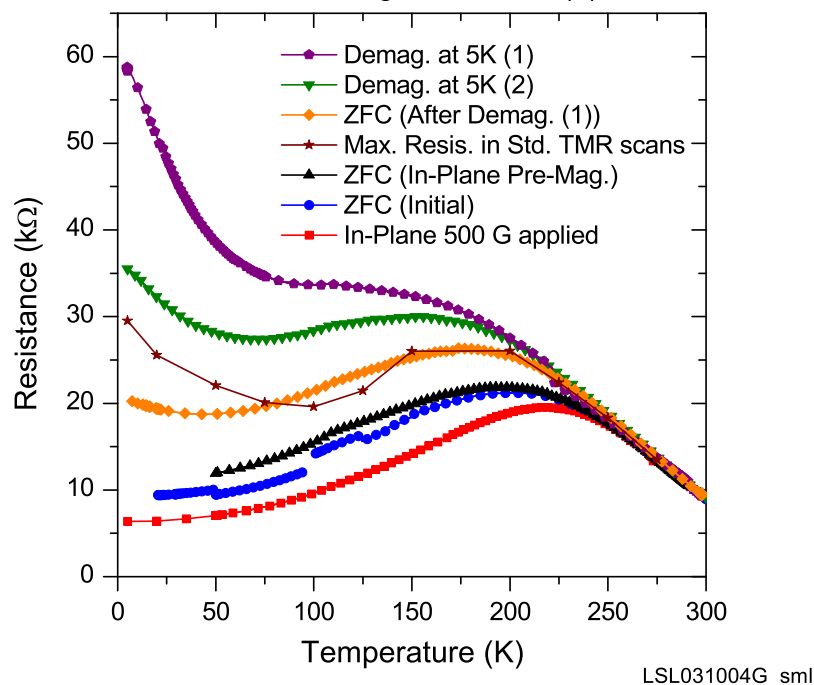


**Figure 3.14:** Resistance vs. temperature for a LSMO/STO/LSMO junction. Results are shown for various magnetic states including, cooling in an applied in-plane 500 Gauss magnetic field, the initial unperturbed zero field cooling, the maximum resistance values found in the standard TMR measurements, warming in zero field after the sample had been pre-magnetized in the plane of the film with a high magnetic field, zero field cooling after sample was warmed to 300K from 5K demagnetized state, and two different warmings after demagnetization at 5K. The difference between the highest and lowest resistance states at 5K indicate a possible TMR of 817% which is higher than the largest value found in all the TMR field scans (See figure 3.9). This junction is the same as that in figure 3.7.

### 3.2.3 TMR Measurements in Demagnetized State

The experimental technique used in all the TMR measurements mentioned in section 3.2.2, involved the initial application of a large magnetic field to place the top and bottom LSMO layers of the junction in a parallel state. For F-I-F junction measurements this is the common practice. However, interesting effects were found for demagnetized junctions. The samples were demagnetized by oscillating the magnetic field while exponentially decreasing the magnitude until it fell below the achievable step size.

When the samples were demagnetized, the junctions took on a high resistance state in which the overall resistance was much higher than that displayed in the TMR scans. The junction shown in figure 3.7 of the previous section 3.2.2 displayed a maximum resistance  $\approx 35 \text{ k}\Omega$  in the 5K TMR scan. The same junction, demagnetized at 5K, yields a resistance of  $60 \text{ k}\Omega$  (see figure 3.15). Demagnetization did not always yield this maximum resistance value ( $60 \text{ k}\Omega$ ), but consistently yielded values larger than seen in the standard TMR scans. Once this demagnetized state was achieved, its resistance was higher than that found in the TMR scans over the entire temperature range.

As shown in figure 3.18, which is the same sample presented in the TMR scans of figure 3.8, the demagnetized state resistance can be several times larger than the peak resistance in the hysteresis scan. If this high resistance state is used in conjunction with the low resistance state (500 Gauss applied in-plane) to calculate the TMR at 5K, a value  $\approx 800\%$  is found for the junction shown in figure 3.7 and  $\approx 400\%$  for that shown in figure 3.8. The TMR % of these two junctions are compared as a function temperature in figure 3.9. Notice that the junction in which the TMR decreases to 100% at 5K in the standard scans, is the junction for which the demagnetized state could yield a TMR of up to 400%.

The demagnetized state was stable up to at least 100K. That is the sample could be demagnetized at 5K, then the temperature could be raised to 100K, cooled to 5K again,

and the initial resistance was recovered. Also, the sample could be demagnetized at 50K, and when cooled to 5K, attained the same high resistance value. When warmed to 300K from the demagnetized state at 5K, and then re-cooled the overall resistance was lower but remained much larger than other zero field coolings. It seems the junction has some memory of it's low temperature state even when warmed above what appears to be a ferromagnetic transition. This shows the ferromagnetic material separate from the STO interface most likely has a transition temperature far above that displayed in the junction R vs. T curves.

The most interesting data was found for TMR measurements on demagnetized samples. See figure 3.15. First the sample was demagnetized at 5K. When the demagnetization was completed the sample was in zero magnetic field. The resistance was then measured as the field was slowly increased from zero. A large abrupt transition was seen at 40 Gauss. This transition was much sharper and larger than that seen in the standard TMR measurements. A TMR scan was then taken keeping the magnitude of the applied field  $\leq 80$  Gauss. Sharp transitions with a maximum TMR  $\approx 476\%$  were found. This TMR is much larger than that found in the standard TMR scans. However, if the magnetic field magnitude was allowed to become greater than 100 Gauss, the TMR drastically decreased and the high resistance state could not be recovered in any way unless the sample was demagnetized again.

The changes in resistance in a field scan after the sample had been placed in a demagnetized state were up to  $\approx 50K\Omega$ , with a width ( $\Delta$ ) on the order of 1 Gauss. Slopes of 40  $K\Omega/\text{Gauss}$ , and TMR changes of 200%/Gauss were measured in several junctions.

Similar results were found at 50K, and yielded a TMR  $\approx 247\%$ . Here again transitions between the high and low resistance states were much sharper ( $\Delta \approx 2$  Gauss) than those previously measured with the standard technique. This effect was also found in the junction shown in figure 3.8, and yield a TMR  $\approx 220\%$ , which is more than twice as large as the standard measurement results.

Hysteresis scans taken at 5K showed much sharper switching between high and low resistance states. See figure 3.16. The curve was much sharper and more repeatable than those previously shown for high field initial states in figure 3.13. This suggests the demagnetized state acts in some way much more like a single domain, than the state created by a high field.

Unlike the high field magnetized samples, rotation in zero field did not produce any change in resistance. See figure 3.12. For the correct field, in this case 41 Gauss (which sits just past the high to low transition), the sample produced nice repeatable switching when rotated out-of-plane. See figure demag3.

Slonczewski's model, given by equation 3.7, states that for an ideal junction (single domains) the highest resistance state is created when the two ferromagnetic layer have opposite magnetization states ( $\theta = 180$ ). Therefore, this large resistance state indicates that a large percentage of the domains between the top and bottom LSMO are oppositely aligned when the sample is demagnetized in this fashion. Perhaps at low temperatures there is a antiferromagnetic interlayer exchange coupling which competes to align the domains. Such coupling has been seen in F-N-F and F-I-F junctions and is based on the thickness of the N and I layers . Also, the lowest magnetic energy state of the junction would be for opposite domain orientation in the top and bottom LSMO layers. Perhaps the magnetic fields of domains which re-orient in-plane first during the demagnetization, influence the nearest neighbor domains of the other layer. The sharp switching in low field hysteresis and a low field angular rotation seem to indicate the ferromagnetic layers act much more like single domains when placed in the demagnetized state. This sharp repeatable switching could be useful in future technological applications, in not only CMR magnetic tunnel junctions, but magnetic tunnel junctions in general. In any case the high resistance state is very interesting and to our knowledge has not been reported before for CMR tunneling junctions.

## LSMO/STO/LSMO Junction Hysteresis After Demagnetization

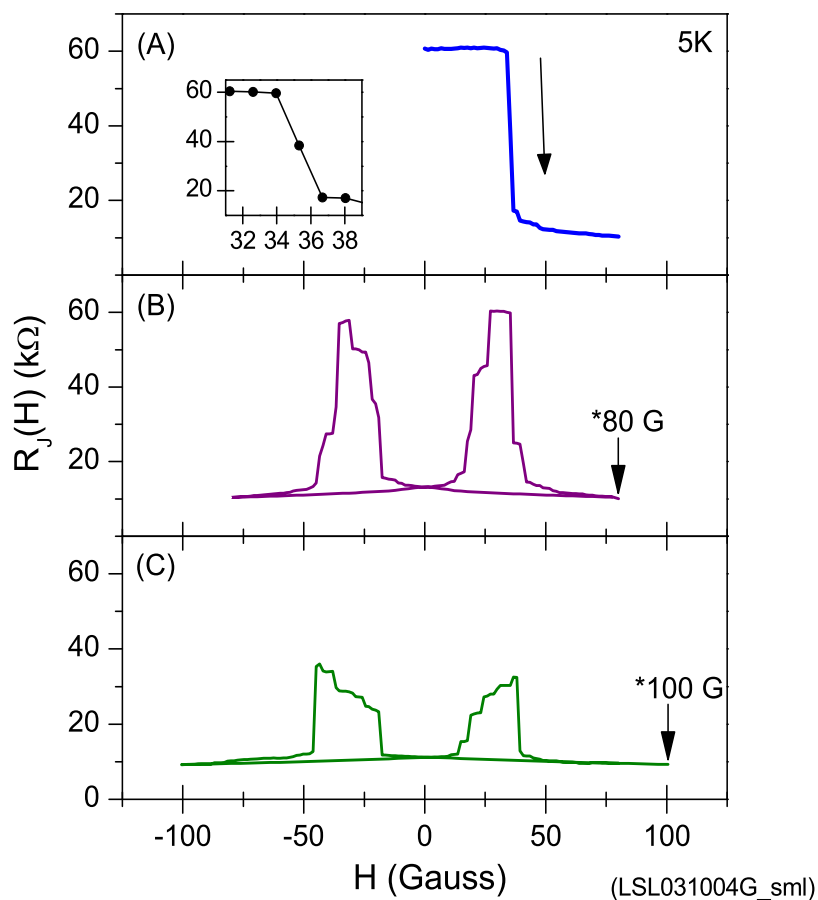


**Figure 3.15:** Resistance vs. applied magnetic field for a LSMO/STO/LSMO junction after demagnetization at 5K. The field was applied in the plane of the sample. This junction is the same as that shown in figure 3.7. (A) The sample was initially demagnetized at 5K. The resistance was then measured as the field was scanned from 0 to 80 Gauss. The inset shows the curve in the sharp transition region. (B) The field was scanned from 80 Gauss after measurement (A). Note, the field magnitude did not exceed 80 Gauss. The result could be repeated as long as the field magnitude was  $< 80$  Gauss. (C) The field was increased from 80 to 100 Gauss after measurement (B). The field was then scanned from 100 Gauss. Result (B) could not be recovered after this measurement.

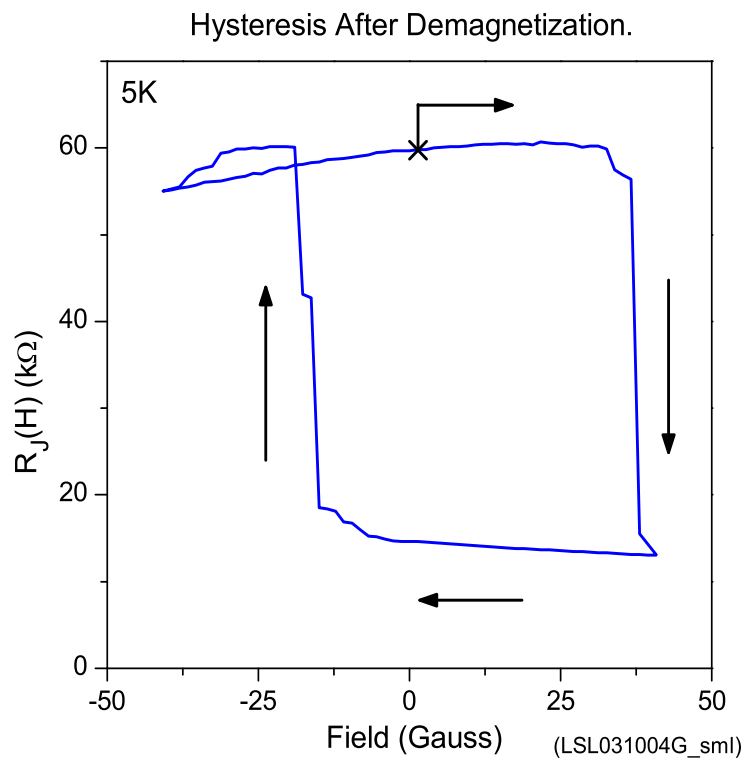


**Figure 3.16:** Hysteresis for a LSMO/STO/LSMO junction after demagnetization at 5K. The field was applied in the plane of the sample. This junction is the same as that shown in figure 3.7. The sample was initially demagnetized at 5K. The resistance was then measured as the field was scanned from 0 to 41 Gauss, 41 gauss to -41 gauss, and back to zero. This curve was highly repeatable.

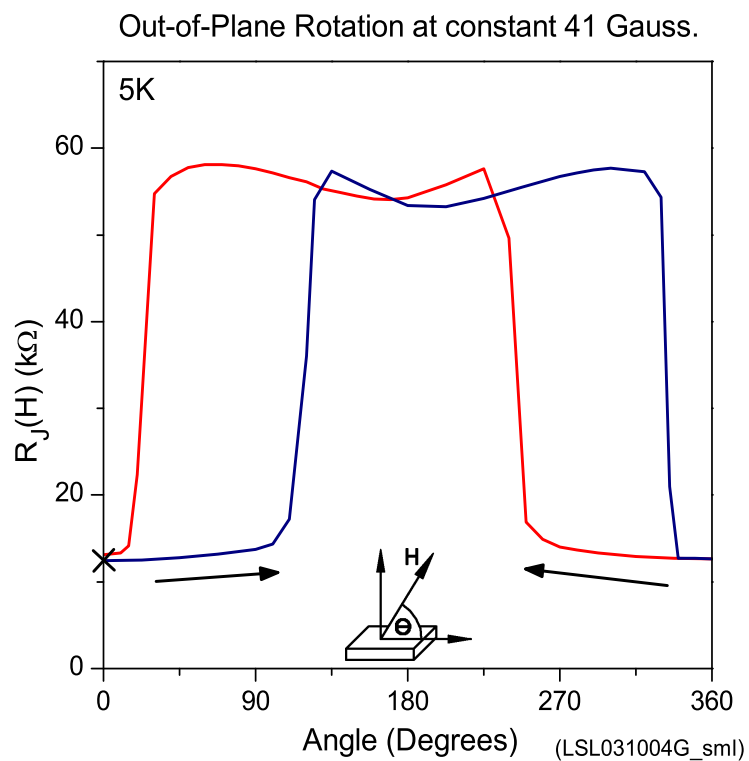


**Figure 3.17:** Resistance vs. Angle for rotation of a LSMO/STO/LSMO junction in a constant magnetic field after demagnetization at 5K. This junction is the same as that shown in figure 3.7. The sample was initially demagnetized at 5K at angle =  $0^\circ$ . Forward and reversed scans are shown. The scan was started at  $0^\circ$ .

Resistance vs. Temperature for a LSMO/STO/LSMO Junction  
in Various Magnetic States (2)

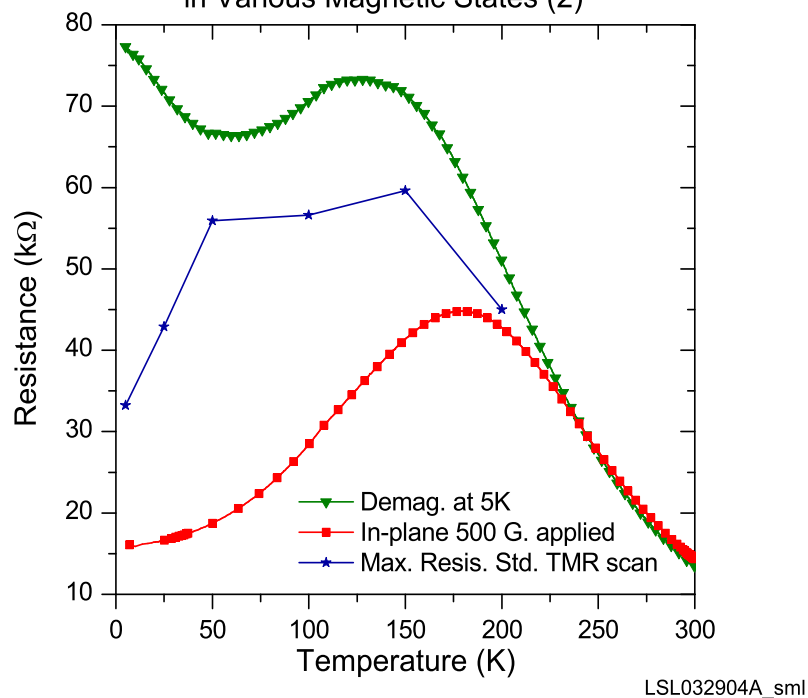


**Figure 3.18:** Resistance vs. temperature for a LSMO/STO/LSMO junction. Results are shown for warming after the sample had been magnetized in the plane of the film with a high magnetic field which was then slowly lowered to a zero field and warming after demagnetizing the sample with an applied perpendicular field at 5K. Note, the points indicate the actual data while the lines are there to guide the eye. This junction is the same as that in figure 3.8. The difference between the highest and lowest resistance states at 5K indicate a possible TMR of 420% which is much higher than the largest value found in the hysteresis field scans (See figure 3.9).

### 3.2.4 I-V Measurements

The I-V characteristics of two junctions are shown in figure 3.19, and of a single junction in a high resistance demagnetized state in figure 3.20. The IV curves show clear non-linear characteristics. The IV curves of the low and high resistance states were used to calculate the TMR dependence on applied current. A distinct decreased in TMR is found with increasing bias current. The origin of this decrease is not well understood. The IV results were fit to the model of Simmons[Simmons 1963-64] in order to attain estimates of the insulating barrier height and thickness. This model assumes a rectangular symmetric barrier with similar electrodes. The current voltage relationship is given explicitly as,

$$J(V, t, \phi) = \eta \left[ \left( \phi - \frac{qV}{2} \right) e^{-A(\phi - \frac{qV}{2})^{1/2}} - \left( \phi + \frac{qV}{2} \right) e^{-A(\phi + \frac{qV}{2})^{1/2}} \right] \quad (3.10)$$

$J$  is the current density,  $V$  is the voltage,  $q$  is the elementary charge (positive), and  $\phi$  is the barrier height in energy.  $A$  and  $\eta$  are related to the barrier thickness by,

$$\eta = \frac{q}{2\pi\hbar t^2} \quad (3.11)$$

and

$$A = \frac{4\pi t}{\hbar} (2m)^{1/2}. \quad (3.12)$$

For low voltages the equation can be expanded in powers of  $V$ . Neglecting powers of  $O(V^5)$  or higher the equation yields,

$$J(V, \alpha, \gamma) = \alpha V + \gamma V^3 \quad (3.13)$$

Where,

$$\alpha(t, \phi) = \frac{1}{2} \eta q e^{-A\sqrt{\phi}} (A\sqrt{\phi} - 2) \quad (3.14)$$

and

$$\gamma(t, \phi) = \frac{1}{192} \eta q^3 e^{-A\sqrt{\phi}} \frac{A}{\phi^{3/2}} (A^2 \phi - 3A\sqrt{\phi} - 3) \quad (3.15)$$

(given by Sun [Sun 1998]).

Results for the thickness ( $t$ ) and the barrier height ( $\phi$ ) for the junctions in figure 3.19 are given in table 3.2 for low and high resistance states at different temperatures. The fitting parameters  $\alpha$  and  $\gamma$  were determined with the computer program Origin, which uses a Levenberg-Marquardt fitting method. The thickness ( $t$ ) and the barrier height ( $\phi$ ) were determined with the computer program Mathematica which uses a Newton iteration to find a numerical solution.

Parameters obtained from a Simmons fitting are not definite for several reasons [Sun 1998, Moodera 1999]. For a real junction it is important to consider, parallel shunts, impurities, imperfect non-uniform interfaces, and degraded interface properties. The Simmons model is for an ideal barrier and does not include the effects of any of these conditions. Therefore, one should be careful in the emphasis placed in the parameters determined from the fittings.

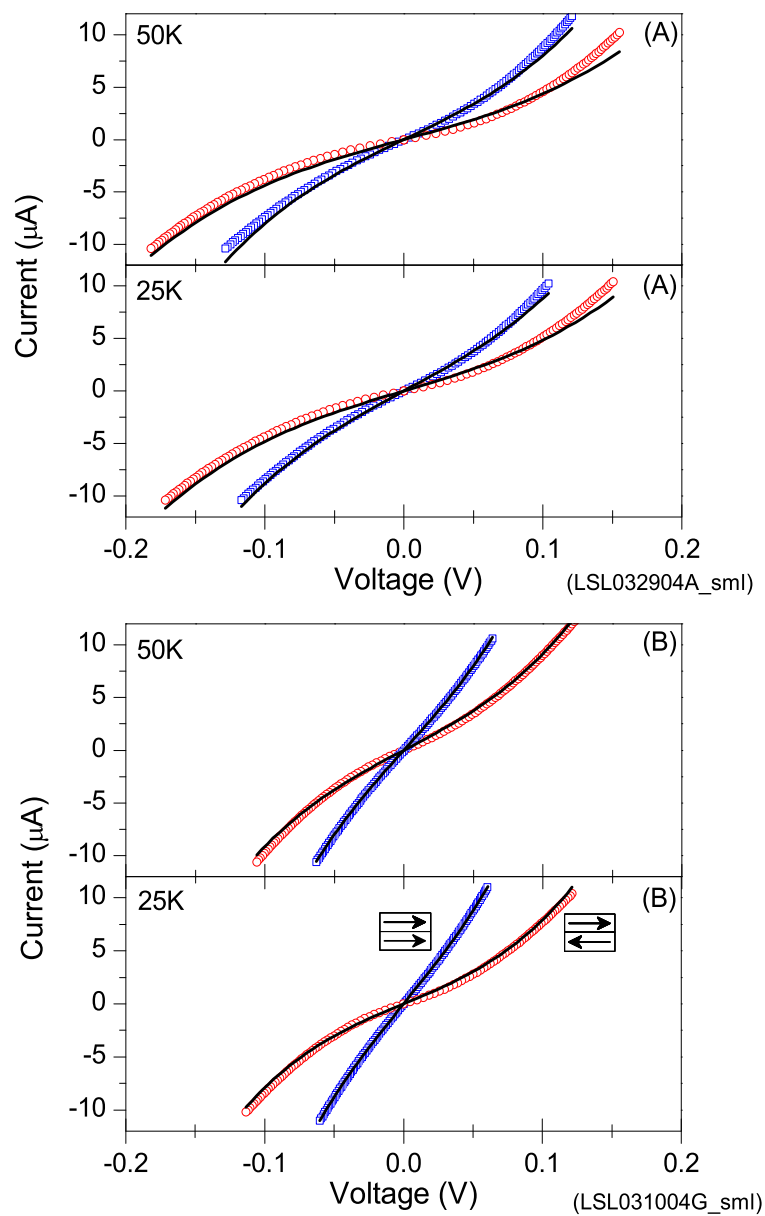


**Figure 3.19:** Current vs. voltage for two LSMO/STO/LSMO junctions at various temperatures and resistive states. The magnetization state of the sample is indicated by the arrows in plot B. The open points are the raw IV data and the solid lines indicate a Simmon's model fit ( $I = aV + bV^3$ ). (A) IV curves for the device in figure 3.8. (B) IV curves for the device in figure 3.7.

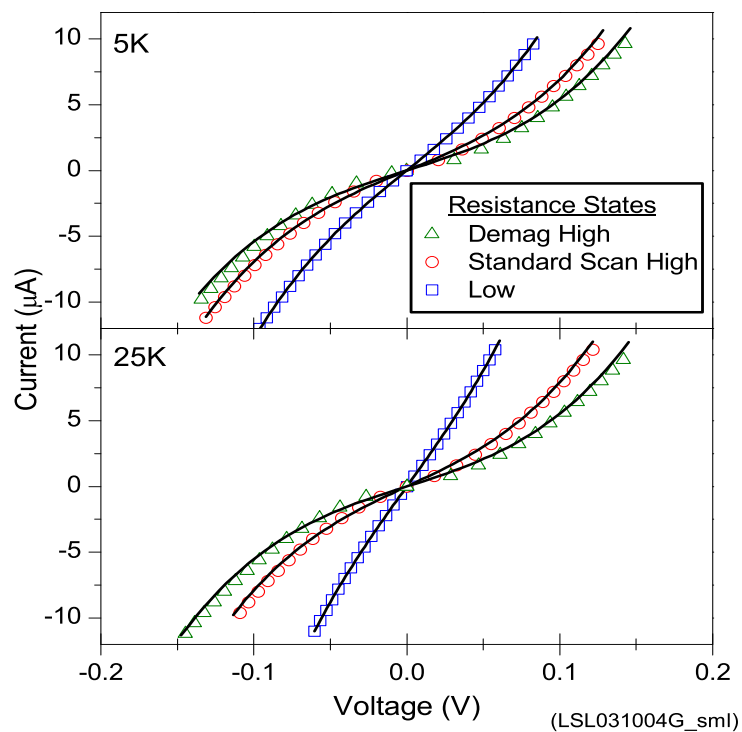


**Figure 3.20:** Current vs. voltage for two LSMO/STO/LSMO junctions at various temperatures and resistive states. The high resistance demagnetized state, the normal scan high resistance state, and the low resistance state are shown. The open points are the raw IV data and the solid lines indicate a Simmon's model fit ( $I = aV + bV^3$ ). The curves are from the same device as shown in figure 3.7.

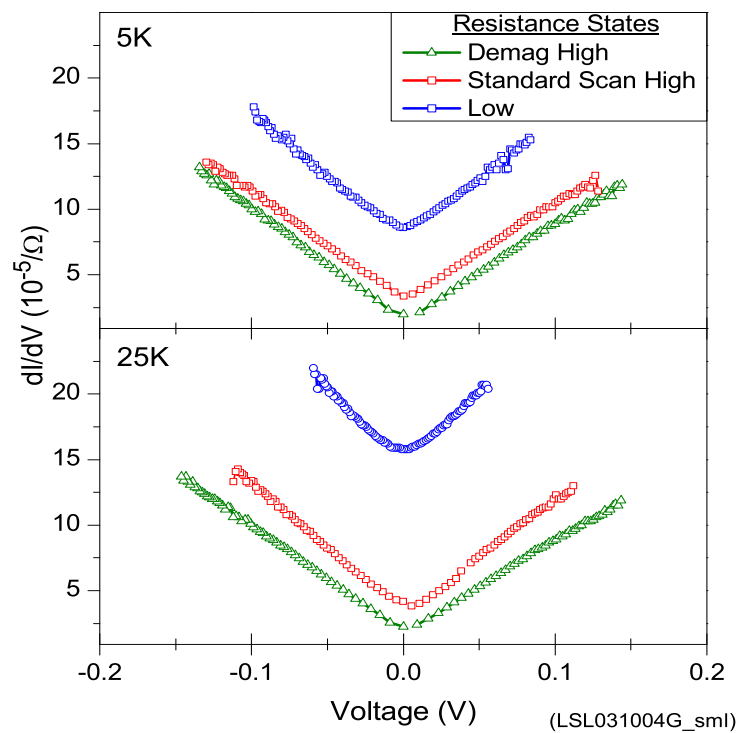


**Figure 3.21:** Conductance ( $dI/dV$ ) vs. voltage for two LSMO/STO/LSMO junctions at various temperatures and resistive states. The high resistance demagnetized state, the normal scan high resistance state, and the low resistance state are shown. The curves are from the same device as shown in figure 3.7.

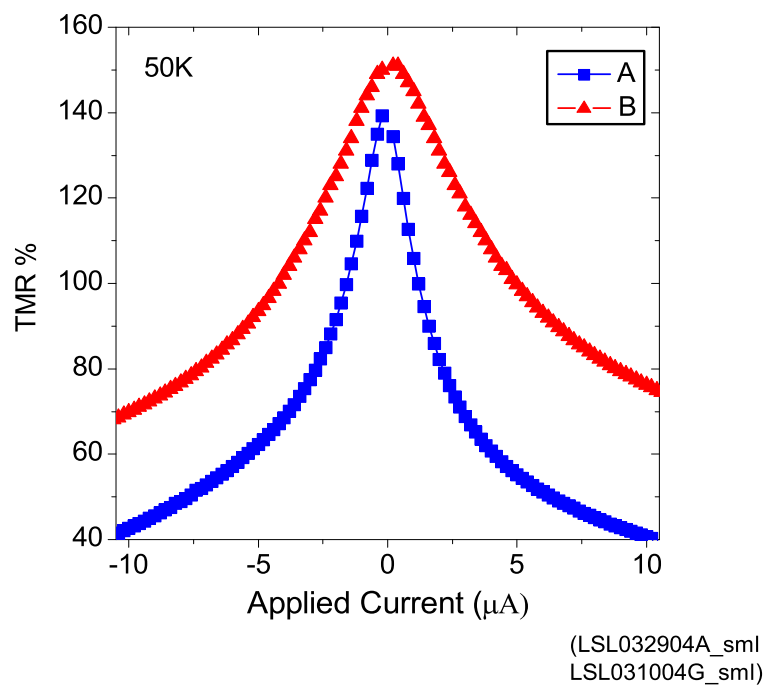


**Figure 3.22:** TMR% vs. applied current for two LSMO/STO/LSMO junctions at 50K. This data was calculated from the IV curves in figure 3.19. The TMR% decreases sharply for increasing current. (A) is the device in figure 3.7. (B) is the device in figure 3.8.

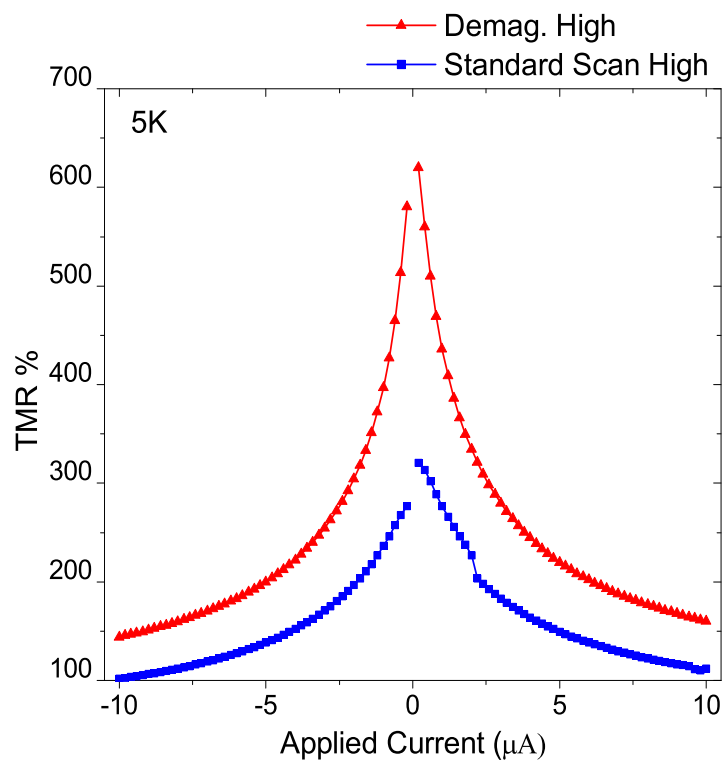


**Figure 3.23:** TMR% vs. applied current for two LSMO/STO/LSMO junctions at 50K in the high resistance demagnetized state and the standard scan high resistance state. This data was calculated from the IV curves in figure 3.20. The TMR% decreases sharply for increasing current. The high resistance demagnetized state has the higher TMR %.

Data from Simmons fitting equation			
Temp.(K)	$t$ (Å)	$\phi$ (eV)	R state
Sample (A)			
25	27.2	.324	low
50	28.1	.308	low
150	28.3	.327	low
25	27.5	.345	high
50	27.1	.359	high
150	29.8	.301	high
Sample (B)			
5	29.9	.252	low
25	29.7	.238	low
50	29.5	.245	low
150	26.5	.342	low
5	32.3	.233	high
25	32.4	.227	high
50	29.4	.273	high
150	29.8	.278	high
5	33.1	.228	high (demag)
25	33.3	.225	high (demag)

**Table 3.2:** Calculated tunneling barrier height  $\phi$  and thickness  $t$  by Simmons equation fit for two LSMO/STO/LSMO tunnel junctions. Sample(A) had a estimated deposited STO thickness of 32Å. The junction TMR and IV curves are in figure 3.8 and 3.19(A) respectively. Sample (B) had a estimated deposited STO thickness of 24Å. The junction TMR and IV curves are in figure 3.7 and 3.19(B) respectively. All values displayed were for an in-plane applied magnetic field. Out of plane measurements were found to yield similar values.

### 3.3 Anomalous angular TMR effects in LCMO/STO/LSMO tunnel junctions

$\text{La}_{0.67}\text{Ca}_{0.33}\text{MnO}_3/\text{SrTiO}_3/\text{La}_{0.67}\text{Sr}_{0.33}\text{MnO}_3$ , LCMO/STO/LSMO, junctions were also created and tested in this study. It is believed that these junctions are possible the first CMR junctions created with different top and bottom materials. LCMO thin films, is also a CMR material which is qualitatively similar to LSMO. LCMO, however, has a much lower Curie temperature around 240K. The structures were grown and patterned similarly to the LSMO/STO/LSMO devices of the previous section (3.2.1). The only difference was the LCMO films required a slightly higher oxygen pressure during their deposition (400 mTorr). Overall resistance of the devices was on the order of  $10\text{k}\Omega$  which was very similar to the LSMO/STO/LSMO devices (see figure 3.26).

A unique out of plane angular dependence was seen for this LCMO/STO/LSMO structure at 100K see figure 3.24. Unlike the LSMO/STO/LSMO junctions, the change in resistance of the junction is dependent on the angle of the applied magnetic field. At a temperature of 100K, a maximum TMR  $\approx 100\%$  was found for angles  $75^\circ - 85^\circ$ . However, the TMR at all other angles was less than 50%. At  $225^\circ$  the TMR was as small as 15%.

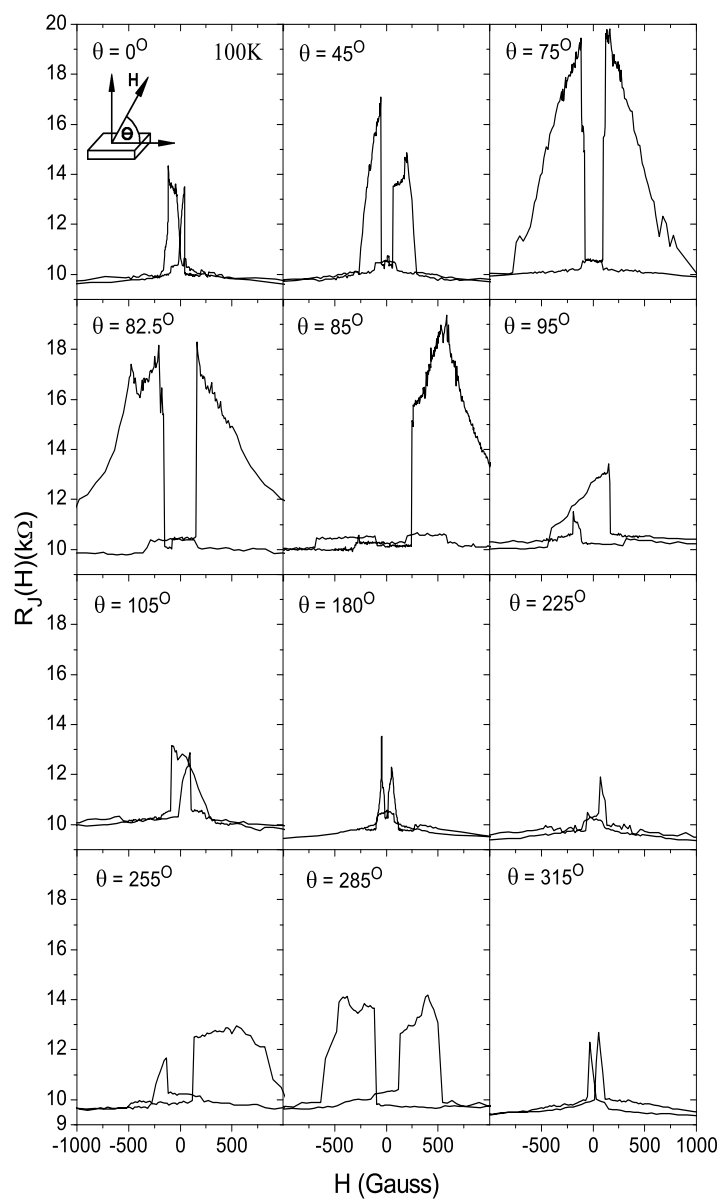
Oddly, the TMR angular dependence at 150K is almost nonexistent. Only a very slight change is seen in the magnitude of the TMR signal with angle. The results at different angles are much more symmetrical.

At 50K, the TMR signal disappears and the junction becomes noisy. See figure 3.25. It is not believed that the noise is brought about by poor Au contacts. A two point resistance measurement of the device shows a negligible difference to that of the measured junction. Also, previous Au/LCMO devices have never shown any substantial contact resistance.

Recently, Sanghamitra *et al.* have conducted magnetization measurements on LCMO/LAO/LSMO films [Sanghamitra 2003]. The measurements showed indications of spin canting below the transition temperature which was  $\approx 220\text{K}$ . Also, below a blocking

temperature in the range of 50K - 100K indications of domain freezing and formation of antiferromagnetically ordered, near-degenerate spin clusters is seen. This may provide an explanation of some of the effects seen in our tunnel junctions.

These effects may also be due to the fact that the two ferromagnets have anisotropy axes that are non-collinear. Junctions constructed of two ferromagnets with different easy axes have a strong dependence on the direction of the applied magnetic field [Grigorenko 2003]. LSMO grown on STO substrate has an easy magnetization axis in the plane of the film due to tensile strain. LCMO, grown on STO also has an easy magnetization axis in the plane of the film. The lattice constant for LSMO is  $3.87\text{\AA}$  and the a-b lattice constant of LCMO is  $3.81\text{\AA}$ . This would suggest the LCMO grown on LSMO is subject to also tensile strain. Tensile strained LCMO would have an easy axis parallel to the sample plane. By these arguments the anisotropy axis would be collinear. Note, the LCMO would at least be under much more strain than the LSMO. Strain is found to be critical to the electrical properties of CMR thin films [Hu 2004], and may play a part in these anomalous effects.



(LcSL061904A\_sml)

**Figure 3.24:** Resistance vs. applied magnetic field for a LCMO/STO/LSMO junction with fields applied at various out-of-plane angles. The angle,  $\theta$ , is relative to the plane of the heterostructure. The junction dimensions are  $10 \times 10 \mu\text{m}$ . The measurement current was  $10^{-7}$  Amps. The junction had a top/middle/bottom layer thickness of  $300\text{\AA}/32\text{\AA}/400\text{\AA}$  respectively.

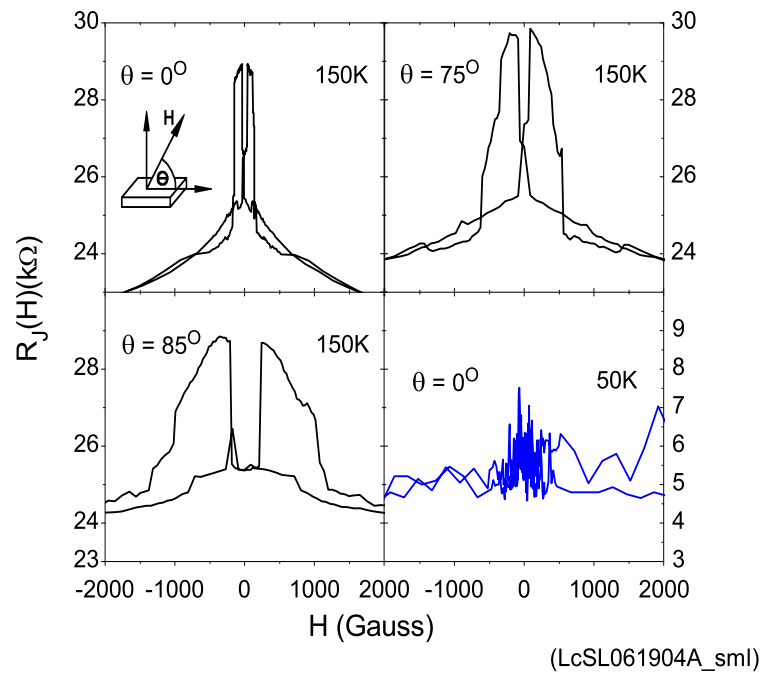


**Figure 3.25:** Resistance vs. applied magnetic field for a LCMO/STO/LSMO junction with fields applied at various out-of-plane angles. The angle,  $\theta$ , is relative to the plane of the heterostructure. This is the same junction as shown in figure 3.24. Note, the temperatures, 150K and 50K, are as labeled.

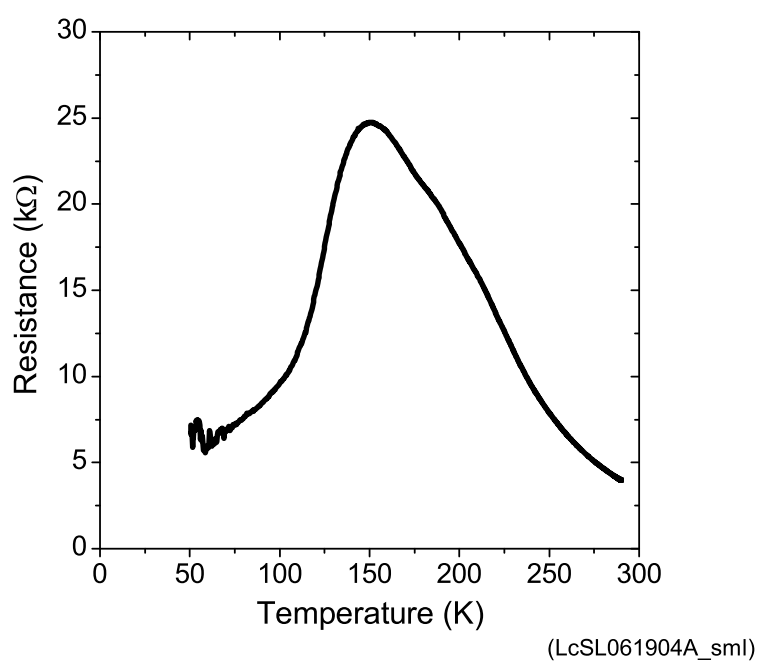


**Figure 3.26:** Resistance vs. temperature for a LCMO/STO/LSMO junction. The results shown are for a zero field cooling. This is the same junction as shown in figure 3.24.

## Spin Diffusion Devices

---

### 4.1 Introduction

The idea of spin current was originally suggested by Mott who proposed that at temperatures low with respect to the Curie temperature, most scattering events would not effect the orientation of an electrons spin [Mott 1936]. In ferromagnets, the band structures of the up and down spins are different. Therefore the conductivities for spin-up and spin-down electrons are generally different.

Aronov proposed that when a current was passed from a ferromagnet into a normal metal, a net magnetization could be imposed [Aronov 1976]. In a ferromagnet, one spin subband holds a majority of the available states at the Fermi energy,  $E_F$ . Only electrons within  $\sim k_B T$  of  $E_F$  will participate in transport. Therefore the current injected from a ferromagnet carries with it net polarization or spin current  $I_M$ . Some ferromagnets are considered to be half metallic, in which all current is carried in one spin channel. Aronov showed through a diffusion model that this spin current would create a magnetization,  $\tilde{M}$ , in the normal metal which falls off exponentially with a characteristic length  $\delta_s$ , such that,

$$\tilde{M} \propto e^{-x/\delta_s}. \quad (4.1)$$

$\delta_s$  is related to a characteristic relaxation time  $T_2$  by the diffusion equation,

$$\delta_s = (DT_2)^{1/2}, \quad (4.2)$$

where  $D$  is the electron diffusion constant.

In 1988, Johnson and Silsbee proposed and created a novel ferromagnetic device, known as the bipolar spin switch, which could measure this diffusion length [Johnson 1988a, 1988b, 1988c, Johnson 1992, Johnson 1995]. Johnson and Silsbee's device consisted of a three layer ferromagnet-normal metal-ferromagnet (F-N-F) thin film heterostructure. See figure 4.1.

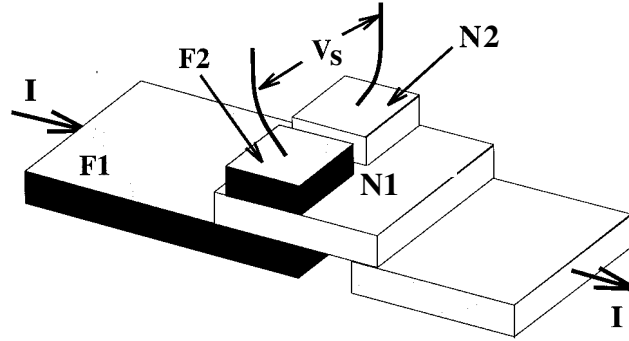


**Figure 4.1:** Schematic of a bipolar spin switch device. Current ( $I$ ) is injected from the base ferromagnet ( $F1$ ) to normal metal ( $N1$ ). The spin voltage ( $V_s$ ) is measured between the ferromagnet pad ( $F2$ ) and normal metal pad ( $N2$ ). [Hershfield 1997]

The bottom ferromagnetic layer ( $F1$ ) was used to inject a spin polarized transport current ( $I_{inj}$ ) into the middle normal metal ( $N1$ ). The top ferromagnet ( $F2$ ) is patterned into a small contact. A small normal metal contact ( $N2$ ) is also made directly to ( $N1$ ). Voltage ( $V_s$ ) is monitored between the top  $F2$  and  $N2$  contact. While under the influence of the injection current, a change in voltage is seen when the  $F1$  and  $F2$  have parallel and anti-parallel magnetization states.

Using a free electron metal and a simple Stoner ferromagnet, the voltage arising between the two top contacts can be related to the spin diffusion length. When a charge current ( $I_e$ ) is injected from  $F1$  into  $N1$ , it carries with it an associated spin current which can be

expressed as ,

$$I_M = \eta_1 \frac{\beta}{e} I_e, \quad (4.3)$$

where  $\beta$  is the Bohr magneton,  $e$  the charge of an electron, and  $\eta_1$  is the intrinsic polarization of the current in F1 ( $\eta_1 \leq 1$ , See equation 3.1). After the polarized spins enter N1, they randomize with a characteristic time of  $T_2$ .

If N1 is thin enough,  $d < \delta_s$ , then the non-equilibrium magnetization can be considered to be uniformly distributed over the volume  $Ad$  and is given as,

$$\tilde{M} = \frac{I_M T_2}{Ad}, \quad (4.4)$$

where  $A$  is the contact area between F1 and N1. Careful consideration of the transfer length between F1 and N1 should be taken into account when determining the area ( $A$ ) to be used. See chapter 5 for more details on transfer length.

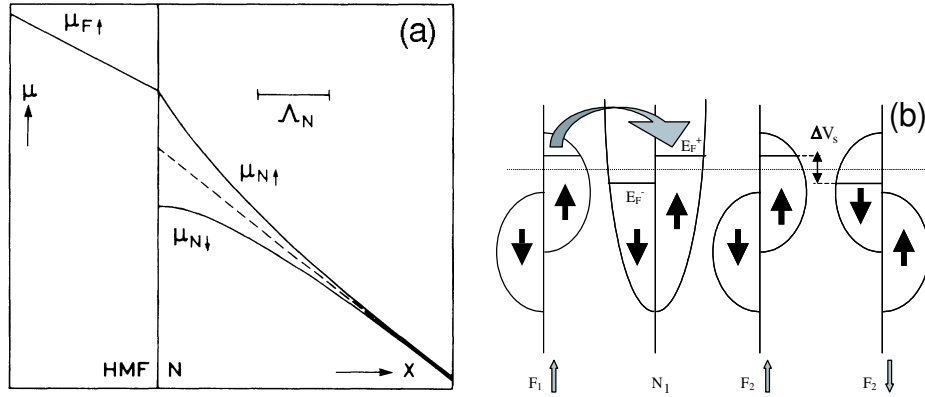


**Figure 4.2:** (a) position dependence of the electrochemical potential  $\mu_{\uparrow}$  and  $\mu_{\downarrow}$  at a normal metal (N) half metallic ferromagnet (HMF) interface. The dashed line represents the electrochemical potential without a nonequilibrium current distribution. [van Son 1987] (b) Splitting of the spin-up and spin-down Fermi energies in the normal metal N when a spin polarized current is injected from ferromagnet F1. For simplicity F1 and F2 are half metallic. Depending on the magnetization orientation of F2 it experiences the chemical potential  $E_F^+$  or  $E_F^-$  yielding the voltage difference  $\Delta V_s$ . [George 2003]

Due to the injected spin, N1's spin-up and spin-down chemical potentials will change.

In the case of injected up spins, the chemical potential of the spin-up band increases, and to maintain charge neutrality, the chemical potential of the spin-down band decreases. Suppose F1 and F2 have the same magnetization direction, and the Fermi level of F2 lies primarily in the spin-up band. When the chemical potential in the spin-up band of N1 increases, the chemical potential (Fermi level) in F2 will rise with it, since no current flows between N1 and F2. However, while the spin-up chemical potential in N2 will similarly rise, N2's spin-down band will decrease as N1's does. Therefore the average change of the chemical potential in N2 remains unchanged relative to N1's at the interface. Therefore, a voltage,  $V_s$ , will arise between F2 and N2 simply due to the imposed magnetization in N1. When the magnetization direction of F1 and F2 are opposite, an opposite voltage will develop to that argued above. This theory was also proposed by van Son *et al.* [van Son 1987] at roughly the same time as Johnson and Silsbee.

Johnson and Silsbee have derived a relation between the measured voltage  $V_s$  and the imposed magnetization  $\tilde{M}$  using thermodynamic arguments. The solution can be arrived at by considering a simple physical argument.  $\tilde{M}$  can be thought to impose a magnetic field  $\tilde{M}/\chi$ , where  $\chi$  is the Pauli paramagnetic susceptibility.  $\beta\tilde{M}/\chi$  is the Zeeman energy of a single spin in the magnetic field. The difference in energy of a single electron in the parallel and anti-parallel cases is then,

$$eV_s = \eta_2 \beta \tilde{M} / \chi, \quad (4.5)$$

where  $\eta_2$  is the polarization of F2. This equation combined with the exponential dependence given by equation 4.1 shows that by increasing the thickness of N1 and measuring the corresponding decrease in  $V_s$  a direct measurement of the diffusion length  $\delta_s$  can be made.

Combining  $I_M$ ,  $\tilde{M}$ ,  $V_s$ , the diffusion equation 4.2, and the free electron expression for  $\chi = \beta^2 N(E_f) = \beta^2 \frac{3n}{2E_F}$ , where  $n$  is the density of conduction electrons, a resistance can be

defined such that ,

$$R_s \equiv \frac{V_s}{I_e} = \frac{\eta_1 \eta_2}{Ad} \frac{T_2 E_F}{1.5 n e^2} = \frac{\eta_1 \eta_2}{Ad} \rho \delta_s^2 \quad (4.6)$$

In the second form Einstein's relation for resistivity  $\rho = 1/e^2 DN(E_F)$  is used.

Fitting the thickness dependences of their derived expressions to measured data, Johnson and Silsbee were able to estimate the spin diffusion length and relaxation time in gold films to be  $\delta_s = 1.5 \mu\text{m}$  and  $T_2 \approx 1 \times 10^{-11} \text{sec}$  at 4K. When the theoretical equations are used to directly predict the measured voltage, the calculations yield voltages that are 10 to 40 times smaller than those actually measured. Johnson accredits this to simplified expression for  $\chi$ , variations caused by interface resistance, and other possible spin flipping events.

Several more detailed theoretical interpretations of Johnson's spin detection device have been put forth by Fert and Lee [Fert 1997a, Fert 1997b, Fert 2002], Hershfield and Zhao [Hershfield 1997], and Valet and Fert [Valet 1993]. These models are derived from Boltzman transport equations and take into account spin relaxation that takes place inside the injection ferromagnet and the role of surface resistance at the ferromagnet/normal metal interface. However, when the ferromagnet is half metallic, that is there is only one spin subband present at the Fermi level, and the contact resistance between the two F-N interface is small, these more complex models reduce to forms which are similar to Johnson's classical result. LSMO is considered by many theoretical and experimental results to be half metallic, and the contact resistance between the YBCO/LSMO is small. Therefore, Johnson's model can be consider in the modeling of results presented in this study.

Recently, other spin injection and detection devices have been tested. Jedema *et al.* have found rather convincing results from nanofabricated Co/Al cross strip structures [Jedema 2001-03]. Co leads are deposited on a Al bridge at different separations. A thin  $\text{Al}_2\text{O}_3$  layer is made between the Co and Al by exposing the Al bridge to oxygen. The spin resistance  $R_s$  is measured by injecting current from a Co lead into the Al strip and measur-

ing the voltage between a neighboring Co lead and the Al strip. By varying the distance between the leads a determination of the spin diffusion distance can be made. These devices also provide results at room temperature. At 300K,  $\delta_s = 350\text{nm}$ , and at 4.2K,  $\delta_s = 650\text{nm}$ . In these devices it was also possible to modulate the  $R_s$  signal by applying a perpendicular magnetic field to a sample which had been premagnetized in an in-plane state (parallel or anti-parallel). The modulation arises from the precession of the spins in the perpendicular field. Of course, at large enough fields the coercive fields of the Co leads are overcome, but until that point a clear precessional effect is seen.

Jedema *et al.* have performed similar experiments in a cross like structure of Cu/Ni<sub>80</sub>Fe<sub>20</sub> [Jedema 2001-03]. The spin depth in Cu was determined to be 1000nm at 4.2K, and 350nm at 293K. George *et al.* have also created a nanofabricated device using a Cu/Co structure which showed spin detection effects.

Jedema and Fert have been critical of Johnson's results stating that the measured voltages are too large when scaled up from their devices and must be due to other effects. Johnson has claimed that Jedema's interpretation of their experimental results may be flawed [Johnson 2002]. In any case, a well established agreement on spin detection experiments and theory has not been reached. There has never been any previous application of Johnson's spin detection device to perovskite CMR materials or high- $T_c$  superconducting materials.

The device measured in this study is similar to the device shown in figure 4.1, however the current is extracted through the top of N1, and F1 is located in all the space below N1. Our device is basically identical to Johnson and Silsbee's, but is significantly smaller in dimension. The voltage measured was perpendicular to the injected current as shown. This was done in order to reduce large voltages due to longitudinal resistance. However, any cross voltage produced by the bottom ferromagnet and middle normal metal will also be present in the measurement. ferromagnets have several cross voltages which display

memory effects. Normal, anomalous, and planar hall effects all cause voltages which could be present in the measurement. Recent experiments have shown that there can be a sizeable in-plane hall voltage in F/N systems which Johnson did not consider in his system. Also, due to small lead misalignment a direct resistance voltage could also be present which displays magnetoresistive and anomalous magnetoresistive effects.

The normal hall effect is present in many materials. Charges in a current are diverted by a perpendicularly applied magnetic field yielding a voltage perpendicular to both the current and the field. The anomalous or extraordinary hall effect (AHE) is found in many ferromagnetic materials and arises due to the interaction of the current with the magnetization of the sample itself. However, these effects are found to require fields that would be much greater than those supplied by the internal magnetization. To date, there is no agreed upon full theoretical explanation, but the origins of the effect are believed to be due to skew-scattering and side-jump mechanisms [Kondo 1962, Giovannini 1971]. The hall resistivity can be modeled as

$$\rho_H(B, T) = R_0(T)B + \mu_0 R_S(T)M(B, T), \quad (4.7)$$

where  $M(B, T)$  is the magnetization,  $R_0(T)$  and  $R_S(T)$  are the normal and anomalous Hall coefficients respectively, and  $B$  is the applied magnetic induction [Smith 1929]. In ferromagnets,  $R_s$  in many cases is much greater than  $R_o$ . In LSMO, memory effects are displayed at low fields in these type of hall measurements [Chen 1999].

The Planar hall effect, sometimes referred to as the psuedo-hall effect (PHE), is a transverse voltage that arises when a anisotropic magnetoresistance (AMR) is present in ferromagnet [McGuire 1975]. AMR manifests itself as a change in resistance dependent on orientation of the magnetization relative to the measurement current. For a thin ferromagnetic film lying in the x-y plane, with a current,  $j$ , directed along the x-axis, the electric fields produced are given by,

$$E_x = j\rho_{\perp} + j(\rho_{\parallel} - \rho_{\perp})\cos^2\theta, \quad (4.8)$$

$$E_y = j(\rho_{\parallel} - \rho_{\perp})\sin\theta\cos\theta, \quad (4.9)$$

where the magnetization of the single domain sample is at angle  $\theta$  with respect to the x-axis, and  $\rho_{\parallel}$  and  $\rho_{\perp}$  are the resistivity when the current and magnetization are parallel and perpendicular respectively. It should be noted, that the magnetization and current are in-plane and most studies are done with fields applied in-plane.

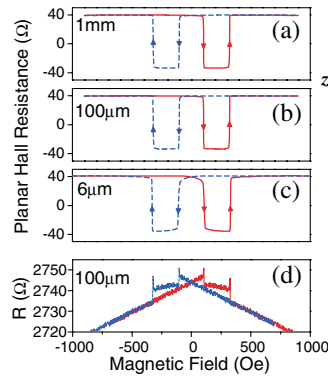


**Figure 4.3:** Giant planar hall effect in (Ga,Mn)As. The dimensions refer to the width of the measured bridge. The longitudinal resistance,  $R$ , is also shown for the 100  $\mu\text{m}$  bridge. [Tang 2003]

When scanned in a magnetic field, abrupt changes in domain orientation can cause the planar hall effect to exhibit switch-like memory effects. Recently Tang *et al.* found what they have coined as "giant" planar hall effects (GPHE) in the ferromagnetic semiconductor (Ga,Mn)As [Tang 2003]. See figure 4.3. (Ga,Mn)As has biaxial magnetocrystalline anisotropy. The magnetization reversal therefore occurs in two  $90^\circ$  steps. When the current path lies between these two crystalline orientations the  $90^\circ$  rotations cause switch-like effects similar to magnetic tunnel junctions. In the case of (Ga,Mn)As the switch is four orders of magnitude greater than that previously found in metallic ferromagnets, hence the connotation of giant.

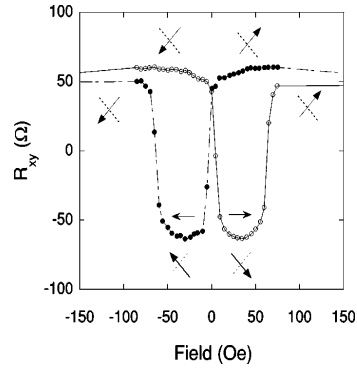


**Figure 4.4:** Giant planar hall effect in  $\text{La}_{0.84}\text{Sr}_{0.16}\text{MnO}_3$ . This data was taken at 120K with an angle of  $10^\circ$  between the current and the magnetic field. Arrows indicate scan direction and easy axis magnetization directions. [Bason 2004]

Giant planar hall effects have also recently been found in the CMR ferromagnet  $\text{La}_{0.84}\text{Sr}_{0.16}\text{MnO}_3$  which is very similar to the  $\text{La}_{0.66}\text{Sr}_{0.33}\text{MnO}_3$  used in this study [Bason 2004]. See figure 4.4.  $\text{La}_{0.84}\text{Sr}_{0.16}\text{MnO}_3$  has biaxial magnetocrystalline anisotropy just as the before mentioned  $(\text{Ga},\text{Mn})\text{As}$ . The difference  $(\rho_{\parallel} - \rho_{\perp})$  for switching events was on the order of  $10^3 \mu\Omega\text{-cm}$ .

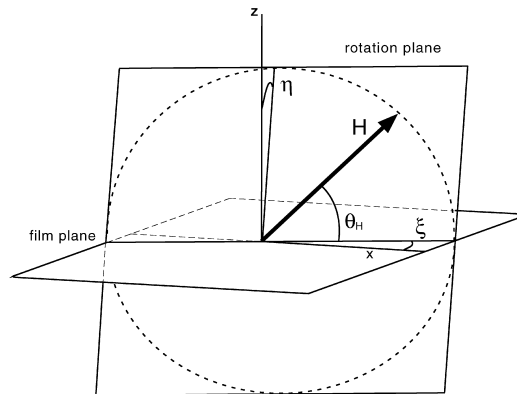


**Figure 4.5:** Diagram of the plane of rotation of the applied field,  $H$ , with respect to the film plane. The intersection of the rotation plane and the film plane makes an angle  $\xi$  with the direction of the applied current ( $x$ -axis). The rotation plane is tilted at an angle  $\eta$  to the perpendicular  $z$ -axis. [Ogrin 2000]

Ogrin *et al.* have measured the planar hall effect with out-of-plane applied magnetic fields to investigate the perpendicular anisotropy of thin ferromagnetic Co films [Ogrin 2000]. Ogrin points out that when a field is applied out-of-plane to a film there is always an uncertainty to its in-plane and perpendicular components relative to an axis defined by the current. See figure 4.5. Thus even at a perpendicular field orientation there is a small in-plane component.

Thin ferromagnetic films have large perpendicular demagnetization fields,  $H_d$ , which must be overcome in order to magnetize a film out-of-plane. (That is unless the perpendicular anisotropic field is large enough, in which case the film has an out-of-plane easy axis. LSMO/STO has a in-plane easy axis.) See equation 3.9 in section 3.2.2. For fields smaller than the demagnetization field, the magnetization will choose a in-plane orientation. As mentioned, the slightly misaligned perpendicular applied magnetic field will provide a in-plane component. Depending on in-plane anisotropies, the magnetization orientation may follow this in-plane component. This is an important consideration for LSMO thin films.

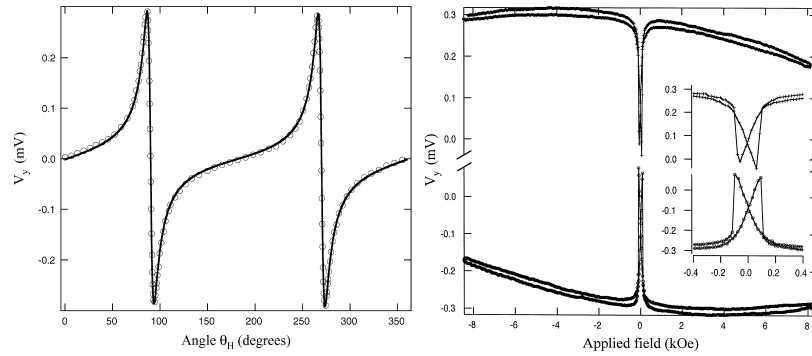


**Figure 4.6:** Voltage vs. angle and magnetic field for planar hall effects in a Co thin film. The magnetic field in the angular measurement was 460 Oe. The solid line is a energy model fit of the raw data (circles). The voltage vs. magnetic field graphs are for out-of-plane angular orientations of  $85^\circ$  (upper) and  $95^\circ$  (lower). [Ogrin 2000]

The Co films studied by Ogrin have an out of plane anisotropy, but the in-plane anisotropies are weak. A planar voltage measurement taken for a varying out-of-plane angle at a constant applied field that is lower than the demagnetization field is displayed in figure 4.6. Ogrin has fit these curves well with a magnetic energy model. The in-plane magnetization is found to rotate with the in-plane field component providing the planar hall signal. Field scans at constant  $85^\circ$  and  $95^\circ$  orientations are shown in 4.6. The voltage jumps indicate a  $180^\circ$  magnetization reversal. Note these measurements show a simple symmetry

defined by the in-plane component of the applied field. LSMO has in-plane anisotropies defined by its crystal axis. At low fields, rotation and reversal of the magnetization will be effected by these anisotropies.

Interesting switching behavior has also been seen in  $(\text{Ga,Mn})\text{As}/\text{Al}_2\text{O}_3/\text{Au}$  (F/I/N) junctions by Gould *et al.* [Gould 2004]. The junction is not a F-I-F junction and therefore any switching is a manifestation of magnetization reversal within the ferromagnetic layer itself. By applying in-plane magnetic fields the junction resistance shows a hysteresis that switches between high and low resistance states. (See figure 4.7.) This is proposed to be due to the anisotropies in the  $(\text{Ga,Mn})\text{As}$  density of states brought about by the orientation of the magnetization relative to the crystal anisotropies. The positive-negative state switching is very symmetric as shown in figure 4.7.

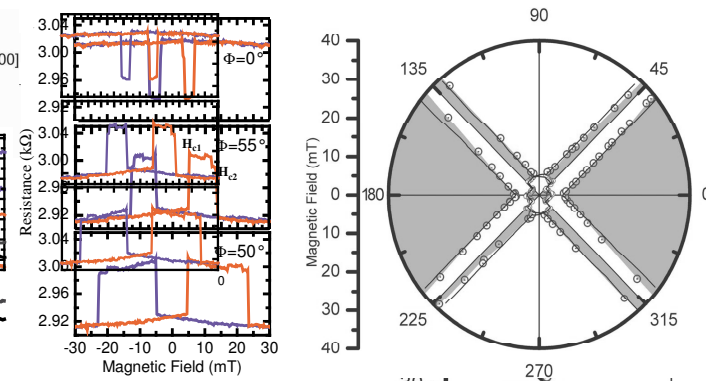


**Figure 4.7:** Resistance vs. Field for a  $(\text{Ga,Mn})\text{As}/\text{Al}_2\text{O}_3/\text{Au}$  (FIN) junction. The angle  $\phi$  is relative to the in-plane crystal axis (100). The polar graph indicates the high (grey) and low resistance states. [Gould 2004]

These planar hall effect and F/I/N junction results show that many anomalous effects are seen in ferromagnetic materials, and heterostructures which include ferromagnetic materials. These effects can be complex to interpret and may be included in any voltage we measure with our spin diffusion measurement.

## 4.2 Device and Measurement

### 4.2.1 Device Geometry and Fabrication

LSMO/YBCO/LSMO Spin diffusion detection were created and tested in this study. The heterostructures were grown *in situ* by PLD on STO substrates using the parameters presented in chapter 2. In this study two different YBCO thicknesses were investigated, 500Å and 1000Å. The top and bottom LSMO layers were 400Å and 500Å respectively. After deposition, the samples were quickly removed from the PLD chamber and placed in an evaporator to deposit a 350Å thick top gold layer. Time between the *ex situ* move from the PLD vacuum chamber to the evaporation vacuum chamber was kept at a minimum (<5 minutes). It has been found that small *ex situ* times have a negligible effect on the contact resistance between gold and LSMO compared to those made *in situ* [Chen 2001].

The explanation of the process which follows is depicted in figure 4.8. First, the base structure was formed by patterning the sample with photolithography and ion milling through the entire heterostructure using a 300 volt Ar ion beam. The top ferromagnetic pad photoresist pattern was applied, and the top LSMO layer was initially milled with the 300V beam to within 150Å of the YBCO layer. The final 150Å of the LSMO and 50Å of the YBCO was milled away using a 100V ion beam to minimize surface damage of the YBCO. A 300Å layer of gold was then DC sputtered *in situ* onto the exposed YBCO layer. All photoresist was removed from the device and another 1500Å of gold was deposited over the entire structure. Then the sample was annealed at 450° for 1 hour in 600Torr of oxygen.

The low voltage ion milling, *in situ* gold sputtering, extra 1500Å of gold, and annealing in oxygen was crucial for the formation of a low resistance gold/YBCO contact. See section 2.8.2 for more details.

The top gold layer was then patterned into separate gold contacts via a wet etching process with a dilute mixture of TFA gold etch to water of 2:1 by volume. The dilute TFA mixture etched approximately 5000Å of gold in 30 seconds, and had no effect on either YBCO or LSMO layers. The YBCO layer was then patterned into the measured area with a wet etch process using a dilute mixture of nitric acid to water of 1:400 by volume. Typically to etch 500 ~ 1000Å of YBCO took 10 ~ 15 seconds. The nitric mix has little to no effect on the LSMO. Silicon dioxide, SiO<sub>2</sub>, was then RF sputtered to allow gold contacts to reach central regions of the device without shorting to lower layers. The SiO<sub>2</sub> was usually 3000-4000Å thick or at least thick enough to overtake any step by 1000Å. A very thin Cr layer ( $\approx 30\text{\AA}$ ) was deposited on top of the SiO<sub>2</sub> to promote adhesion of the to-be-deposited gold leads. Finally, a 6000-5000 Å gold layer was DC sputtered and patterned with a the TFA wet etch process already mentioned to make the final gold contacts. The Cr was also wet etched away with a purchased Cr etchant in order to prevent shorting of the gold leads. Cr etchant will damage YBCO, however, at this point in the process all the YBCO is protected by SiO<sub>2</sub> and Au.

All PLD, ion milling, and sputtering were done with conditions provided in chapter 2. Dimensions of the device are given in figure 4.8. The main measurement was made by applying the injection current between the large LSMO pad to the large YBCO pad, and measuring the voltage between the top two Au and LSMO pads. Voltage current measurements were done in the same way as those mentioned in section 2.10 and section 3.2.1. The samples was measured in the same cryostat/magnet system as described in section 3.2.1.

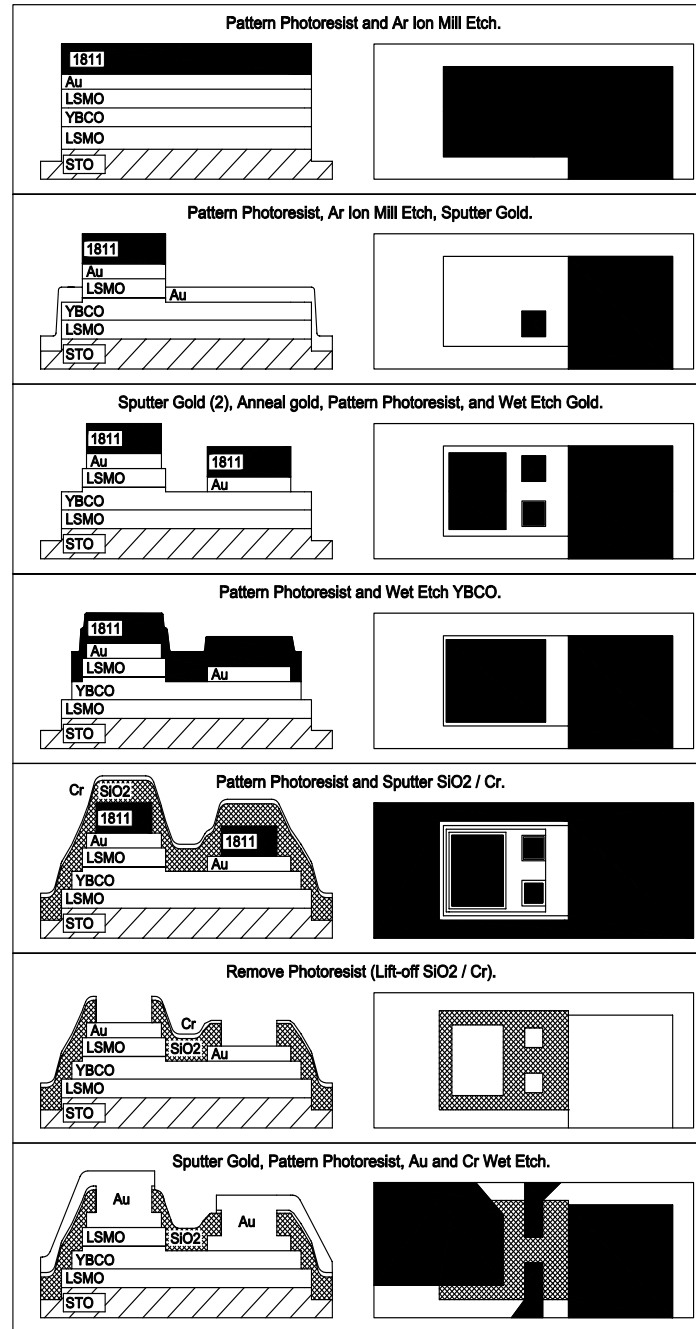


**Figure 4.8:** A schematic of the diffusion measurement device fabrication process. All PLD, ion milling, and sputtering were done with conditions provided in chapter 2. The width of the bottom LSMO layer was  $200\mu\text{m}$ . The area of the middle YBCO region was  $160 \times 100\mu\text{m}$ . The area of the top Au and LSMO voltage pads was  $35 \times 35\mu\text{m}$ . The area of the top Au current pad was  $90 \times 90\mu\text{m}$ . The voltage leads were flush against the edge of the YBCO region,  $20\mu\text{m}$  from the Au current pad, and had a  $12\mu\text{m}$  gap between them.

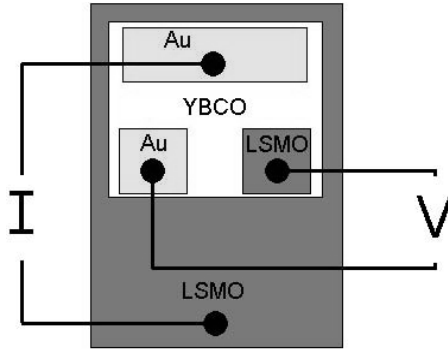


**Figure 4.9:** A schematic of the diffusion measurement device used in this study. Current was applied between the bottom LSMO (F1) layer and the large top Au pad incontact with the middle YBCO (N1) layer. A top LSMO (F2) pad was used to detect any spin overpopulation present in the YBCO. The small top Au pad (N2) attached to the YBCO is used as a ground relative to F2. N2 and F2 are arranged perpendicular to the current path to minimize any longitudinal signal. The measured voltage is referred to as the detection voltage. A resistance is calculated by dividing the detection voltage by the injected current. The device fabrication process is shown in figure 4.8.

#### 4.2.2 Data and Discussion

The LSMO/YBCO/LSMO spin diffusion detection devices were measured in this study. The device is depicted in figures 4.1, 4.8, and 4.9. Current was injected from the bottom LSMO to the top YBCO. The top LSMO was patterned into a pad and used to detect any spin population in the YBCO. A top gold pad was used as a ground relative to LSMO pad, and the voltage was measured between them referred to in this study as the detection voltage. This configuration is almost identical to that used by Johnson and Silsbee in their bipolar spin transistor [Johnson 1988a, 1988b, 1988c]. A resistance is presented in the data which is the measured detection voltage divided by the injected current.

The devices were measured in several different field-current orientations. Measurements were taken for the magnetic field applied in-plane as well as out-of-plane. In the out-of-plane case the field and current form a plane that is perpendicular to the surface of the sample. Data was taken for a constant applied field and a changing angle as well as for a constant angle and scanned field. The results for a LSMO/YBCO/LSMO (400Å/500Å/500Å respectively) device at 100K are shown in figures 4.11 - 4.16.

The resistance, detection voltage/injected current, for fields applied at various in-plane angles is shown in figure 4.10 and 4.14. A hysteresis signal was seen with a change in resistance  $\approx 1 \text{ m}\Omega$ . This change in resistance is the spin resistance,  $R_s$ , given in equation 4.6. Sharp switching was seen between high and low resistance states. The signal was seen to sharpen and invert in passing through  $90^\circ$  (where the current is perpendicular to the field). There is a background resistance signal  $\approx 0.2 \Omega$  in the measurement which may be due to a longitudinal resistance created by a slight misalignment of the top Au-LSMO pads.

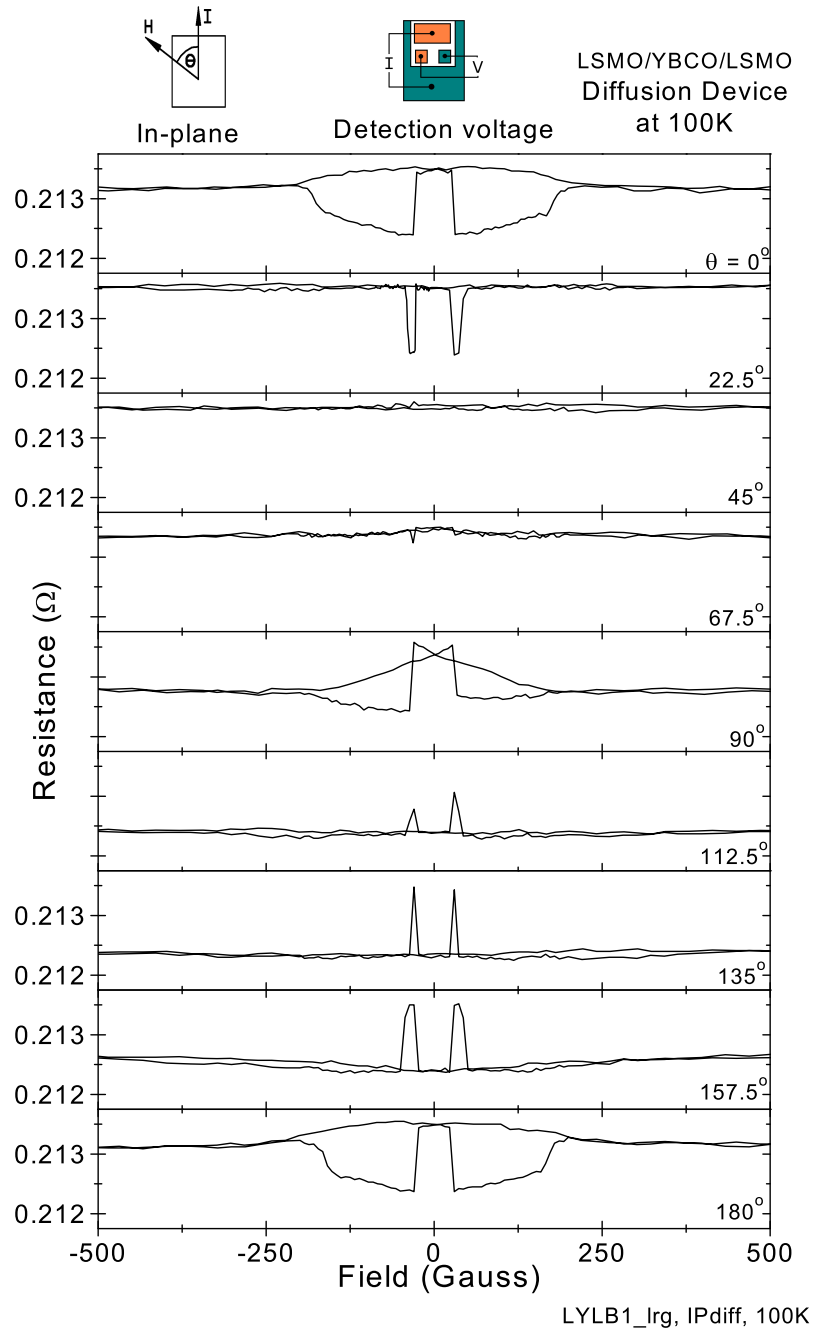


**Figure 4.10:** Resistance vs. applied magnetic field for a LSMO/YBCO/LSMO spin diffusion device. Data is shown for fields applied at various in-plane angles. The resistance is equal to measured detection voltage divided by the injected current. The thickness of the LSMO/YBCO/LSMO layers was 400Å/500Å/500Å respectively. The magnetic field direction,  $\theta$ , is relative to the current path indicated in the device. The temperature was 100K. The injection current was  $1 \times 10^{-2}$  Amps.

The resistance, detection voltage/injected current, for fields applied at various out-of-plane angles is shown in figures 4.11 - 4.13 and 4.14. A hysteresis signal is seen yielding a spin resistance,  $R_s \approx 1 \text{ m}\Omega$ . An inversion of the hysteresis signal was seen in the diffusion device at  $180^\circ$ , while no inversion is shown at  $0^\circ$ . These results yielded an unusual symmetry not seen in the magnetic device measurements mentioned in the previous section 4.1. All measurements were taken in the same run and the sample was never removed between measurements. The signal inversion seems to take place between two resistance states. See figure 4.13. This switching shows an odd similarity to the F/I/N junctions results presented by Gould *et al.* in the section 4.1 [Gould 2004].

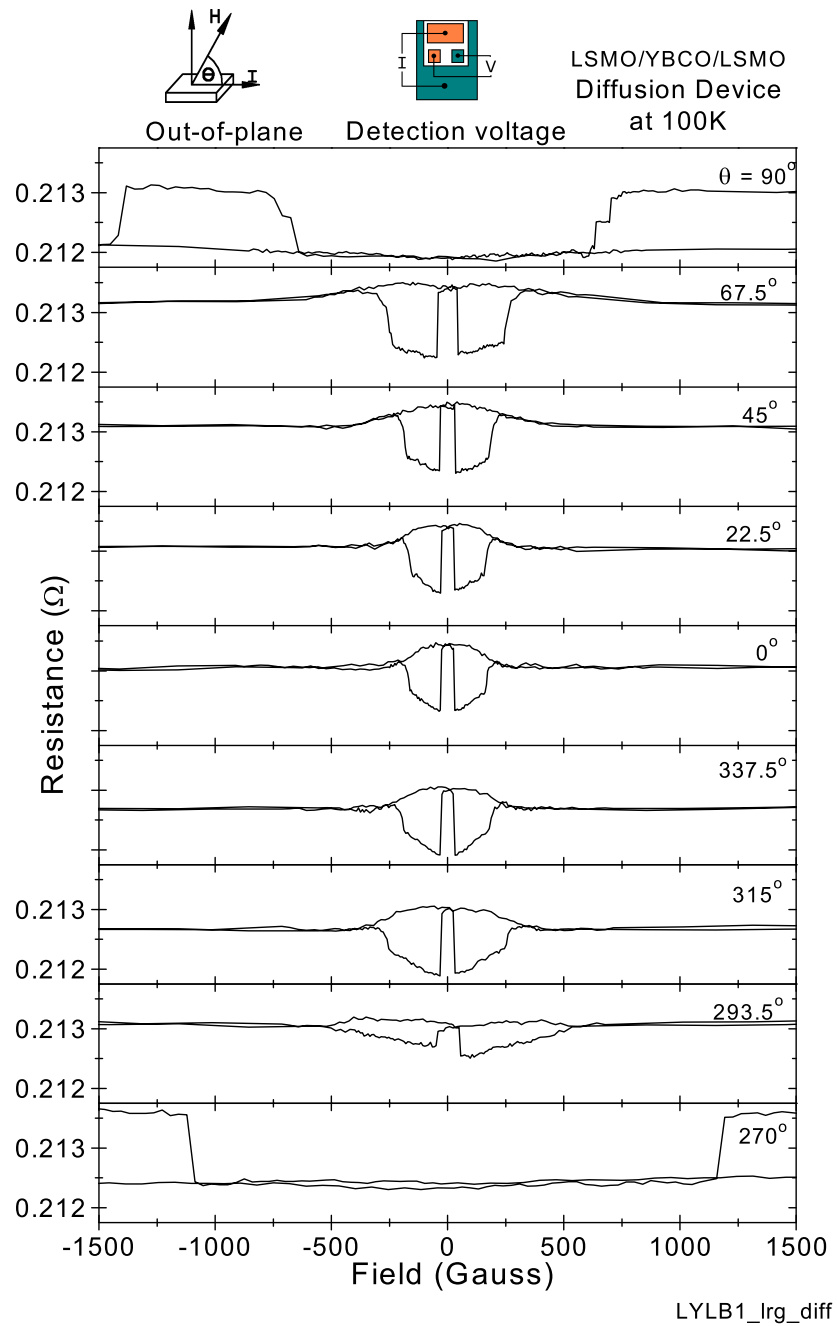


**Figure 4.11:** Resistance vs. magnetic field for a LSMO/YBCO/LSMO spin diffusion device. The displayed data is for fields applied at various out-of-plane angles. The resistance is equal to measured detection voltage divided by the injected current. The magnetic field direction,  $\theta$ , is relative to the plane of the heterostructure and is parallel to the injection current at  $0^\circ$ . The temperature was 100K. The injection current was  $1 \times 10^{-2}$  Amps. This is the same sample as that shown in figure 4.10.

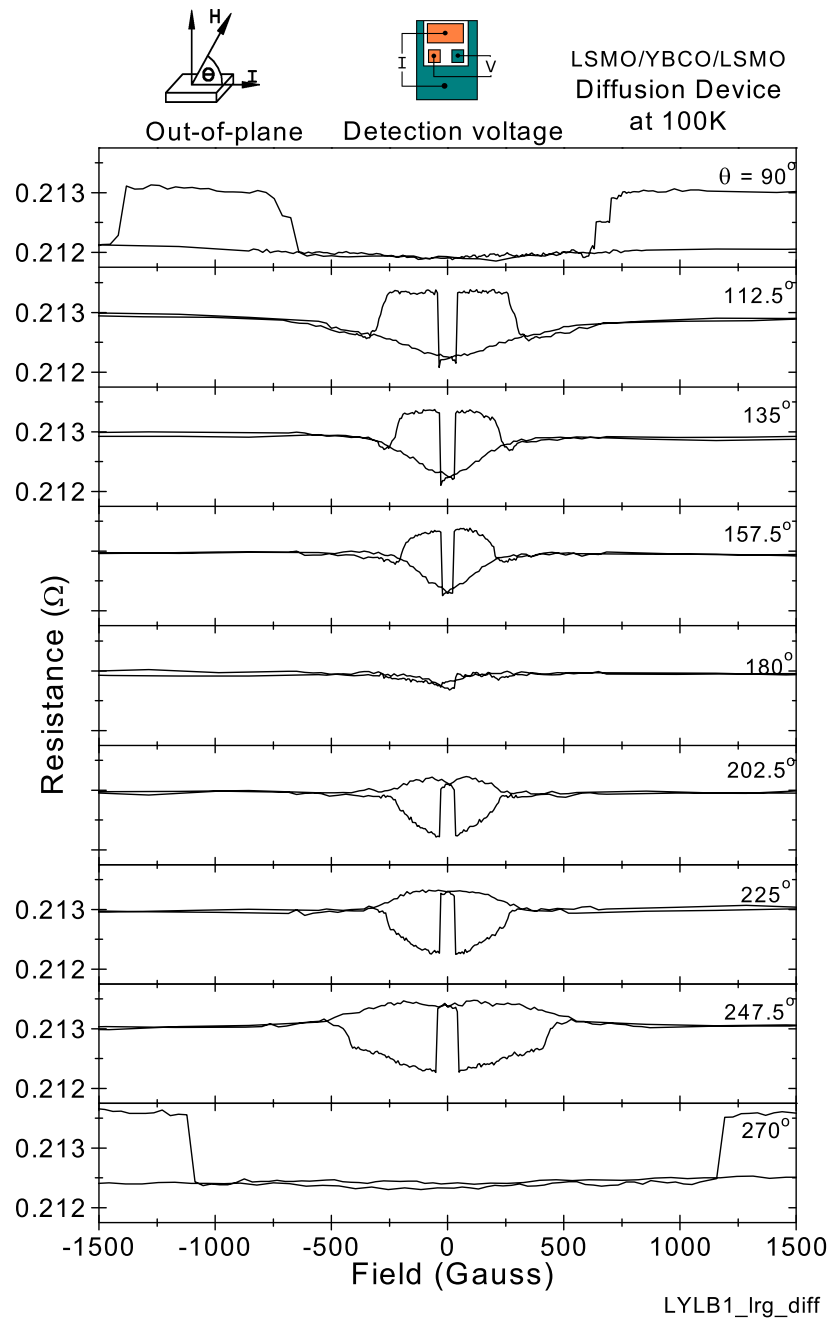


**Figure 4.12:** Resistance vs. magnetic field for a LSMO/YBCO/LSMO spin diffusion device. The displayed data is for fields applied at various out-of-plane angles. The resistance is equal to measured detection voltage divided by the injected current. The magnetic field direction,  $\theta$ , is relative to the plane of the heterostructure and is parallel to the injection current at  $0^\circ$ . The temperature was 100K. The injection current was  $1 \times 10^{-2}$  Amps. This is the same sample as that shown in figure 4.10.

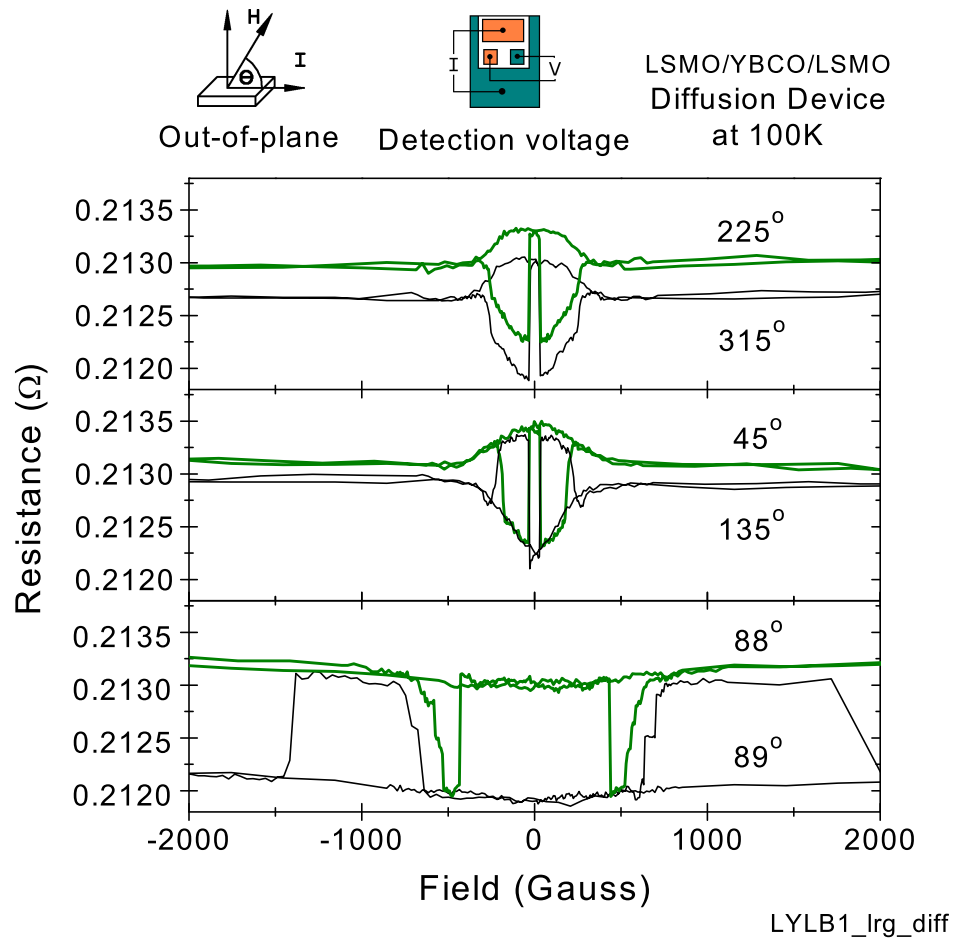


**Figure 4.13:** Resistance vs. magnetic field for a LSMO/YBCO/LSMO spin diffusion device. Data is shown for fields applied at various out-of-plane angles. The resistance is equal to measured detection voltage divided by the injected current. The magnetic field direction,  $\theta$ , is relative to the plane of the heterostructure and is parallel to the injection current at  $0^\circ$ . The temperature was 100K. The injection current was  $1 \times 10^{-2}$  Amps. Note, the high-low switching behavior near  $90^\circ$ , and between  $45^\circ$  and  $135^\circ$ . There is no switching behavior between  $225^\circ$  and  $315^\circ$ . This is the same sample as that shown in figure 4.10.

The detection voltage was also measured for the rotation of the sample in a constant field. See figure 4.14. Results are shown both in-plane and out-of-plane rotation. Very sharp switching is seen at low fields with little to no hysteresis due to the direction of the angle scan.

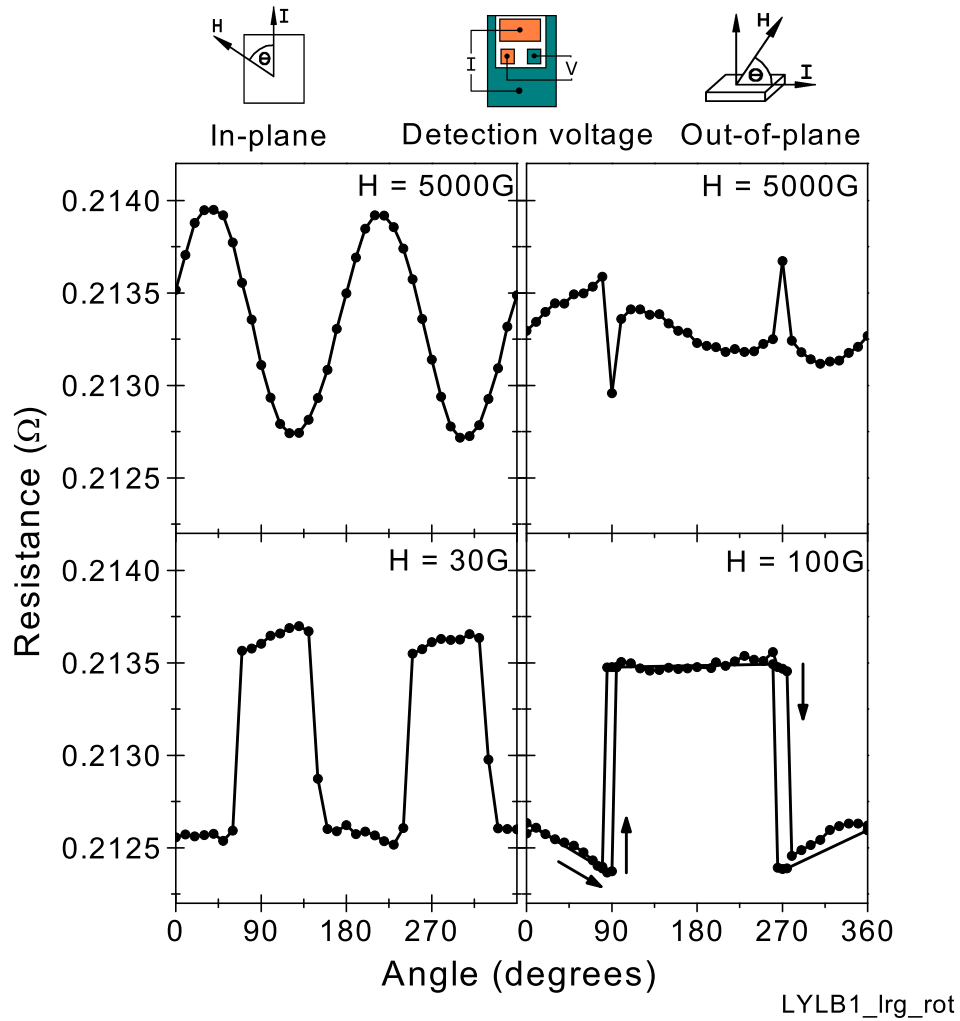


**Figure 4.14:** Cross resistance vs. angle for a LSMO/YBCO/LSMO spin diffusion device in a constant applied magnetic field. The magnetic field direction,  $\theta$ , is relative to the plane of the heterostructure and is parallel to the injection current at  $0^\circ$ . The resistance is equal to measured detection voltage divided by the injected current. The temperature was 100K. The injection current was  $1 \times 10^{-2}$  Amps. This is the same sample as that in figure 4.10. The arrows in the out-of-plane 100 Gauss scan indicate the scan direction.

The detection voltage in the diffusion device is found to disappear around 25-50K. This is assumed to be due to the full onset of superconductivity in the YBCO layer. Two point resistance measurements between the current leads of the sample showed clear dips in resistance in this temperature range. Given that no signal is seen for these low temperatures a few statements can be made about the diffusion of spin in the superconducting state of YBCO. Perhaps the spin diffusion length is greatly reduced in the superconducting state of YBCO. Also, the spin diffusion signal may be smaller than the thickness of the YBCO in our devices.

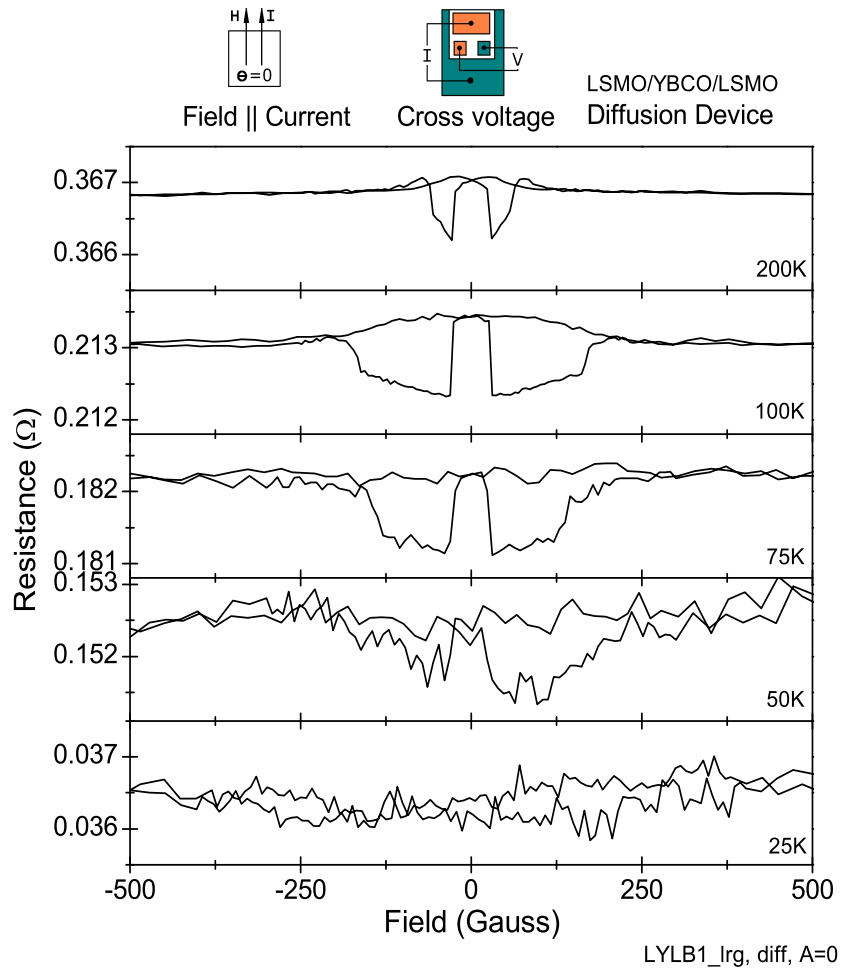


**Figure 4.15:** Resistance vs. magnetic field for a LSMO/YBCO/LSMO spin diffusion device. Data is shown for parallel current and field at various temperatures. The resistance is equal to measured detection voltage divided by the injected current. The injection current was  $1 \times 10^{-2}$  Amps. This is the same sample as that shown in figure 4.10. Note the reduction in the background signal with decreasing temperature.

Measurements were taken using the two top gold leads of the diffusion device to measure voltage and the bottom and top LSMO leads for current. Here one would expect no spin signal since the leads are simply both normal metals. However the current path in this configuration is complex. Hall and resistance signals may be mixed, and the relation of the current direction to the field orientation is hard to determine. In any case, some hysteresis is still seen in this configuration. It maybe that the anomalous hall and magnetoresistance effects given by the bottom LSMO layer are present and are at least as large as the signals given from the standard spin diffusion measurement. However, switching between the top an bottom LSMO layers may change current distributions in the heterostructure and create a change in the voltage signal measured my the to Au leads.

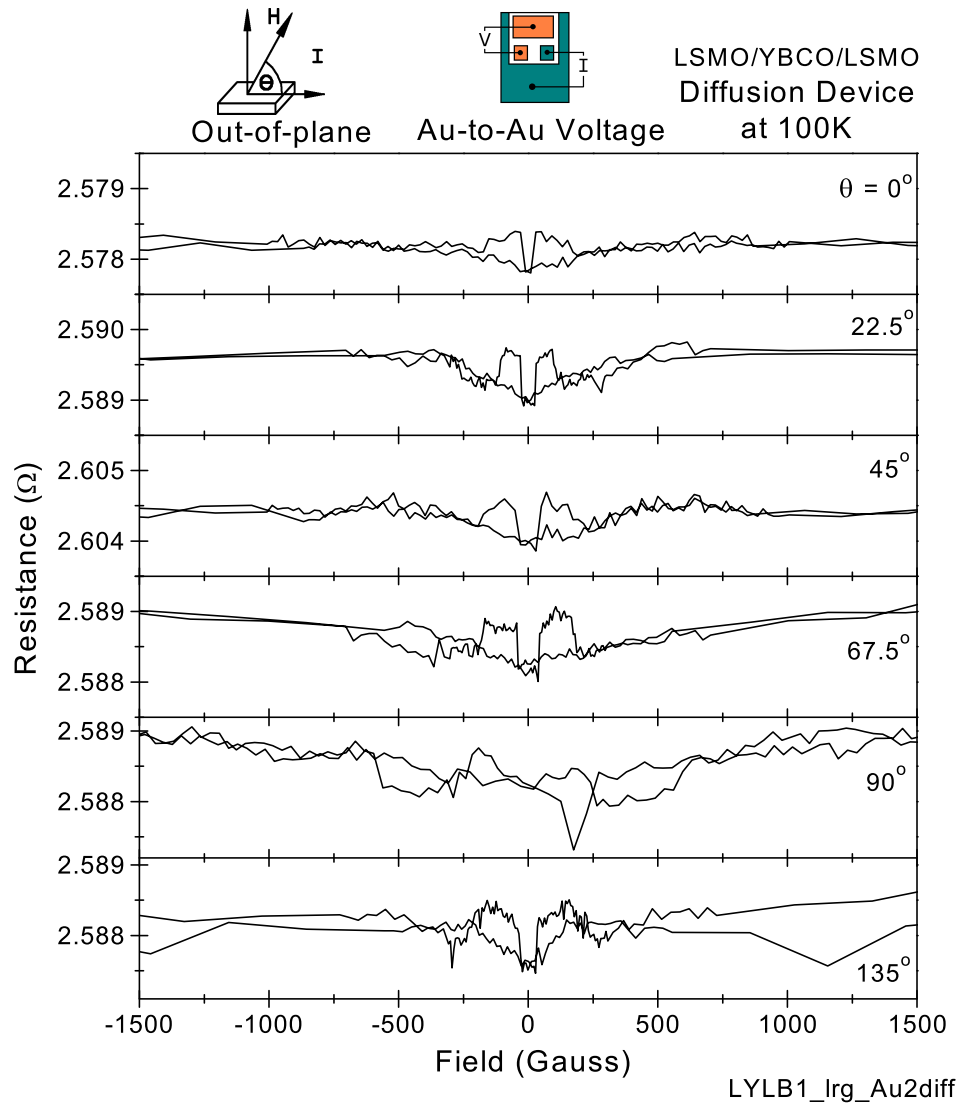


**Figure 4.16:** Gold-to-gold resistance vs. magnetic field for a LSMO/YBCO/LSMO spin diffusion device. Data is shown for a voltage measurement between the two Au/YBCO pads with current applied from the bottom to the top LSMO pads. Fields were applied at various out-of-plane angles. The resistance is equal to measured voltage divided by the injected current. The magnetic field direction,  $\theta$ , is relative to the plane of the heterostructure and is parallel to the injection current at  $0^\circ$ . The temperature was 100K. The injection current was  $1 \times 10^{-2}$  Amps. This is the same sample as that shown in figure 4.11.

A sample with a 1000Å YBCO barrier, which is similar to the previously mention device in all other respects, was also measured. The device showed similar results although the transitions between the high and low resistance states no as well defined. Also, the positive/negative hysteresis flipping was not seen in the same orientaions as the 500Å sample.

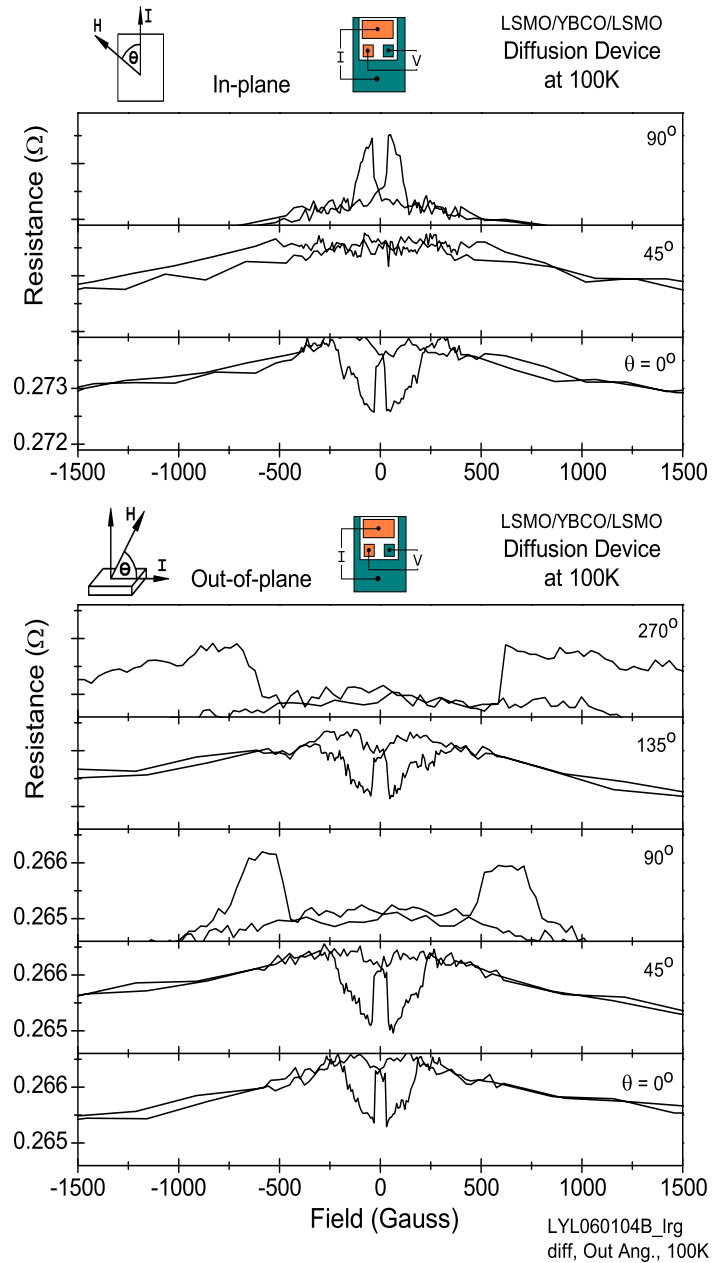


**Figure 4.17:** Resistance vs. magnetic field for a LSMO/YBCO/LSMO spin diffusion device. The thickness of the LSMO/YBCO/LSMO layers are 400Å/1000Å/500Å respectively. Data is shown for fields applied at various out-of-plane angles. The resistance is equal to measured detection voltage divided by the injected current. The magnetic field direction,  $\theta$ , is relative to the plane of the heterostructure and is parallel to the injection current at  $0^\circ$ . The temperature was 100K. The injection current was  $1 \times 10^{-2}$  Amps.

The cross voltage as well as the resistance of a test LSMO sample was also measured. The LSMO was 400 Å thick and was patterned into a 10 μm wide bridge. This sample was measured in all the conditions mentioned previously for the L/Y/L samples. The results for measurements made at 100K are displayed in figures 4.19 - 4.21. This measurement was taken to provide insight into any signals which maybe mixed with the spin voltage measured in the spin diffusion devices.

The in-plane results for the diffusion device and the cross voltage of the test LSMO sample, figure 4.19, were found to be very similar. For field scans taken at constant angles it was likely that the memory effects of the diffusion device were a product of the planar hall effect from the LSMO layer. The constant field measurements yielded a very similar signal to those reported for LSMO by Bason *et al.* (see section 4.1). However, LSMO films deposited on STO substrates have an in-plane easy axis. In the diffusion devices, the in-plane coercive fields of the top and bottom LSMO may be very small and close and the rotation of the domains may occur within a very small field range making any spin diffusion signal difficult to see.

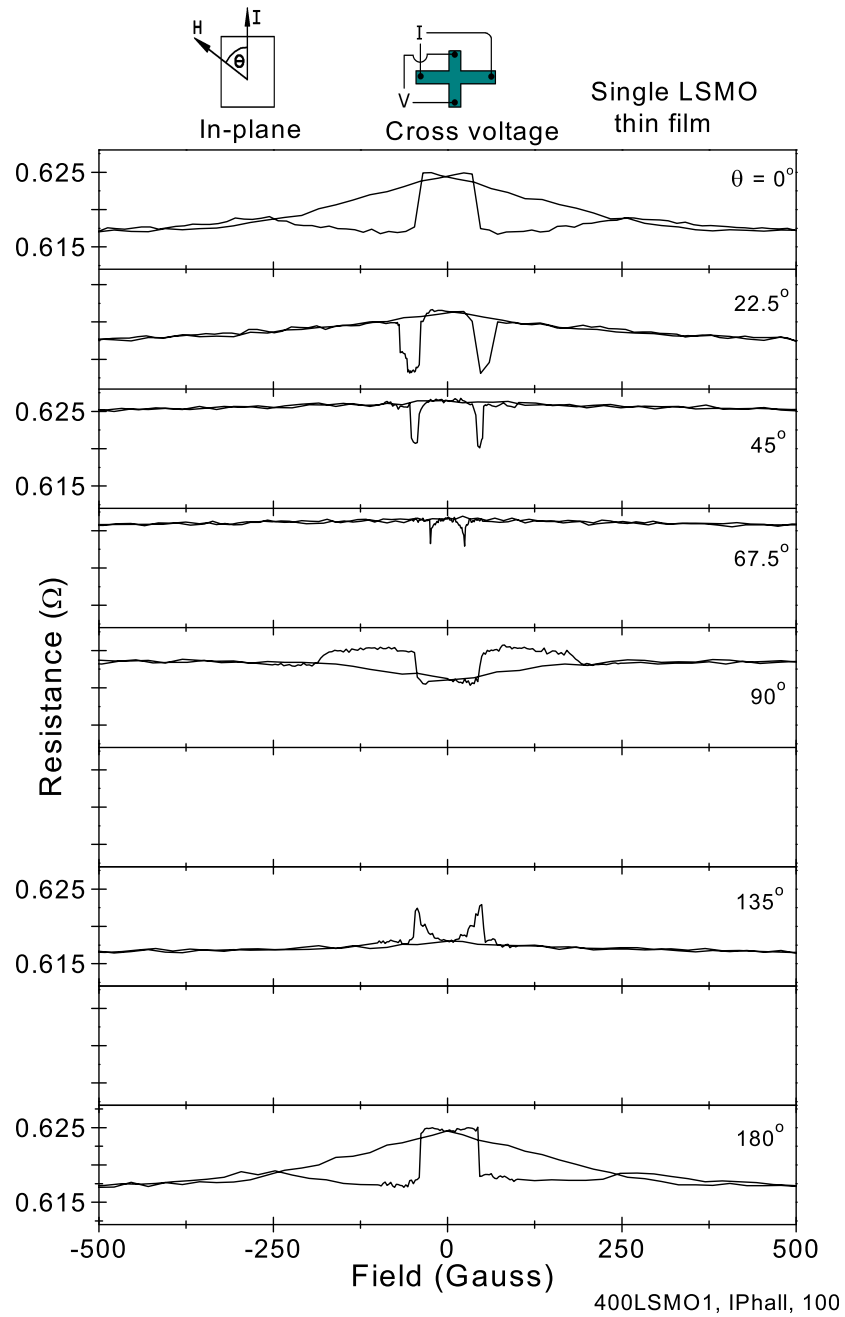


**Figure 4.18:** Cross resistance vs. applied magnetic field for a patterned single layer LSMO thin film. Data is shown for fields applied at various in-plane angles. The film was patterned into a  $10\mu\text{m}$  wide bridge. The magnetic field direction,  $\theta$ , is relative to the current path indicated in the device. The temperature was 100K. The measurement current was  $1 \times 10^{-3}$  Amps.

The out-of-plane measurements made on the diffusion devices displayed noticeable differences from the LSMO test samples. An inversion of the hysteresis signal was seen in the diffusion device at  $180^\circ$ , while no inversion is shown at  $0^\circ$ . For the LSMO test sample this inversion is not seen. Also the magnitude of the change in resistance does not change with angle as in the diffusion device.

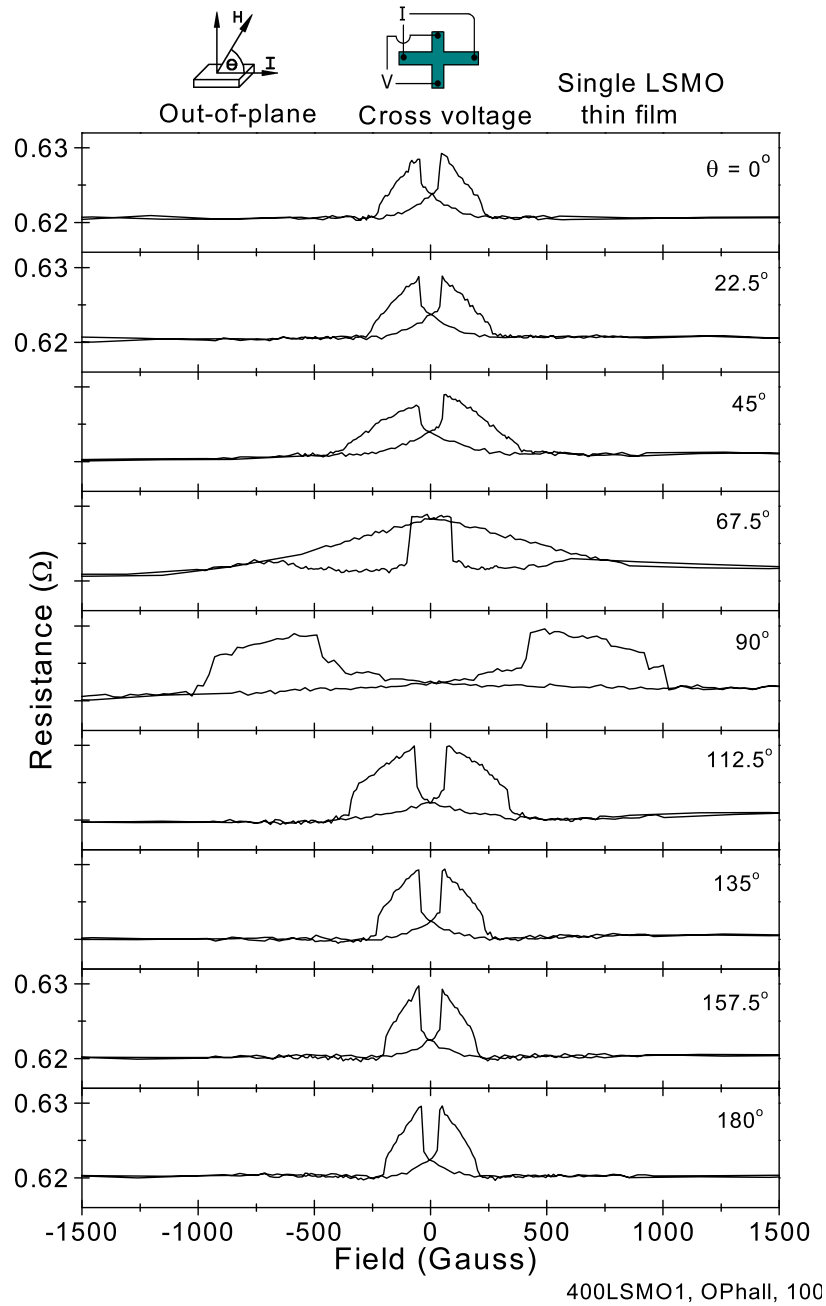


**Figure 4.19:** Cross resistance vs. magnetic field for a patterned single layer LSMO thin film. Data is shown for fields applied at various out-of-plane angles. The film was patterned into a  $10\mu\text{m}$  wide bridge. The magnetic field direction,  $\theta$ , is relative to the plane of the heterostructure and is parallel to the measurement current at  $0^\circ$ . The temperature was 100K. The measurement current was  $1 \times 10^{-3}$  Amps.

The longitudinal resistance measurements for in-plane and out of plane applied fields do not resemble the diffusion device results. Also the hysteresis effects are very small and are a much smaller percentage of the over all signal than the signal to background measurement in the diffusion devices.

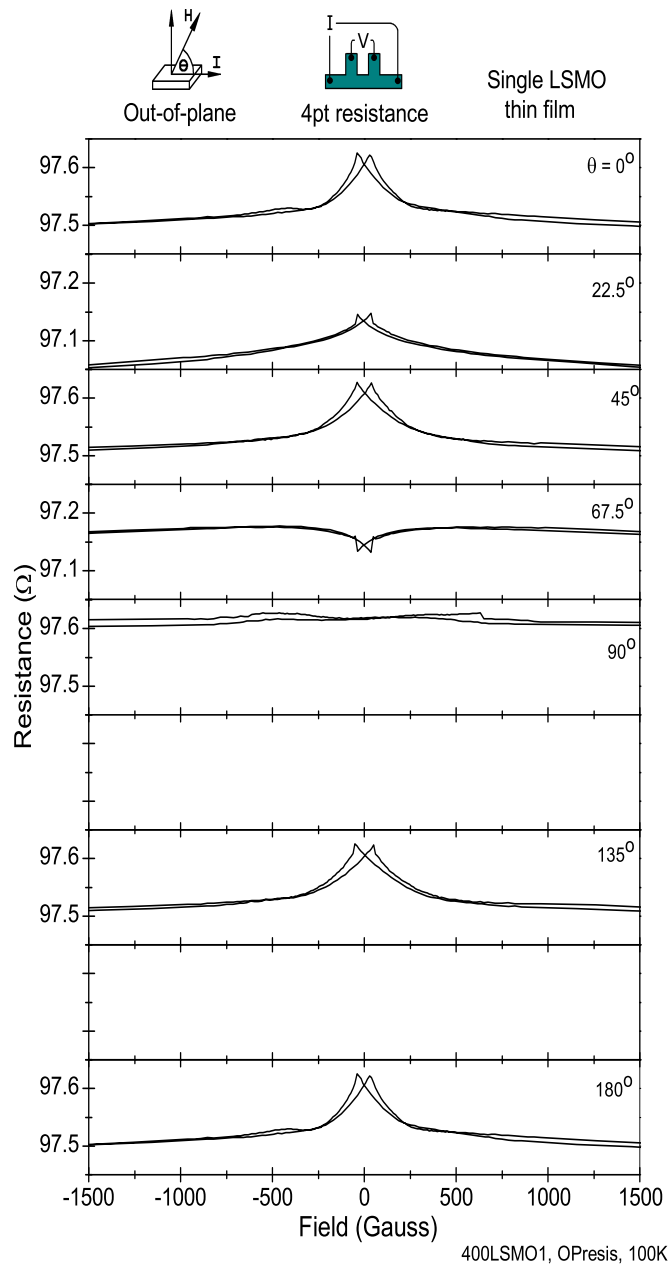


**Figure 4.20:** Resistance vs. magnetic field for a patterned single layer LSMO thin film. Data is shown for fields applied at various out-of-plane angles. The film was patterned into a  $10\mu\text{m}$  wide bridge. The magnetic field direction,  $\theta$ , is relative to the plane of the heterostructure and is parallel to the measurement current at  $0^\circ$ . The temperature was 100K. The measurement current was  $1 \times 10^{-3}$  Amps.

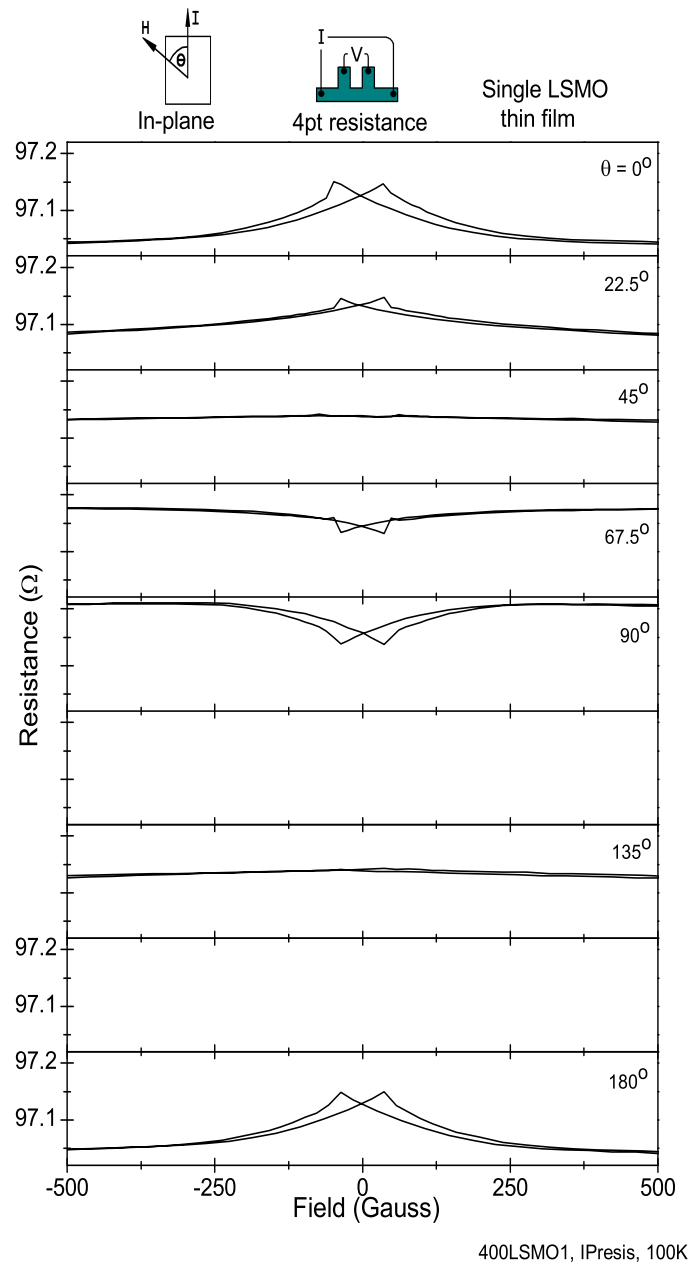


**Figure 4.21:** Resistance vs. magnetic field for a patterned single layer LSMO thin film. Data is shown for fields applied at various in-plane angles. The film was patterned into a  $10\mu\text{m}$  wide bridge. The magnetic field direction,  $\theta$ , is relative to the current path indicated in the device. The temperature was 100K. The measurement current was  $1 \times 10^{-3}$  Amps.

It is difficult to say whether the displayed results for the LSMO/YBCO/LSMO device are caused by spin diffusion effects or not. It appears there are obvious anomalous hall effect signals mixed into the result. In such a complex structure as this, it is extremely difficult to separate the two. Also, while the 1000Å and 500Å YBCO devices, display different hysteresis curves, their magnitudes are not incredibly different. Therefore obtaining spin diffusion lengths from a distance dependence fitting does not seem possible.

If we take a slightly naive approach and assume that the signal measured in the 500Å devices is totally due to spin diffusion, we may make a rough estimation of the diffusion length using equation 4.6. At the very least, we can estimate an upper bound for the spin diffusion distance in YBCO.

A spin resistance  $R_s$  of 1.5 mΩ is given at 100K (see figures 4.12 and 4.12). A conservative estimate of the polarization of the injection current at 100K can be obtained from the LSMO/STO/LSMO junction data in chapter 3 and is roughly  $\eta_1 = \eta_2 = .6$  (see figure 3.9). The thickness of the YBCO,  $d$ , was 500Å and the width of YBCO layer,  $w$ , was 100 μm. The area of the injection region,  $A$ , is equal to the width ( $w$ ) times the transfer length ( $l$ ). When current runs between two parallel layers, the current will transfer from the higher to the lower resistive material over a characteristic distance know as the transfer length. For low contact resistances, most current will transfer from one layer to the other within a short distance. We will consider the total length of the YBCO layer was 160 μm ( $l_1$ ) and a shorter more realistic tranfer length of 1 μm ( $l_2$ ). (See section 5.2.5 in chapter 5 for a complete discussion of transfer length.) The resistivity of YBCO at 100K is approximately  $2 \times 10^{-4} \Omega - cm$  as given in chapter 2.

For  $l_1 = 160 \mu m$  the spin diffusion length  $\delta_s \approx 1 \mu m$ . For  $l_2 = 1 \mu m$  the spin diffusion length  $\delta_s \approx 0.1 \mu m$ . For polarizations of 100%, the spin diffusion length is 0.7 μm for  $l_1$  and .07 μm for  $l_2$ . In either case the distance is rather long. In a theoretical paper, Qimiao Si estimated the spin diffusion length in YBCO to be on the order of 0.1 μm [Si 1996] in

the normal state. It appears this estimated distance falls within the upper bound created by our study. It may be within the reach of e-beam lithography techniques to create a measurable in-plane spin diffusion device. In any case the attempt to create such a device cannot be discouraged by our data.

## Critical Current Suppression Injection Devices

---

### 5.1 Introduction

#### 5.1.1 Controllable Weak Links and Quasi-particle injection devices

The first experimental three terminal superconducting device with a significant gain was created by Wong *et al.* [Wong 1976-77]. The design and premise of the device was simple. A bottom tin, Sn, bridge  $10\mu\text{m}$  in width and  $600$  to  $1000\text{\AA}$  thick intersected a  $5\mu\text{m}$  wide top bridge of lead, Pb (see figure 5.1). The temperature was lowered until the Sn bridge became superconducting (at which point the Pb bridge was also superconducting). Current was then transported, or injected ( $I_{inj}$ ), from the Pb to the Sn and the critical current of the Sn bridge was measured. This device was referred to as a controllable weak link or "CLINK". Quasiparticles arriving from the Pb created a non-equilibrium state in Sn. In this way the critical current of the Sn could be controlled by the injected current from the Pb. A gain,

$$G = \frac{-\Delta I_c}{\Delta I_{inj}}, \quad (5.1)$$

of about 20 at a temperature of 2K was created in these devices.

The results were found to be modeled well by Parker's  $T^*$  model [Parker 1975]. The model assumes that the imposed non-equilibrium creates an elevated temperature,  $T^*$ , for the phonons above the energy gap  $2\Delta$ , of the superconductor. The phonons below the gap

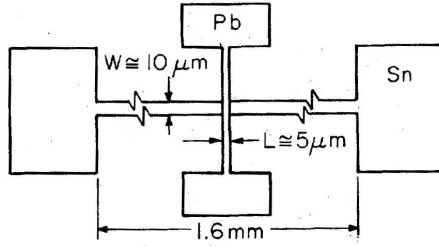


**Figure 5.1:** Schematic of 3 terminal controllable weak link (CLINK). [Wong 1997]

remain at the bath temperature  $T$ . This model is different from a simple heating model in which all the phonons are at the same elevated temperature. The properties of the non-equilibrium superconductor quasiparticle distribution are then provided by the same BCS equations with the adjusted temperature  $T^*$  in place of the bath temperature  $T$ . Parker's model assumes that phonons within the superconductor are more likely to be reabsorbed by the superconductor with the creation of a quasiparticle pair than they are to escape the superconductor. It also assumes the time required for quasiparticles to thermalize with the low energy phonons ( $< 2\Delta$ ) is large compared to their recombination time.

With an increased temperature  $T^*$ , the number of quasiparticles in the superconductor quasiparticle distribution would increase. Due to charge neutrality, the number of cooper pairs would decrease, thereby decreasing the critical current. Parker's model gives the superconductor gap dependence on the quasiparticle density,

$$\frac{\Delta(n_{qp})}{\Delta(0)} \simeq 1 - \frac{2n_{qp}}{4N(0)\Delta(0)}, \quad (5.2)$$

where  $n_{qp}$  is the quasiparticle density,  $N(0)$  is the single-spin density of states in the superconductor,  $\Delta(n_{qp})$  is the perturbed energy gap, and  $\Delta(0)$  is the equilibrium gap at  $T = 0$ . The critical current is proportional to the superconducting gap,  $J_C \propto \Delta$ . This shows the gap decreases as the quasiparticle density increases, thereby decreasing the critical current.

Another popular non-equilibrium model is provided by Owen and Scalapino [Owen 1972].

In this model rather than a increased temperature, a new chemical potential,  $\mu^*$ , is applied the BCS equations. This model assumes the opposite of Parker's in that, the time required for quasiparticles to thermalize with the low energy phonons ( $< 2\Delta$ ) is small compared to their recombination time. The quasiparticles then maintain the bath temperature  $T$  and a constraint on the number of quasiparticles gives rise to the additional chemical potential  $\mu^*$ . The modified quasiparticle distribution would give rise to a decrease in critical current, similar to that of Parker's model mentioned above.

The reduction of the order parameter decreases much faster than the prediction of Parker's model. A first order transition to the normal state is predicted for

$$n_{qp} > 0.6N(0)\Delta(0) \quad (5.3)$$

In either case, Parker or Scalapino, a decrease in the order parameter is created by the quasiparticle injection, and in turn a reduction of the critical current.

When current is injected into a superconductor a non-equilibrium population of quasiparticles,  $\delta_{qp}$ , is created over a finite region [Gim 2001].

$$\delta_{qp} = \frac{J_{inj}\tau_{eff}}{ed}, \quad (5.4)$$

where  $J_{inj}$  is the injected current density,  $\tau_{eff}$  is the effective quasiparticle recombination time,  $e$  is the electron charge, and  $d$  is the thickness of the perturbed region. If the superconductor is thin enough,  $d$  is the thickness of the film.

Combining equations 5.4 and 5.2 yields [Gim 2001],

$$\frac{d\Delta}{dJ_{inj}} \cong \frac{-\tau_{eff}}{2eN(0)d}. \quad (5.5)$$

Both the non-equilibrium quasiparticle density and the suppression of the gap with injection are linearly dependent on  $\tau_{eff}$ . The quasiparticle recombination time,  $\tau_r$ , decreases exponentially at lower temperatures due to the exponential decrease in the number of available

quasiparticles to pair with [Dynes 1978].

$$\tau_r \cong \tau_0 \left( \frac{\Delta(T)}{kT} \right)^{1/2} e^{\frac{\Delta(T)}{kT}}, \quad (5.6)$$

where  $\tau_0$  is the characteristic relaxation time related to the electron-phonon coupling strength, and  $k$  is Boltzman's constant. This combined with equations 5.5 and 5.2 predicts that the gain of a quasiparticle injection device should increase with decreasing temperature. That is if the effects are prescribed to quasiparticle injection.

In 1987, with the invention of high  $T_c$  superconducting materials, experiments in superconducting three terminal quasiparticle injection devices, also known as "QPIDs", were revisited with hopes of creating a high gain device at temperatures above the liquid nitrogen temperature of 77K. Theoretically, high  $T_c$  superconductors are not found to be well described by BCS theory and currently remain unresolved. Also, the critical current of high  $T_c$  materials is generally dependent on flux pinning, and it's detailed dependence on the order parameter is unknown. Generally one assumes, the critical current is related to the order parameter,  $J_c \propto \Delta$ , dictated by Ginsburg-Landau theory. Thus the suppression of the order parameter given by BCS non-equilibrium quasiparticle injection arguments is at least qualitatively correct.

A good review of early YBCO QPID results can be found in [Mannhart 1996]. Low temperature experiments were first carried out by Kobayashi *et al.* with aluminum cross-strip on YBCO and ErBCO [Kobayashi 1989]. A current gain of  $\sim 5$  -7 was found at 4.2K.

Boguslavskij *et al.* tested the first YBCO injection device at high temperature [Boguslavskij 1994]. The device consisted of a Au or Au/PBCO injection pad on YBCO. A gain of  $\sim 2$  was found at 65K in the Au/YBCO structures.

In 1994, Iguchi *et al.* also tested a Au/MgO/YBCO cross strip quasiparticle injection device, achieving a gain of  $\sim 1.2$  at 4.2K.

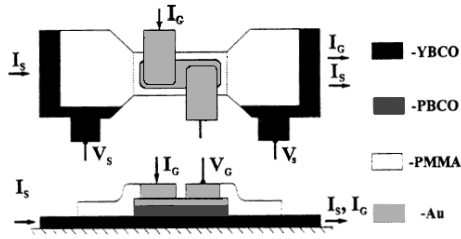


**Figure 5.2:** Schematic of a quasiparticle injection device. The YBCO bridge was  $8\text{-}20\mu\text{m}$  wide and  $800\text{\AA}$  thick. The Au and PBCo were  $300\text{\AA}$  and  $0\text{-}400\text{\AA}$  thick respectively. [Boguslavskij 1994]

More recent quasiparticle injection experiments on YBCO have been performed. Schneider *et al.* found gains up to 15 at 81K in cross strip devices consisting of Au/STO/YBCO heterostructures [Schneider 1999]. But more recently, Morán *et al.* from this same group published an excellent paper for similar Au/STO/YBCO devices [Morán 2003]. Taking current addition and heating into account Moran estimated a possible gain caused by quasiparticle effects of 3.5 at 77K, and experimentally obtained a gain of 5 at 77K. This result will be returned to later.

In these cross-strip devices current summation effects were accounted for in the measurement of gain. A good explanation of current summation can be found in Boguslavskij *et al.* [Boguslavskij 1994]. Consider a 3 terminal quasiparticle injection experiment. One attaches a current source to their sample and applies a test current. With no injection current applied, one finds a voltage appears at the application of a positive test current with an amplitude  $|I_t^+|$  and a negative current with an amplitude  $|I_t^-|$ . The critical current,  $I_c(0)$ , is then calculated as

$$I_c(0) = \frac{|I_t^+| + |I_t^-|}{2}. \quad (5.7)$$

When one applies an injection current and repeats the above experiment, one finds a

voltage appears at the application of a positive test current with amplitude  $|I_t^+|$  and a negative test current with amplitude  $|I_t^-|$ . One might be inclined to calculate the critical current,  $I_c(I_{inj})$ , in the same way as above. This calculation is inaccurate however.

This can be seen by considering the maximum current amplitude present in the superconducting bridge,  $|I_{max+}|$ , when the injection current and the test current are applied in the same direction.

It is easily seen the currents add together at the edge of the injection region yielding,  $|I_{max+}| = |I_t^+| + |I_{inj}|$ .

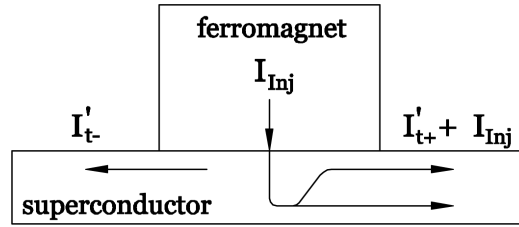


**Figure 5.3:** Schematic of current summation in 3 terminal device.

Notice this current is not the same as what you would read on your test current source! The maximum current amplitude present in the superconducting bridge when the test current is applied opposite to the injected current is simply what is measured,  $|I_{max-}| = |I_t^-|$ . This yields an actual critical current of,

$$I_c(I_{inj}) = \frac{|I_t^+| + |I_t^-|}{2} + \frac{|I_{inj}|}{2} \quad (5.8)$$

We define the measured critical current given by the test currents when a injection current is imposed as,

$$I_c^*(I_{inj}) = \frac{|I_t^+| + |I_t^-|}{2} \quad (5.9)$$

The mistake many published experiments make is to calculate the gain of their device, defined as,

$$G \equiv -\delta I_c / \delta I_{inj} \quad (5.10)$$

using only the test currents, and not taking current summation into effect. This results in a incorrect gain ( $G^*$ ) calculation of ,

$$G^* = -\frac{[I_c^*(I_{inj}) - I_c(0)]}{(I_{inj} - 0)} = -(I_c(I_{inj}) - I_c(0))/(I_{inj}) + 1/2 \quad (5.11)$$

Notice an extra factor of 1/2 is added to what should be the actual gain. Therefore a gain of up to 1/2 can be measured in a injection device, even when no non-equilibrium effects are present. In the case of more complex injection current geometries the offset to the gain caused by injection can vary due to the injected current distribution in the measured region. This is especially important to consider when there is a distinct possibility of injected current being delivered outside the measured critical current region. Also, when different insulating barriers and materials are used in such devices it can be hard to precisely discriminate between results. This error will be noted in the review of certain spin injection devices in this section.

### 5.1.2 Spin Injection Critical Current Suppression Devices

In 1993, interest in superconducting three terminal devices was again revitalized with the 're'-discovery of ferromagnetic colossal magnetoresistance materials [Helmolt 1993] [Chahara 1993]. These materials were found to have a high degree of spin polarization (see chapter 3), and their perovskite crystal structure made them compatible with the high- $T_c$  superconducting oxides. An injected current with a spin polarization  $\neq 0$  has been suggested to have a larger effect on the critical current than the usual quasi-particle injection. The possible technological applications of high gain superconducting devices above the liquid nitrogen temperature of 77K spurred the investigation of such devices.

The premise of increased gain due to spin injection, aside from the standard quasiparticle injection effects, was based on the following concept. Suppose a ferromagnet is in contact with a superconductor. (Often a thin insulating barrier is placed between them to prevent

Andreev reflection and the proximity effect from complicating the interaction.) If a voltage is applied between the ferromagnetic and the superconductor, electrons will travel from the ferromagnet into the superconductor (or vice versa). In a BCS theory framework, the superconductor carries current via a condensate of cooper pairs (charge  $2e$ ). Cooper pairs consist of a spin up and a spin down electron and pair due to an attractive potential brought about by interaction with the ion lattice. At an energy gap of  $2\Delta$  above the cooper pair condensate, single electron states, known as quasiparticles, exist in a Fermi distribution. The net spin orientation of the quasiparticles in the Fermi distribution is neutral. A superconductor is therefore a spin neutral entity, that is it has just as many up spins as down spins. Quasiparticles of opposite spin can pair via an interaction with a phonon and relax into the condensate. An equilibrium is created for a given temperature between the condensate and quasiparticle states.

A ferromagnet on the other hand has a surplus of spins aligned in a direction dictated by its' magnetic axis. A split is created in the up and down spin energy bands. At the Fermi level one spin orientation has more available states in relation to the other. Due to this imbalance an electrical current in a ferromagnet also carries with it a net spin polarization known as a 'spin current'. When a current is delivered from a ferromagnet to a superconductor a surplus net spin is injected into the superconductor. Hence, the term 'spin injection'.

Quasiparticles have a lifetime  $T_s$  inside a superconductor, after which they pair and decay into the cooper pair condensate. With an applied spin injection, one spin branch of the quasiparticle distribution, i.e. the up spin, is over populated. Thus there is a decreased probability that two quasiparticles will form a cooper pair simply because the available pairs of electrons with opposite spins is diminished. With no down spin electron to pair with, injected quasiparticles have an additional lifetime,  $T_{spin}$ . This time corresponds to the time in which a up spin quasiparticle scatters into a down spin state at which point it

would acquire the normal quasiparticle lifetime due to the ample supply of up spins to pair with.  $T_{spin}$ , maybe quite a bit longer than the normal quasiparticle life time because there are not many available scattering process to flip spin. The most accessible mechanism is the spin-orbital interaction in which the spin interacts with a pseudo-relativistic magnetic field it perceives from the electric field of ion lattice. Also, spins may scatter off of magnetic impurities. Due to the injected spins extended lifetime inside a superconductor, a quasiparticle bottleneck would be created in which the quasiparticle distribution is over populated in comparison with it's unperturbed state. Due to charge neutrality, the overpopulation of the quasiparticle distribution must correspond to a decrease of the number of cooper pairs, and in turn the critical current of the superconductor.

Extended spin lifetimes could allow for far reaching effects due to diffusion. While a superconductor screens electric fields from its interior by setting up competing surface currents, it has no known mechanism for screening out a spin imbalance. A unbalanced spin current could then diffuse throughout a superconductor within the quasiparticle population.

It has been found by Abrikosov *et al.* that metallic superconductors doped with even small amounts of magnetic impurities show a dramatic reduction in critical current [Abrikosov 1961]. This effect is believed to be due to an increased pair breaking effect caused by the local moments of the impurities. This effect has also been, seen when the Cu site of the copper oxide superconductor  $\text{Bi}_2\text{Sr}_2\text{CaCu}_2\text{O}_{8+\delta}$  is doped with Fe, Ni, and Zn [Hedt 1994].

In 1997, Vas'ko *et al.* suggested that a highly polarized current injected into a superconductor may cause cooper pair breaking in a qualitatively similar manner to a superconductor doped with magnetic impurities. For this reason spin injected from a ferromagnet into a superconductor may have an appreciable measurable effect on the critical current of a superconductor.

The first, rather crude, YBCO spin injection critical current suppression device was

presented by Vas'ko *et al.* [Vas'ko 1997]. The device consisted of a bottom unpatterned  $\text{La}_{0.67}\text{Sr}_{0.33}\text{MnO}_3$  layer, a middle insulating layer  $\text{La}_2\text{CuO}_4$ , and a top patterned bridge of  $\text{DyBa}_2\text{Cu}_3\text{O}_7$  (DBCO) with a  $T_c(0) \approx 70\text{K}$ .

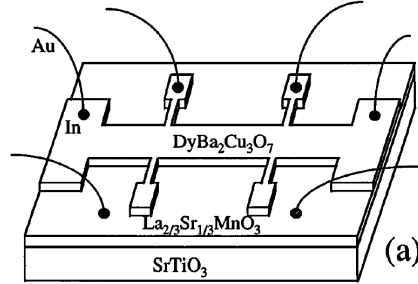


**Figure 5.4:** Schematic of spin injection  $I_C$  suppression device with unpatterned injection layer. The DBCO bridge was  $300\mu\text{m}$  wide. The substrate was  $6\times 6\text{mm}$ . The DBCO/LCO/LSMO heterostructure layers were  $400\text{\AA}/24\text{\AA}/600\text{\AA}$  respectively. [Vas'ko 1997]

Current was injected by applying it to the bottom LSMO layer in various orientations relative to the DBCO bridge. See figure 5.4 for a schematic of the device. The assumption was made that the injection current would enter the superconductor due to the low resistance short it created. No current summation effects were taken into account in this study. An increasing gain of 0.5 - 1 was found for the corresponding temperature range of 60 - 40K. But below 40K, the gain remained equal to 1.

A control experiment was performed in which a bare DBCO bridge had a layer of gold deposited over the top. Current was injected from the gold to the DBCO in the same manner as previously mentioned. This was done to compare the suppression effects caused by random spin oriented quasiparticle injection to those of the proposed highly spin oriented injection. In this case the gain was found to be  $\approx 0.1$  at 60K, which was significantly less than LSMO injection

Gim *et al.* raised several criticisms to this experiment, aside from not taking current

summation into account [Gim 2001]. One is the lack of an increase in gain below 40K, where the previously mentioned theoretical models of non-equilibrium superconductivity point to an increase of gain with decreasing temperature.

Another major criticism had to do with current transfer length. When a metal layer, such as the LSMO, is in contact with a superconducting layer, such as the YBCO, current transfers from one to the other as an exponential decay with a transfer length  $L_T$ . This transfer length is given by a transmission line model [Berger 1972, Gim 2001] as,

$$L_T = \sqrt{\frac{r_c}{R_{sq}}}^{1/2}, \quad (5.12)$$

where  $r_c$  is specific contact resistance between the metal and the superconductor, and  $R_{sq}$  is the square resistance of the metal layer. The transfer length gives a good estimation of the region most directly effected by injected current. This model is discussed in more detail in section 5.2.

Estimates of transfer lengths for Va'sko's device were on the order of 1  $\mu\text{m}$  while the width of the device bridge was 300 $\mu\text{m}$ . Also, the control sample made with gold as the injecting layer would have largely different transfer lengths due the different square resistance and contact resistance for the material. Therefore it is very difficult to draw relevant conclusions from the comparison of the spin injection and the control sample.

Numerous alternate spin injection experiments followed with a variety of results. The following are some of the more popularly referenced of the initial reports.

Almost simultaneously to Va'sko *et al.*, Chrisey *et al.* produced a three terminal device consisting of a bottom bridge consisting of a 200 nm thick YBCO strip with a 50 nm top gold layer, and two cross-strip top bridges, one of gold and one of  $\text{Ni}_{0.8}\text{Fe}_{0.2}$  [Chrisey 1994]. The gold on top of the YBCO is seen as a spin transparent chemical barrier to prevent proximity and chemical effects caused by direct contact of the permalloy. A larger gain ( $\approx 10$ ) was found in one sample for the ferromagnetic injection as compared to the Au contact

injection ( $\approx 5$ ). A small percentage of other samples showed a similar difference though not as large. For most samples however little difference was seen between the two different scenarios! No current summation was taken into effect, and test currents were rather high being on the order of 100mA. In general the conclusions were not very convincing.

Dong *et al.* created a parallel injection device, seen in figure 5.5, consisting of either a metallic  $\text{LaNiO}_3$  (LNO) or a ferromagnetic  $\text{Nd}_{0.7}\text{Sr}_{0.3}\text{MnO}_3$  (NSMO) bottom layer, an insulating  $\text{LaAlO}_3$  (LAO) middle layer, and a top YBCO layer (with Au deposited for contacts) [Dong 1997]. All three layers were patterned into a single strip with varying widths of  $20\text{-}250\mu\text{m}$ . The top YBCO layer was then etched away on either end and four gold leads were patterned on the surface. Current was injected into the YBCO by applying a current between the bottom layer and one of the gold leads on the top YBCO surface. Critical current was measured via a four point measurement using the four top leads.

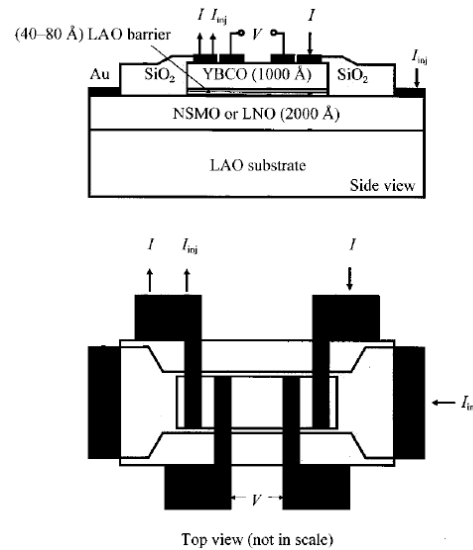


**Figure 5.5:** Schematic of 4 terminal spin injection  $I_C$  suppression device. [Dong 1997]

A gain of 1.4 was observed for the NSMO device, as compared to a gain of .09 for the

LNO device with the same LAO barrier thickness. For all devices, the NSMO provided a gain 10 - 30 times larger than the LNO. A gain as large as 5 at 74K was measured with the NSMO device. It should be noted that no current summation effects were taken into account in this study. The total power density caused by the injected current, calculated as  $P_{Inj} = J^2 R_1 A$  (where  $R_1$  was the junction resistance,  $J$  the injected current density, and  $A$  the cross-sectional area), was  $\approx 2 \text{ W/cm}^2$ .

This power density was claimed to be insufficient to cause enough temperature change to create the effects. Often an upper bound of  $3700 \text{ W/cm}^2$  is used. Joose made this estimate [Mannhart 1996] based on an experiment by Shi *et al.* [Shi 1993] in which a  $50 \mu\text{m}$  YBCO bridge was optically radiated with a laser pulse train for varying times. Several early spin injection papers make reference to this result. But there are not many other reasons given to exclude heating from the device gain.

Gim *et al.* also criticized Dong's study due to the issue of transfer lengths [Gim 2001]. See equation 5.12. Estimations made by Gim using values provided in Dong's study yield a larger transfer length for the LSMO samples rather than the NSMO sample. With the discrepancy in transfer length, a larger gain would be expected in the LSMO samples due to quasiparticle injection regardless of spin effects. Also, since current transfers from the bottom metallic layer to the top superconductor over a finite width which was less than the total length of the device, using the entire area of the YBCO to calculate power density would yield a gross under estimation. This error is made in almost all the YBCO spin injection studies to date. However, aside from some ambiguities, Dong's experiment is one of the better spin injection studies made to date.

Stroud *et al.*, from the Navel Research Laboratory (NRL), found a gain of 35 at 77K in YBCO/STO/LSMO cross strip 3 terminal device [Stroud 1998]. The device consisted of  $1000\text{\AA}$  LSMO  $100\mu\text{m}$  wide bottom bridge, with a  $400\text{\AA}$  STO barrier and a  $1000\text{\AA}$  YBCO  $100\mu\text{m}$  wide top cross strip. The device had a critical current of  $100\text{mA}$  at 77K and was

suppressed to  $\sim 30\text{mA}$  with a  $2.5\text{mA}$  injection current. The effect of heating was simulated by running current through the bottom LSMO without injecting it. A gain of 6 was found in that configuration. Current summation was not taken into account, although it could only account for a 0.5 gain.

Stroud's study is often quoted as having the highest gain. However, as pointed out by Gim *et al.* the determination of the critical current is made by extrapolating the roughly linear region of the measured V-I curves in the 1 mV voltage range to zero. This mostly linear region is associated with vortex motion and there was clearly dissipation below the determined critical current values. The actual value of the critical current could be orders of magnitude below the reported values. Also, the thickness of the STO barrier ( $400\text{\AA}$ ) is far beyond and barrier width normally associated with the tunneling region.

In another paper from the same group at NRL by Koller *et al.* published at roughly the same time (1998) a significant doubt is placed on Stroud's results [Koller 1998]. The resistance of YBCO/STO/LSMO interface was given as  $3\text{K}\Omega$ . 22 mWatts of power were claimed to be dissipated in the substrate at higher injection currents. But, most importantly, in this paper the claim was made that when devices were made with exceedingly better film qualities (Better  $T_c(0)$  for YBCO, better ferromagnetic transition temperature for the LSMO  $\sim 300\text{K}$ ) the devices then showed little to no gain! While this group is widely reported as attaining the highest gain, the physical process it is obtained by is very much in doubt by their own admission.

Yeh *et al.*, in 1999, tested a perpendicular spin injection device consisting of a YBCO strip atop a LSMO or LNO plane with barriers of YSZ and STO of varying thickness in between. Current was injected by passing a current through the LSMO layer perpendicular to the top YBCO strip and extracting that current through one of the YBCO test current leads. A pulsed current was used to minimize heating. The current pulse width used was  $200\ \mu\text{sec}$  in length. Currents applied for longer amounts of time yielded larger gains which

were attributed to heating. Small gains near  $T_c$  of about 1 were found for the LSMO structure while no gain was found for the LNO structures with similar injected currents.

Yeh's devices were, however, rather large. The YBCO strip was 2 x 6 mm in size, with the bottom LSMO equal to the size of the substrate 6 x 6 mm! The transfer length for such devices would provide an injected region  $\ll 1\%$  as noted by Gim [Gim 2001]. Even if suppression was caused by diffusion of spin throughout the superconducting region, the carrier diffusion constant in YBCO is on the order of a few  $\text{cm}^2/\text{s}$ . Therefore the injected current would have to at least be applied for 2ms in order to allow enough time for the large device are to be completely effected. This is far beyond the time of the pulsed current time presented.

A few other spin injection devices have been reported with varying degrees of gain. Goldman *et al.* [Goldman 2001], the same group that published the Va'sko *et al* [Vas'ko 1997] results above, found a maximum gain of 1.3 at 2K in a  $\text{La}_{0.67}\text{Ba}_{0.33}\text{MnO}_3/\text{DyBa}_2\text{Cu}_3\text{O}_7$  device. LBMO was the top layer in this device, and was patterned with ion milling into a 10 x 20  $\mu\text{m}$  injection region. The critical current of the bottom layer was then measured with injection. There was no mention of current addition being taken into account. Also, there was no insulating barrier in this experiment.

Plausinaitiene *et al.* [Plausinaitiene 2001] reported gains of  $\approx 3$  in devices similar to those of Wei *et al* [Wei 1997]. However device size is in the order of millimeters with LSMO and YBCO film thicknesses of 2000  $\text{\AA}$ .

Also, Sakar *et al.* reported differences in injection effects between normal metal and ferromagnet injection in an unusual device [Sakar 2001]. Critical currents were compared in the millivolt region of measured V-I curves (see Stroud above).

Dumont *et al.* found very small gains in an unusual injection scheme [Dumont 2003]. Samples consist of a bottom 2000 $\text{\AA}$  LSMO layer with a top 500 $\text{\AA}$  layer in which the top YBCO is patterned into a 40 $\mu$  wide bridge. A relation to heating due to the injected current

is evident in their device although no information is provided about applied current times.

An interesting related experiment was done by Mikheenko *et al.* in which the magnetic moments of a YBCO/LCMO, YBCO/STO/LCMO, and YBCO/LNO film were measured [Mikheenko 2001]. The samples were 5 x 5mm in size, and a small region of the top YBCO layer was removed to provide an way to inject current from the bottom layer. By applying a perpendicular magnetic field to the sample while in it's superconducting state, the sample was placed in a Bean critical state [Bean 1964]. The Bean state is attained when the current flowing around the superconductor to maintain the trapped magnetic field is equal to the critical current. The measured magnetic moment is then determined by this trapped flux.

Upon the application of a single 60 mA current pulse from the LCMO and LNO layer to the YBCO, a decrease in the measured magnetic moment was found. For current pulses applied for longer than 100 ms, a large change in magnetization was seen which was the same for both LSMO and LNO films. This change was attributed to heating. For pulses applied with lengths less than 100 ms, the change in magnetization was distinctly smaller. However, an obvious difference was displayed between the LCMO and LNO films. The LCMO was found to yield larger suppression of the moment. Also, below a time length of 1 ms, no measurable suppression was found in the LNO sample where suppression in the LCMO sample persisted. The authors provide a comparison to transport measurements by considering a gain determined by the change in the circulating supercurrent with the applied current pulse. In the proposed long pulse heating regime a gain of 30 is found, and in the non-heating short pulse regime a gain  $\approx 0.1$  is found. Although the samples are rather large, and the role of transfer lengths creates some doubt, the measurement technique and results are interesting.

In general the results of previous spin injection studies involving YBCO are scattered and unreliable. Thus, nearly eight years after this branch of experimental work was conceived, the field is still wide open to new experimental results and interpretations. A definitive

experiment has not yet been obtained and no indication has been given as to the best experimental direction to proceed. In the following sections results of our measurements on our own unique injection devices are presented.

## 5.2 Devices and Measurements

### 5.2.1 YBCO/LBMO Cross Strip $I_C$ Suppression Device

Early in this study, a few cross strip type devices were constructed. See figure 5.6. The devices consisted of a bottom 1000 Å  $\text{La}_{0.67}\text{Ba}_{0.33}\text{MnO}_3$  (LBMO) stripe, with an overlying 1000 Å YBCO bridge. The substrate was  $\text{NdGaO}_3$ . LBMO is a CMR ferromagnetic material similar to LSMO, but with a lower ferromagnetic transition temperature.

The LBMO stripe was created by masking of the substrate with two sapphire ( $\text{Al}_2\text{O}_3$ ) strips. Sapphire was chosen for its thermal conducting properties, and the strips were placed as close together as visually possible. In PLD, physical masking is difficult due to shadowing effects and thermal non-uniformity caused on the sample surface due to the mask. It is very difficult to obtain good quality films with this method. The LBMO was deposited on the masked substrate, the mask was then removed *ex situ*, and the YBCO layer was finally deposited on top. The YBCO was then patterned, via photolithography and wet etching with dilute nitric acid into a 10  $\mu\text{m}$  wide bridge. The ferromagnet layer was magnetized by cooling it below its ferromagnetic transition temperature, removing the vacuum tight probe from the cooling environment, applying a magnetic field, and then reinserting the probe.

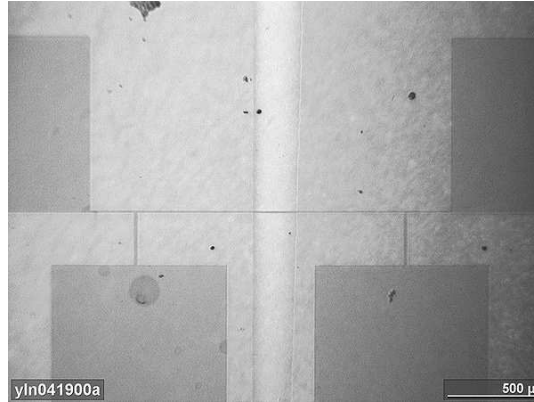


**Figure 5.6:** Picture of YBCO/LBMO  $I_C$  suppression cross strip device. The LBMO is the 200  $\mu\text{m}$  wide stripe and was created by *in situ* masking. The YBCO is the thin photolithographic patterned 10 $\mu\text{m}$  stripe.

These three terminal devices were found to have gains almost exactly equal to  $1/2$  for a large temperature range. This seems to directly point to the device being dominated by current summation effects. However, the YBCO bridge could have had weak links outside of the injected region that dominated the critical current measurement. Also, the 200 x 10  $\mu\text{m}$  injection region was rather large. Therefore, an even distribution of current was unlikely. At points where the YBCO strip intersects the LBMO strip the YBCO crystal structure, composition, and thickness is not well defined. These regions could also dominate the critical current yet not be in the injection region. This type of device was abandoned for these reasons.

### 5.2.2 YBCO/LBMO $I_C$ suppression device with unpatterned LBMO

A  $I_C$  suppression device with an unpatterned bottom injection layer, similar to that of Vas'ko *et al.* [Vas'ko 1997], was also tested. See figure 5.4. The heterostructure consisted of a patterned 1000 $\text{\AA}$  YBCO top layer with a bottom unpatterned 1000 $\text{\AA}$  LBMO layer. The YBCO/LBMO heterostructure was grown *in situ*. The top YBCO was then patterned using photolithography and wet etching with dilute nitric acid. The bottom LBMO was

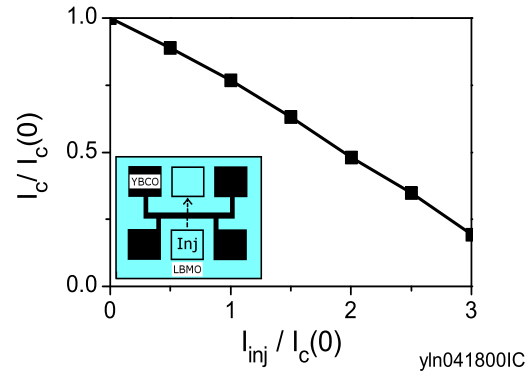


**Figure 5.7:** Critical current vs. injected current for YBCO/LBMO injection device with unpatterned LBMO. The YBCO bridge was  $1000\text{\AA}$  thick and  $10\mu\text{m}$  wide. This data was taken at 80K. The device is similar to that of Vas'ko *et al.* [Vas'ko 1997]

not etched by the nitric acid and was left fully intact.

Current was passed between leads attached to the LBMO layer on opposite sides of the patterned YBCO bridge (see figure 5.7). The YBCO bridge was  $10\mu\text{m}$  wide. The voltage and current leads were also YBCO and connected to  $400 \times 400\mu\text{m}$  pads. This makes the effective injection area difficult to define. The current injection was expected to take place from the shorted current through the superconductor as in Vas'ko's experiment. The device was found to have small gains  $\approx 0.3$  at 80K. This gain is similar to that of Vas'ko's.

With small gains and no direct way to tell whether the injected current was arriving in the tested superconducting bridge or not, it was impossible to determine if the reduced critical current was caused by a spin effect or simple current summation. Therefore this experiment was abandoned.

### 5.2.3 YBCO/I/LSMO Four Terminal $I_C$ Suppression Device

A device similar to that of Dong *et al.* [Dong 1997], see figure 5.5, was also tested. The device consisted of a top patterned YBCO bridge with four gold leads, a middle insulating STO layer, and a bottom LSMO layer with two injection leads. See figure 5.8.

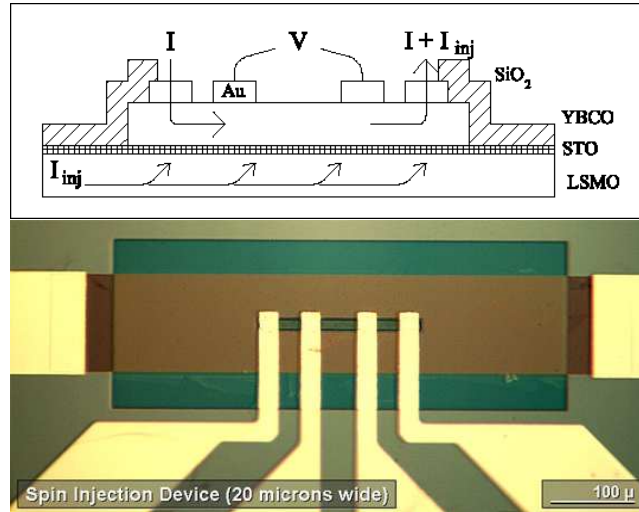


**Figure 5.8:** Schematic and picture of a YBCO/STO/LSMO side injection 4 terminal device. The YBCO bridge was  $1000\text{\AA}$  thick, the bottom LSMO  $1000\text{\AA}$ , and the STO from  $0 - 80\text{\AA}$ . The device was similar to that of Dong *et al.*[Dong 1997]

Current was injected from a side ferromagnetic pad into the opposite side YBCO current pad and the critical current of the device was measured. The critical current was defined as the current necessary to cause a  $1\ \mu\text{V}$  voltage reading in the bridge. This is a popularly used criteria for these measurements. All results presented here are for  $20\ \mu\text{m}$  wide YBCO bridges.

The varying STO insulating barrier thickness showed a large difference in critical current suppression. Samples with no barrier showed very little to no gain, while devices with barriers from  $40-80\text{\AA}$  showed similar gains of  $.3 - 2$  for temperatures from  $80 - 60\text{K}$  respectively. Current summation can provide gains up to  $.5$  and most likely accounts for a large

fraction of the measured gain.

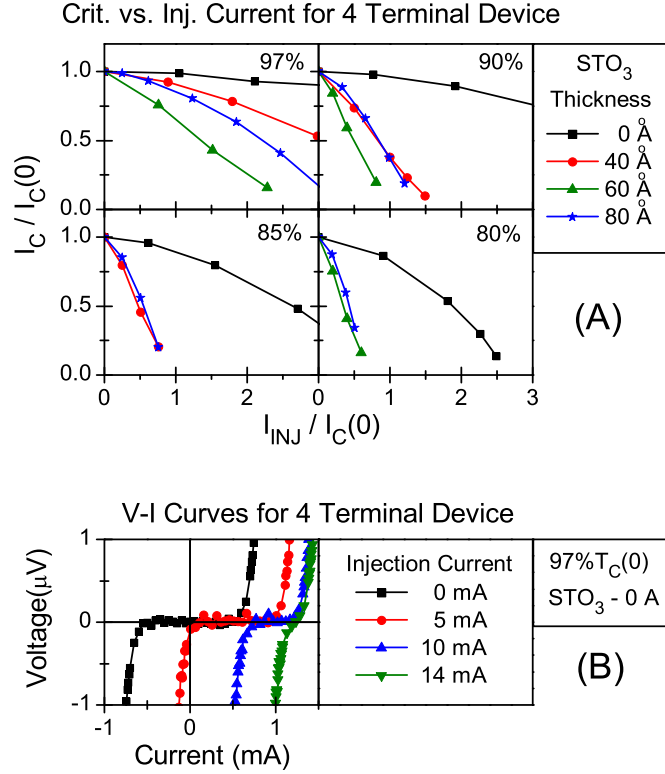
These devices have similar downsides to those mentioned for Dong's device above, (see section 5.1.2). Injected current arrives in the superconducting layer within a transfer length that can be small compared with the length of the YBCO bridge. Therefore, most spin injection effects could take place at the edge of the device away from the central measurement region. It was difficult to estimate the resistance of the YBCO/STO/LSMO interface for these devices as there was some significant contact resistance in the gold/LSMO injection current leads. This made it difficult to ascertain what transfer length was present in our devices. The measured V-I curves are offset as seen in figure 5.9. This indicates that some current summation was most likely included in the measurement.

Also, at the time these devices were made the STO target used for PLD was not a single crystal target, but a fine grain pressed target. It was later found that the single crystal target provided far superior insulating barriers. Therefore, there may be pin hole effects present in these devices. Also, it was later determined in a AFM study that LSMO films thicker than  $500\text{\AA}$  yield rough surfaces and out growths of  $> 100\text{\AA}$ . Current injection could be dominated by these pin holes and scatter effects throughout the bridge. This could explain the closely matched data of the various STO thicknesses.

In order to reduce heating of the sample, the duration of the applied current and the timing of the measurement of the voltage were precisely controlled and minimized. For our equipment, Keithley 2400 sourcemeter and 2182 nanovoltmeter, the fastest the measurement could be made, while retaining an acceptable noise level was by applying the test current for 3 msec settling period and maintaining it through the 16 msec (1 PLC) measurement cycle of the voltmeter. Making the total time for the applied current  $\approx 20$  msec. (The actual time the current was applied was for 65 msec. but the extra 45 ms took place after the measurement cycle. An explanation of the exact timing scheme and reasons for the extra current are given in section 2.10.) Time between measurements was 3 seconds, creating a

duty cycle of  $< 10^{-2}$ . This measurement scheme was used for all measurements shown here after.

At lower temperatures, the larger test currents necessary for measurement ( $>50\text{mA}$ ) combined with the large injection currents required made measuring the samples difficult. Often the samples were damaged due to the large currents involved (the test current lead had to transport the test current plus the injection current and was usually the first to be damaged). Also, noise from the source meter increase as the required current range increases. Due to the poor Au/LSMO contacts, this sometimes caused noise beyond the  $1\mu\text{V}$  parameter used to determine the critical current. Due to these difficulties, low gains, and no good way to overcome the transfer length problem, these experiments were abandoned.



YLS021

**Figure 5.9:** Critical current vs. injection current and V-I curves for side injection 4 terminal suppression device. (A) Normalized critical current as a function of normalized injection current for a four terminal side injection suppression device.  $I_C(0)$  is the critical current with no injected current. The samples consisted of a YBCO/STO/LSMO heterostructure. The top and bottom YBCO and LSMO layers were both 1000Å thick. The STO thickness was varied from 0 - 80Å. All data is for a 20 μm wide YBCO bridge. Critical currents were  $\approx$  1.5 mA at 97% $T_C(0)$  to 40 mA at 80% $T_C(0)$ . (B) Voltage vs. current for a four terminal side injection critical current suppression device. The curves were taken at 80K (97%  $T_C(0)$ ) for a 0Å thick STO device. Note, the offset is almost equivalent to the injected current.

#### 5.2.4 YBCO/I/LSMO Five Terminal $I_C$ Suppression Device

An original five terminal suppression devices was then created to side step some problems associated with the previous cross strip and four terminal devices. It also consisted of a F-I-S structure, with the ferromagnet as the bottom layer. In this device however, the injection current travels through the bottom ferromagnet in a perpendicular direction to the top superconductor strip under test, and then upwards through the superconductor into a middle gold pad. This is referred to as injection scheme #1, (See figure 5.10). This is done in an attempt to ensure a effected injection region is created between the two voltage measurement leads. Injection current was also delivered through a top side contact and the voltage measurement made in an adjacent region. This is referred to as injection scheme #2 (See figure 5.10). This was done in an attempt to observe any possible injection effects caused at a distance due to diffusion of spins. Also, the side injection scheme was used as a way to ascertain if there were significant heating effects in the device.

The data shown in figure 5.11 shows the normalized critical current vs. injection current for devices with STO barriers of 0 - 60 Å. The data is normalized by dividing the critical current,  $I_C$ , and the injection current,  $I_{inj}$ , by the critical current attained with no injected current  $I_C(0)$ .

Several problems with the side injection 4 terminal device were avoided by the five terminal device. The central injection scheme prevented any large current summation effects. This also prevented any one gold pad from having to carry the test current and the injection current together. There was no offset of the voltage-current measurements. The side injection provided a better chance for spin effects to be present in the measured voltage region. The large low resistance injection lead lowered any global heating effects.

The created gains were rather small ( $\approx 1$ ). Results were found to be similar regardless of STO barrier in contrast with the 4 terminal devices. Side injection effects (Injection 2)

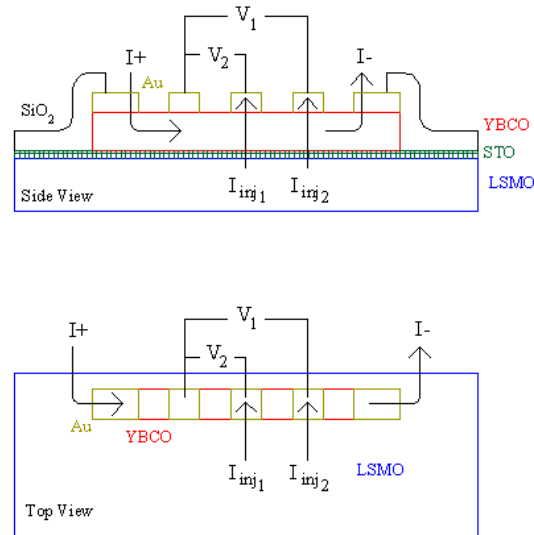


**Figure 5.10:** The top and side cross-section schematic of YBCO/STO/LSMO five terminal injection device are shown. Voltage #1,  $V_1$ , and injection current #1,  $I_{inj1}$ , are the measured voltage and injection current for the central injection scheme #1. The side injection scheme #2 is similarly shown. All results shown are from  $20 \times 150 \mu\text{m}$  YBCO bridges. The top middle gold injection pad was  $10 \times 20 \mu\text{m}$ . The gold voltage terminals were  $20 \times 20 \mu\text{m}$  and the end test current leads were  $30 \times 20 \mu\text{m}$ . There was a  $10 \mu\text{m}$  gap between leads. The bottom LSMO layer was  $400 \times 800 \mu\text{m}$  in total size with a  $400 \times 600 \mu\text{m}$  gold pad for injection. The top YBCO layer of the  $400 \times 600 \mu\text{m}$  contact region was left intact because the contact resistance between the YBCO and top gold layer was negligible.

were very small  $< 0.1$ . This at least indicates there is no global heating effects that account for the suppression effects. But, the side injection cannot rule out localized heating. Also, it is difficult to tell whether the side measurements have anything to do with spin effects due to diffusion or not.

Interestingly the critical vs. injection curves of these devices have a tendency to collapse onto a single curve at lower temperatures. As shown before, BCS models predict an increasing gain as temperature decrease.

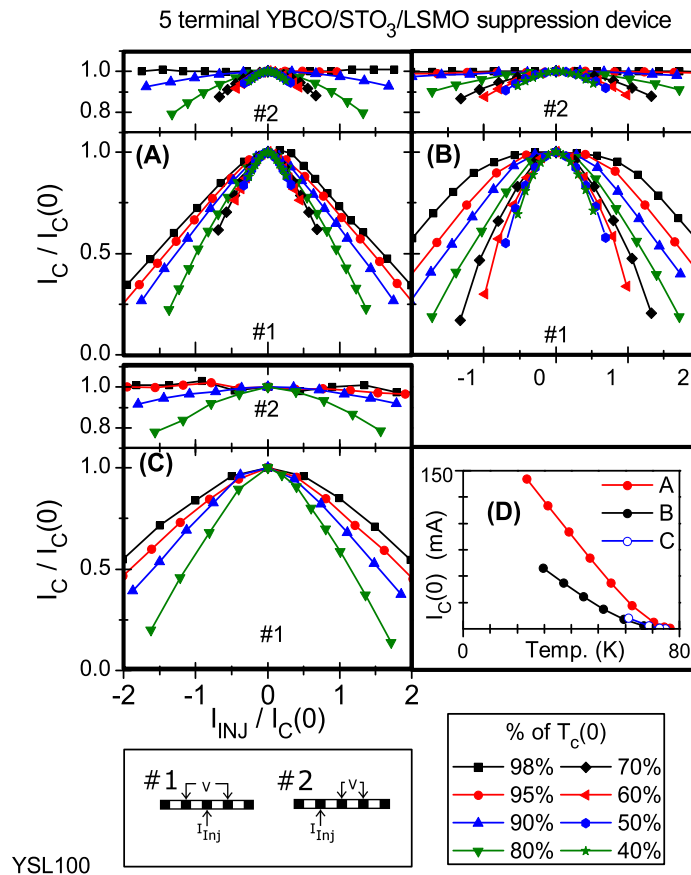


**Figure 5.11:** Critical vs. injection current for a several five terminal YBCO/STO/LSMO devices. Labels #1 and #2 refer to injection schemes shown. Sample (A) and (B) had a 1000Å thick 20 x 150 μm YBCO bridge, a 60Å STO barrier, and a 1000Å bottom LSMO layer. Sample (C) was the same except it had a 20Å STO barrier. (D) shows the critical current vs. temperature for the three devices.

### 5.2.5 YBCO/I/LSMO Multi-Terminal $I_C$ Suppression Device

Finally, a multi-terminal device was created to allow better injection localization (see figure 5.12). The device consisted of the usual YBCO/STO/LSMO structure, but YBCO/STO/LNO structures were tested as well. Injection was still made from the bottom ferromagnet to the top superconducting region. However the bottom injection lead was confined to a small area before connecting to the top superconductor. Only a small region of the top YBCO was removed on the injection lead in order to keep its resistance at a minimum. This was done to reduce any heating effects. If injection current leaked, due to pinholes, into the above superconducting film, any effects would at least be localized to a known region. The voltage measurement leads were patterned YBCO to reduce resistance and nullify any quasiparticle injection provided by metal leads.

YBCO leads were available at different distances from the injection in order to measure any distance suppression effects. These samples were tested in a continuous flow cryostat which allowed the application of a magnetic field during measurement. See section 2.9 for more details.

All data presented was for 10  $\mu\text{m}$  wide YBCO bridges. A new ion mill provided a better means by which to etch the devices making 10  $\mu\text{m}$  more attainable. See section 2.8.1 for ion mill details. The YBCO measurement leads were also 10  $\mu\text{m}$  in width with 10  $\mu\text{m}$  distance between.

Special attention was paid the resistance of the current injection path. A criticism of previous injection devices in other studies has been over the subject of current transfer length (see introduction 5.1.2). Current transfer between two layers with a contact resistance between them can be modeled with a transmission line model [Berger 1972, Gim 2001].

The model describes a 2 layer structure with a bottom metallic layer and a top superconducting layer, both of which are uniform (see figure 5.13). Assuming a uniform current

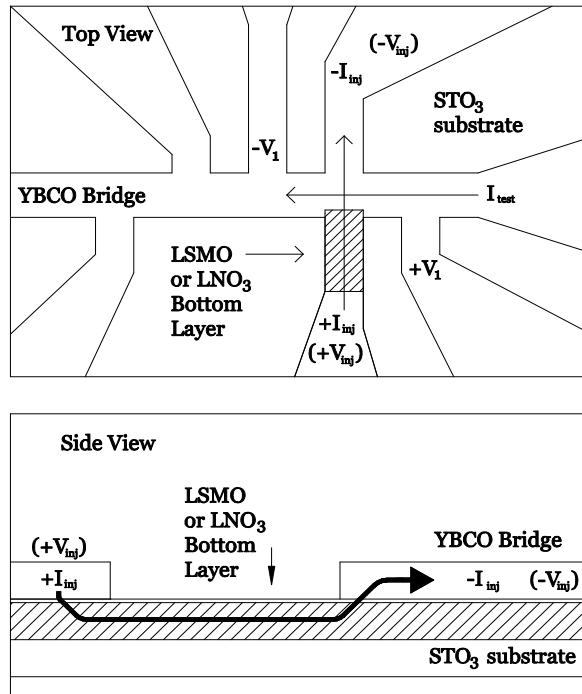


**Figure 5.12:** Multi-terminal device for YBCO/STO/(LSMO or LNO) device. Injection current was directed through the bottom LSMO or LNO in to the top YBCO as shown. The device bridge and leads were 10  $\mu\text{m}$  wide.

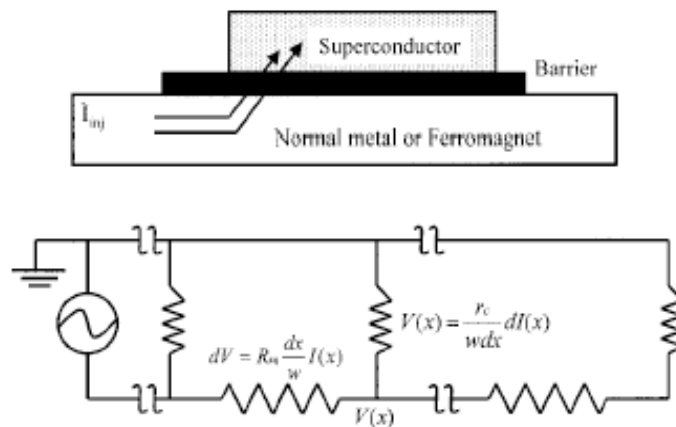


**Figure 5.13:** Schematic of transmission line model. [Gim 2001, Berger 1972]

flow along the two layers, consider a small piece of current  $dI$  that flows across a small portion of the barrier of Area  $w dx$ . This results in a voltage drop of,

$$V(x) = \frac{r_c}{w} \frac{dI(x)}{dx}, \quad (5.13)$$

where  $r_c$  is the specific resistance of the barrier and  $w$  is the width of the device.  $V(x)$  is then the voltage between the bottom LSMO and the top YBCO.

The current flowing along the bottom layer also causes a little piece of voltage  $dV$  along a small distance  $dx$  which yields,

$$I(x) = \frac{tw}{\rho} \frac{dV(x)}{dx} = \frac{w}{R_{sq}} \frac{dV(x)}{dx}, \quad (5.14)$$

where in relation to the bottom layer,  $t$  is the thickness,  $\rho$  is the resistivity, and  $R_{sq}$  is the sheet resistance or square resistance.

Combining equation 5.13 and 5.14 yields,

$$\frac{d^2 V(x)}{dx^2} - \frac{R_{sq}}{r_c} V(x) = 0, \quad (5.15)$$

which, for a long contact, yields an exponential decay with a characteristic length,

$$L_T = \sqrt{\frac{r_c}{R_{sq}}}. \quad (5.16)$$

In reference to the picture in figure 5.13, if the top layer had a finite length  $L$ , and current was to flow between the left and right bottom ferromagnet leads, the effective resistance of the superconductor/ferromagnet sandwich structure, given by combining equations 5.14, 5.16, and the solution of 5.15, is,

$$R_{eff} = \frac{V(L) - V(0)}{I_{inj}} = \frac{2\sqrt{r_c R_{sq}}}{w} \tanh \frac{L}{2L_T}. \quad (5.17)$$

For a long contact,  $L \gg L_T$ ,  $R_{eff} \approx 2(r_c R_{sq})^{1/2} / w$ . In the case of long contact in which the current is extracted from the top layer the effective resistance is half of this result,

$$R_{eff} \approx \frac{\sqrt{r_c R_{sq}}}{w}. \quad (5.18)$$

For the YBCO/STO/LSMO and the YBCO/STO/LNO devices shown in figure 5.14, the total resistance of the injection path,  $R_{inj}$ , was recorded simultaneously to the critical current measurement. Using the known conductivities of LSMO and LNO, the resistance of the small exposed region before the injection point,  $R_{bot}$ , was subtracted from  $R_{inj}$ . Since the measurement of  $R_{inj}$  also includes both the resistance of the injection lead and the YBCO bridge injected region the effective junction resistance is taken as half the remaining resistance to yield  $R_{eff} = (R_{inj} - R_{bot})/2$ .

The transfer length for the YBCO/STO/LSMO sample was found to be 10 - 5  $\mu\text{m}$  for the temperature range of 95 - 30% $T_c(0)$  (72 - 22K) respectively. This shows a large fraction (>50%) of the width of the 10 $\mu\text{m}$  bridge was directly subject to the injected current. This fraction of directly effected area is the large compared to most published devices analyzed with the same criteria. We credit these results to an excellent STO barrier similar to that of the LSMO/STO/LSMO junctions already presented. See section 3.2.1. Therefore these results can be considered a good indication of the suppression caused by current injection.

The transfer length for the YBCO/STO/LNO sample was found to be  $\approx 50\mu\text{m}$  for the temperature range of 90 - 30% $T_c(0)$  (73 - 24K) respectively. The lower resistivity of LNO compared to LSMO can account for this longer transfer length. In the critical current suppression results this difference should be noted. The longer transfer length results in a larger directly injected area making the comparison of LSMO and LNO devices somewhat difficult.

A YBCO/LSMO device with no insulating barrier was also tested. The overall measured resistance along the injection path of the YBCO/LSMO device,  $R_{inj}$ , is very close to the predicted resistance of the open LSMO area. The resistance of the interface is considered negligible in this case. The transfer length can then be considered to be  $< 1\mu\text{m}$ . Therefore, in this devices a negligible part of the YBCO bridge is directly under the influence of the injected current. YBCO/LNO devices were also constructed and tested. The critical

temperature in the YBCO/LNO devices tended to be much lower than the other devices ( $\Delta T_c > 20\text{K}$ ) making a comparison difficult. The reason for the lower critical current is not entirely clear. Although not shown here, results were found to be very similar to the YBCO/LSMO.

Unlike the 5 terminal device data, the YBCO/STO/LSMO (Y-S-LSMO) and the YBCO/STO/LNO (Y-S-LNO) (see figure 5.14) multi-terminal device's gain shows a definite temperature dependence at all temperatures. Recall the BCS equations 5.6, 5.5, and 5.4 for quasiparticle injection predict this dependence for the gain. In the Y-S-LSMO structure, the gain is seen to increase from .5 - 2.5 with reducing temperature. However, for the Y-S-LNO structure the gain is seen to increase from .5 - 4.0.

The larger gain observed in the LNO device can arise for numerous reasons. The first is the fact that the Y-S-LNO device has a much larger transfer length than the Y-S-LSMO device. Therefore a larger region of the YBCO is subject to direct quasiparticle injection in the LNO device. Also, while both devices have a similar STO barrier ( $32\text{\AA}$ ), surface roughness and defects can cause fluctuations in the effective barrier created, leading to different injected quasiparticle energy levels as well as current distributions.

Measurements were made in the region of the YBCO bridge neighboring the injection point. The experimental setup allowed the direct injection area and the side area to be monitored simultaneously. No voltage appeared in the neighboring regions until after a voltage which was much larger than  $1\mu\text{V}$  ( $> 3 - 4\mu\text{V}$ ) arose in the directly injected region. This indicates that there are no long reaching diffusion effects which cause large areas ( $> 10 \times 10\mu\text{m}$ ) of the YBCO bridge to become normal under injection. All effects are primarily isolated to the direct injection point.

Finally the interfaces of YBCO/STO and STO/LSMO are not well understood. It was seen in the LSMO/STO/LSMO junction study that the LSMO properties are most likely deteriorated at the STO interface. It is difficult to tell what effects may be present in

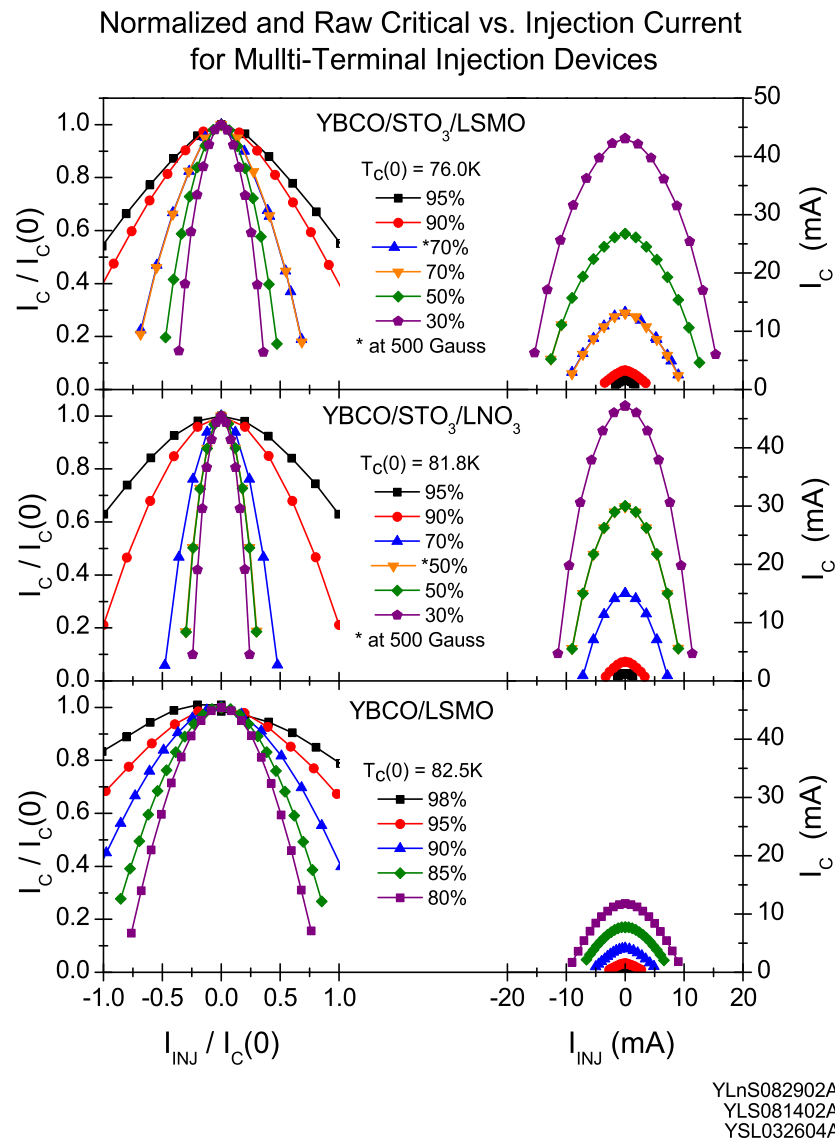


**Figure 5.14:** Normalized and raw critical vs. injection current for various multi-terminal injection devices. The device bridge was  $10\mu\text{m}$  wide. The thickness of the layers in the YBCO/STO/LSMO device were  $600\text{\AA}/32\text{\AA}/400\text{\AA}$  respectively. The thickness of the layers in the YBCO/STO/LNO device were  $600\text{\AA}/32\text{\AA}/400\text{\AA}$  respectively. The thickness of the layers in the YBCO/LSMO device were  $1000\text{\AA}/500\text{\AA}$  respectively. Measurements at different percentages of  $T_C(0)$  are shown. Note, data marked with a "\*" was made in a 500 Gauss magnetic field applied in the plane of the sample.

the YBCO/STO interface. The spin polarized current arriving from the LSMO could be scattered to yield a normal quasiparticle current. In this way the LSMO would be similar to the LNO in critical current suppression.

Various magnetic fields were applied during the measurements in an attempt to see differences arising from the domain structure of the LSMO layer. Neither device was effected by the application of a in plane magnetic field. The results from the application of a 500 Gauss in plane field are shown with the data. This field was sufficient to overcome the in-plane coercive field of the LSMO layer, yet small enough to leave the YBCO largely unaffected. The in-plane critical field for YBCO is on the order of 100 Tesla. The fact that the gain shows no deviation with applied field for the Y-S-LSMO sample does not bode well for a spin injection picture. However domain sizes for LSMO in the measured temperature range are found to be larger than tens of  $\mu\text{m}$  [Kwon 1997, Soh 2000]. Therefore, the magnetization direction could be varied with the application of a magnetic field, this change may not be reflected in the critical current suppression. Out-of-plane fields were also applied to the sample. Very small similar deviations were seen for both samples.

Resistances along the injected current path are similar for both devices. The total resistance shown by both devices is  $\approx 500 \Omega$ . The resistance derived for the current injection junction region of the devices at  $30\%T_c(0)$  is  $\approx 60\Omega$  for the Y-S-LSMO device, and  $\approx 220\Omega$  for the Y-S-LNO device (see transfer length discussion above). Maximum injection currents were on the order of 10 mA at these temperatures. The effective injection area was around  $10 \times 10 \mu\text{m}$  for the Y-S-LSMO, and  $10 \times 50 \mu\text{m}$  for the Y-S-LNO (effective injection area taken as the width of the device times the determined transfer length). This yields a power density of  $6000 \text{ W/cm}^2$  for the Y-S-LSMO and  $4400 \text{ W/cm}^2$  for the Y-S-LNO device.

These values surpass the critical power value of  $3700\text{W/cm}^2$  [Shi 1993] often quoted by spin injection studies. However if these effects were simply attributed to heating the LSMO would clearly have a larger suppression effect, which is opposite of what is shown. Although

it is also noted that the power density for the two samples are on the same order. Some heating may arise in these devices for lower temperatures and higher currents. However, the time of the applied current before the voltage measurement took place was varied in this experiment. Normally the current was applied for a 3 msec settling period before the voltage measurement occurred. The voltage measurement is taken for 17 msec after which the current is turned off. The time of the applied current before voltage measurement was increased to 300 msec before any real deviation was seen in the critical current data. This would make a heating argument seem a bit counter intuitive. If all suppression was due to heating even slight variations in the applied current time should have be reflected in larger suppression. It should be noted that when the time was increased to 30 msec, no deviation was seen in the data.

A YBCO/LSMO device with no STO barrier is presented in figure 5.14. The total resistance of the injection path for this device was  $\approx 150\Omega$ . As mentioned before, transfer lengths in this devices are hard to determine and are considered to be very short ( $\ll 1\mu m$ ). This device has a much thicker YBCO layer than the devices with STO barriers. Also, heating in these devices would most likely be greatly reduced from that present in the devices with barriers. The suppression of the critical current is not as large as the device with the STO. A clear temperature dependence is seen in the suppression. Measurements below 80% of the critical temperature could not be made due to the large critical currents and therefore the large injection currents required for suppression. When currents became too high, the devices were sometimes found to fail.

All the multi-terminal device data suggests a few different possibilities. Suppression effects may be due to quasiparticle injection effects, where there is no polarized spin transfer due to scattering at the interface. Possibly heating effects are causing gains by simply changing the temperature of the YBCO bridge. However in order to create the observed differences in critical current the temperature changes would have to be on the order of 10K

in some situations. I believe while heating may contribute it is not the sole mechanism of suppression. Finally it is possible that the effect of the polarization of the injection current is very little in terms of critical current. For YBCO the critical current relation to the order parameter is unknown because tunneling experiments are difficult and inconclusive.

In any case, the indications for a YBCO three terminal device are not good. Of the hundreds of spin injection suppression devices created in this study no gains were ever seen greater than 5 for any temperature. And, all gains larger than 1 were seen at temperatures far below the critical temperature of YBCO, and therefore much less than 77K.

### Conclusions and Future Work

---

The magnetic tunnel junctions investigated in this study show some hope for the very real attainment of a valuable technological device. LSMO/STO/LSMO tunnel junctions were found to operate very close to room temperature (275K), but this is still far below the Curie temperature of LSMO ( $>350\text{K}$ ). It seems a deterioration of the LSMO at the STO/LSMO interface may be the cause of this decreased operating temperature. If the nature of this deterioration can be better understood it may be possible to insert a very thin interface buffer layer to prevent this degradation. For example if the barrier region is found to be Sr deficient or rich, a corresponding over or under doped LSMO layer could be inserted.

The high resistance demagnetized state and the corresponding sharp switching high valued tunneling magnetoresistance is very promising and offers a new research area for magnetic tunnel junctions. The results found in this study indicates that a premagnetized state in which the field is ramped to a high value and returned to zero is not as stable and yields inferior results compared to samples initially placed in a demagnetized state. It seems the junctions maybe more adept at picking their own stable state than when one is imposed on them. The demagnetized junctions show single domain behaviour. It would be interesting via MFM or another technique to see the domain structure of such a device after demagnetization.

Currently, when junctions are created in industry the ferromagnetic layers are deposited and magnetized by applying a high magnetic field. An antiferromagnetic layer is then deposited in order to couple to the exposed ferromagnetic layer and pin its magnetization. But, perhaps industrial junctions could be demagnetized before applying the antiferromagnetic layer and yield better or at the very least unique and useful results. Of course, junctions created in industry have precise geometrical design and are very small which induces their ferromagnetic layers to have a nearly single domain while the our junctions seem to be subject to multiple domains. Multi-domains may play a key part in this effect. Also, the demagnetization effects found here maybe unique to manganite junctions, but perhaps the effect is more fundamental to magnetic junctions in general.

It is also interesting that when demagnetized, the junction picks out a high resistance, which according to current theories, corresponds to the opposite alignment of domains in the top and bottom ferromagnetic layers of the junction. This is the lower energy state when magnetic energy is involved. But, perhaps other mechanisms are at work including interlayer antiferromagnetic exchange coupling.

The combination of other colossal magnetoresistive ferromagnetic materials in magnetic tunnel junctions could also lead to many useful devices. It has been shown here, in what is believed to be one of the first mixed CMR material junctions, that LCMO/STO/LSMO junctions can show interesting directional effects. Such devices could be very useful in sensory applications. To date there is very little data available on the angular dependence of CMR magnetic tunnel junctions. Also, the combination of different CMR materials and perovskite insulating barriers can provide a better understanding of the fundamental ferromagnetic mechanism of CMR materials as well as the interface interaction within a heterostructure.

The spin diffusion measurement results, for the LSMO/YBCO/LSMO devices, are unusual. The results for an out-of-plane applied field shows a strange symmetry which is

different than other similar ferromagnetic device measurements. It may be necessary to measure the hall effect of bi-, tri-, and multi-layer LSMO-YBCO heterostructures at various out-of-plane applied field angles to obtain a better experimental understanding of what is being observed.

It is difficult to say whether the obtained results are due to spin diffusion effects or not. While some part of the signal may be due to diffusion, obviously various hall effect signals are also at work. Separating the two in such a complex devices is very difficult. Also, devices with 1000Å and 500 Å YBCO layers similar signal sizes but different curves. Therefore it is hard to make a distance dependent fitting to obtain diffusion information. All that can be said, is that a spin diffusion signal can not be ruled out.

A rough upper bound to the spin diffusion distance in YBCO was made. By naively assuming that the signal found in the devices is strictly a product of the spin diffusion signal, a spin diffusion distance  $\approx 0.1 \mu\text{m}$  was found at 100K. In any case these at least places an upper bound on the spin diffusion distance. Previous theoretical estimates fall within this value. Therefore, the possible in-plane detection of spin signal in YBCO can not be deterred.

In the future, now that good Au/YBCO contact can be made, a new injection device in which the top Au pad is separated from the injection region in such a way as to reduce any hall signals could be produced. This combined with better understanding of the angular applied field effects in  $(\text{LSMO}/\text{YBCO})_x$  structures may allow a precise isolation of the spin diffusion signal.

The results of the suppression of critical current of YBCO by spin injection have not yielded any distinct characteristics which largely separate them from normal quasiparticle injection. Also, gains are found to be rather small, especially above 77K. This combined with the fact that submicron YBCO device fabrication is exceedingly difficult seem to indicate the no technologically applicable 3 terminal YBCO device is viable in the near future. These

result are echoed in a quasiparticle study on similar Au/STO/YBCO devices conducted by Schneider et al. [Schneider 1999]. However, since there does not appear any large long range suppression effects, it would seem very plausible that YBCO could be used in future complex low temperature CMR magnetic devices. There are also still a rather wide range of untested ferromagnets and insulators which could be used to conduct this experiment. It could be that a complex interaction between YBCO, STO, and LSMO interfaces which is not yet understood, may be hampering the injection of the spin current.

In any case I believe a better theoretical and experimental understanding of YBCO/I and YBCO/F surface structure is required. Simple S-I-F models usually do not take into account complex surface interactions which can make them difficult to realize experimentally. Perhaps a better model would involve S/ $\delta$ /I/ $\delta$ /F type structures. Of course, future magnetic materials or growth techniques may provide better devices. Also, theoretical work may shed new light on fundamental YBCO superconducting mechanism. Most importantly it should be noted that the hope for a technologically applicable three terminal superconducting device does not end with YBCO. Recently discovered superconductor MgB<sub>2</sub> has a  $T_C(0)$  of around 40K making it a feasible candidate for such devices. To date, no spin injection effects have been investigated with MgB<sub>2</sub>.

## Appendix A

# Determination of Maximum Beam Current and Beam Stabilization for the ion mill.

---

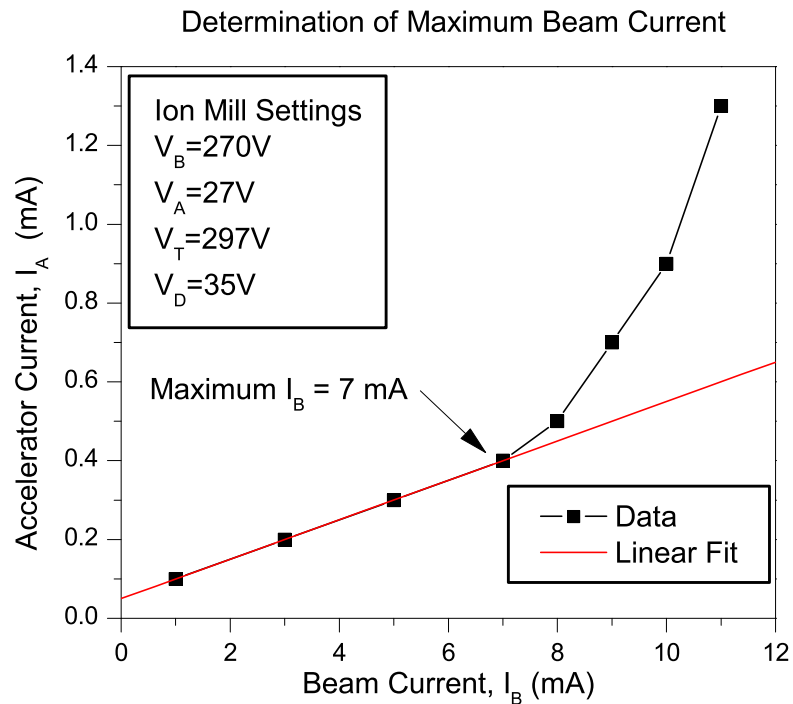


**Figure A.1:** The accelerator current is plotted as function of the beam current for the ion mill. The beam voltage ( $V_B$ ) is 270V, accelerator voltage ( $V_A$ ) 27 volts, the total voltage ( $V_T = V_B + V_A$ ) 297 volts, and the discharge voltage ( $V_D$ ) 35V. The accelerator current deviates from a linear relationship with the beam current at the maximum beam current. Readings above this current are not precise due to electron back streaming. Maximum beam currents were given in the ion mill manual (as a function of total voltage) and were found to be similar to those measured in our lab. A good explanation of broad beam ion sources is given in [Kaufman 1989]

Beam current shown as a function of time after initial startup.

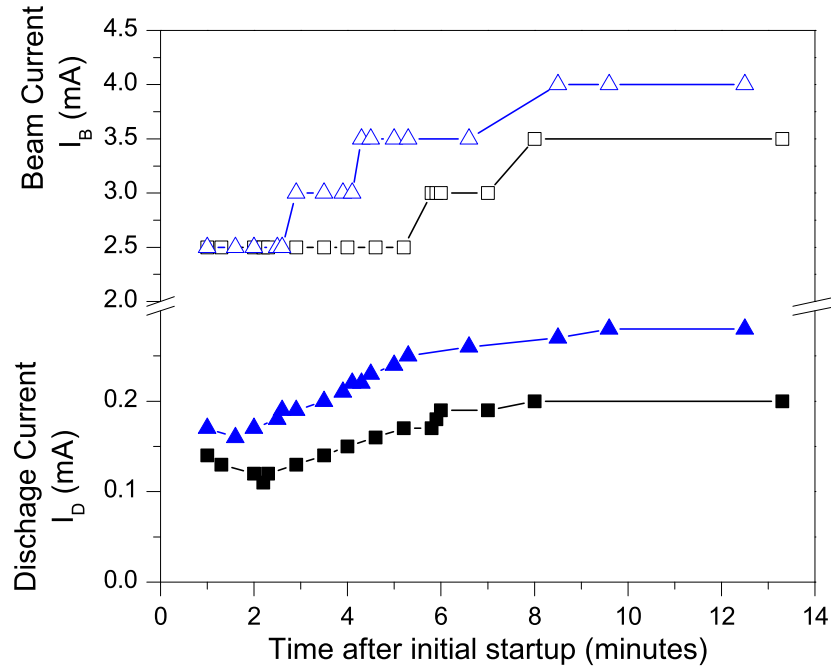


**Figure A.2:** Beam current shown as a function of time after initial startup. Two different sets of data are shown. Discharge current and beam current are shown for each set.

The ion mill also requires some time to achieve a stable equilibrium after it's initial start up. I believe this has to do with the temperature of the mill reaching an equilibrium value. A graph of beam current vs. time shows approximately 8 minutes of operating time is necessary to achieve a stable beam. This only needs to be considered when a high level of accuracy is required. In most cases, a 1 minute warm up time is sufficient to stabilize all other parameters, and beam current deviation is usually less than 20% in the time that follows.

The beam current and the discharge current are shown as a function of time. The ion mill settings for this data are, beam voltage ( $V_B$ ) 300 volts, accelerator voltage ( $V_A$ ) 30 volts, discharge voltage ( $V_D$ ) 35 volts, and beam current ( $I_B$ ) 3.5 mA. The neutralization current ( $I_N$ ) is set automatically by the power source (TBN mode). Notice although the beam current is set to 3.5mA the power source sometimes finds a stable equilibrium slightly above or below the desired setting. Often the desired setting can be reached by turning off the mill, for a few seconds and then turning it back on again. Also, a correspondence between discharge current and beam current is clearly seen. Times may differ for higher beam voltages and currents. Most milling done in this thesis was at the parameters mentioned above.

**Appendix B**

**Magnetic Field vs. Current for GMW model 5403**

**Electromagnet**

---

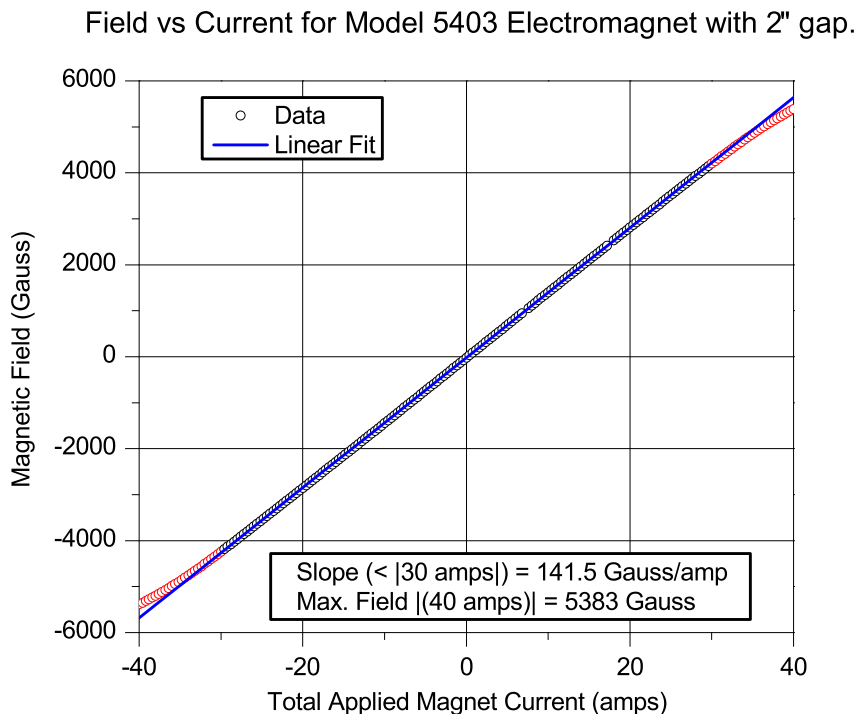


**Figure B.1:** This magnetic field measurement was made with a gaussmeter. The hall probe was inserted directly into the cryostat. This data then gives the field present with the cryostat in place. There was a 2 inch gap between the poles of the magnet. The magnet poles were 76mm in diameter with circular faces.

Note there is some non-linearity above 30 Amps. For an applied current below |30 Amps| a slope of 141.5 Gauss/amp can be used to calculate the field. Fields (H) created by current above |30 Amps| can be approximated by with the linear equation,  $H = 119(I) \pm 652$ , where I is the total applied magnet current (+ for positive current, - for negative current). The maximum achievable field was 5383 Gauss at |40 Amps|.

Also, note the current ranges from 40 to -40 Amps. However, the power supplies only range from 20 to -20. 40 Amps is achieved by the two power supplies working in series. Only one power supply is programmable from the computer via the GPIB line. The other supply acts as a slave to the programmable supply. Therefore if a current of 20 Amps is programmed, both supplies provide 20 Amps, yielding a total current of 40 Amps. See section 2.9 for more details on the magnet system.

## Appendix C

### **YBa<sub>2</sub>Cu<sub>3</sub>O<sub>7</sub> (YBCO) PLD parameters**

---

Deposition Parameters for $\text{YBa}_2\text{Cu}_3\text{O}_7$	
Temperature	805°C
Pressure	100 mTorr
Oxygen flow	100 sccm
Set Laser Energy	700 mJ
Aperture area	$\approx 15 \times 8\text{mm}$ (sml)
Energy inside chamber (after aperture and window)	150 mJ
Focused Beam area	$0.11\text{cm}^2$
Energy density	$1.35 \text{ J/cm}^2$
Laser pulse frequency	4 Hz
Heater/Target distance	8 cm
Pre-ablation time	1 minute
Cooling	60°C/minute to 450°C Annealed 30 minutes at 450°C 15°C/minute to room temp.
Cooling Pressure	600 Torr
Deposition rate	$0.89\text{Å/pulse}$

**Table C.1:** Optimal parameters for pulsed laser deposition of  $\text{YBa}_2\text{Cu}_3\text{O}_7$  are shown.

## Appendix D

### **La<sub>0.67</sub>Sr<sub>0.33</sub>MnO<sub>3</sub> (LSMO) PLD Parameters**

---

Deposition parameters for $\text{La}_{0.67}\text{Sr}_{0.33}\text{MnO}_3$	
Temperature	805°C
Pressure	200 mTorr
Oxygen flow	100 sccm
Set Laser Energy	900 mJ
Aperture area	$\approx 18 \times 8.5$ mm (sml)
Energy inside chamber (after aperture and window)	230 mJ
Focused Beam area	0.14 cm <sup>2</sup>
Energy density	1.6 J/cm <sup>2</sup>
Laser pulse frequency	4 Hz
Heater - Target distance	8 cm
Pre-ablation time	1 minute
Cooling	60°C/minute to Room Temp.
Cooling Pressure	600 Torr
Deposition rate	0.64Å/pulse

**Table D.1:** Optimal parameters for pulsed laser deposition of  $\text{La}_{0.67}\text{Sr}_{0.33}\text{MnO}_3$  are shown.

## Appendix E

### LaNiO<sub>3</sub> (LNO) PLD Parameters

---

Deposition parameters for LaNiO <sub>3</sub>	
Temperature	805°C
Pressure	100 mTorr
Oxygen flow	100 sccm
Set Laser Energy	900 mJ
Aperture area	≈ 15 x 8 mm (sml)
Energy inside chamber (after aperture and window)	180 mJ
Focused Beam area	0.11 cm <sup>2</sup>
Energy density	1.6 J/cm <sup>2</sup>
Laser pulse frequency	4 Hz
Heater - Target distance	8 cm
Pre-ablation time	1 minute
Cooling	60°C/minute to Room Temp.
Cooling Pressure	600 Torr
Deposition rate	0.53Å/pulse

**Table E.1:** Optimal parameters for pulsed laser deposition of LaNiO<sub>3</sub> are shown.

## Appendix F

### SrTiO<sub>3</sub> (STO) PLD Parameters

---

Deposition parameters for SrTiO <sub>3</sub> (single crystal target)	
Temperature	700°C
Pressure	150 mTorr
Oxygen flow	100 sccm
Set Laser Energy	700 mJ
Aperture area	≈ 15 x 8 mm (sml)
Energy inside chamber (after aperture and window)	150 mJ
Focused Beam area	0.11 cm <sup>2</sup>
Energy density	1.35 J/cm <sup>2</sup>
Laser pulse frequency	1 Hz
Heater - Target distance	8 cm
Pre-ablation time	1 minute
Cooling (for thin barriers)	60°C/minute to 450°C Anneal at 450°C, 6 hours, 600 Torr 15°C/minute to Room Temp.
Cooling Pressure	600 Torr
Deposition rate	1.0Å/pulse

**Table F.1:** Optimal parameters for pulsed laser deposition of SrTiO<sub>3</sub> (single crystal target) are shown.

## Appendix G

### Notes on the Excimer Laser

---

#### G.0.6 General Notes

Always wear appropriate eye protection when operating the laser. Goggles should be specifically designed to block the 348nm light emitted from the laser. CO<sub>2</sub> laser goggles can be used, are readily available from commercial suppliers.

\* The cooling water valves should never be opened all the way. This provides too much pressure and the tubes inside the laser may leak. Turn the valve to about 1/3 to 1/2 of the full position. This provides sufficient cooling. Also, be wary of condensation during the summer months. The temperature of the water should always be below 60° while the water is running. If it rises above this value, either the water pump has turned off or the chiller has shut off. The pump is located in the basement of the building, and the chiller is located on the roof. The water filter, in the lab, should be changed at least every two months. The filters can be purchased from the company listed on the filter apparatus.

There is a fan on the roof of the building that is attached to the exhaust of the laser and the gas cylinder cabinet. There is an interlock in the laser connected to the fan. If the fan stops running, so does the laser. A quick way to check whether the fan is running or not is to place a piece of paper over one of the air inlets on the front of the laser. The suction should be enough to hold it in place. The fan is always running whether the laser is running or not. There is also a circuit breaker for the fan located in the main breaker

box in the lab.

The computer control software can get confused. Sometimes this causes the laser to stop functioning. This can be fixed by simply restarting the computer. If the laser doesn't seem to respond to the computer's commands, this is the first thing to try. There is a copy of the software that runs the laser in the lab. It can be obtained from Lamda Physik if necessary. If a 'Low Light' status is displayed, press 'c' to return to the main menu.

The laser has two gas refill modes, PGR and NGR. The current setting can be located on the gas menu. If the laser is run in constant energy mode and requires a voltage of 21.5kV or higher to attain the set energy level, and the gas refill mode is set to PGR, the laser will automatically try to refill the laser gas. This is bad. This may allow contamination to enter the laser tube since the laser gas tank is closed when not in use. The laser is always set to NGR mode, in which no attempt is ever made the software to refill the gas without user intervention. But, every once in a while, for some reason, the software has been known to change the mode by itself. These problems can be avoided by running the laser in constant voltage mode. The laser will not try to automatically fill new gas when constant voltage mode is used, regardless of the refill mode setting. In any case, it is a good idea to check the refill mode on occasion.

The cables from the computer to the laser are fiber optic cables. The trigger signal from the computer is actually a small flashing light. When the computer is triggering the laser, this light can be seen emanating from the fiber optic port marked "Trigg." on the computer card when the fiber optic cable is removed. Also, the fiber optic cable can be removed from the port marked "Trigger In" on the back of the laser, and the laser can be triggered by flashing a flashlight in the fiber optic port. The triggering light can also be faintly seen emanating from the fiber optic cable at this point. These are all good ways to make sure the computer and the cables are functioning correctly. The laser can be triggered with an external TTL source by connecting it to the coaxial "Ext. Trig." port on the computer,

and selecting "EXT" as the triggering mode. "Burst mode", located under options, can be used in conjunction with external triggering to yield pockets of a specified number of pulses with time breaks in between.

If the laser stops running, there are fuses on the back of the laser which can also be checked. Make sure the power to the laser is off before checking. Also, there is a circuit breaker for the laser in the main lab breaker box.

There is a beam splitter in the back of the laser which directs light into the laser's energy meter. The back panel must be removed to get at it. Always turn off the laser when working inside. There are very high voltages at work, which can still be present long after the laser is shut down! The beam splitter can be removed with a hex wrench. If the laser's energy reading seems to be falling sharply from calibration to calibration, the splitter may need to be cleaned. Use acetone, isopropanol, and lens paper to clean it. Be careful, there is currently no replacement beam splitter in the lab.

The laser's thyatron was replaced in the summer of 2002. The thyatron is just a high energy switch capable of handling up to tens of kilovolts. If the laser over triggers (sometimes triggers faster than the programmed frequency) or under triggers (misses pulses) the thyatron heater voltage may need adjustment. The controls are located on the front right side of the laser. The front right side panel must be removed to get at it. Contact the Lambda Physik technicians for information on how to measure and adjust the thyatron voltages to prevent over and under triggering.

If the thyatron is considered to have gone bad, it is best to borrow a thyatron from another laser, install it, and make sure, as they are rather expensive. Always turn off the laser when working on the thyatron. There are very high voltages at work, which can still be present long after the laser is shut down! The thyatron is located on the right side of the laser. There is an interlock between the right panel and the laser. When this panel is open the laser will not operate. When the right panel is removed a removable long plastic

rod with a metal tip and an attached ground strap can be seen. This is to ground the high energy electronics of the laser before working. The tip of the rod is to be placed in the port marked ground. BE EXTREMELY CAREFUL WHEN GROUNDING THE LASER! High voltages can linger for long periods of time in the laser.

The premixed laser gas is connected to the buffer gas inlet on the laser. The Laser gas has fluorine in it which is corrosive. Keep this in mind when changing tanks or working on the gas flow system.

### G.0.7 New Gas Fill Procedure

This procedure should be followed step by step. Do not skip steps!

⇒ Gas fume hood steps and others are not indented and have a "⇒" symbol.

\* Computer steps are indented and have a "\*" symbol.

⇒ Turn on the laser power. Do not turn on the cooling water. Let the laser stay this way for one hour. (This step allows the laser tube to warm slightly. More contaminated gas will be removed this way. This technique provides much more consistent energy results. DO NOT FIRE THE LASER DURING THIS TIME AND MAKE SURE NO ONE ELSE DOES!

⇒ Make note of number of counts.

⇒ **C**lose valve from helium (Inert) line to mix (Buffer) line.

\* Open **G**as menu.

\* Open **G**asflow menu.

\* Turn on **P**ump.

\* Wait 20 seconds.

\* Open **V**acuum valve.

\* Open **B**Uffer valve 3 times. (It closes automatically.)

- \* Close **V**acuum valve.
  - \* Turn off **P**ump.
  - \* **Q**uit Gasflow menu.
- ⇒ Open mixed gas cylinder valve.
- ⇒ Make note of mixed gas pressure. (Before:)
- \*Select **N**ew Fill.
- ⇒ Wait for gas to evacuate laser and new gas to fill. When new fill is complete,
- ⇒ make note of mixed gas pressure. (After:)
- ⇒ Close mixed gas cylinder valve.
- ⇒ Open vent valve.
- ⇒ Close vent valve.
- \* Open **G**asflow menu.
  - \* Turn on **P**ump.
  - \* Wait 20 seconds.
  - \* Open **V**acuum valve.
  - \* Open **B**Uffer valve.
  - \* Wait for valve to automatically close.
- ⇒ Open valve from helium (Inert) line to mix (Buffer) line.
- ⇒ Close valve from helium (Inert) line to mix (Buffer) line.
- \* Open **B**Uffer valve.
  - \* Wait for valve to automatically close.
- ⇒ Open valve from helium (Inert) line to mix (Buffer) line.
- ⇒ Close valve from helium (Inert) line to mix (Buffer) line.
- \* Open **B**Uffer valve.
  - \* Wait for valve to automatically close.
- ⇒ Open valve from helium (Inert) line to mix (Buffer) line. (**Leave open!**)

- \* Close **V**acuum valve.
  - \* Turn off **P**ump.
  - \* Open **I**ert valve.
  - \* Wait for Inert valve to automatically close.
- ↳ \*Turn on the cooling water and wait 20 minutes.
- ↳ Calibrate laser energy reading using a value of 1100mJ with external Molelectron meter reading of 1100mJ (1Hz).
- ↳ Finished

## Appendix H

### PLD Multi-Target Rotation System

---

A PLD multi-target rotation system was designed to fit through an 8" port. It can hold up to four targets. All pieces were made of 316 stainless steel when available, else 304 stainless steel was used. In hind sight it may have been possible to use thinner steel plates and support rods in the design. The constructed design is a little heavy, but works very well.

Note a special feature of the design is the ability to completely remove the target carousel from the from the rest of the apparatus by simply removing the target shield and one set screw collar. This allows positioning and changing of targets to take place external to the chamber.

A peripheral instrument was proposed, in which the target carousel could me mounted upsidedown on a shaft. The four targets could then be simply lowered onto set levels, providing an instant and simple way of ensuring the targets are all at the same height.

Other target rotation system designs are available in [Xu 1998, Clark 1996, Jackson 1995, Campion 1996].

Presented here are the drawings of custom made parts, a list of purchased parts, and an overall schematic of the system.

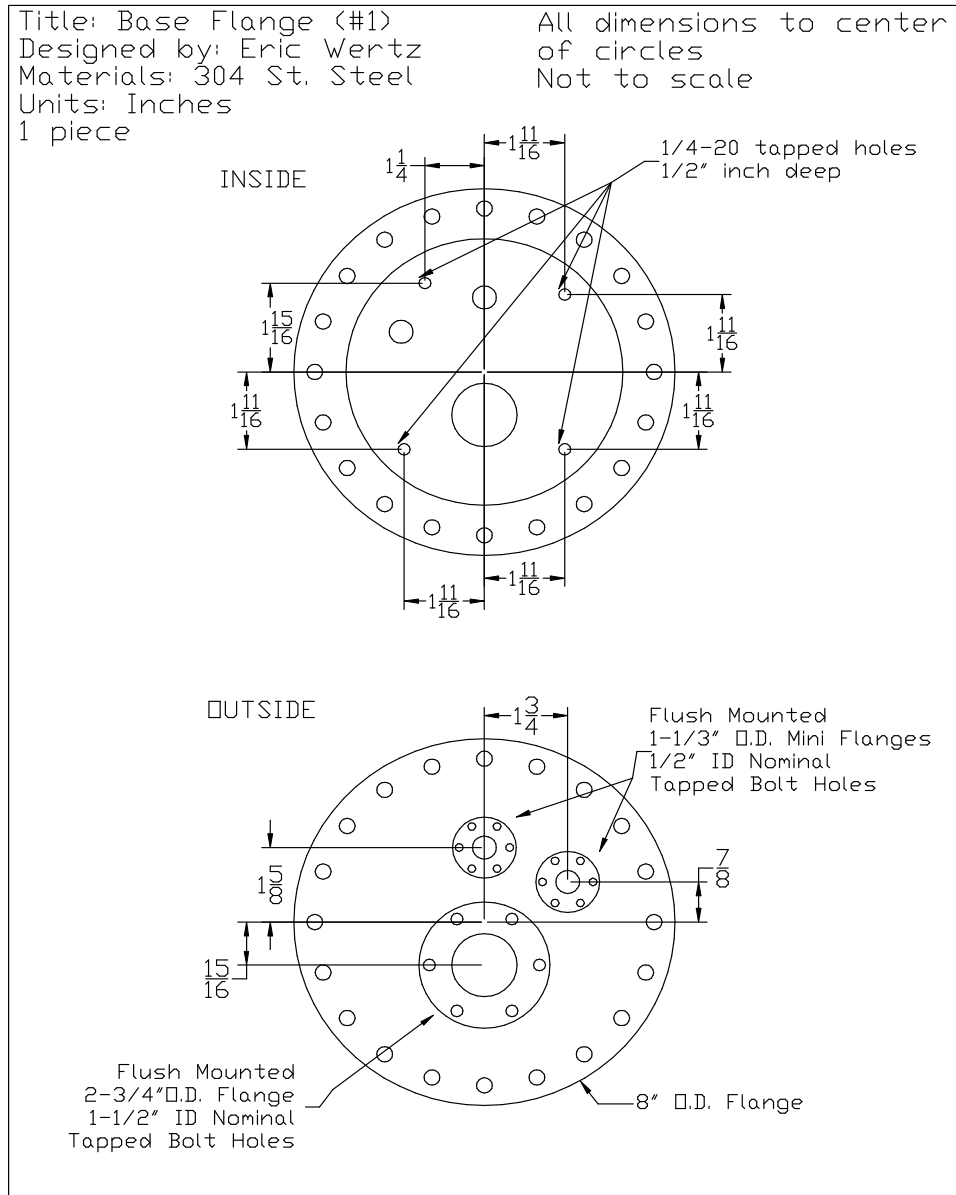


Figure H.1: 8" CF flange base plate

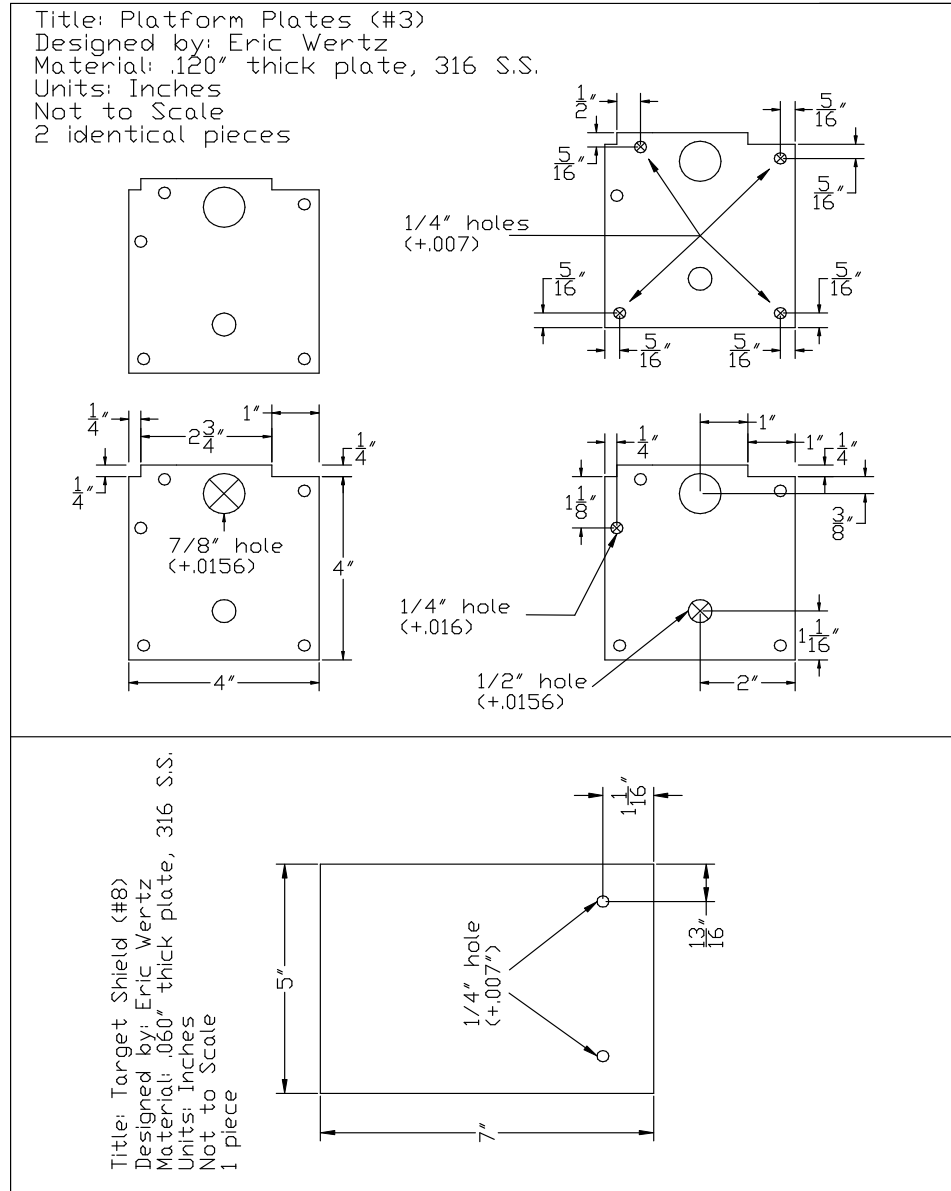
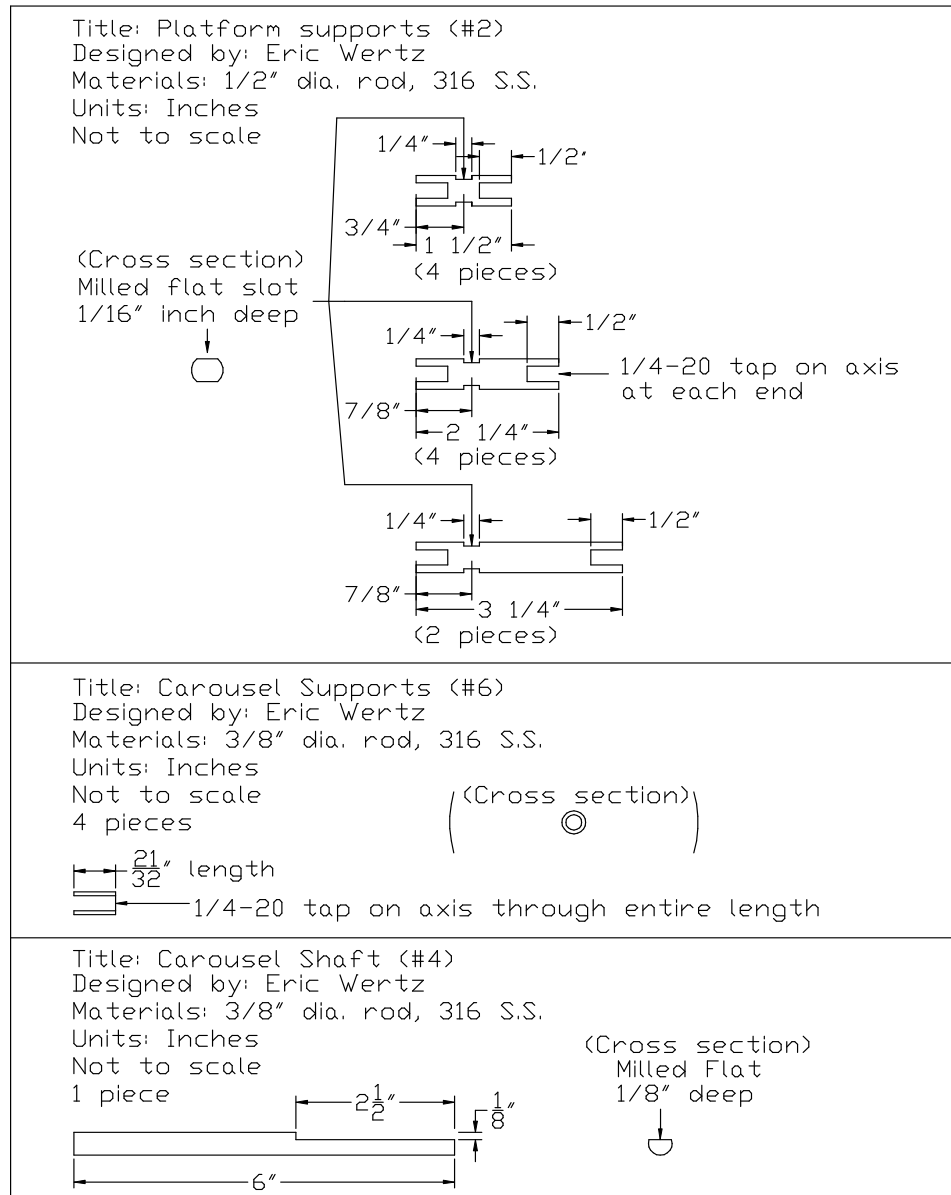
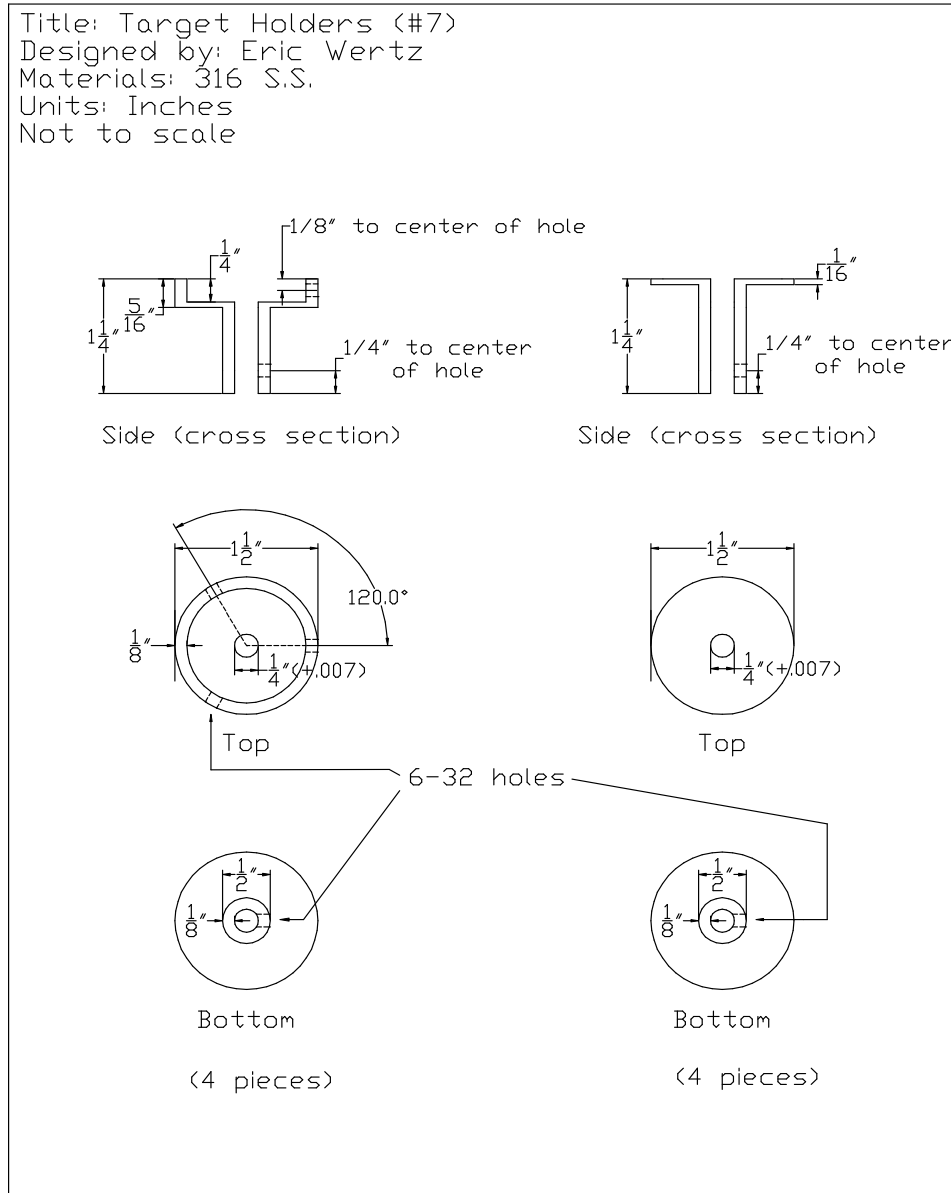


Figure H.2: Middle platform plates and shield



**Figure H.3:** Middle platform supports, carousel supports, and carousel rotation shaft



**Figure H.4:** Target holders. Screw clamp for thick targets and glue held for thin.

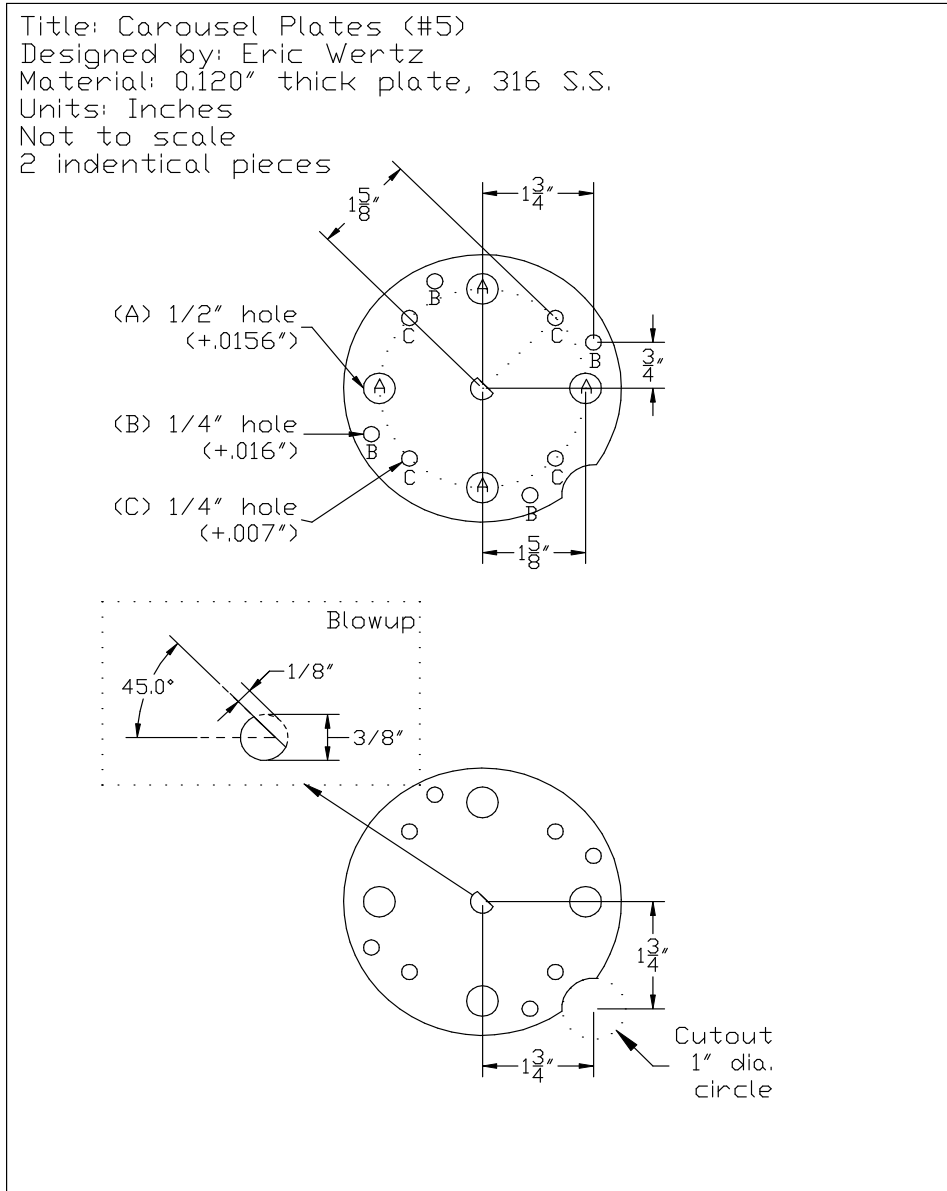
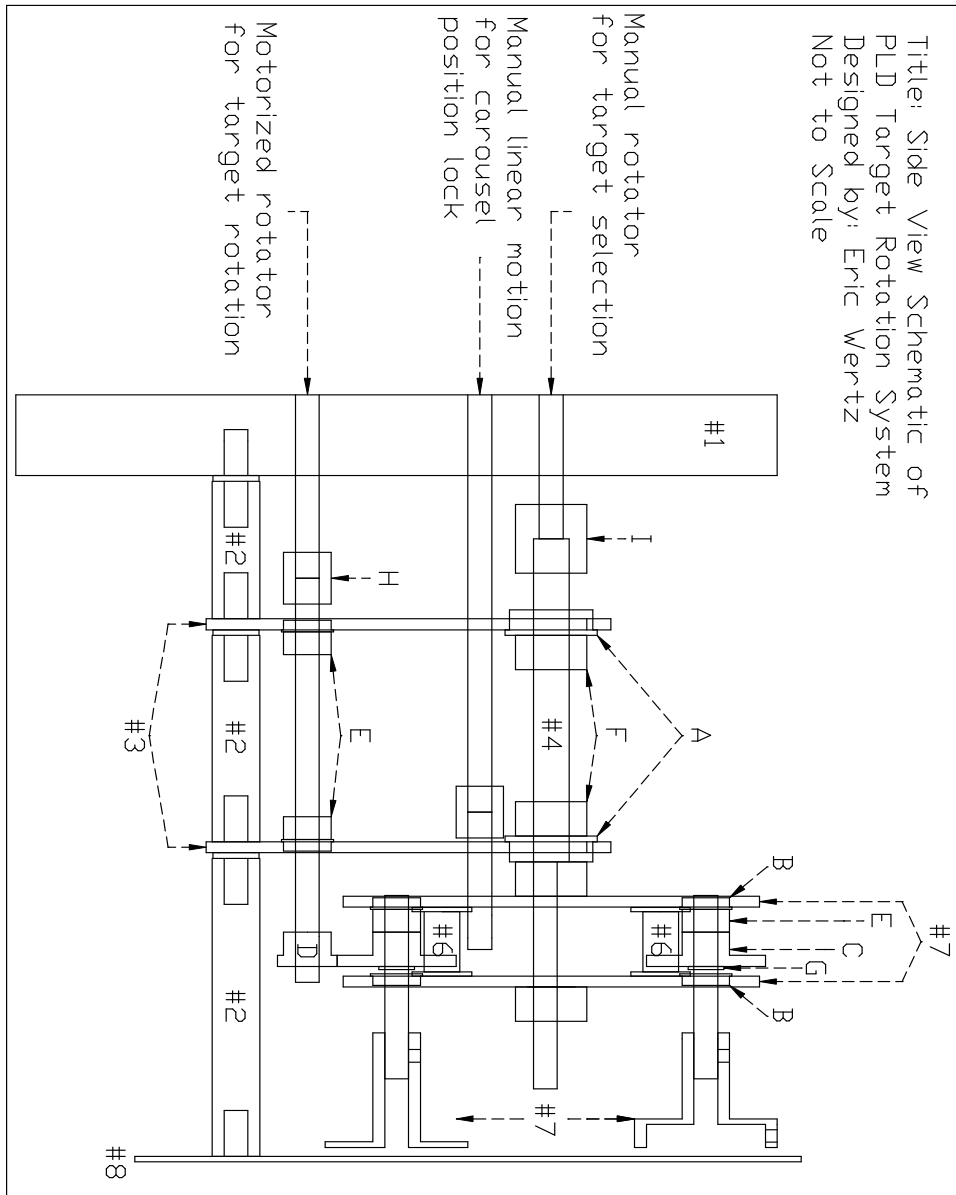
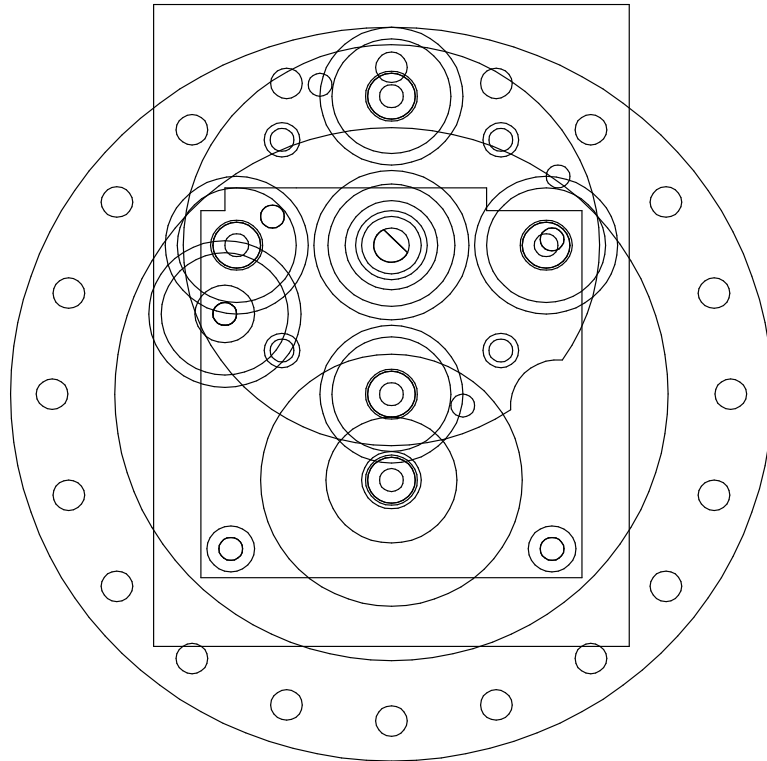


Figure H.5: Carousel plates



**Figure H.6:** Side view of PLD target rotation system

Title: Top View Schematic of  
PLD Target Rotation System  
Designed by: Eric Wertz  
Not to Scale



**Figure H.7:** Top view of PLD target rotation system

Items ordered from W. M. Berg, Inc.			
Description	Part #	Qty	Schematic Letter
Flanged Radial Ball Bearings	B2-11	12	A
Flanged Radial Ball Bearings	B2-8	2	B
Precision Spur Gear	P48S26-60	4	C
Precision Spur Gear	P48S26-30	1	D
Set Screw Collar Clamp	CS-7	8	E
Set Screw Collar Clamp	CS-9	6	F
Solid Shim Spacer	SS2-31	10	G
Sleeve Coupling	CT-3	4	H
Sleeve Coupling	CT-19	2	I
All items made of 316 Stainless Steel except			
*Ball Bearings which were made of 304 Stainless steel.			

**Table H.1:** Table of parts purchased for target rotator system. All screws, washers, and raw materials were 316 stainless steel and were purchased from McMaster-Carr.

## Appendix I

### Substrate Heater

---

A full description of the substrate heater is presented in section 2.1. Another design is available in Kumar *et al.* [Kumar 1993]



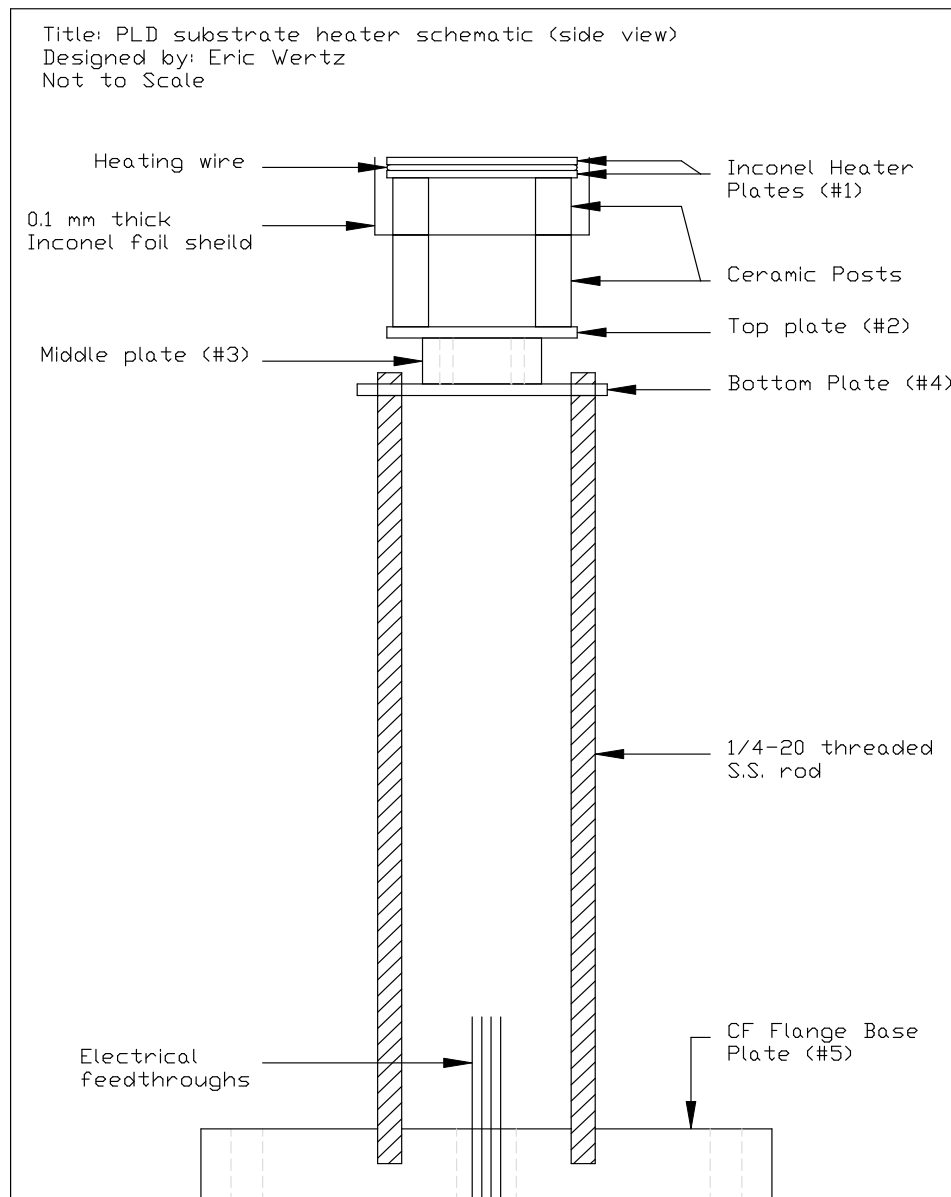


**Figure I.2:** PDL heater schematic (side view)

## Appendix J

# Photolithographic Processing

---

For most applications Shipley Microposit S1811 photoresist was used. 1827 was available from the EMPRL facility. To make 1811 the 1827 had to be mixed with Shipley type-N thinner in a 1827 to thinner ratio of 5:2 respectively. All photoresist and thinner was purchased from Microposit.

Samples were first blown off with a nitrogen gun to remove any particles from the surface.

1811 was then applied and spun at 4000 rpm for 40 seconds to obtain a  $1.1\mu\text{m}$  thick layer of photoresist. It was possible to spin samples as small as 3 x 4 mm and retain a 1 x 2 mm patternable area. (Small samples always have a thick photoresist region at the edge of the sample roughly 0.5 mm in width in which no pattern can be made. Another technique for spinning very small samples is to use 1811 to glue the small sample to the edge of a larger Si substrate. The sample can then be spun in the usual way.)

The sample was then baked at  $100^{\circ}\text{C}$  for 60 seconds and afterwards placed on a room temperature cooling block for 1 minute.

The sample was then aligned to the desired mask pattern. Care should be taken when bringing the sample in contact with the mask. Small samples have a tendency to stick if pressed too hard. Also, since the area of the sample is small, a large amount of force can be applied to a point on the mask which can end up cracking or shattering the mask.

The sample was then exposed for 0.55 minutes using channel 1 of the UV source power

supply in the EMPRL. For samples in which a majority of the top surface was covered in gold an exposure time of 0.6 minutes was used. MgB<sub>2</sub> samples required 1.2 ~ 1.5 minutes of exposure. Sometimes the UV bulb in the aligner is changed. Exposure times may vary slightly due to an old or new bulb.

Samples were then developed in diluted Shipley 351 developer. 351 developer is primarily sodium hydroxide. The ratio of water to 351 was 5:1 respectively. Samples were developed for 45 seconds. (For water sensitive samples (MgB<sub>2</sub>) 10 seconds with agitation would suffice.) Samples were then placed in a distilled water bath for 1 minute and finally blown dry with nitrogen.

Samples could be post baked for 1 minute to provide a more durable photoresist layer, but this was found to rarely be necessary.

## Appendix K

### Labview Programs

---

Several data acquisition programs were written in the Labview graphical language. The follow is an explanation of some of the special functions of several of these programs. Many different programs exist which record the same measurement, but through the use of different equipment. The most common set of equipment interfaced in this study was the Keithley 2400 sourcemeter (2400), the Keitley 2182 nanovoltmeter (2182), the Lakeshore 340 temperature controller (340), the Lakeshore 330 temperature controller (330), the EG&G 7260 DSP lock-in amplifier (lock-in), and the Kepco BOP 20-20M-4882 power supply (kepco). The programs described here used this equipment unless otherwise noted.

#### **K.0.8 Resistance vs. Temperature Program**

The resistance vs. temperature (R vs T) program described here is in reference to the program Resis\_vs\_Temp\_wertz\_01.vi located in the VI library Resis\_vs\_Temp\_wertz\_01.llb. However, many similar features are present in other programs.

The RvsT program uses a 2400 sourcemeter to apply a current, a 2182 nanovoltmeter to measure the created voltage, and either the 340 or 330 temperature controller to measure the corresponding temperature. The applied time of the current, delay of the voltage measurement after the application of the current, and the time between successive measurements is controlled. For a detailed analysis of the measurement timing and technique see

section 2.10 and figure 2.12.

Here is a list of buttons and their functions in the RvsT program.

**Sample Name** - Creates a default sample name for dialog after *save data* is selected

**2400 Current (Amp)** - Measurement current in use. May be changed at any time while program is running. Negative currents may also be used.

**Pos/Zero or Pos/Neg** - For Pos/Zero, voltage at positive current,  $V_+ = V(+I)$ , and voltage at zero current,  $V_0 = V(I = 0)$ , are used to calculate the resistance,  $R = (V_+ - V_0)/(+I)$ . For Pos/Neg,  $V_+ = V(+I)$  and  $V_- = V(-I)$  measurements are used to calculate the resistance,  $R = (V_+ - V_-)/(+I - (-I))$ .

**Time between current flip (msec)** - Time between each measurement in milliseconds.

If the value is set too low there can be errors created. It just takes time for the equipment to receive and process commands.

**Lakeshore 340 / 330** - Selects desired temperature controller.

**Push this button to change, 2400, 2182 ...** - Changes listed parameters when pushed.

Note, the listed parameters are set to the values displayed at the program startup, but do not automatically update. This button must be pushed to change the parameters.

**2182 Volt Range (volt)** - Enter the value of your estimated maximum voltage reading here and the 2182 will automatically pick the appropriate voltage range.

**2400 Comp Volt (volt)** - Sets the 2400 compliance voltage in Volts.

**2400 Dwell Time (msec)** - Sets the 2400 Dwell time in milliseconds.\*

**2182 Delay time (msec)** - Sets the 2182 delay time in milliseconds.\*

**Address Controls** - Set GPIB addresses for equipment in use.

**Stop and Save data** - Stops the measurement and saves the data.

**Stop Do Not Save** - Stops measurement. Does not save the data. Puts all equipment into a default state.

All other displays are indicators and do not control the data output. Graph viewing controls are located in the graph palette.

### **K.0.9 Resistance vs. Magnetic Field Program**

Several of the controls in the Resistance vs. Magnetic Field program (R vs. H), `Resis_vs_Mag_wertz_01.vi` located in the VI library `Resis_vs_Mag_wertz_01.llb.`, are the same as those given in the R vs. T program section (K.0.8) above. Only those controls which differ from the R vs. T program will be discussed here.

This program uses the 2400, 2182, Lakeshore 340, and the Kepco power supply, in conjunction with the GMW magnet / Janus cryostat system. For details on the magnet see appendix B.

For a detailed analysis of the measurement timing and technique see section 2.10 and figure 2.12.

Here is a list of buttons and their functions in the R vs. H program.

**File Path** - Path to the file in which the sample will be saved. The program still prompts for a saving location. But, this can save time if several measurements on the same sample are preformed.

**Run#** - Gets appended to the filename.

**Mag Starting Field\*** - The starting magnetic field. The maximum value is  $\approx 5600$  Gauss and the minimum value is  $\approx -5600$  Gauss.

**Mag Field Limit\*** - The magnet field at which the field sweep either stops or changes directions. \*Note: the starting field and the field limit determine the initial sweep direction of the magnetic field. The starting field and the field limit can be changed during a sweep, but should always remain in the same order of least to greatest when changed.

**# of Turns\*** - Specifies the number of times the magnetic field sweep changes directions. The turning points are the starting magnetic field and the magnet field limit.

**Mag Field after finish\*** - The field sweep ends at either the magnet starting current or the magnet current limit depending on the number of turns specified. This control ramps the field from it's final value to the specified value when the program finishes. If the magnetic field current is held at a large value for too long the magnet will become very hot and could be damaged.

**Mag Settle Time (ms)** - Amount of time between the time the magnetic field current is changed and any measurement is performed.

**Temperature (K)** - The program keeps track of the temperature using the 340 Lakeshore temperature controller. If the temperature falls outside of the allowed temperature deviation of the set value the program stops and the temperature light is illuminated.

**Allowed Temperature Dev (K)** - This is the allowed temperature deviation. If the temperature falls outside of the set temperature +/- this value the program stops and the temperature light is illuminated.

**Shutdown Voltage (V)** - If the measured voltage minus the *Voltage Offset* rises above this value the program stops and the volt light is illuminated.

**Offset Voltage (V)** - see the *Shutdown Voltage* definition above.

**2400 Meas Curr (Amps)** - The applied measurement current. This may be changed during measurement, and can be set to negative values.

**Field Step1 (gauss)<\*\*** - Magnetic field step size when the magnetic field is less than the value set in *Field 1 (gauss)*. See *Field to Zero Multiple* also.

**Field Step2 (gauss)<\*\*** - Magnetic field step size when the magnetic field is greater than the value set in *Field 1 (gauss)* less than the value set in *Field 2 (gauss)*.

**Field Step3 (gauss)<\*\*** - Magnetic field step size when the magnetic field is greater than the value set in *Field 2 (gauss)* less than the value set in *Field 3 (gauss)*.

**Field Step3 (gauss)<\*\*** - Magnetic field step size when the magnetic field is greater than the value set in *Field 3 (gauss)*.

**Field 1-4 (gauss)<\*\*** - See field step definitions above.

**Field1 to Zero Multiple<\*\*** - When the field sweep starts, or immediately after it changes directions the field step used between *Field1 (gauss)* and Zero Field is *Field Step1 (gauss)* multiplied by this value. This is useful for hysteresis scans where the interesting part of the curve occurs after zero field.

#### K.0.10 Temperature Control Programs

There are two temperature control programs. One is for use with the Janus cryostat, and one for the temperature control dip probe.

The temperature for the Janus cryostat was controlled with the program

janus\_cryo\_tempcontrol\_340lk.vi

located in the vi library

janus\_cryo\_tempcontrol\_340lk.llb.

There is also a initialization program in the same vi library called

Lakeshore\_340\_janus\_cryostat\_initialize.vi. The initialization program loads the appropriate thermometer curves into the 340, and generally makes the 340 ready to work with the Janus cryostat.

The Janus cryostat has two heaters and two thermometers. The neck heater and thermometer are connected to the 10 pin military style connector on the panel. The neck thermometer connections are A,B,C,D and the heater connections are G,H. The neck thermometer should be connected to input B and the neck heater connected to the heater output on the lakeshore 340. The Heater Output is analogous to loop 1, and Input B to Channel B in the instrument. The initialization program sets Channel B to control loop 1, thereby the neck thermometer reading is used to control the neck heater.

The sample heater and thermometer are connected throughout the 19 pin military style connector on the panel. The sample thermometer connections are B,C,R,P and the heater connections are G,K. The sample thermometer should be connected to input A. The sample heater should be connected to the Lakeshore Analog Output 2 with a special cable that has a 75  $\Omega$  resistor wired in series with it. This ensures the total resistance of the sample heater path is greater than 100  $\Omega$ . See the Lakeshore 340 manual for details. Analog Output 2 is analogous to loop 2, and Input A to Channel A in the instrument. The initialization program sets Channel A to control Loop 2, thereby the sample thermometer reading is used to control the sample heater.

Here is a list of some of the important controls and their functions in the Janus cryostat temperature control program.

**Setpoint A (K)**- Set value of the sample stage. The *Change Setpoint A* button must be pressed to change the value in the instrument.

**Change Setpoint A**- See *Setpoint A (K)* above.

**P,I,D (A)** - Sets the PID values for the sample stage temperature control. Values of

$P = 600, I = 300, \text{ and } D = 0$  should provide sufficient control. The *Change PID (A)* button must be pressed to change the values in the instrument.

**Change PID (A)** - See *P, I, D (A)* above.

**Heater On / Heater Off** - Turns the neck heater on and off. The *Change Heater Setting* button must be pressed to change the value in the instrument.

**Change Heater Setting** - See *Heater On/ Heater Off* above.

**Clear Graphs** - Clears all points from graphs. Program will continue to run.

The controls for the neck temperature control (B) are similar to those for the sample stage (A) shown above. Usually the neck heater should be set to 1K below the sample stage temperature. This allows the stage heater to act as a fine control.

The temperature control program for the dip probe, *Probe\_Tempcontrol\_340lk.vi*, located in the library *Probe\_Tempcontrol\_340lk.llb*, is similar to the program for the Janus cryostat. The controls are the same as those in the Janus cryostat control program. There is also a initialization program, *Lakeshore\_340\_probe\_initialize.vi*, located in the library. The probe only has one heater and thermometer. The probe thermometer should be connected to input A and the probe heater to the heater output on the Lakeshore 340. No special cables are required.

#### **K.0.11 The IV programs**

There are two current-voltage (IV) programs in the library *Crit\_vs\_Inj\_01\_wertz.llb*. The basic VI program is *V\_vs\_I\_01\_wertz.vi*. This program applies a current and measures the created voltage. The current is swept from a starting value until a voltage limit is reached. The program then starts again at the starting current and scans in the opposite direction until the voltage limit is reached again. The program then stops and saves the recorded

data. For a detailed analysis of the measurement timing and technique see section 2.10 and figure 2.12.

Several of the controls in the VI program are the same as those given in the R vs. T program section (K.0.8) above. Only those controls which differ from the R vs. T program will be discussed here. Here is a list of some of the important controls and their functions in the IV program *V\_vs\_I\_01\_wertz.vi*. Note, the values enclosed in the *Set Values* box will not change in the instruments unless the *Set Values* button is pressed.

**Flip voltage** - when the VI program starts, it takes progressive current steps until the absolute value of the measured voltage reaches this value. It then starts again at the *Starting Current or some % of the current at flip* and steps current in the opposite direction. When the absolute value of the measured voltage again reaches this value the program stops and saves the recorded data.

**Emergency Volt.** - If the absolute value of the measured voltage exceeds this value the program immediately stops.

**Cont. Avg.** - this box displays a running average of the measured voltage from the time the red button is pushed until it is pushed again.

**Starting Current** - This is the current the IV scan starts at.

**Current Increment** - This is the step size of the current in the IV scan if *Auto Measure* button is set to off. This value can be changed at any time and can also be set to negative values.

\* **Injection Current** - A second 2400 sourcemeter can be used to provide this current at the same time as the measurement current. The *\*Inj 2400 is on/off* button must be in the on position. The value of the injection current does not change during the measurement. This is useful for spin injection experiments.

**% of flip curr. to sub. from strt curr** - The current applied when the measured voltage first reaches the *Flip Voltage* setting is multiplied by this number and added to the *Starting Current* to create the current at which the program starts the second half of the IV scan. This can save time with symmetric IV curves. Especially critical current measurements.

**Set Values** - This button must be pressed to change any of the values in the box in which it is located. The values do not change in the instruments unless this button is pressed.

**Auto Measure** - This button enables the auto measure function. Auto Measure changes the current increment based on the measured voltage.

**Curr Step1 (< Volt 1)** - When *Auto Measure* function is on, this is the current increment used when the absolute value of the measured voltage is < *Volt 1*.

**Curr Step2 (> Volt 1)(< Volt 2)** - When Auto measure is on, this is the current increment used when the absolute value of the measured voltage is > *Volt 1* and < *Volt 2*.

**Curr Step3 (> Volt 2)** - When Auto measure is on, this is the current increment used when the absolute value of the measured voltage is > *Volt 2*.

**Volt 1 (V)** - See *Curr Step1* and *Curr Step2*.

**Volt 2 (V)** - See *Curr Step2* and *Curr Step3*.

**\*2400 Inj is ON/OFF** - This button either enables or disables the 2400 that provides the \* *Injection Current (A)*.

There is a critical current vs. injection current program, *Crit\_vs\_Inj\_01\_wertz.vi*, in the library *Crit\_vs\_Inj\_01\_wertz.llb* that can be used in conjunction with the IV program,

V\_vs\_I\_01\_wertz.vi. This program takes a series of IV measurements each with a different injection current, and plots the results. Note, this program determines what starting measurement current to use (see *2nd Step Mult Const* below) in the VI program unless the *Override start current* button is pushed. The controls are very similar to the VI program. Here is a list of some of the different controls.

**Injection Curr Increment (A)** - size of the injected current steps in the sweep.

**# of steps** - Number of steps in the sweep.

**2nd Step Mult Const.** - This program has the capability to measure any non-symmetric current offset in a measured VI and predict the next starting measurement current to be used in conjunction with the next injection current. However, the first VI curve measured usually has no offset because the injected current is zero and the 2nd step cannot be predicted. Therefore, the starting current for the 2nd step is set to the injection current times this constant.

**override start current** - If this button is pressed the starting measurement value is the value entered in *Override start current (A)*.

**Override first two steps** - if this button is pushed, the program will start at the next injection current value after the value entered in *Injection Current (A)*. If the program is used to predict the starting measurement current, all values in the *Override* box must be completed. The values with the (*Prev*) label are those recorded previous to those without the label. *Pos Curr* and *Neg Curr* are the currents at which the flip voltage was attained.

There are two VI programs similar to those previously described, except they carry a label of 2, (*Crit\_vs\_Inj\_02\_wertz.vi* and *V\_vs\_I\_02\_wertz.vi*). These programs are nearly identical to those described before except a 2nd voltmeter is used to measure a second

voltage. This voltage has no control over the program (Flip voltage, Emergency Voltage, etc.). It is only there to make a voltage measurement.

#### **K.0.12 The dI/dV program**

The dI/dV program, dI\_dV\_wertz\_01.vi, located in the library dI\_dV\_wertz\_01.llb, uses the 7260 Lock-in Amplifier to supply an oscillating current dI and measures the voltage dV. The 2400 sourcemeter provides a constant current (I) sweep under the oscillating dI. The current (I) sweeps from the starting current to the maximum current, then starts over at the starting current and sweeps in the opposite direction until the maximum current level is reached again. The program then finishes and saves the recorded data. The 2182 measures the voltage (V) created by the constant current. Therefore, dI/dV vs. I, dI/dV vs. V, and I vs. V can be measured and plotted simultaneously. However, the current from the 2400 remains on while the 7260 makes its measurements and then proceeds to the next current level in the sweep without reversing or going to zero. Making large changes in current, causes large noise jumps in the lock-in signal that can take a long time to settle. There is no noise cancelation in the 2182 voltage (V) measurement.

The dI/dV program controls are very similar the IV program controls given in the previous section K.0.11. Therefore only the controls unique to the dI/dV program are given here.

Applied Magnetic Field (Amps) - This is just a text control that helps create a file name.

It has no control over the measurement.

Run Number - This is just a text control that helps create a file name. It has no control over the measurement.

Max Current 2400 - Maximum level of the current sweep.

Resistor -The 7260 Lock-In puts out an oscillating voltage signal. I usually put a resistor in series with my sample that was much larger than the resistance of the sample itself. Then dI is determined as the oscillating voltage divided by the Resistor value. The resistance of this in series resistor was entered here so that dI could be calculated in the program.

The lock-in controls are fairly self explanatory. Note, many of the controls work with buttons that must be pushed in order to enter the value into the instruments. For example to change the 2400 compliance voltage (*Comp Volt 2400*), the nearby *Change* button must be pressed to enter the value into the 2400.

## Sputtering conditions for Au and SiO<sub>2</sub>

---

Sputtering conditions at EMPRL	
SiO <sub>2</sub> (Rear gun or Gun #2)	
Argon pressure	3 mTorr
RF power	125 Watts
Distance from gun to sample	4 in.
Deposition rate	50 Å/min.
Au (Front gun or Gun #1)	
Argon pressure	5 mTorr
DC power	50 Watts
Distance from gun to sample	5 in.
Deposition rate	240 Å/min.

**Table L.1:** Sputtering conditions for Au and SiO<sub>2</sub> are shown for the system in the EMPRL. See section 2.7 for more details on sputtering and the apparatus.

Sputtering conditions in our lab.	
Au	
Argon pressure	3 mTorr
Turbo pump rotation speed	450 Hz
DC power	30 Watts
Distance from gun to sample	15 cm.
Deposition rate	
Sample stage parallel to gun surface	163Å/min.
Sample stage at 45° to gun surface	109Å/min.

**Table L.2:** Sputtering conditions for Au are shown for the system in our laboratory. Note the relation between the deposition rate for the parallel stage and the stage at 45° is  $\cos(45) * 163 \approx 109$ . Therefore, deposition rates at other angles can be approximated. See section 2.7 for more details on sputtering and the apparatus.

## Appendix M

### Ion Milling Conditions

---

Ion mill settings		
$V_B = 300\text{V}$ , $V_A = 30\text{V}$ , $V_D = 35\text{V}$ , $I_B = 3.5\text{mA}$		
Material	$\text{\AA}/\text{mA}\cdot\text{min.}$	$\text{\AA}/\text{min}$ (at 3.5mA beam)
YBCO < 700 $\text{\AA}$	34.3	121
YBCO > 700 $\text{\AA}$	39.3	138
LSMO < 400 $\text{\AA}$	19.6	69
LSMO > 400 $\text{\AA}$	29.4	103
Au	$\approx 73.9$	$\approx 259$
STO	$\approx 24.2$	$\approx 85$
LNO	$\approx 33.3$	$\approx 117$
Accurate for total distances < 1500 $\text{\AA}$ .		
$V_B = 100\text{V}$ , $V_A = 200\text{V}$ , $V_D = 35\text{V}$ , $I_B = 5.5\text{mA}$		
Material	$\text{\AA}/\text{mA}\cdot\text{min.}$	$\text{\AA}/\text{min}$ (at 5.5mA beam)
YBCO	$\approx 1.87$	$\approx 10.3$
LSMO	$\approx 1.4$	$\approx 7.7$
Accurate for total distances < 500 $\text{\AA}$ .		

**Table M.1:** Ion milling parameters and rates are shown. The  $V_B = 300\text{V}$  settings were used most frequently. The  $V_B = 100\text{V}$  settings were used for cleaning the surface of a material (see section 2.8.2). Sometimes  $V_B = 500\text{V}$  settings (not shown) were used for obstinate films.

## Appendix N

### Sherlock Holmes

---

"Quite so," he answered, lighting a cigarette, and throwing himself down into an armchair.

"You see, but you do not observe. The distinction is clear. For example, you have frequently seen the steps which lead up from the hall to this room."

"Frequently."

"How often?"

"Well, some hundreds of times."

"Then how many are there?"

"How many? I don't know."

"Quite so! You have not observed. And yet you have seen. That is just my point. Now, I know that there are seventeen steps, because I have both seen and observed."

- Sherlock Holmes speaking with Dr. John H. Watson in *A Scandal in Bohemia*, written by Sir Arthur Conan Doyle in 1891.

The thesis of Eric Wertz has been reviewed and approved\* by the following:

Qi Li

Professor of Physics

Thesis Advisor

Chair of Committee

Jainendra K. Jain

Erwin W. Mueller Professor of Physics

Roy F. Willis

Professor of Physics

Thomas N. Jackson

Professor of Electrical Engineering

Jayanth R. Banavar

Professor of Physics

Head of the Department of Physics

\*Signatures are on file in the Graduate School.

## Bibliography

---

- [Abrikosov 1961] Abrikosov, A.A., and L.P. Gor'kov, 1961, Sov. Phys. JETP **12**, 1243.
- [Argonne National Laboratory Website] Argonne National Laboratory Website
- [Aronov 1976] Aronov, A.G., 1976, JETP Lett. **24** No.1, 32.
- [Anderson 1955] Anderson, P.W., and H. Hasegawa, 1955, Phys. Rev. **100**, 675.
- [Bardeen 1961] Bardeen J., L.N. Cooper, and J.R. Schrieffer, 1961, Phys. Rev. Lett. **6**, 57.
- [Bardeen 1957] Bardeen J. 1957, Phys. Rev. **108**, 1175.
- [Barns 1987] Barns R.L., and R.A. Laudise, 1987, Appl. Phys. Lett. **51**, 1373.
- [Bason 2004] Bason, Y., L. Klein, J.-B. Yau, X. Hong, and C.H. Ahn, 2004, Appl. Phys. Lett. **84**, 2593.
- [Bean 1964] Bean, C.P., 1964, Rev. Mod. Phys. **36**, 31.
- [Bednorz 1986] Bednorz, J.G., and K.A. Müller, 1986, Z. Phys. B **64**, 189.
- [Bendre 1989] Bendre, S. T., V. N. Koinkar, R. D. Vispute, R. Viswanathan, A. M. Dhote, S. M. Chaudhari, S. M. Kanetkar, and S. B. Ogale, 1989, Solid State Commun. **73** (5), 345.
- [Berger 1972] Berger, H.H., 1972, Solid State Electron. **15**, 145.

- [Boguslavskij 1994] Boguslavskij, Y.M., K. Joose, A.G. Sivakov, F.J.G. Roesthuis, G.J. Gerritsma, and H. Rogalla, 1994, *Physica C* **220**, 195.
- Boguslavskij, Y.M., K. Joose, F.J.G. Roesthuis, G.J. Gerritsma, and H. Rogalla, 1994, *Physica B* **194-196**, 85.
- [Börner 1989] Börner, H., M. Wurlitzer, H. -Ch. Semmelhack B. Lippold, R. -M. Böttcher, and M. Krötzsch, 1989, *Phys. Stat. Sol.* **116** (a), 537.
- [Bowen 2003] Bowen, M., M. Bibes, A. Barthélémy, J.-P. Contour, A. Anane, Y. Lemaitre, and A Fert., 2003, *Appl. Phys. Lett.* **52** (2), 233.
- [Campion 1996] Campion, R.P., D.R. Dye, P.J. King, and R.G. Ormson, 1996, *Vacuum* **47** (1), 1.
- [Cava 1990] Cava, R.J., A.W. Hewat, E.A. Hewat, B. Batlogg, M. Marezio, K.M. Rabe, J.J. Krajewski, W.F. Peck Jr., and L.W. Rupp Jr., 1990, *Physica C* **165**, 419.
- [Chahara 1993] Chahara, K., T. Ohno, M. Kasai, and Y. Kozono, 1993, *Appl. Phys. Lett.* **63**, 1990.
- [Chang 1990] Chang, C. C., X. D. Wu, R. Ramesh, X. X. Xi, T. S. Ravi, T. Venkatesan, D. M. Hwang, R. E. Muenchausen, S. Foltyn, and N. S. Nogar, 1990, *Appl. Phys. Lett.* **57** (17), 1814.
- [Chen 1999] Chen, J.C., S.C. Law, L.C. Tung, C.C. Chi, and W. Gaun, 1999, *Phys. Rev. B* **60**17, 12143.
- [Chen 2001] Chen, Z. Y., A. Biwas, I. Zutic, T. Wu., S. B. Ogale, R. L. Greene, and T. Venkatesan, 2001, *Phys. Rev. B* **63**, 212508.
- [Chmaissem 1999] Chmaissem, O., J.D. Jorgensen, S. Short, A. Knizhnik, Y. Eckstein, and H. Shaked 1999, *Nature* **397**, 45.

- [Chrisey 1994] Chrisey, D. B., and G. K. Hubler, *Pulsed Laser Deposition of Thin Films* (Wiley-Interscience, 1994), p.614.
- [Chrisey 1997] Chrisey, D. B., M.S. Osofsky, J.S. Horowitz, R.J. Soulen, B. Woodfield, J. Byers, G.M. Daly, P.C. Dorsey, J.M. Pond, and M. Johnson, 1997, IEEE Trans. App. Suppercond. **7** (2), 2067.
- [Chu 1991] Chu, W.K., J.R. Liu, and Z.H. Zhang, 1991, Nuc. Inst. Meth. Phys. Res. B **59**, 1447.
- [Cox 1992] Cox, A.P., 1992, in *Transition Metal Oxides*, (Oxford University Press, Oxford).
- [Clark 2001] Clark, Anna, 2001, Ph.D. Thesis, The Pennsylvania State University.
- [Clark 1996] Clark, J.H., and R.G. Weston, 1996, Meas. Sci. Technol. **7**, 823.
- [Dagotto 2001] Dagotto, E., T. Hotta, and A. Moreo, 2001, Physics Reports **344**, 1.
- [Dam 1994] Dam, B., J. Rector, M. F. Chang, S. Kars, D. G. de Groot, and R. Griessen, 1994, Appl. Phys. Lett. **65** (12), 1581.
- [Dijkkamp 1987] Dijkkamp, D., T. Venkatesan, X. D. Wu, S. A. Shaheen, N. Jisrawi, Y. H. Min-Lee, W. L. McLean, and M. Croft, 1987, Appl. Phys. Lett. **51** (8), 619.
- [Dong 1997] Dong Z.W., R. Ramesh, T. Venkatesan, M. Johnson, Z.Y. Chen, S.P. Pai, V. Talyansky, R.P. Sharma, R. Shreekala, C.J. Lobb, and R.L. Greene, 1997, Appl. Phys. Lett. **71** (12), 1718.
- [Du 2001] Du, J., S.K.H. Lam, and D.L. Tilbrook 2001, Supercond. Sci. Technol., **14**, 820.
- [Dumont 2003] Dumont, J., M. Moraguès, B. Leridon, J. Lesueur, and J.P. Contour 2003, Eur. Phys. J. B, **35**, 331.

- [Dyer 1990] Dyer, P. E., A. Issa, and P. H. Key, 1990, Appl. Phys. Lett. **57** (2), 186.
- [Dynes 1978] Dynes, R.C., V. Narayanamurti, and J.P. Garno, 1978, Phys. Rev. Lett. **41**, 1509.
- [Ece 1994] Ece, M., E. G. Gonzalez, H. -U. Habermeier, and B. Oral, 1994, J. Appl. Phys. **77** (4), 1646.
- [Eidelloth 1991] Eidelloth, W., and R.L. Sandstrom, 1991, Appl. Phys. Lett. **59** (13), 1632.
- [EMPRL] Electronic Materials and Processing Research Laboratory, *Mastering Photolithography*, (The Pennsylvania State University, Pennsylvania)
- [Fenner 1991] Fenner, D.B., A.M. Viano, D.K. Fork, G. Connell, J.B.Boyce, F.A. Ponce, and J.C. Tramontana, 1991, J. Appl. Phys. **69** (4), 2176.
- [Fert 2001] Fert, A., A. Barthelemy, J.B. Youssef, J.-P. Contour, V. Cros, J.M. De Teresa, A. Hamzic, J.-M. George, G. Faini, J. Grollier, H. Jaffres, H. Le Gall, F. Montaigne, F. Pailloux, and F. Petroff, 2001, Mat. Sci. Eng. **B84**, 1.
- [Fert 1997a] Fert, A., and Lee S.-F., 1997, J. Mag. Magn. Mater. **165**, 115.
- [Fert 1997b] Fert, A., and Lee S.-F., 1997, Phys. Rev. B **53** 10, 6554.
- [Fert 2002] Fert, A., J.-M. George, H. Jaffres, and G. Faini, 2002, J. Phys. D: Appl. Phys. **35**, 2443.
- [Foltyn 1991a] Foltyn, S. R., R. E. Meunchausen, R. C. Dye, X. D. Wu, L. Luo, and D. C. Cooke, 1991, Appl. Phys. Lett. **59** (11), 1374.
- [Foltyn 1991b] Foltyn, S. R., R. C. Dye, K.C. Ott, E. Peterson, K.M. Hubbard, W. Hutchinson, R. E. Meunchausen, R.C. Estler, and X. D. Wu, 1991, Appl. Phys. Lett. **59** (5), 594.

- [Foote 1992] Foote, M. C., B. B. Jone, B.D. Hunt, J. B. Barner, R. P. Vasquez, and L. J. Bajuk, 1992, *Physica C* **201**, 176.
- [Fujishiro 1998] Fujishiro H., M. Ikebe, and Y. Konno, 1998, *J. Phys. Soc. Jpn.* **67** (5), 1799.
- [Fukushima 1995] Fukushima, K., 1995, *Int. J. Mod. Phys. B* **9** (28), 3625.
- [Garcia-Munoz 1992] Garcia-Munoz, J.L, J. Rodriguez-Carvajal, P. Lacorre, and J.B. Torrance, 1992, *Phys. Rev. B* **26**, 1738.
- [George 2003] George, J.-M., A. Fert, and G. Faini, 2003, *Phys. Rev. B* **67**, 012410.
- [Ghigna 1998] Ghigna, P., G. Spinolo, G. Flor, and N. Morgante, 1998, *Phys. Rev. B* **57**, 13426.
- [Gim 2001] Gim, Y., A.W. Kleinsasser, and J.B. Barner, 2001, *J. Appl. Phys.* **90** (8), 4063.
- [Ginzburg 1950] Ginzburg, V.L., L.D. Landau, 1950, *Zh. Eksp. Teor. Fiz.* **20**, 1064.
- [Giovannini 1971] Giovannini, B., 1971, *Phys. Lett.* **36A**, 381.
- [Goldman 2001] Goldman, A.M., P.I. Krauss, K. Nikolaev, V. Vas'ko, A. Bahattacharya, and W. Cooley, 2001, *J. Supercond.* **14** (2), 283.
- [Goerke 1996] Goerke, F., A. Thorns, and U. Merkt, 1996, *Appl. Surf. Sci.* **96-98**, 708.
- [Goerke 1995] Goerke, F. and A. Thorns, 1995, *Physica C* **251**, 247.
- [Gould 2004] Gould, C., C. Rüster, T. Jungwirth, E. Girgis, G.M. Schott, R. Giraud, K. Brunner, G. Schmidt, and L.W. Molenkamp, 2004, *Phys. Rev. Lett.* **93** 11, 117203.
- [Greer 1995] Greer, J.A. and M.D. Tabat 1995, *Jnl. Vac. Sci. Technol. A* **13**(3), 1175.

- [Grigorenko 2003] Grigorenko, A.N., and D.J. Mapps, 2003, *J. Phys. D: Appl. Phys.* **36**, 791.
- [Guo 1999] Guo, X., C. Li, Y. Zhou, and Z. Chen, 1999, *Jnl. Vac. Sci. Technol. A* **17**(3), 917.
- [Haghiri-Gosnet 2003] Haghiri-Gosnet, A.-M., and J.-P. Renard, 2003, *J. Phys. D: Appl. Phys.* **36**, R127.
- [Hedt 1994] Hedt, B. von, W. Lisseck, K. Westerholt, and H. Bach, 1994, *Phys. Rev. B* **49**, 9898.
- [Heinsohn 1997] Heinsohn, J. -K., D. Reimer, A. Richter, K. -O. Subke, and M. Schilling, 1997, *Physica C* **299**, 99.
- [Helmolt 1993] Helmolt, J., J. Wecker, B. Holzapfel, L. Shultz, and K. Samwer, 1993, *Phys. Rev. Lett.* **71**, 2331.
- [Hershfield 1997] Hershfield, S., and H.L. Zhao, 1997, *Phys. Rev. B* **566**, 3296.
- [Hirata 1994] Hirata, A., A. Ando, K. Saiki, and A. Koma, 1994, *Surf. Sci.* **310** (1-3), 89.
- [Huh 1998] Huh, Y., J.-T. Kim, Y. Hwang, Y. Park, Y. So, I.-S. Kim, S.-G Lee, G. Park, Y. K. Park, and J.-C. Park, 1998, *Jpn. J. Appl. Phys.* **37**, 2478.
- [Inam 1988] Inam, A., M. S. Hedges, X. D. Wu, T. Venkatesan, P. England, P. F. Miceli, E. W. Chase, C. C. Chang, J. M. Tarascon, and J. B. Wachtman, 1988, *Appl. Phys. Lett.* **53** (10), 908.
- [Jackson 1994] Jackson, J. T. and S. B. Palmer, 1994, *J. Phys. D Appl. Phys.* **27**, 1581.
- [Jackson 1995] Jackson, J. T., N.J. Appleyard, M.J. Cooper, D.H. Richards, and S. B. Palmer, 1995, *Meas. Sci. Technol.* **6**, 128.

- [Jedema 2001-03] Jedema, F. J., M.S. Nijboer, A.T. Filip, and B.J. van Wees 2003, Phys. Rev. B, **67**, 085319.
- Jedema, F. J., H.B. Heersche, A.T. Filip, J.J. A. Baselmans, and B.J. van Wees 2002, Nature, **416**, 713.
- Jedema, F. J., M.S. Nijboer, A.T. Filip, and B.J. van Wees 2001, Jnl. Superconduct., **15** 1, 27.
- [Jia 1990] Jia, Q.X., and W.A. Anderson, 1990, J. Appl. Phys. **68**, 6336.
- [Jo 2000] Jo, M.-H., N. D. Mathur, N. K. Todd, and M. G. Blamire, 2000, Phys. Rev. B **61**, R14905.
- [Johnson 1985] Johnson, M., and R.H. Silsbee, 1985, Phys. Rev. Lett. **55**, 1790.
- [Johnson 1988a, 1988b, 1988c] Johnson, M., and R.H. Silsbee, 1988, Phys. Rev. B **37**, 5312.
- Johnson, M., and R.H. Silsbee, 1988, Phys. Rev. B **37**, 5326.
- Johnson, M., and R.H. Silsbee, 1988, J. Appl. Phys. **63**, 3934.
- [Johnson 1992] Johnson, M., 1992, Phys. Rev. Lett. **70** 14, 2142.
- [Johnson 1995] Johnson, M., 1995, J. Magn. Magn. Mater. **140-144**, 21.
- [Johnson 2002] Johnson, M., 2002, Nature **416**, 809.
- [Jorgensen 1987] Jorgensen, J. D., M. A. Beno, D. G. Hinks, L. Soderholm, K. J. Volin, R. L. Hitterman, J. D. grace, and I. K. Schuller 1987, Phys. Rev. B **36** (7), 3608.
- [Julliere 1975] Julliere, M., 1975, Phys. Lett. A **54**, 225.
- [Kaufman 1989] Kaufman, H.R., and R.S. Robinson, 1989, in *Handbook of ion beam processing technology: principles, deposition, film modification, and synthesis*, edited by J.J. Cuomo, S.M. Rosnagel, and H.R. Kaufman (Noyes Publications, New Jersey).

- [Kawasaki 1994] Kawasaki, M, K. Takahashi, T. Maeda, R. Tsuchiya, M. Shinohara, O. Ishiyama, T. Yonezawa, M. Yoshimoto, and H. Koinuma, 1994, *Science* **266** (5190), 1540.
- [Kim 1992] Kim, H. S., and H. S. Kwok, 1992, *Appl. Phys. Lett.* **61** (18), 2234.
- [Kingston 1990] Kingston, J.J., F.C. Wellstood, P. Lerch, A.H. Miklich, and J. Clarke, 1990, *Appl. Phys. Lett.* **56** (2), 189.
- [Kinoshita 1994] Kinoshita, K., H. Ishibashi, and T. Kobayashi, 1994, *Jpn. J. Appl. Phys.* **33** (Pt. 2, No. 3B), L 417.
- [Kobayashi 1989] Kobayashi, T., Hashimoto K., Kabasawa U., and Tonouchi M., 1989, *IEEE Trans. Magn.* **MAG-25**, 927.
- [Koller 1998] Koller D., M.S. Osofsky, D.B. Chrisey, J.S. Horwitz, R.J. Soulen, Jr., R. M. Stroud, C.R. Eddy, J. Kim, R.C.Y. Auyeung, J.M. Byers, B.F. Woodfield, G.M. Daly, T.W. Clinton, and M. Johnson. 1998, *J. Appl. Phys.* **83** (11), 6774.
- [Kondo 1962] Kondo, J. 1962, *Prog. Theor. Phys.* **27**, 1466.
- [Kumar 1993] Kumar, V., and A.K. Gupta, 1993, *Meas. Sci. Technol.* **4**, 790.
- [Kumuduni 1995] Kumuduni, W. K. A., Y. Nakata, Y. Sasaki, T. Okada, M. Maeda, T. Kisu, M. Takeo, and K. Enpuku, 1995, *J. App. Phys.* **77** (11), 5961.
- [Kwon 1997] Kwon, C., M.C. Robson, K.-C. Kim, J.Y. Gu, S.E. Lofland, S.M. Bhagat, Z. Trajanovic, M. Rajeswari, T. Venkatesan, A.R. Kratz, R.D. Gomez, and R. Ramesh, 1997, *J. Magn. Magn. Mater.* **172**, 229.
- [Liu 1989] Liu, Y. P., K. Warner, and C. Chan, 1989, *J. App. Phys.* **66** (11), 5514.
- [London 1935] London, F., H. London, 1935, *Proc. Roy. Soc.* **A149**, 71.

- [Lu 1996] Lu, Y., X.W. Li, G.Q. Gong, G. Xiao, A. Gupta, P. Lecoeur, J.Z. Sun, Y.Y. Wang, and V.P. Dravid, 1996, Phys. Rev. B **54** (12), R8357.
- [Lyonnet 2000] Lyonnet, R., J.-L. Maurice, M.J. Hytch, D. Michel, and J.-P. Contour, 2000, App. Surf. Sci. **162-163**, 245.
- [Mannhart 1996] Mannhart, J., 1996, Supercond. Sci. Tech. **9** (2), 49.
- [McGuire 1975] McGuire, T.R., and R.I. Potter, 1975, IEEE Trans. Magn. **MAG-11**, 1039.
- [Mikheenko 2001] Mikheenko, P., M.S. Colclough, C. Severac, R. Chakalov, F. Welhoffer, and C. M. Muirhead, 2001, Appl. Phys. Lett. **78** (3), 356.
- [Miyazaki 1995] Miyazaki, T. and N.J. Tezuka, 1995, Magn. Magn. Mater. **139**, L231.
- [Moodera 1995] Moodera, J. S., L.R. Kinder, T.M. Wong, and R. Meservey 1995, Phys. Rev. Lett. **74**, 3273.
- [Moodera 1999] Moodera, J. S., and G. Mathon, 1999, Jnl. Mag. Mag. Mat. **200**, 248.
- [Mourachkine 2002] Mourachkine, A., 2002, *High-Temperature Superconductivity in Cuprates*, edited by A. Van Der Merwe (Kluwer Academic Publishers, Netherlands).
- [Morán 2003] Morán, O., R. Hott, R. Schneider, H. Wühl, and J. Halbritter, 2003, Jnl. App. Phys. **94** (10), 6667.
- [Mott 1936] Mott, N.F., 1936, Proc. Roy. Soc. A **153**, 699.
- [Mukaida 1990] Mukaida, M., S. Miyazawa, M. Sasaura, and K. Kuroda 1990, Jpn. J. Appl. Phys. **29** (6), L 936.
- [Mukaida 1992] Mukaida, M., and S. Miyazawa, 1992, Jpn. J. Appl. Phys. **31** (Pt. 1, No. 10), 3318.

- [Mukaida 1989] Mukaida, M., K. Kuroda, and S. Miyazawa, 1989, *Appl. Phys. Lett.* **55** (11), 1129.
- [Muzeyyan 1994] Muzeyyan, E., E. G. Gonzalez, H. -U. Habermeier and B. Oral, 1994, *J. Appl. Phys.* **74** (4), 1646.
- [Noh 2001] Noh, J.S., T.K. Nath, C. B. Eom, J.Z. Sun, W. Tian, and X.Q. Pan, 2001, *Appl. Phys. Lett.* **79** (2), 233.
- [Obata 1999] Obata, T., T. Manako, Y. Shimakawa, and Y. Kubo, 1999, *App. Phys. Lett.* **74** (2), 290.
- [Ogimoto 2003] Ogimoto, Y., M. Izumi, A. Sawa, T. Manako, H. Sato, H. Akoh, M. Kawasaki, and Y. Tokura, 2003, *Jpn. J. Appl. Phys.* **42** Pt. 2, L369.
- [Ogrin 2000] Ogrin, F.Y., S.L. Lee, and Y.F. Ogrin, 2000, *J. Magn. Magn. Mater.* **219**, 331.
- [Ohnishi 1999] Ohnishi, T., K. Takahashi, M. Nakamura, M. Kawasaki, M. Yoshimoto, and H. Koinuma, 1999, *Appl. Phys. Lett.* **74** (17), 2531.
- [Okimoto 1995] Okimoto, Y., Katsufuji, K., Ishikawa T., Urushibara A., Arima T., and Tokura Y., 1995, *Phys. Rev. Lett.* **75** (1), 109.
- [Olšan 1993] Olšan, V., and M. Jelínek, 1993, *Physica C* **207**, 391.
- [Onnes 1911] Onnes, H.K. 1911, *Comm. Phys. Lab. Univ. Leiden* Nos. **119,120,122**.
- [Owen 1972] Owen C.S. and D.J. Scalapino, 1972, *Phys. Rev. Lett.* **28** (24), 1559.
- [Pailloux 2002] Pailloux, F., D. Imhoff, T. Sikora, A. Barthelemy, J.-L. Maurice, J.-P. Contour, C. Colliex, and A. Fert, 2002, *Phys. Rev. B* **66**, 014417.
- [Park 1998] Park, J.H., E. Vescovo, H.-J. Kim, C. Kwon, R. Ramesh, and T. Venkatesan, 1998, *Nature* **392**, 794.

- Park, J.H., E. Vescovo, H.-J. Kim, C. Kwon, R. Ramesh, and T. Venkatesan, 1998, *Physical Review Letters* **81** (9), 1953.
- [Parker 1975] Parker, W.H., 1975, *Phys. Rev. B* **12** (9), 3667.
- [Pauthenet 1970] Pauthenet, R., and C. Veyret, 1970, *J. Phys.* **31**, 65.
- [Pippard 1953] Pippard, A.B., 1953, *Proc. Roy. Soc.* **A216**, 547.
- [Plausinaitiene 2001] Plausinaitiene, V., A. Abrutis, B. Vengalis, R. Butkute, J.P. Senateur, Z. Saltyte, and V. Kubilius, 2001, *Physica C*, **351**, 13.
- [Roshko 1991] Roshko, A., R.H. Ono, J.A. Beall, J. Moreland, A.J. Nelson, and S.E. Asher, 1991, *IEEE Trans. Magn.* **27**, 1616.
- [Saenger 1994] Saenger, K. L., 1994, in *Pulsed laser deposition of Thin Films*, edited by D. B. Chrisey and G. K. Hubler (Wiley, New York).
- [Sakar 2001] Sakar, S., P. Raychaudhuri, P.K. Mal, A.R. Bhangale, and R. Pinto, 2001, *J. App. Phys.* **89** (11), 7502.
- [Sanghamitra 2003] Sanghamitra, K., D.C. Kundaliya, J. John, S. Rayaprol, S.R. Shinde, D.G. Kuberkar, R. Pinto, and S.K. Malik, 2003, *J. App. Phys.* **93** (10), 8203.
- [Schilling 1993] Schilling, M., F. Goerke, and U. Merkt, 1993, *Thin Solid Films* **235**, 202.
- [Schweitzer 1995] Schweitzer, D., T. Bollmeier, B. Stritzker, and B. Rauschenbach,, 1995, *Thin Solid Films* **280**, 147.
- [Schneider 1999] Schneider, C.W., R. Moerman, D. Fuchs, R. Schneider, G.J. Gerritsman, and H. Rogalla, 1999, *IEEE Trans. App. Supercond.* **9** (2), 3648.
- [Sheats 1993] Sheats, J.R., R.C. Taber, P. Merchant, and J. Amano, 1993, *J. Vac. Sci. Technol. A* **11** (3), 574.

- [Shi 1993] Shi, L., G.L. Huang, C. Lehane, D.H. Kim, and H.S. Kwok, 1993, Appl. Phys. Lett. **63** (20), 2830.
- [Shih 1988] Shih, I. and C.X. Qiu, 1988, Appl. Phys. Lett. **52** (18), 1523.
- [Shipley Company] Shipley Company, Microposit S1800 series photoresist flyer.
- [Olsson 1994] Olsson, E., and S. L. Shinde', 1994, in *Interfaces in high-Tc superconducting systems*, edited by S.L. Shinde' and D.A. Rudman (Springer-Verlag, New York).
- [Siegal 1992] Siegal, M.P., R.B. van Dover, J.M. Phillips, E.M. Gyorgy, A.E. White, and J.H. Marshall, 1992, Appl. Phys. Lett. **60** (23), 2932.
- [Si 1996] Si, Qimiao, 1996, Phys. Rev. Lett. **78** 9, 1997.
- [Slonczewski 1989] Slonczewski, J.C., 1989, Phys. Rev. B **39**, 6995.
- [Simmons 1963-64] Simmons, J.G., 1964, J. Appl. Phys. **35**(9), 2655.
- Simmons, J.G., 1963, J. Appl. Phys. **34**(9), 2581.
- Simmons, J.G., 1963, J. Appl. Phys. **34**(6), 1793.
- Simmons, J.G., 1963, J. Appl. Phys. **34**, 238.
- [Singh 1989] Singh, R. K., L. Ganapati, P. Tiwar, and J. Narayan, 1989, Appl. Phys. Lett. **55**, 2351.
- [Smith 1929] Smith, A.W., and R.W. Sears, 1929, Phys. Rev. **34**, 1466.
- [Soulen 1998] Soulen, R.J., J.M. Byers, M.S. Osofsky, B. Nadgorny, T. Ambrose, S.F. Cheng, P.R. Broussard, C.T. Tanaka, J. Nowak, J.S. Moodera, A. Barry, and J.M.D. Coey, 1998, Science **282** (5386), 85.
- [Soh 2000] Soh, Y.-A., G. Aeppli, N.D. Mathru, and M.G. Blamire, 2000, J. Appl. Phys. **87**, 6743.

- [Stroud 1998] Stroud, R. M., J. Kim, C.R. Eddy, D.B. Chrisey, J.S. Horwitz, D. Koller, M.S. Osofsky, and R.J. Soulen, Jr., 1998, *J. Appl. Phys.* **83** (11), 7189.
- [Sun 1997-2001] Sun, J.Z., L. Krusin-Elbaum, P.R. Duncombe, A. Gupta, and R.B. Laibowitz, 1997, *Appl. Phys. Lett.* **70**(13), 1769.
- Sun, J.Z., D.B. Abraham, K. Roche, and S.S.P. Parkin, 1998, *Appl. Phys. Lett.* **73**(7), 1008.
- Sun, J.Z., 2001, *Physica C* **350**, 215.
- [Sun 1996] Sun, J.Z., W.J. Gallagher, P.R. Duncombe, L. Krusin-Elbaum, R.A. Altman, A. Gupta, Yu Lu, G.Q. Gong, and G. Xiao, 1996, *Appl. Phys. Lett.* **69** (21), 3266.
- [Sun 1998] Sun, J.Z., 1998, *Phil. Trans. R. Soc. Lond. A* **356**, 1693.
- [Tang 2003] Tang, H.X., R.K. Kawakami, D.D. Awschalom, and M.L. Roukes, 2003, *Phys. Rev. Lett.* **90** 10, 107201.
- [Tedrow 1970-73] Tedrow, P.M., R. Meservey, and P. Fulde, 1970, *Phys. Rev. Lett.* **25**, 1270.
- Tedrow, P.M. and R. Meservey, 1971, *Phys. Rev. Lett.* **26**, 192.
- Tedrow, P.M. and R. Meservey, 1973, *Phys. Rev. B* **7**, 318.
- [Tedrow 1994] Tedrow, P.M. and R. Meservey, 1994, *Phys. Rep.* **238**, 173.
- [Teresa 1999] Teresa, J.M. De, A. Barthélémy, A. Fert, J.P. Contour, R. Lyonnet, F. Montaigne, P. Seneor, and A. Vaurès, 1999, *Phys. Rev. Lett.* **82**, 4288.
- [Timm 1996] Timm, R., P.R. Willmott, and J.R. Huber, 1996, *J. Appl. Phys.* **80** (3), 1794.
- [Tokura 1999] Tokura, Y., and Y. Tomioko 1999, *J. Magn. Magn. Mater.* **200**, 1.

- [Urushibara 1995] Urushibara, A., Y. Moritomo, T. Arima, A. Asamitsu, G. Kido, Y. Tokura, 1995, Phys. Rev. B **51**, 14103.
- [Valet 1993] Valet, T., and A. Fert, 1993, Phys. Rev. B **48** 10, 7099.
- [van Son 1987] van Son, P. C., H. van Kemp, and P. Wyder, 1987, Phys. Rev. Lett. **58** 21, 2271.
- [Vas'ko 1997] Vas'ko, V.A. Larkin, P.I. Krauss, K.R. Nikolaev, D.E. Grupp, C.A. Nordman, and A.M. Goldman, 1997, Phys. Rev. Lett. **78** (6), 1134.
- [Veerdonk 1997] Veerdonk, R.J.M. van de, J. Nowak, R. Meservey, J.S. Moodera, and W.J.M. de Jonge, 1997, Appl. Phys. Lett. **71** (19), 2839.
- [Viret 1997] Viret, M., M. Drouet, J. Nassar, J. P. Contour, C. Fermon, and A. Fert, 1997, Europhysics Letters **39**, 545.
- [Wollan 1953-55] Wollan, E.O., and W.C. Koehler, 1953, Phys. Rev. **19**, 120.  
Wollan, E.O., and W.C. Koehler, 1955, Phys. Rev. **100**, 545.
- [Wellstood 1993] Wellstood, F. C., J. J. Kingston, and J. Clarke, 1993, J. Appl. Phys. **75** (2), 15.
- [Willmott 2000] Willmott, P. R., and J. R. Huber, 2000, Rev. Mod. Phys. **72** (1), 315.
- [Wei 1997] Wei, J.Y.T., N.-C. Yeh, and R.P. Vasquez, 1997, Phys. Rev. Lett. **79**, 5150.  
J.Y.T. Wei, N.-C. Yeh, and R.P. Vasquez, 1998, J. Appl. Phys. **83**, 7366.
- [Wold 1957] Wold, A., B. Post, and E. Banks, 1957, J. Am. Chem. Soc. **70**, 4911.
- [Wong 1997] Wong, A., R. Liang, M. Gardener, and W. N. Hardy, 1997, J. Appl. Phys. **82** (6), 3019.

- [Wong 1976-77] Wong, T.-W., J.T.C. Yeh, and D.N. Langenberg, 1976, Phys. Rev. Lett. **37** (3), 150.
- Wong, T.-W., J.T.C. Yeh, and D.N. Langenberg, 1977, IEEE Trans. Magn. **MAG-13** (1), 743.
- [Wu 1994] Wu, J. Z., and W. K. Wu, 1994, Phys. Rev. B **49** (2), 1381.
- [Wu 1987] Wu, M. K., J. R. Ashburn, C. J. Torng, P. H. Hor, R. L. Meng, L. Gao, Z. J. Huang, Y. Q. Wang, and C. W. Chu, 1987, Phys. Rev. Lett. **58** (9), 908.
- [Xu 1998] Xu, S.Y., C.W. Tan, and C.K. Ong, 1998, Meas. Sci. Technol. **9**, 1912.
- [Yan 1987] Yan, M. F., R. L. Barns, H. M. O'Bryan, Jr., P. K. Gallagher, R. C. Sherwood, and S. Jin, 1987, Appl. Phys. Lett. **51** (7), 532.
- [Hu 2004] Hu, Yufeng, 2004, Ph.D. Thesis, The Pennsylvania State University.
- [Yu 1996] Yu, T., Y.F. Chen, Z.G. Liu, X.Y. Chen, L. Sun, N.B. Ming, and L.J. Shi, 1996, Mater. Lett. **26** (1-2), 73.
- [Zegenhagen 1998] Zegenhagen, J., T. Haage., and Q.D. Jiang, 1998, Appl. Phys. A **67**, 711.
- [Zener 1951] Zener, C 1951, Phys. Rev. **81**, 440.
- [Zheng 1992] Zheng, X. -Y., D. H. Lowndes, S. Zhu, J. D. Budai, and R. J. Warmack, 1992, Phys. Rev. B **45** (13), 7584.

## Vita

Eric Tyson Wertz

### Education

- B.S., Physics, 1996, Bucknell University, Lewisburg, PA.
- Ph.D., Physics, 2004, The Pennsylvania State University, University Park, PA.

### Honors and Awards

- Excellence in Teaching Award, The Pennsylvania State University, 2000
- Duncan Fellowship, The Pennsylvania State University, 1996-1998
- Roberts Fellowship, The Pennsylvania State University, 1996
- The Lowry Prize for most promising physicist, Bucknell University, 1996

### Professional Experience

- Research Assistant, The Pennsylvania State University, 1998-2004
- Teaching Assistant, The Pennsylvania State University, 1996-2000
- Research Assistant, The College of William and Mary, 1995
- Teaching Assistant, Bucknell University, 1993-1996